FACULTEIT WETENSCHAPPEN
Vakgroep fysica en sterrenkunde

MAPPING THE INTERSTELLAR DUST IN GALAXIES THROUGH RADIATIVE TRANSFER MODELLING

Gert De Geyter

Supervisor: Prof. Dr. Maarten Baes

Supervisor:

Maarten Baes
Vakgroep Fysica & Sterrenkunde
Universiteit Gent

Reading Committee:

Prof. Dr. Reynier Peletiers
Kapteyn Astronomical Institute
Rijksuniversiteit Groningen

Dr. Simone Bianchi
Instituto Nationale di Astrofisica
Osservatorio Astrofisico di
Arcetri

Prof. Dr. Sven De Rijcke
Vakgroep Fysica & Sterrenkunde
Universiteit Gent

Examination Board:
President:

Prof. Dr. Jan Ryckebusch
Vakgroep Fysica & Sterrenkunde
Universiteit Gent

Prof. Dr. Herwig Dejonghe
Vakgroep Fysica & Sterrenkunde
Universiteit Gent

Prof. Dr. Dimitri Van Neck
Vakgroep Fysica & Sterrenkunde
Universiteit Gent

Prof. Dr. Freddy Callens
Vakgroep
Vastestofwetenschappen
Universiteit Gent

Contents

1 Introduction **12**
- 1.1 Spiral galaxies . . . 12
- 1.2 ISM and interstellar dust . . . 15
- 1.3 Dust radiative transfer . . . 19
- 1.4 Inverse radiative transfer . . . 22
- 1.5 Dust energy balance . . . 25
- 1.6 Overview of this thesis . . . 26

2 FitSKIRT **29**
- 2.1 Genetic Algorithms . . . 29
  - 2.1.1 Genetics and evolution . . . 29
  - 2.1.2 Genetic Algorithms . . . 30
  - 2.1.3 The GAlib library . . . 33
- 2.2 FitSKIRT in a nutshell . . . 40
  - 2.2.1 SKIRT . . . 40
  - 2.2.2 General overview of FitSKIRT . . . 47
- 2.3 Particular aspects of FitSKIRT . . . 50
  - 2.3.1 Oligochromatic fitting . . . 50
  - 2.3.2 Convolution . . . 52
  - 2.3.3 Luminosity Fitting . . . 52
  - 2.3.4 Error analysis . . . 61
  - 2.3.5 Parallelisation . . . 63
- 2.4 A concise FitSKIRT user manual . . . 63
  - 2.4.1 Data preparation . . . 63
  - 2.4.2 Structure and setup . . . 66
  - 2.4.3 Results and analysis . . . 68

3 Test cases **71**
- 3.1 Test case 1: monochromatic fitting to a mock image . . . 71
  - 3.1.1 The model . . . 71
  - 3.1.2 One free parameter . . . 74
  - 3.1.3 Three free parameters . . . 75

3.1.4 Eleven free parameters . . . 76
3.1.5 Tests using alternative optimisation methods . . . 79
3.2 Test case 2: V-band fitting of NGC 4013 . . . 82
3.3 Test case 3: Oligochromatic Fitting . . . 85
3.4 Conclusions . . . 88

4 Sample of edge-on spiral galaxies 90
4.1 Radiative transfer modelling of edge-on spiral galaxies . . . 90
4.2 Sample selection . . . 91
4.3 Radiative transfer modelling . . . 93
4.3.1 The model . . . 93
4.3.2 FitSKIRT fits . . . 95
4.4 Results . . . 98
4.4.1 IC 2098 . . . 98
4.4.2 UGC 4136 . . . 98
4.4.3 IC 2461 . . . 103
4.4.4 UGC 5481 . . . 103
4.4.5 NGC 3650 . . . 103
4.4.6 NGC 3987 . . . 104
4.4.7 NGC 4175 . . . 104
4.4.8 IC 3203 . . . 104
4.4.9 IC 4225 . . . 105
4.4.10 NGC 5166 . . . 105
4.4.11 NGC 5908 . . . 105
4.4.12 UGC 12518 . . . 106
4.5 Discussion . . . 106
4.5.1 Quality of the FitSKIRT radiative transfer fits . . . 106
4.5.2 The stellar disc and bulge . . . 109
4.5.3 The star-dust geometry . . . 110
4.5.4 Optical depth . . . 112
4.5.5 Dust mass and the dust energy balance . . . 113
4.6 Conclusions . . . 115

5 Dust energy balance study 117
5.1 The targets . . . 118
5.1.1 Target selection . . . 118
5.1.2 Data . . . 119
5.2 Panchromatic radiative transfer modelling . . . 119
5.2.1 Modelling approach . . . 119
5.2.2 Case A models . . . 121
5.2.3 Case B models . . . 124

5.3 Discussion and conclusions 128

6 Other applications **132**
6.1 FitSKIRT applications 132
6.1.1 The edge-on spiral galaxy NGC 5908 132
6.1.2 Large edge-on spiral galaxies from the HEROES sample . . . 135
6.1.3 The dusty early-type galaxy NGC 4370 140
6.1.4 Mock galaxies from hydrodynamical simulations 142
6.1.5 Irregular edge-on galaxies 144
6.2 Future improvements 145
6.2.1 Peanut/Boxy bulges 145
6.2.2 Spiral arms and clumpiness 145
6.2.3 Different optimisation techniques 146
6.2.4 Panchromatic modelling 148

7 Conclusion **151**

8 Samenvatting **155**

List of Figures

1.1 Hubble classification . . . 13
1.2 Andromeda galaxy . . . 13
1.3 NGC891 . . . 14
1.4 Spectral energy distribution . . . 16
1.5 NGC 253 . . . 17
1.6 Forward radiative transfer . . . 23
1.7 Inverse radiative transfer . . . 24
1.8 Dust energy balance . . . 25

2.1 Crossover and mutation . . . 31
2.2 Function 2.1 . . . 34
2.3 Genetic algorithms minimisation of Function 2.1 . . . 35
2.4 Function 2.2 . . . 36
2.5 Genetic algorithms minimisation of Function 2.2 . . . 37
2.6 DIAMONDS code . . . 39
2.7 SKIRT schematics . . . 41
2.8 SKIRT SPH simulation input . . . 42
2.9 SED NGC4565 . . . 43
2.10 Ski file . . . 45
2.10 (continued) . . . 46
2.11 χ^2 definition . . . 48
2.12 FitSKIRT flowchart . . . 49
2.13 Convolution . . . 53
2.14 Golden section search . . . 54
2.15 Two component fitting . . . 56
2.16 Downhill simplex optimisation . . . 58
2.17 Position fitting . . . 60
2.18 Uncertainty determination . . . 61
2.19 Sky background . . . 64
2.20 Cleaned FitSKIRT sample . . . 65
2.21 FitSKIRT scheme . . . 66
2.22 Fski file . . . 69

2.22 (continued) . . . 70

3.1 1D dust mass determination . . . 75
3.2 3D dust disk determination . . . 76
3.3 Test case . . . 77
3.4 LM and DS method . . . 81
3.5 Residuals DS . . . 81
3.6 NGC 4013 . . . 83
3.7 Cumulative pixel distribution . . . 84
3.8 Oligochromatic test validation . . . 86

4.1 Sample thumbnails . . . 92
4.2 Best FitSKIRT models . . . 99
4.2 (continued) . . . 100
4.2 (continued) . . . 101
4.2 (continued) . . . 102
4.3 Cumulative pixel distribution of sample . . . 106
4.4 Dust ratios . . . 111
4.5 Sample mass ratios . . . 114

5.1 SED IC 4225 . . . 122
5.1 SED NGC 5166 . . . 122
5.2 Observations and models for IC 4225 . . . 126
5.3 Observations and models for NGC 5166 . . . 127

6.1 Residuals NGC 5908 . . . 133
6.2 SED NGC 5908 . . . 134
6.3 NGC4013 PACS and SPIRE data . . . 136
6.4 HEROES models . . . 137
6.4 (continued) . . . 138
6.5 NGC 4370 . . . 141
6.6 R13 and ERIS models . . . 143
6.7 NGC 7321 . . . 144
6.8 Peanut . . . 145
6.9 NGC891 model . . . 147

8.1 NGC891 . . . 156
8.2 χ^2 definitie . . . 157
8.3 Beste FitSKIRT modellen . . . 158
8.4 SED NGC 5166 . . . 159

List of Tables

3.1 Monochromatic test model and results 73
3.2 Comparison GA and DS 78
3.3 Comparison FitSKIRT and other codes 83
3.4 Oligochromatic test results 86

4.1 Sample properties 94
4.2 FitSKIRT results 96
4.2 (continued) 97
4.3 Sample averages 108

5.1 Observed fluxes 120

6.1 HEROES fits 139

Acknowledgement

This PhD thesis should contain way more names on the cover as this would have never been realised without the support of so many people. First of all, my (literal) eternal gratitude goes to my supervisor Maarten. You were always there with the necessary advice, suggestions and support and I will never forget the many opportunities you gave me. In fact, the trust you have placed in me when I was a thesis student, was exactly what I needed to really get me started. I would also like to thank Sven for the many interesting discussions we have had over lunch. The large variety of discussed topics, going from existential matter to down right ridiculous stuff, were always very enjoyable. In addition you are a great person with an amazing sense of humor.

I also greatly appreciate the efforts of the other members of the jury. Thanks Simone for the interesting discussions we have had (usually involving NGC 891 sooner or later). Thank you Reynier for your useful insights you have had on my work at the workshop in Leiden and reading my thesis. Of course I also want to thank Herwig for introducing me to astronomy on a professional level and whose passionate way of lecturing infected me. I also want to thank Jan for the interesting lessons he gave on statistical physics and the organised lectures on econophysics. I was happily surprised by how much I remembered when I was recently confronted with an Ising spin model. Also the other members of the jury Dimitri and Freddy, thank you for spending your time and effort in reading my thesis.

I would also like to thank all the people I have shared an office with. Thank you for listening enthusiastically when I had yet another completely irrelevant and uninteresting story while you were working vigorously. Sorry for those! Jacopo, I can not thank you enough for everything you did for me. Not only did you assist me in everything whenever I had a problem, your enthusiasm and complete devotion to help is inspiring to say the least. You and Mariannetje will no doubt be the most amazing, cool parents of which Angelica and Rebecca's future friends will be so jealous. Peter, thank you for all the interesting conversations we have had over the last few years and for all the effort and time you have spend in learning me various things. I have learned both professional and personality skills and always admired your focus, determination and unrivalled honesty. Sebastien, thank you for all the

great moments we have had the last years and for helping me out whenever I had another filthy data set. I will never forget the numerous trips, receptions or "networking" drinks we had together! (Well maybe I don't really recall all of them but let's just say most of them). Thank you Bert for all the great conversations (some of them involving beer) and the occasional youtube movie of one of internet undiscovered gems. I'm confident that Shadowfax will blow away the competing codes really soon (and who needs gravity in astronomy anyway). Annelies, thank you for all the great moments we had over the last nine years. It is hard to imagine any more down to earth and straightforward person. I wish you all the best with Anna (and Simon of course) and in your future career (whatever you choose that is :))

Thank you to all other members of the astronomy department for all the great moments we have had the past years; Flor, Mina, Joeri, Waad, Ilse, Tom, Steven, Gianfranco, Joachim, Joris, Sumana, Robbert, Sam, (and who ever I might have forgotten, sry!). Also a big thanks to Inge, Gerbrand and Guy for helping me out with a lot of practical stuff! A thanks to all the bachelor, master and thesis students I have had (Marjorie, good luck with your thesis!). Also a thanks to the many people I have met in my (short) academic career, Franka, Stephan and Tullio to only name a few. I would also like to thank all the people from the Volkssterrenwacht Armand Pien (in particular An) for all their support.

A big thank you for all the fun moments I have had with all the people I've met at the S9. Nele (Verbiest), Karel and Sofie, thank you for all the fun moments we had over the last years! Thanks to Arne, Ben, Nele (Vandersickel), Nele (Callebaut), Boy, Matthias, Karel, ... and all other people for the numerous coffee breaks, inside-out lectures, etc. Also the other physicists I have studied with (yes all of them). Especially Lena, thank you for all the fun moments we have had and for being such an amazing person.

Of course I also want to thank all my other friends. First of all the "fetkloss" gang (and plus ones), thanks for all the cheap holidays, cheap drinks and cheap jokes we had the last (more than) a decade. Saar, thanks for putting up with all my graphic designer BS I've been annoying you with (including the cover of this thesis). You'll be glad to know that I won't be making academic posters any time soon. Thanks to all other Gent/Filo crowd, Gert-jan, Katrien, Doro and Schutzieboy in particular.

Also thanks to all my high school friends Sylvie, Jasmine, Lies, Anke, Greet, Dorien, Sara (and plus ones)! I have the feeling that Lies and Koen just gave the unofficial start for family expansion. Nele, Bart, Gijs (and Sarah), Anne-Sofie, Pieter and Mira thanks for all the great moments ever since we were (extremely) young. I also want to thank all the people I have met since being together with Peter, his family and

friends, in particular Eveline, Emilie, Ellen and Rino. I also want to thank all other people I have met at parties, festivals, lectures, gym, etc.

I would also like to thank my new colleagues at Deloitte, in particular Jeroen, Nikos and Kristof, for giving me this amazing opportunity, being so patient and assisting me with my transition from the academic world.

Of course, I also want to thank my family for helping and supporting me all these years. In particular I would like to thank my parents and my brother for believing in me, although some teacher did not always agree on that. Your support really meant a lot to me!

Last but certainly not least I want to thank Peter. You are the most important thing to have happened to me and I can not thank you enough. You are the kindest and simply the best (see what I did there) person I know. And you put up with my endless nagging and bullying like no one else can. The past seven years and a half have been so great and it makes me wonder what is yet to come.

Gert De Geyter

Introduction 1

1.1 Spiral galaxies

Since the invention of the telescope in 1608, gradually more and more galaxies were discovered. Although a few scientists, e.g. Kant, proposed the possibility that these objects were independent island universe like our own Milky Way, it took about another three hundred years before the general consensus changed. It was only after the Great Debate in 1920, that it was believed that these galaxies were not part of our galaxy but, in fact, located well beyond the borders of the Milky Way. This was later consolidated by Edwin Hubble who used cepheid stars to calculate the distance to a number of galaxies, including the Andromeda galaxy. Today,our observable Universe is estimated to contain several hundreds of billions of galaxies.

In order to get a clear overview of the different types, multiple classification schemes are used. In figure 1.1 we can see an overview of the most commonly used scheme for galaxies, the Hubble Classification Diagram. The galaxies on the left typically consist of an older stellar population with an elliptical distribution. A bit counter-intuitive these galaxies are called early-type. In general, they do not contain large quantities of interstellar matter (ISM). These systems are pressure driven and their stars have no particular orbit but rather move on random trajectories around the center. In the center of the diagram we find the lenticular galaxies which are disk galaxies who have used up most of their interstellar matter (ISM) and have little to no ongoing star formation. The right side represent the disk or late-type galaxies, which are split up into two distinct branches. The upper branch are the regular spiral galaxies while the lower ones are the spiral galaxies with the presence of a bar. In the center most of them have a bulge, an additional tightly packed group of stars. These can again be either pressure supported and shaped more like an elliptical galaxy (called classic bulges) or are more shaped like a disk galaxy (pseudo-bulges) (Gadotti, 2009). In most cases, the bulge and disk also have distinct stellar populations, where the disks are blue and the bulges contain older, redder stars.

For the most part of this thesis (apart from Section 6.1.3) we will only consider disk galaxies, without separately handling the regular and barred galaxies. The disks of these galaxies usually contain the larger portion of the baryonic mass and angular

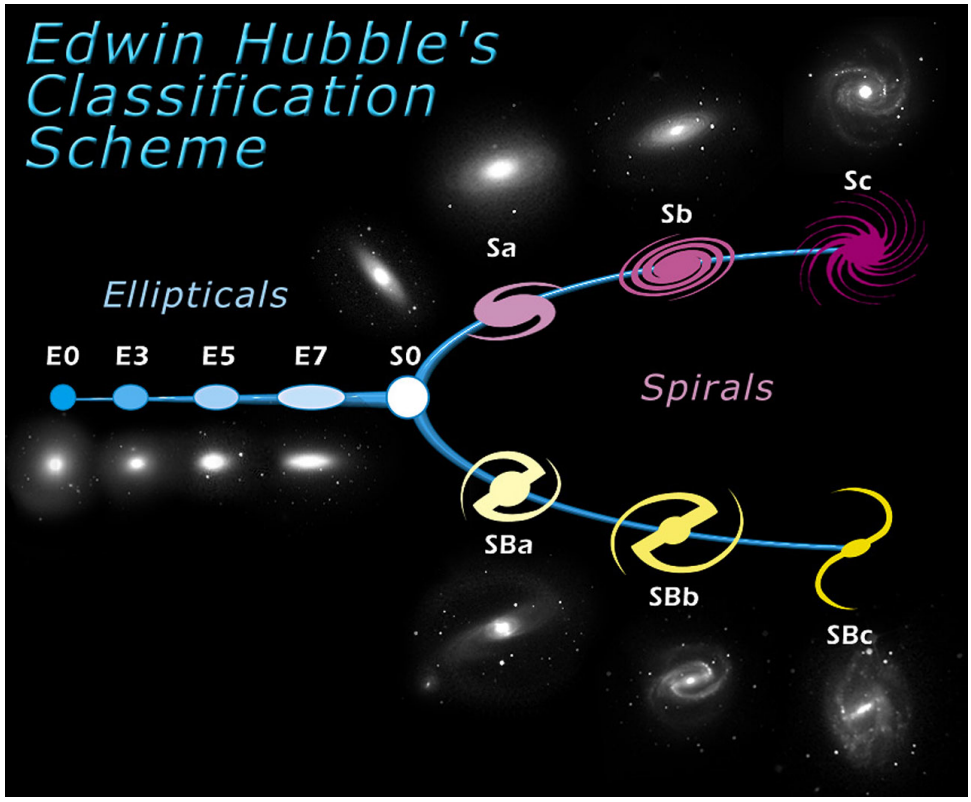

Figure 1.1: The Hubble classification diagram showing the major types of galaxies. On the left we see the early-type elliptical galaxies (E) and the late-type spiral galaxies, either barred (SB) or regular (S) on the right. Galaxies not falling within this diagram are classified as irregular. The image is taken from `http://www.spacetelescope.org/`.

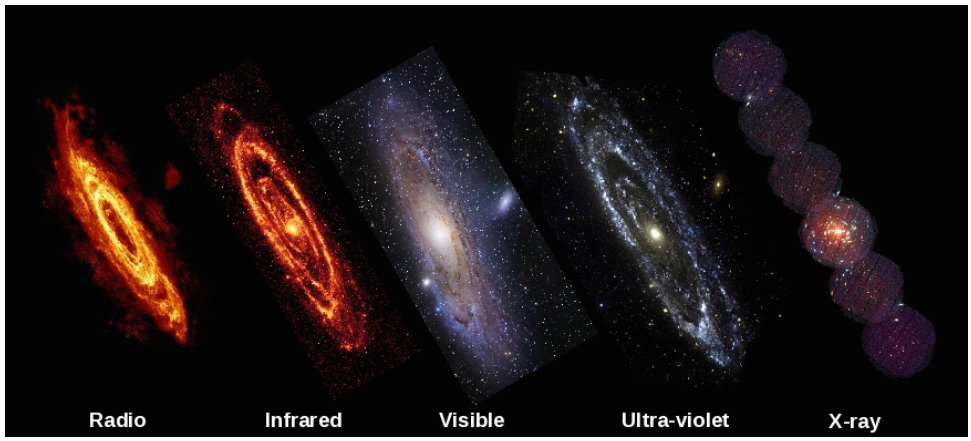

Figure 1.2: The Andromeda galaxy as seen at different wavelengths. The image is taken from `http://www.astroblogs.nl/`.

Figure 1.3: NGC 891, a nearby spiral galaxy seen edge-on. The left is slightly bluer than the right side, possible the effect of a spiral arm. The image is taken from `http://www.feraphotography.com/AM14/pics/`.

momentum and consist out of younger stars. In Figure 1.2 we can see the Andromeda galaxy, observed at different wavelengths. Notice that in the Ultra-Violet (UV), the rings are particularly prominent, as these are the places where massive, short-lived and UV emitting stars are formed. Consequently, UV is a useful tracer for actively star forming regions. It also clear from Figure 1.2 that the UV shows a lot of similarities with an infrared image. As will be discussed in detail in Section 1.2 and 1.3, dust is the primary emitting source in the infrared wavelength regime and is also a good tracer for star formation.

The main focus of this thesis will be the study of spiral galaxies seen edge-on. Using galaxies with an inclination close to 90 degrees offers some unique advantages. In Figure 1.3, a composite colour image of NGC 891, a nearby spiral galaxy seen edge-on, is shown. Notice that, in this case, one can easily identify all the separate components of the galaxy: the stellar disk, the bulge and the dust disk. Not only the radial structure can be determined, but the vertical distribution of the star-dust geometry can be studied in this projection. While face-on galaxies might reveal more structures like spiral arms, bars and rings, they completely lack the information about the disks and bulge heights. From a modeller's point of view, the smoothening of small-scale structures in the edge-on projection also allows for more basic models. In Figure 1.3 we can only see a very subtle hint of the spiral arm, resulting in a blue left side and a slightly more attenuated right side. The dust disk blocks the light coming from the stars, which, in this case, results in a clearly visible dust lane. Therefore edge-on spiral galaxy allow us to study the dust content in two ways: one being the observed extinction in optical bands and the other being the observed infrared emission from the dust itself. As we will be investigating structural parameters of spiral galaxies and its dust content in this thesis, all these assets are of crucial importance. In Chapter 6 we will investigate a few other non edge-on galaxies.

1.2 ISM and interstellar dust

The interstellar medium (ISM) is essentially defined as the very broad collection of all matter in galaxies not including stars or dark matter. It serves as a reservoir of material out of which new stars are formed. The ISM is comprised of two major components: gas and dust. A variety of different phases of the gaseous ISM exist, depending on a number of conditions like the density, temperature, etc. (Tielens, 2005; Kwok, 2007). The ISM is usually defined as atomic or molecular referring to the state of the hydrogen element.

- Atomic gas is often the most dominant cold gas component in galaxies and can be observed at the hydrogen 21 cm or HI line. Although this transition (with a transition probability of about 3×10^{-15} s) is highly forbidden, due to the extreme quantities of atomic hydrogen, HI maps of nearby galaxies are commonly used to trace the cold gas in late-type galaxies.
- Hydrogen can also be completely ionised. The stripped electrons can later be captured by the ions while the energy is re-emitted as recombination lines. These HII are of particular interest when one wants to study the regions where new stars are formed. As ionising atomic hydrogen requires quite hard radiation coming from very hot, young stars, it is a very good tracer for actively star forming regions.
- Molecular hydrogen, the basic building block to form new stars, is harder to observe. The H_2 molecule has no intrinsic dipole moment. Therefore, tracing this component is only possible through some vibrational states in the MIR or in absorption in the UV. Tracing the colder molecular hydrogen is usually done by observing CO rotational line emission as CO is the second most abundant molecule in the ISM. However, due to the uncertainty of the CO/H_2-ratio, only a rough estimate on the cold molecular gas is feasible in most cases.

In Figure 1.4 we can see how the stars, dust and gas each contribute to the spectral energy distribution (SED) of a typical spiral galaxy. This SED is essentially the total amount of energy emitted by the galaxy at a certain wavelength and is commonly used to investigate the general energy house holding of galaxies. Roughly speaking, stars dominate the UV/optical/near-infrared (NIR), dust dominates the mid-infrared (MIR), far-infrared (FIR) or submillimeter (submm) regime while gas is the most luminous component at radio wavelengths, and at specific lines across the entire electromagnetic spectrum, corresponding to atomic or molecular transitions. Typically, the ISM only contributes to about 3% of the total baryonic mass of galaxies, however this percentage depends strongly on the galaxy type. Of this mass, only a few percent is attributed to interstellar dust. However, while utterly

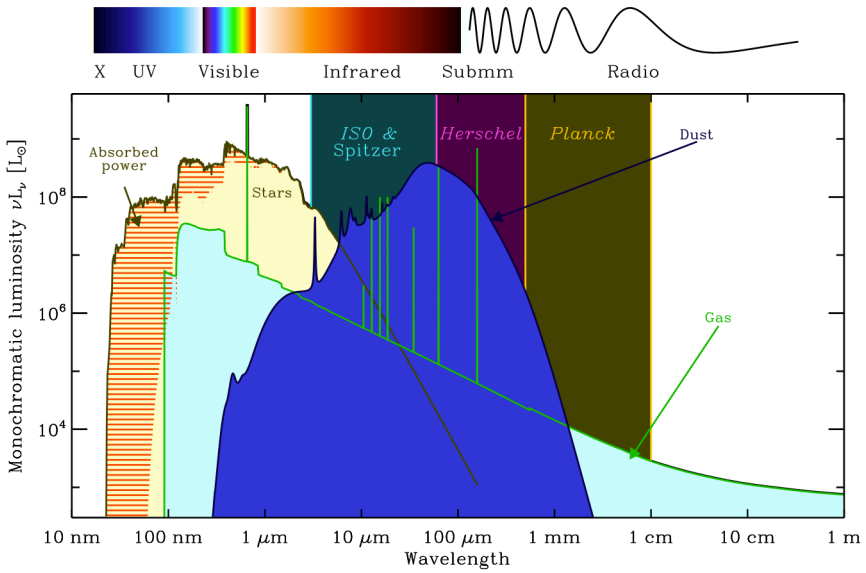

Figure 1.4: A typical view of the panchromatic SED of a spiral galaxy with the contribution of the main components; stars, gas and dust (Galliano et al., 2008).

insignificant in mass, this dust is responsible for about one third of the total luminosity output of galaxies. Interstellar dust is created mainly in the atmospheres of AGB stars (Ferrarotti and Gail, 2006; Dwek and Cherchneff, 2011) and during supernova explosions (Dwek, 1998; Cherchneff, 2010; Indebetouw et al., 2014). Usually it consists of a combination of amorphous graphitic carbonaceous grains, silicates and polycyclic aromatic hydrocarbons (PAHs). Silicates are mainly formed in O-rich stars while carbonaceous grains form in, logically, C-rich environments. Dust grains can be destroyed by a variety of events like cosmic rays, hard interstellar radiation or thermal shocks. Due to the complexity of both the formation and destruction processes, the exact location and migration of these dust grains is hard to model.

However, these dust grains play an important role in a number of physical and chemical processes. They regulate the heating of gas in the ISM through photoelectric heating and inelastic interactions with gas particles, because they effectively shield regions from hard radiation. Dust grains allow the production and survival of a wide range of molecules; in particular, their surface works as a catalyst for the production of molecular hydrogen, which consequently regulates star formation (Hollenbach and Salpeter, 1971). They are also the basic building blocks of planets, comets and meteoroids (Küppers et al., 2005; Watson et al., 2009). Apart from their role in a number of physical and chemical processes, like dust grains are important as they absorb at least one third of the UV/optical light in galaxies (Popescu and Tuffs, 2002). As can be seen in Figure 1.3 and 1.5 this extinction can be very clear in

Figure 1.5: An RGB-image of NGC 253 and 2MASX J00482185-2507365 made using Hubble Space Telescope observations. The overlapping dust disk from 2MASX J00482185-2507365 seems to attenuate the light coming from NGC 253. The image taken from the HST heritage site `http://hubblesite.org/newscenter/archive/releases/2008/33/image/a/`.

the optical bands.

The most direct method to trace the dust grains in galaxies is to measure the thermal emission of the dust grains at MIR, FIR and submm wavelengths. However, as the Earth's atmosphere is largely opaque in this window, most observations are either done from high altitude or space telescopes. With a range going from 12-100 μm, the InfraRed Astronomical Satellite (IRAS) (Neugebauer et al., 1984), launched in 1983 was the first space-based IR telescope. In the coming decades a series of instruments would follow, improving the wavelength range and/or precision. However even the IR telescope that observed at the longest FIR wavelength, the *Infrared Space observatory* (ISO) (Kessler et al., 1996) or Spitzer (Werner et al., 2004), were only able to observe up to 240 μm. As can be seen from Figure 1.4, this means that a large fraction of the cold dust is still not observed. This changed with the launch of the *Herschel* Space Observatory (Pilbratt et al., 2010) in 2009. In particularly, the SPIRE photometer is revolutionary as it filled a gap in the wavelength coverage between

previous FIR missions as IRAS, ISO and Spitzer on the one side, and ground-based submm instruments as SCUBA (Holland et al., 1999) and LABOCA (Siringo et al., 2009) on the other side.

By using FIR and submm observations, it has become possible to determine the total dust mass in galaxies with a reasonable accuracy. The dust mass can be directly estimated by fitting a modified blackbody or more advanced models to the observed spectral energy distribution (e.g., Dunne et al., 2011; Dale et al., 2012; Smith et al., 2013; Ciesla et al., 2014). However, apart from a few nearby targets, these observations lack the spatial resolution to resolve the individual regions and getting a more detailed picture of the dust distribution. However, there are a number of problems with this approach. One complication is the notoriously uncertain value of the dust emissivity at long wavelengths (Bianchi et al., 2003; Kramer et al., 2003; Alton et al., 2004; Shirley et al., 2011) and the mysterious anti-correlation between the dust emissivity index and dust temperature (Dupac et al., 2003; Shetty et al., 2009; Veneziani et al., 2010; Juvela and Ysard, 2012b,a; Kelly et al., 2012; Smith et al., 2012b). A second problem is, as said before, the difficulty to observe in the FIR/submm window, which necessarily needs to be done from space using cryogenically cooled instruments. Therefore observations are usually hard to come by. Finally, the third and most crucial limitation is the poor spatial resolution of the available FIR/submm instruments (typically tens of arcsec). This drawback is particularly important if we want to determine the detailed distribution of the dust in galaxies rather than just total dust masses. This poor spatial resolution limits a detailed study of the dust medium to the most nearby galaxies only (e.g. Meixner et al., 2010; Bendo et al., 2010, 2012; Xilouris et al., 2012; Foyle et al., 2012; De Looze et al., 2012b; Smith et al., 2012b; Galametz et al., 2012a). Moreover, several authors have demonstrated that even estimating total dust masses from global fluxes induces an error due to resolution effects (Galliano et al., 2011; Galametz et al., 2012a).

An alternative method to determine the dust content in galaxies is to use the extinction effects of the dust grains on the stellar emission in the UV, optical or near-infrared (NIR) window. This wavelength range has the obvious advantages that observations are very easy and cheap, and that the spatial resolution is an order of magnitude better than in the FIR/submm window. Also the optical properties of the dust are much better determined in the optical than at FIR/submm wavelengths. The main problem in using this approach is the difficulty to translate attenuation measurements from broadband colors to actual dust masses, mainly because of the complex and often counter-intuitive effects of the star/dust geometry and multiple scattering (Disney et al., 1989; Witt et al., 1992; Byun et al., 1994; di Bartolomeo et al., 1995; Baes and Dejonghe, 2001b; Inoue, 2005). Simple recipes that directly link an attenuation to a dust mass are clearly not sufficient; the only way to proceed is to perform detailed radiative transfer calculations that do take into

account the necessary physical ingredients (absorption, multiple anisotropic scattering) and that can accommodate realistic geometries.

1.3 Dust radiative transfer

The radiation we receive from distant objects provides us with a wealth of information. Not only the emitting sources but also the attenuating medium can be analysed by investigating the transport of the radiation. While making up a negligible fraction of the ISM, interstellar dust grains can have a significant effect on the observed radiation. As they are efficient at absorbing and scattering photons at shorter wavelengths (roughly UV to NIR) and reradiate the absorbed energy at longer wavelengths (MIR to FIR), they can distort our views on structural parameters of galaxies. In order to study these effects properly, one needs to solve the radiative transfer equations keeping in mind all the physical processes in the correct geometrical settings. This requires performing radiative transfer (RT) calculations.

Many techniques have been developed to solve this problem in varying dimensions. One dimensional radiative transfer calculations have been crucial to isolate and demonstrate the often counter-intuitive aspects of important parameters such as star-dust geometry, dust scattering properties and clumping (Bruzual A. et al., 1988; Disney et al., 1989; Witt et al., 1992; di Bartolomeo et al., 1995; Baes and Dejonghe, 2001b; Inoue, 2005). However, when studying systems like disk galaxies, using more complicated models to study 2D and 3D radiative transfer simulations are necessary. Although these problems are harder, using new techniques and the ever increasing computing power, solving these problems has recently become possible (e.g. Xilouris et al., 1999; Popescu et al., 2000; Gordon et al., 2001; Steinacker et al., 2003; Semionov and Vansevičius, 2005; Pinte et al., 2006; Jonsson, 2006; Bianchi, 2008).

The complexity of the RT problem becomes clear when we construct the 3D dust radiative transfer equations. The specific intensity of the radiation field, defined as the amount of energy transported through photon radiation at a position x in space and in the direction of the unit vector $\boldsymbol{k}$, per wavelength unit interval around its wavelength λ, per unit of solid angle and per unit of time, crossing a unit of area perpendicular to $\boldsymbol{k}$, is usually denoted as $I_\lambda(\boldsymbol{x},\boldsymbol{k})$. The continuum radiative transfer equation, describing the variations in the specific intensity due to interactions with the medium, can be written in the general form (Chandrasekhar, 1960; Rybicki and Lightman, 1979; Steinacker et al., 2013):

$$\boldsymbol{k}\cdot\nabla I_\lambda(\boldsymbol{x},\boldsymbol{k}) = j_\lambda(\boldsymbol{x},\boldsymbol{k}) - \kappa_\lambda(\boldsymbol{x})\,\rho(\boldsymbol{x})\,I_\lambda(\boldsymbol{x},\boldsymbol{k}) \tag{1.1}$$

Here, the change of the specific intensity over an infinitesimal path length, determined by the position $\boldsymbol{x}$ and the propagation direction $\boldsymbol{k}$, is equal to contribution of the source minus the sink terms. The source term is the added luminosity emitted at the position $\boldsymbol{x}$ in direction $\boldsymbol{k}$, while the sink term is proportional to the specific intensity and the mass density of the medium ρ at position $\boldsymbol{x}$. This proportional constant is denoted as $\kappa_\lambda(\boldsymbol{x})$.

We can rewrite equation 1.1 in terms of path length where s is a one-dimensional variable defining the distance along the path determined by the position $\boldsymbol{x}$ and direction $\boldsymbol{k}$:

$$\frac{dI_\lambda(s)}{ds} = j_\lambda(s) - \kappa_\lambda(s)\rho(s)I_\lambda(s) \tag{1.2}$$

We can then define the optical depth between two positions $s1$ and $s2$ as

$$\tau_\lambda = \int_{s1}^{s2} \kappa_\lambda(s)\rho(s)ds \tag{1.3}$$

This differential equation has the following formal solution:

$$I_\lambda(s) = \int_{-\infty}^{s} j_\lambda(s')e^{-\tau_\lambda(s',s)}ds' \tag{1.4}$$

From equation 1.1 we can construct the radiative transfer equation for a dusty medium. When assuming only absorption and the primary emission $j^*_\lambda(\boldsymbol{x},\boldsymbol{k})$, usually from stars, we get:

$$\frac{dI_\lambda}{ds}(\boldsymbol{x},\boldsymbol{k}) = j^*_\lambda(\boldsymbol{x},\boldsymbol{k}) - \kappa_{\lambda,abs}(\boldsymbol{x})\rho(\boldsymbol{x})I_\lambda(\boldsymbol{x},\boldsymbol{k}) \tag{1.5}$$

Here the proportionality constant $\kappa_{\lambda,abs}(\boldsymbol{x})$, or absorption coefficient, defines the part of the light which is removed from the radiation field by the dusty medium. This depends on the size, shape, chemical composition, etc. of the dust grains (Draine, 1988). As a result of the absorbed photons, the internal energy of the dust grains will rise. They redistribute this absorbed energy among the internal energy levels according to a Boltzmann distribution depending only on the dust temperature. Because of the re-emitted photons, larger dust grains usually reach a state of local thermal equilibrium (LTE) in the interstellar radiation field (ISRF). These large grains typically emit as a modified black-body at an equilibrium state of 15-30K, hence dominating the far-infrared (FIR) part of the spectral energy distribution (SED) of galaxies. For smaller grains and polycyclic aromatic hydrocarbon (PAH) molecules on the other hand, the ISRF can heat the grains well above their LTE and

the heating due to absorbing photons is a stochastic process. This non local thermal equilibrium (NLTE) usually results in more energetic photons. The emission of very small grains (VSGs) and PAH molecules is therefore usually most prominent in the mid-infrared (MIR) regime.

When the dust emission $j_{\lambda,d}(\boldsymbol{x})$ is included, equation 1.5 takes on the form:

$$\frac{dI_\lambda}{ds}(\boldsymbol{x},\boldsymbol{k}) = j^*_\lambda(\boldsymbol{x},\boldsymbol{k}) + j_{\lambda,d}(\boldsymbol{x}) - \kappa_{\lambda,abs}(\boldsymbol{x})\,\rho(\boldsymbol{x})\,I_\lambda(\boldsymbol{x},\boldsymbol{k}) \tag{1.6}$$

Under the assumption of LTE, where the dust grains have a equilibrium temperature $T_i(\boldsymbol{x})$, this term can be expressed as a sum of emitting modified black-bodies $B_\lambda(T)$:

$$j_{\lambda,d}(\boldsymbol{x}) = \sum_i w_i(\boldsymbol{x})\,\kappa_{\lambda,abs,i}(\boldsymbol{x})\,\rho(\boldsymbol{x})\,B_\lambda(T_i(\boldsymbol{x})) \tag{1.7}$$

However, as each of these dust grains must hold up the balance of absorbed and emitted energy we also get the following condition:

$$\int_0^\infty \kappa_{\lambda,abs,i} J_\lambda(\boldsymbol{x})\,d\lambda = \int_0^\infty \kappa_{\lambda,abs,i} B_\lambda(T_i(\boldsymbol{x}))\,d\lambda \tag{1.8}$$

where $J_\lambda(\boldsymbol{x})$ is the mean intensity of the radiation field, defined as:

$$J_\lambda(\boldsymbol{x}) = \frac{1}{4\pi}\int_{4\pi} I_\lambda(\boldsymbol{x},\boldsymbol{k})\,d\Omega \tag{1.9}$$

The final important ingredient in the radiative transfer equations through a dusty medium is to incorporate the effects of photons scattering of dust grains. This is both a sink and source term as radiation can both be removed from the direction $\boldsymbol{k}$ as well as being scattered from a different direction towards direction $\boldsymbol{k}$. The probability of scattering between these two directions at the position $\boldsymbol{x}$ is given by the scattering phase function $\Phi_\lambda(\boldsymbol{k},\boldsymbol{k'},\boldsymbol{x})$. The proportionality in this case is defined as the scattering coefficient $\kappa_{\lambda,sac}(\boldsymbol{x})$. As the complete radiative transfer equation describing the transfer of photon packages, originally emitted from stars, passes through a dusty medium including dust absorption, dust emission and scattering we then get:

$$\begin{aligned}\frac{dI_\lambda}{ds}(\boldsymbol{x},\boldsymbol{k}) = {} & j^*_\lambda(\boldsymbol{x}) - \kappa_{\lambda,abs}(\boldsymbol{x})\,\rho(\boldsymbol{x})\,I_\lambda(\boldsymbol{x},\boldsymbol{k}) - \kappa_{\lambda,sca}(\boldsymbol{x})\,\rho(\boldsymbol{x})\,I_\lambda(\boldsymbol{x},\boldsymbol{k}) \\ & + j_{\lambda,d}(\boldsymbol{x}) + \kappa_{\lambda,sca}\int I_\lambda(\boldsymbol{x},\boldsymbol{k'})\,\Phi_\lambda(\boldsymbol{k},\boldsymbol{k'})\,d\Omega'\end{aligned} \tag{1.10}$$

Solving this equation is an extremely arduous task. Essentially it is six-dimensional: three spatial dimensions, two directional dimensions and one wavelength dimension. On top of this, it is a non-local and non-linear problem, as at each location in the system, the radiation has to be determined for each wavelength and for all directions. As photons can traverse the complete system, be absorbed and re-emitted or be scattered, the non-locality is present in all spatial, directional and wavelength dimensions.

Due to the complex nature of this problem, in general, analytical solutions are impossible. Therefore, gridding the dimensions of this problem in an intelligent way is necessary (Steinacker et al., 2013). The two most popular approaches to solve this problem are ray-tracing and Monte Carlo radiative transfer. In the Monte Carlo approach, a large number of random numbers from probability distributions are drawn to simulate the involved processes, physics and geometries. While it can be computationally quite exhaustive, the method has a very natural way to handle complicated processes such as scattering.

Thanks to an increase in computational power and the development of efficient algorithms, dust radiative transfer codes have become increasingly more realistic and powerful. They can now be applied to arbitrary geometries, and can include physical processes as absorption, multiple anisotropic scattering, polarisation, thermal and non-thermal emission (e.g. Gordon et al., 2001; Baes et al., 2003, 2011; Jonsson, 2006; Bianchi, 2008; Robitaille, 2011). An overview of the most important developments, advantages and disadvantages of different approaches regarding 3D dust radiative transfer codes can be found in Steinacker et al. (2013).

1.4 Inverse radiative transfer

A state-of-the-art radiative transfer code on itself, however, is not sufficient to determine the dust content of galaxies from UV/optical/NIR images. In Figure 1.6 we see a typical case of a forward radiative transfer problem. A radiative transfer simulation typically starts from a 3D distribution of the stars and the dust in a galaxy model and calculates how this particular system would look for an external observer at an arbitrary viewing point, i.e. it simulates the observations. However, in reality, often the opposite case is necessary. Figure 1.7 shows the basics of the inverse radiative transfer problems. When we would like to model real galaxies, we do not need to simulate how they look like because the observations already hold that information. However, in this case we have no direct link between the parameters and the resulting frame. The inverted problem, determining the 3D distribution of stars and dust from a given reference frame, is a hard nut to crack. It requires the combination of a radiative transfer code and an optimisation procedure to constrain

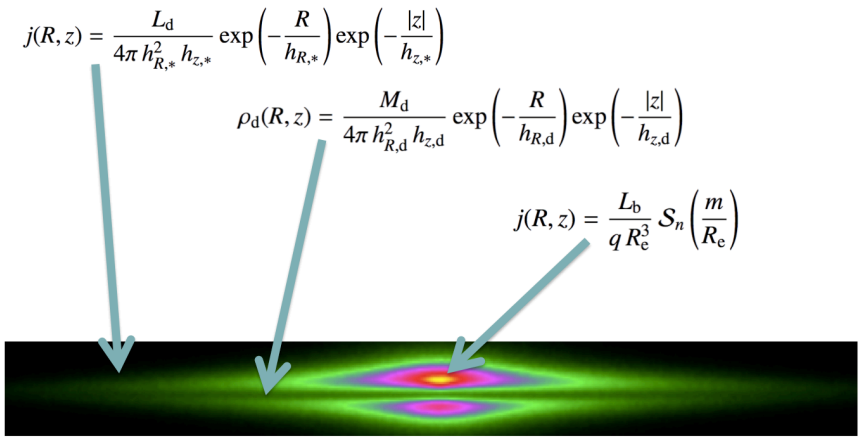

Figure 1.6: A typical case of forward radiative transfer. When all the parameters of the analytical models are provided, the RT code simulates the resulting frame.

the input parameters. Several fitting codes that combine a radiative transfer code with an optimisation algorithm have been set up (Xilouris et al., 1997; Steinacker et al., 2005; Robitaille et al., 2007; Bianchi, 2007; Schechtman-Rook et al., 2012). All too often, however, this optimisation procedure is neglected and *chi-by-eye* models are presented as reasonable alternatives.

Several codes, like BUDDA (de Souza et al., 2004) or GALFIT (Peng et al., 2002), exist which give a fit of the galaxy as it is projected on the sky. While they have the advantage that they are orders of magnitude faster than inverse radiative transfer codes, they are usually limited to 2D models. Additionally, even when using 3D models, these codes are not appropriate to study the dust content of galaxies. At most they include a very basic attenuation model or use *ad hoc* corrections to compensate for extinction on the observed stellar parameters (Pastrav et al., 2013a). However, especially when including scattering, actual radiative transfer simulations are required when more accurate dust constraints are required. As a result, every evaluation of the parameter space which needs to be investigated requires a complete radiative transfer simulation to solve the equation (1.10).

To optimise this given problem it is important to realise that the parameter space is often quite large, easily going up to 10 free parameters or more. As discussed in the previous section, the complexity of the dust/star geometry and scattering off dust particles is often counter-intuitive and results in a non-linear, non-differentiable search space with multiple local optima. On top of this there is another bothersome feature induced by the radiative transfer code. Most state-of-the-art radiative transfer codes are Monte Carlo codes where the images are constructed by detecting a number of predefined photon packages. Because of the intrinsic randomness

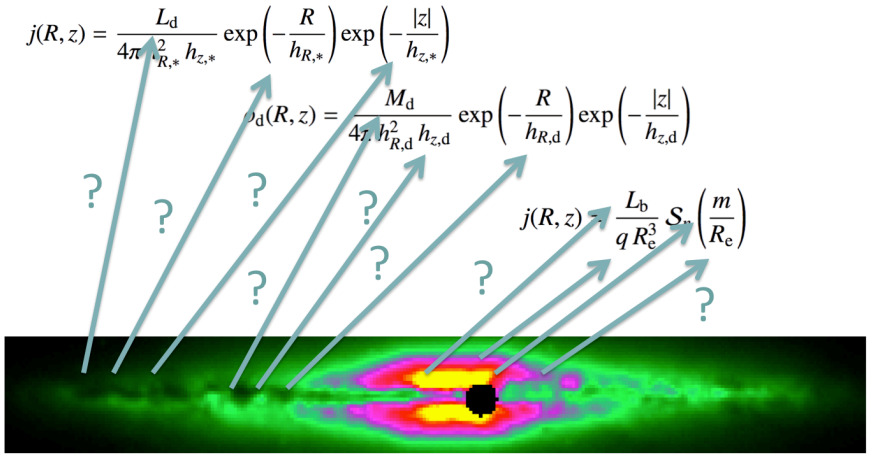

Figure 1.7: A typical case of the inverse radiative transfer problem. The bottom plot shows the observed image of an edge-on spiral galaxy, but, unlike for forward RT, we have no direct measures on what parameters correspond to this frame.

of the Monte Carlo code, images always contain a certain level of Poisson noise. If one runs a forward Monte Carlo radiative simulation, it is usually straightforward to make the number of photon packages in the simulation so large that this noise becomes negligibly small. However, if we want to couple the radiative transfer simulation to an optimisation routine, typically many thousands of individual simulations need to be performed, which inhibits excessively long run times for each simulation and hence implies that some noise will always be present. The result is that we have to fit noisy models to noisy data, as reduced CCD data will always contain a certain level of noise (Newberry, 1991).

For complex optimisation problems like this, it is advisable not to use classical optimisation methods like downhill-simplex method or Levenberg-Marquardt but rather to apply a stochastic optimisation method instead. The main advantage of stochastic methods like simulated annealing, random search, neural networks, genetic algorithms, etc. over most classical optimisation methods is their ability to leave local optima and search over broad parameter spaces (Fletcher et al., 2003; Theis and Kohle, 2001; Rajpaul, 2012). Genetic algorithms (Goldberg, 1989; Mitchell, 1998) are one class of the stochastic optimisation methods that stands out when it comes to noisy handling because it works on a set of solutions rather than iteratively progressing from one point to another. Genetic algorithms are therefore often applied to optimise noisy objective functions (Metcalfe et al., 2000; Larsen and Humphreys, 2003). These, and other, optimisation methods will be discussed in more detail in Section 2.3.

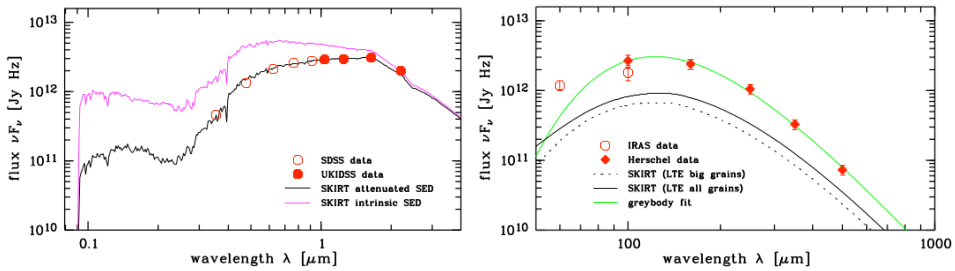

Figure 1.8: The optical/NIR (left) and FIR/submm (right) spectral energy distribution of UGC 4754. As can be seen, the FIR emission of the model determined from the extinction in the optical bands fails to predict the observed fluxes (Baes et al., 2010).

1.5 Dust energy balance

As discussed in Section 1.1, edge-on spiral galaxies offer some unique features when one wants to determine structural parameters. Their dust content often shows as a distinctive narrow lane where almost all of the stellar light is attenuated. Edge-on galaxies allow us to observe both the radial and vertical extent of the dust and stellar disk. Because the extinction effects are so clearly shown in edge-on spiral galaxies, they are the ideal targets when one wants to determine the dust content and distribution (e.g., Xilouris et al., 1997, 1999; Misiriotis et al., 2001; Alton et al., 2004; Bianchi, 2007; Baes et al., 2010; Popescu et al., 2011; MacLachlan et al., 2011; Schechtman-Rook et al., 2012; De Looze et al., 2012b,a; De Geyter et al., 2013, 2014)

As the starlight absorbed by dust grains in the UV/optical/NIR region is re-emitted in the MIR/FIR/submm wavelength regime, one would expect the absorbed luminosity to be equal to the total thermal IR/submm luminosity. However, there seems to be a deficit in this dust energy balance for a number of radiative transfer simulations (Popescu et al., 2000, 2011; Misiriotis et al., 2001; Alton et al., 2004; Dasyra et al., 2005; Bianchi, 2008; Baes et al., 2010; Holwerda et al., 2012b). The left panel in Figure 1.8 shows the optical part of the SED of the best fitting radiative transfer model matching the optical images and fluxes of the galaxy, UGC 4754. This model can then be used to perform a complete panchromatic radiative transfer simulation encompassing both the UV/optical/NIR and the MIR/FIR window. It is clear from the right panel that, in this case, the model determined from extinction fails to predict the observed fluxes in the FIR.

This is a problem typically encountered using self-consistent radiative transfer simulations. Averaged models SED fitting tools like MAGPHYS (da Cunha et al., 2008) or CIGALE (Burgarella et al., 2005; Noll et al., 2009) have the advantage that they

do not have a similar problem as they use an energy balance method while fitting the SED. However, these methods cannot take into account the effect of stardust geometries in galaxies and therefore can not explicitly calculate the radiation fields and heating sources. Radiative transfer codes, on the other hand, can incorporate all the geometrical effects, position and strength of the heating sources to self-consistently predict the FIR emission. Because this requires a significant increase in computational cost, and the loss of a guaranteed energy balance, they are less useful to study larger samples. While methods to predict results of radiative transfer simulations by using artificial neural networks are extremely promising, it is advisable to use them for statistical purposes (Silva et al., 2012).

Possible explanations for the discrepancy in the energy balance found in radiative transfer simulations include the underestimation of the FIR emission coefficients (Alton et al., 2004; Dasyra et al., 2005; MacLachlan et al., 2011), or the presence of additional dust distributed in such a way that it hardly contributes to the attenuation (Popescu et al., 2000; Misiriotis et al., 2001; Popescu et al., 2011; Bianchi, 2008; De Looze et al., 2012a, 2014; Saftly et al., 2015).

1.6 Overview of this thesis

In this thesis we will focus in detail on how to solve the inverse radiative transfer problem discussed in Section 1.4.

In Chapter 2 we present FitSKIRT, a code based around the radiative transfer code SKIRT to automatically determine the best fitting model to set of observations. The code uses genetic algorithms to optimise the output of the radiative transfer. We start by explaining how genetic algorithms work and apply them to some analytical test cases. The SKIRT code and the way how it solves radiative transfer equations 1.10 are discussed in detail and we describe the general outline of the FitSKIRT code. Next, we describe the actual properties of the FitSKIRT code. We start by explaining the problem at hand and how it can be solved using FitSKIRT. Section 2.3.1 handles the advantages and disadvantages of fitting to more than one observed image of a single target. Before discussing the actual structure and setup FitSKIRT, we describe some additional features and considerations regarding the data reduction that come along with it.

Chapter 3 contains three distinct test cases to validate the workings of our code. To compare both the images as well as the recovery of the best fitting parameters, we apply the code to a mock image created using the radiative transfer code. We start with the simple case where only one reference is fitted to and incrementally increase the number of free parameters. This test case is also used to justify are choice of genetic algorithms as an optimisation method by comparing the results

with other methods. The second test case consists of the same method as the first test case but this time we apply it to an real V-band observation of galaxy NGC 4013. We compare the best fit provided by FitSKIRT with the results of two other inverse radiative transfer methods applied to this galaxy. The final test case revisits the first test, but this time a set artificial observations is created. We discuss how this is an improvement over the monochromatic method when it comes to handling the many degeneracies, intrinsic to the inverse radiative transfer problem.

In Chapter 4, we apply the FitSKIT code to a sample of 12 edge-on spiral galaxies. We discuss the importance of some structural features that will be investigated and explain how our sample was selected accordingly. For every galaxy, we fit the SDSS g, r, i and z-band simultaneously with a model consisting of stellar disk, central bulge and a dust disk. The best fitting models for this 19 free parameter problem and the results are presented for each galaxy individually. In Section 4.5 we discuss the results and implications of the entire sample. We asses the quality of our fits, the star-dust geometry, optical depth and dust mass of the galaxies in our sample and compare the results to existing work before drawing some general conclusions.

In the following chapter, we extend our investigation to study the implications of our "new" models on the dust energy balance problem. First, we give a brief overview of the necessary components to allow for a panchromatic study using optically constrained models. We present two models, one with and one without a younger stellar population to compensate for the unconstrained UV frames in our previous study. We compare both the predicted SED and images with the actual observations for our two target galaxies, IC 4225 and NGC 5166 and discuss our results.

In Chapter 6 some other, past and future, applications of the FitSKIRT code are presented. We revisit one of the galaxies, NGC 5908, investigated in Chapter 4, and use a different geometry to constrain the dust distribution. We compare both distributions and discuss the implications on the predicted panchromatic SED in light of the dust energy balance. We show the best fitting results to the HEROES galaxies, a sample of seven nearby, massive edge-on spiral galaxies and briefly discuss how this sample can be used to investigate the dust distribution and dust energy balance in edge-on spiral galaxies in greater detail. NGC 4370 is the first elliptical/lenticular galaxy our code was applied to. The results of our fit are shown in Section 6.1.3. FitSKIRT is also applied to two galaxies modelled in hydrodynamical simulations. We compare the dust masses returned by FitSKIRT with the actual values in these realistically looking galaxies. We conclude this chapter by discussing four possible improvements to the code.

Next, we briefly discuss the use a spiral arm geometry in the case of NGC 891 and

how this can be used in follow-up studies.

Chapter 7 starts by giving a general overview of what was discussed in this thesis. We summarise the results and discuss a few of the main conclusions found in light of this thesis.

FitSKIRT 2

In this chapter we discuss the details of the FitSKIRT code. The first section gives an introduction to genetic algorithms. We apply it to an analytical function and compare the results with the results from another code. In Section 2.2.1 we explain the core concepts and some of the features of the radiative transfer code which will be used in our case. Section 2.3 explains the FitSKIRT code and how it works in detail. This chapter explains some of the results published in De Geyter et al. (2013).

2.1 Genetic Algorithms

2.1.1 Genetics and evolution

Genetic algorithms (GAs) are problem solving systems based on evolutionary principles. In essence evolution theory describes an optimisation process of a population to a given environment. The terminology used in GAs is therefore related to actual biological processes. It is therefore relevant to discuss what they do in reality before we translate them into an algorithmic form. DNA can be seen as two matching sequences made up of four different bases, usually represented as A, T, C and G. A gene is a stretch of DNA that codes for a specific type of protein and they hold the information to maintain an organism's cell and pass genetic traits to offspring. An allele is one of many possible forms of the DNA sequence of a particular gene. Sometimes different alleles will have the same result in the expression of a gene. A genome is the complete set of all genes, so in most cases: the DNA itself.

A genotype is a specific instance of a genome. This is then translated to a specific physically observable property, the phenotype. It is important to realise that there is no one-to-one relationship between the genotype and the phenotype. Suppose you have a flower with genotype R-R (red, being dominant) and one with genotype g-g (green, being recessive). The phenotype of these flowers will indeed be red and green respectively. However if they would have an offspring with genotype R-g, the phenotype will be red, but this would hold no direct information on what your complete genotype looks like. An individual (having one specific genome)

can be categorised by either his geno- or phenotype. A population is a set of these individuals.
Evolution in general can be seen as a set of three different mechanisms of adaption: mutation, crossover and duplication.

- Mutation is the random alteration of the genomic sequence. Not all mutations have an immediate effect on the observable properties of the individual. Their immediate effect is usually very small but can add up over a longer period.
- Crossover is the exchange of genetic material between two genomes in a new one. The resulting phenotype usually changes more in this way compared to mutation.
- Duplication is the process where the new genome is the exact copy of the original one without any alteration.

Evolution can be seen as a sort of optimiser of the population for given conditions or environment. Individuals that have been well adapted to the environment will produce more offspring or, even more drastic, the unadapted ones simple do not survive. Therefore the genes matching to the suited physical properties will become more abundant in the entire population. Mutation, on the other hand, allows the creation of individuals with properties that are not yet present in the population. After some time the population will then exist of individuals fitted for the given environment. This law is sometimes referred to as "survival of the fittest" and is the core of the evolution theory, first described by in "On the origin of species" by (Darwin, 1859).

It is possible to use this same mechanism to create an optimisation algorithm. The core difference between GAs and most other algorithms is that a GA works with a set (population) of possible solutions (individuals) to the problem (environment). Each individual consists of a number of parameters (genes). For each of these genes there is a number of possible values which we call alleles. These alleles however do not have to be a discrete set, but can be defined as a range or pool where the genes should be drawn from. One specific genome is of a specific genotype and can be translated to a certain phenotype, for example the image that is obtained using a radiative transfer code. We have to bear in mind though that there is no direct way to determine the genotype starting from the phenotype.

2.1.2 Genetic Algorithms

The algorithm starts by defining both the size and content of the initial population (generation 0). The genomes can be created randomly out of the gene pool or can be manually defined. Each of the initial solutions is then evaluated and given a

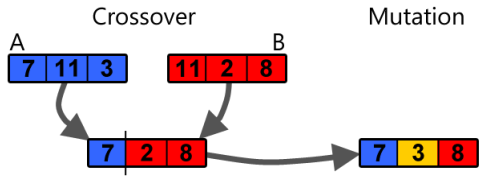

Figure 2.1: The crossover and mutation operators in genetic algorithms.
Source: `http://www.klopfenstein.net/lorenz.aspx/genetic-algorithms`

certain "fitness" value. This is usually done by comparing the function values obtained using the genetic algorithm parameters, $g(x)$. For example, the χ^2 function is often used when fitting models to a set observed data. We can use it to rank the individuals from good to bad (or low χ^2 value to high χ^2 value). The individuals that meet a certain criteria of fitness are then used to crossover and produce the first offspring (generation 1). Another, more convenient way of determining which individuals are fit for reproduction is by determining a crossover-rate. If, for example the crossover-rate is 0.6, then the 60% best values will be used to produce offspring. We can also define a mutation-rate in the same way. This rate determines how many genes (and not individuals) of the offspring undergo a random mutation. In practice this is done by removing one of the gene values and replacing it with a new possible value. After this step we return to the determination of fitness by calculating the value $g(x)$. Then we select the individuals fit for reproduction and create a new generation (generation 2). We repeat this cycle until a certain fitness value is obtained or until we reach a pre-defined number of generations.

Generally speaking, it is now clear why the algorithm evolves towards the optimal values. Since we always prefer the better individuals of a population we expect the average population to shift to a better value and we again prefer the better individuals, etc. It has to be noted however that this is not a sufficient proof, since it is not guaranteed that the best genomes will generally shift to better values if the population average changes. Genetic algorithms are seen as a sort of artificial intelligence since they can react to changes in the input values and therefore mimic intelligent behaviour. They have the advantage that you do not need a lot of function specific coding. How the function looks like does not alter the way your algorithms looks for the optimal value. In fact they have a lot of similarities with another stochastic method, Simulated Annealing. Both of them are extremely useful for cases in which you have to deal with an inverse problem. These problems are computationally hard although the straightforward case usually is not. GAs only need the solution of the forward problem to determine the fitness value and are therefor much easier to use. Although GAs can require a lot of CPU time, they do not require a lot of memory. Another advantage is that the two biggest time consuming processes,

i.e. phenotype construction and fitness evaluation, can be computed parallel next to each other. You can therefore decrease the amount of needed CPU time by letting these processes run on two independent processors. They differ from other stochastic methods in three ways (Charbonneau (1995)). First of all, the created population is a genotype and not a phenotype. Secondly, the crossover and mutation occurs randomly and is not fixed as opposed to averaging, etc. Finally, the selection process is based on the most fit individuals rather than randomly. It is important though to realise that, because of the random nature of the GA algorithm, the results differ from one run to another. Up until now there is no strong proof that a GA is able to converge to a global optimisation point for a general problem (Forrest, 1993).

The evolutionary process can be subdivided into two more or less distinct phases (Baier et al., 2010). The first is characterised by a large-scale exploration of the parameter space, made possible by the action of crossover and the extreme variety of genotypes making up the gene pool. This phase of rapid evolution effectively comes to a close when a large subset of the population has found the highest peak in the landscape. From that point on evolution occurs more slowly and leads to slow, incremental improvement in the population's fitness as favourable mutation becomes fixed in the population. It is important to realise that the relationship between population size, number of generations, crossover and mutation is not at all linear or easy. For example one might think that a larger population always leads to better results. This however is not always the case. The large population will converge rapidly at first but will create a larger inertia in the later evolutionary stages. This means that it will become difficult to spread to a more favourable mutation (Charbonneau (1995)).

The two frequently used genome representations for physical problems are the binary string genome and the real number genome. The binary string genome translates the parameters to a string using an allele set containing only 0 and 1. They have the advantage that they can be analysed by so called "schema" methods. Their main disadvantage is that they do not optimise the objective function itself but rather optimise a decoded version of it. This implies that decoding the function can create a extra local optima making the global search harder. Another, more stable method is to immediately use real numbers as gene parameters, but for which there are no known, general schema methods to analyse the result.

Many techniques have been devised to optimise the use of genetic algorithms for specific problems. It is however not relevant for the goal of this thesis to discuss them all so we will only discuss the most relevant options (Forrest, 1993). To start with it is not necessary to stick to just one offspring per individual for each generation. It might be more favourable to create more offspring of the individuals

with the highest fitness. This strategy, called ranking, relates the fitness value immediately to the number of offspring created by one individual. Another popular strategy is the use of elitism. This technique ensures the survival of the fittest genotype for at least one generation. This simple technique significantly improves the performance of any GA based optimisers, especially in combination with a variable mutation rate. The manner of reproduction is another way to change the performance of the GA. The two most used reproduction plans are generational replacement and steady-state. In the generational replacement the offspring is contained in temporary storage until enough offspring is created to replace the entire parent population. Steady-state is however a more natural way of replacement; the offspring is inserted in the population as soon as it is bred.

Genetic algorithms have three main advantages: the global optimisation, noise handling properties and parallelisation options.

- Unlike many, often faster, optimisation methods, genetic algorithms are great global optimisers. Indeed, both through crossover and mutation, the algorithm easily jumps out of local optima towards a more globally optimal region and it does so without the need of additional information like gradients.
- GAs have the advantage over other global optimisers, that they have the ability to appropriately handle noise (Metcalfe et al., 2000; Larsen and Humphreys, 2003). Because it is a population based optimiser, which works on a set of solutions instead of iteratively progressing from one point to another, fluctuations due to noise tend to be smoothened out in the end. While there are other population based optimisation methods like particle swarm optimisation (Kennedy, 2010) or ant colony optimisation (Colorni et al., 1991) which would be suited for this problem, genetic algorithms are one of the best and most applied algorithms among them.
- While GAs are essentially computationally more demanding than other optimisation methods, a generation can be handled completely in parallel. Therefore, especially longer function evaluations greatly benefit from this advantage over iteratively progressing from one point to another.

2.1.3 The GAlib library

Genetic algorithms have been applied successfully to a large range of test problems, and are nowadays widely used as a reliable class of global optimisers. They are becoming increasingly popular as a tool in various astrophysical applications. Most astrophysical applications so far have used the publicly available PIKAIA code (Charbonneau, 1995), originally developed in Fortran 77 and now available in Fortran 90 and IDL as well. We have selected the publicly available GAlib li-

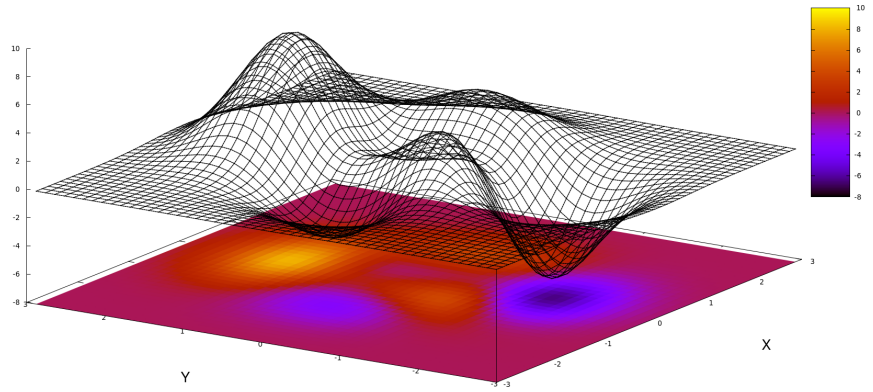

Figure 2.2: The function defined by equation 2.1 with projected density plot.

brary (Wall, 1996) for our purposes. One of the main reasons for choosing GAlib is that, like the SKIRT radiative transfer code, it is written in C++ and thus guarantees straightforward interfacing. Moreover, the library has been properly tested and adapted over the years and has been applied in many scientific and engineering applications. It comes with an extensive overview of how to implement a genetic algorithm and examples illustrating customisations of the GAlib classes.

As a first example of how the genetic algorithm works, we apply it to find the global maximum of the following function, which can be seen in Figure 2.2.

$$f(x,y) = 3(1-x)^2 \exp(-x^2 - (y+1)^2) \\ - 10(\frac{x}{5} - x^3 - y^5) \exp(-x^2 - y^2) - \frac{\exp(-(x+1)^2 - y^2)}{3} \quad (2.1)$$

Instead of plotting the 3D structure and position of the evaluated points, we will plot them on top of the contour maps of the function. Yellow regions indicate high values of the objective function, while black and and purple values represent the lowest regions. It should be clear that this function is a perfect, simple first test case. It overs some minor challenge to locate the global maximums as this function has three local maxima.

In Figure 2.3 we can see the distribution of the individuals of the individuals of the different generations 0 (top left), 1 (top right), 2, 3, 4, 5, 10 and 25 where the green points represent the evaluated points or individuals within that generation. Every generation consists of 100 individuals with a crossover rate of 65% and a mutation probility of 6%. Notice that these points first condense in the yellow, high value, regions before converging to the optimum in the end.

However, this is still only a moderately difficult function, which would also not

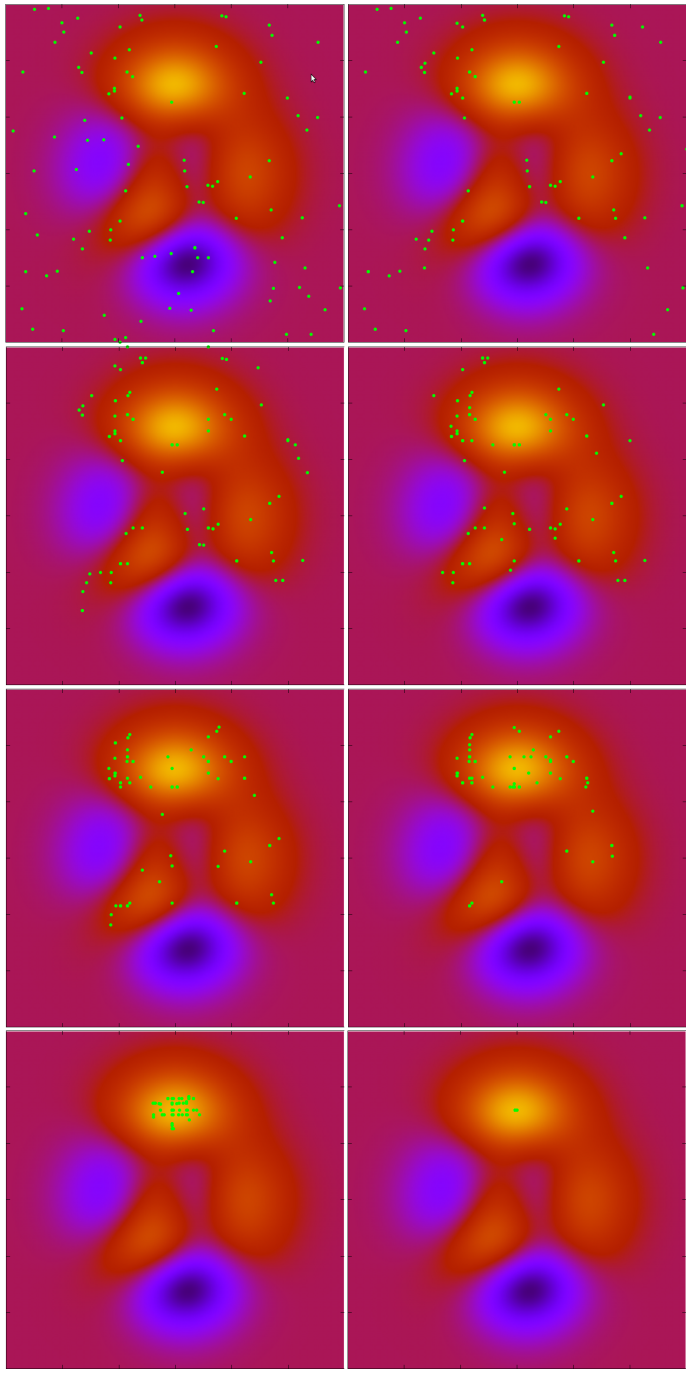

Figure 2.3: The contour maps of Function 2.1 shown in Figure 2.2. From top left to bottom right we respectively see generations 0, 1, 2, 3, 4, 5, 10 and 25 of the genetic algorithms optimisation. The green points represent the individuals within that generation.

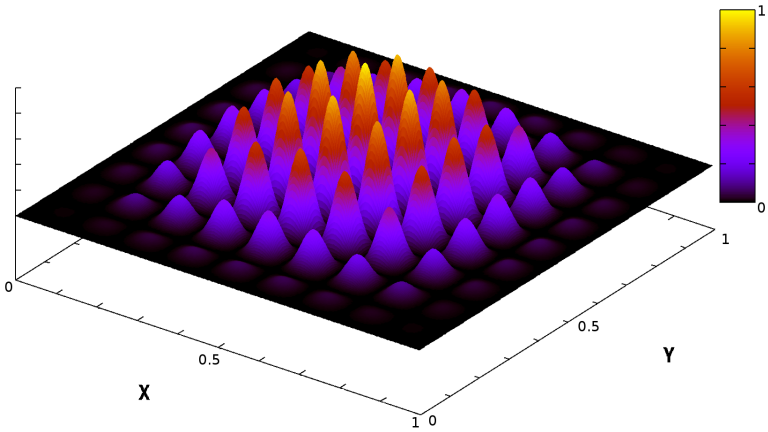

Figure 2.4: The function defined by equation (2.2) for $n = 9$. It contains many steep local maxima surrounding the global maximum at $(x, y) = (0.5, 0.5)$ and is therefore a strong test function for global optimisation algorithms.

hinder some classical methods like a Newton Method, downhill simplex method, Levenberg-Marquardt, etc. At most, some algorithms should be restarted at a random new position but even restarting these algorithms about 10 times would still result in a faster optimisation method then using the computationally more expensive genetic algorithms.

A more extreme case can be seen when trying to find the maximum of the following function

$$f(x, y) = \left[16\, x\, (1 - x)\, y\, (1 - y) \sin(n\pi x) \sin(n\pi y)\right]^2 \tag{2.2}$$

More specifically, we have considered the case for $n = 9$ shown in Figure 2.4. This function is the same test function as first suggested by Charbonneau (1995) but also investigated by others (Cantó et al., 2009; Rajpaul, 2012) to determine the performance of their optimisation method. It is clear that this function is a severe challenge for most optimisation techniques: the search space contains many steep local maxima surrounding the global maximum at $(x, y) = (0.5, 0.5)$. In addition, the global maximum is not significantly higher compared to the surrounding local maxima. A classical hill climbing method would most definitely get stuck in a local maximum. An iterative hill climbing method, which restarts at randomly chosen points, would also be able to solve this problem but in this case it would normally take much longer to do so compared to a genetic algorithm.

We demonstrate how the GAlib genetic algorithm library behaves in this complex search space by plotting the density and over plotting the position of the individuals for each generation. The results are shown in Figure 2.5. For these tests we use

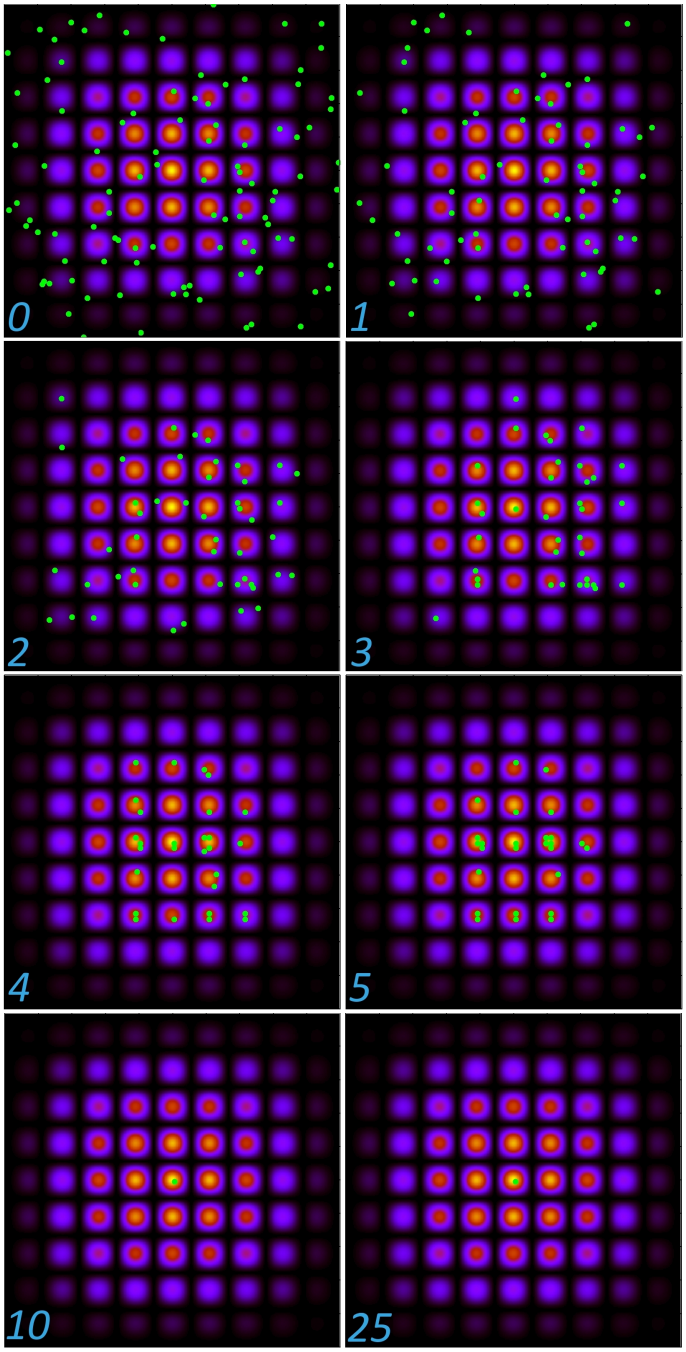

Figure 2.5: Illustration of GAlib's approach to find the global maximum of the function (**??**). The different panels show the 100 individuals of a population 0, 1, 2, 3, 4, 5, 10 and 25, characterised by a mutation probability of 0.3% and a crossover rate of 65%. For the first few generations, the individuals are distributed randomly, starting from generation 5 the individuals are clearly centred around the local maxima and continue to converge to the true maximum.

the same values for the mutation probability and crossover rate as Charbonneau (1995), namely 0.3% and 65% respectively, and the population size is set to 100. As it is shown, the algorithm is capable of efficiently determining the maximum. Starting from generation 5 the individuals are clearly centred around the local maxima and continue to converge to the true maximum. At generation 10 all individuals are very close to the global maximum, and we note few changes between generations 10 and 25. This can be explained by the large population inertia. The large population prohibits the fast alteration to a favourable mutation. Higher mutation rates could be a possible way to increase accuracy but we have to keep in mind that this could come at the cost of losing the global maximum (Charbonneau, 1995). Furthermore it is not our ultimate goal to optimise this given problem in the best possible manner.

The final result we get using this method after 25 generations is: $(x, y) = (0.502, 0.498)$ with $f(x, y) = 0.994$. It should be noted that this solution is not a special case and that the algorithm delivers this result almost every time. After 1000 consecutive runs we get an average result

$$x = 0.501 \pm 0.004 \tag{2.3}$$

$$y = 0.500 \pm 0.004 \tag{2.4}$$

When we increase the number of generations, we obviously still recover the global maximum and reduce the standard deviation: for a population of 100 and 100 generations we get

$$x = 0.500 \pm 0.003 \tag{2.5}$$

$$y = 0.501 \pm 0.003 \tag{2.6}$$

As a final example, we increase the mutation rate to 30% to show it improves the accuracy. Again after 100 generations, we now find

$$x = 0.5000 \pm 0.0002 \tag{2.7}$$

$$y = 0.5000 \pm 0.0002 \tag{2.8}$$

Looking at Figure 2.5 and comparing with the result, $f(x, y) = 0.978322$ (ranked case, 40 generations), obtained by Charbonneau (1995), it can be seen that, for this problem, GAlib performs at least as good (see the 25 generation case) as the PIKAIA code and we can be confident to use the GAlib code for our purposes.[1]

This test case should, however, not be considered as a validation towards the fi-

[1] A possible explanation for this difference might be the generational versus the steady state reproduction. It has to be noted, however, that the PIKAIA results we quote are from Charbonneau (1995). Many researchers have adapted and updated the PIKAIA code since 1995, probably also increasing its efficiency.

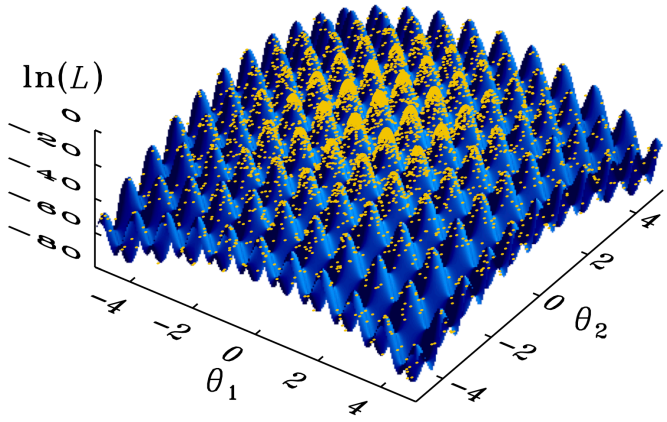

Figure 2.6: Figure taken from Corsaro and De Ridder (2014) with permission. It shows the results of a nested sampling method on top of the actual parameter space of the Rastrigin function in blue. Notice the similarity with the test case use for genetic algorithms in Figure 2.4

nal purpose of the program. More elaborate and problem specific testing will be handled separately in Chapter 3. While it will be shown that genetic algorithms, especially combined with a Monte Carlo radiative transfer code, form a powerful combination, one should always consider possible improvements.

One very interesting option for improvement on the optimisation part is the use of a new, bayesian fitting approach to this problem known as nested sampling (Skilling, 2004). This approach could potentially be useful as it is a bayesian fitting with all the advantages of a population based optimiser (noise handling properties, ease of parallelisation,...). In particular, the DIAMONDS code (Corsaro and De Ridder, 2014) is worth investigating as it is public available and also written in C++ (like our radiative transfer code). It has also been tested on some relevant cases. In Figure 2.6 we can see the method being applied to the Rastrigin function, a function known to be difficult to explore using the commonly used Markov Chain Monte Carlo (MCMC) method. It is clear that this function is quite similar to the test case used before, see Figure 2.4.

2.2.1 SKIRT

SKIRT (Baes et al., 2011; Camps and Baes, 2015), an acronym for Stellar Kinematics Including Radiative Transfer (Baes and Dejonghe, 2002; Baes et al., 2003), is a state-of-the-art C++ software code for simulating continuum radiation transfer in dusty astrophysical systems, such as galaxies and AGN tori. It comes with a extensive documentation, available at `http://www.skirt.ugent.be/`, and is publicly available at `https://github.com/SKIRT/SKIRT`. SKIRT is a Monte Carlo radiative transfer code which includes scattering, absorption and emission by the dust. The code comes with a large number of geometries, light source spectra, dust characterisations, dust grids, and detectors. SKIRT has continuously been adapted and upgraded to a general and multi-purpose dust radiative transfer code. It now includes many advanced techniques to increase the efficiency, including forced scattering (Mattila, 1970; Witt, 1977), the peeling-off technique (Yusef-Zadeh et al., 1984), continuous absorption and scattering (Lucy, 1999), smart detectors (Baes, 2008) and frequency distribution adjustment (Bjorkman and Wood, 2001; Baes et al., 2005). SKIRT has been used to predict and interpret the far-infrared emission from a variety of objects, including edge-on spiral galaxies (Baes et al., 2010, 2011; De Looze et al., 2012b), elliptical galaxies (De Looze et al., 2010; Gomez et al., 2010), active galactic nuclei (Stalevski et al., 2011, 2012) and post-AGB stars (Vidal and Baes, 2007).

SKIRT uses the the Monte Carlo algorithm to solve the radiative transfer equations (RTE) discussed in Section 1.3. Here the radiation field is represented as a flow of a large number of photons packages, all being followed individually through the dusty medium. While, strictly speaking, not solving the RTEs, adding all the contributions of these photon packages results in an approximation of the solution. The advantage of this approach is that it is conceptually simple and allows for relatively easy implementation of complex processes like absorption, scattering, polarisation, etc.

In Figure 2.7 we can see the basic elements of a SKIRT simulation. The configuration for a particular simulation is defined at run-time through a user-friendly, either (basic) graphical or non-graphical, interface suitable for both occasional and power users. The wavelength grid defines the wavelengths at which the RTEs are solved. In SKIRT two mains choices are possible. The oligochromatic mode[2] requires a short list of distinct wavelengths. This mode has the advantage that the overhead is much smaller and the computational time is spent on calculating the

[2] oligo- or olig-, as in oligopoly, oligarchy or oligosaccharide, derived from the Greek *olígos*, meaning "few" or "a little".

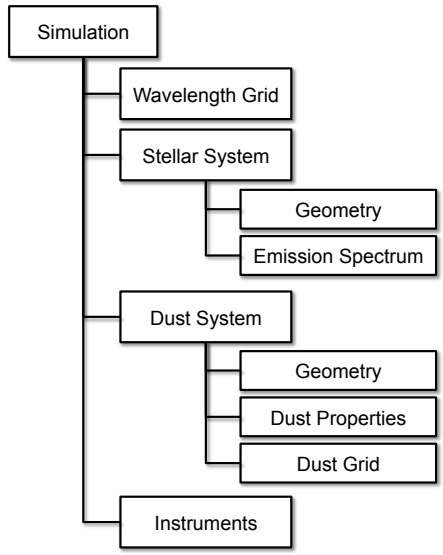

Figure 2.7: A schematic representation of the basic elements which need to be configured for a particular SKIRT simulation (Camps and Baes, 2015).

necessary wavelengths. However, this is only possible in the optical regime where each wavelength can be calculated independently. In order to correctly incorporate dust emission, a panchromatic grid, spanning a wider range of wavelengths, is necessary.

The second main component of a SKIRT simulation is the stellar system, which consists of several stellar components each comprising two main elements: the geometry and the emission spectrum. For a panchromatic wavelength grid, the latter has to be defined by choosing an appropriate SED, either by choosing a built-in template or providing a custom SED template. SKIRT comes with an extensive list of possible choices of geometries like a double exponential disk, a Sérsic bulge, multi-gaussian models, etc. On top of that, transformations of these models like offsets, rotations, spiral arms, clumpiness, etc. can be made to make even more specialised geometries.

The third component of the simulation characterises the dust system. Again a suitable geometry can be selected from the extensive list. Additionally, one has to select or construct an appropriate dust mix and therefore set the dust properties like scattering and absorption coefficients, asymmetry parameter, scattering phase function, etc. As a last step, the continuous dust distribution has to be discretised on a grid. The position and size of these grid cells have to be placed efficiently in order to get acceptable results within a reasonable computation time. This can be very problem specific and the choice of the dust grid is not always straightforward. As a result, in order to deal with a variety of problems, SKIRT includes a wide range of dust

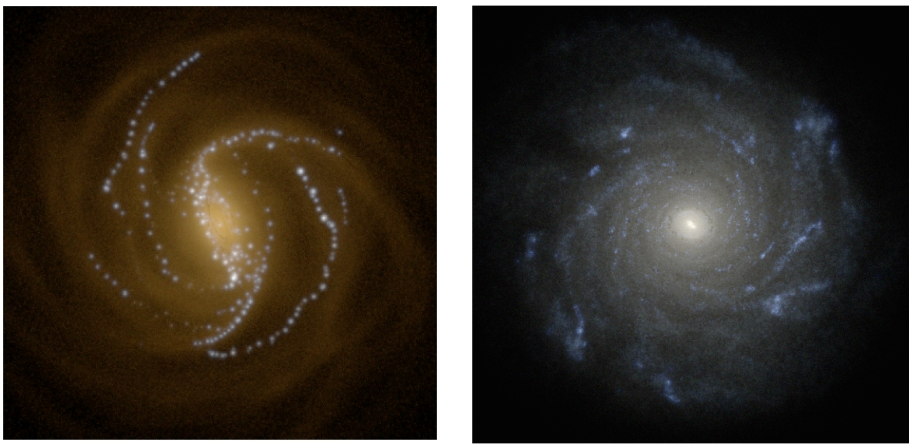

Figure 2.8: This figure from Saftly et al. (2015) shows some SKIRT mock images for the face–on view of the realistic galaxies. These images combine the results of three SKIRT simulations in three distinct wavelengths r, g , and u bands. The left panel is the face–on view of galaxy as modelled by Guedes et al. (2011) using a smoothened particles hydrodynamics (SPH) code. The right image is the galaxy modelled by Renaud et al. (2013) using an adaptive mesh refinement (AMR) code.

grids, ranging from simple equidistant cartesian grids to hierarchical octree and *k*-d trees (Saftly et al., 2013, 2014) and unstructured Voronoi grids (Camps et al., 2013). As an alternative for setting the stellar and dust system, SKIRT includes various mechanisms for importing models generated by hydrodynamical simulations. Figure 2.8 shows an RGB composite image of a SKIRT simulation at three different wavelengths, from two galaxies modelled using different codes.

The final component in the SKIRT simulation is the choice of the instruments, which collect and write down the information about the simulated radiation received at some specified viewpoints. The SED instrument outputs the SED of the received flux and can be plotted in order to be compared against observed fluxes. Figure 2.9 shows the SED as found for a model of NGC 4565 against the observed values. The Frame instrument collects a complete 3D data cube, consisting of a rectangular frame at each wavelength in the wavelength grid, and outputs the results as a FITS file (Flexible Image Transport System). However, in this data cube, every frame has the same dimensions, both in physical and pixel units. As will be discussed in Section 2.4.1, sometimes it is necessary to have frames with altering pixel scales and field-of-views. For this the MultiFrame instrument was introduced, so every wavelength can have different dimensions. This is useful when running FitSKIRT (see later sections).

All the components, options and settings described above can be changed by running the SKIRT code without arguments. This starts a Q&A session handling all

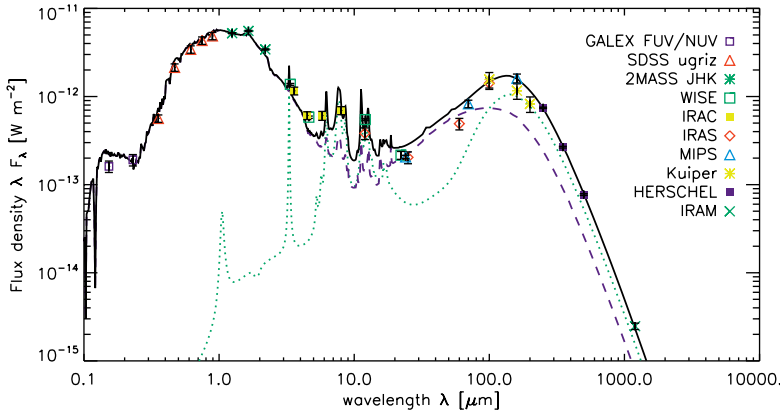

Figure 2.9: The modelled SED as obtained with the SKIRT model with star formation and an additional dust reservoir distributed in clumps overlaid with the observed fluxes for NGC 4565 (De Looze et al., 2012a).

the necessary variables. At the end of the Q&A session, all options and parameters are stored in a single, so called *ski* file with an XML (eXtended Markup Language) format as can be seen in Figure 2.10. This has the advantage that, features can be nested in a hierarchical structure and human-readable XML tags. Because it has such a clear structure and is stored as a plain text format, the file can be easily adjusted afterwards without having to go through the entire Q&A session again. As will be discussed in Section 2.4.2, this ski file can be used as a template to fit to observed galaxies.

To start the actual SKIRT simulation, one just has to start SKIRT and give the name of the ski file as an argument. The simulation then starts by setting up all the necessary components, the random number generator, calculating the dust properties, constructing the dust grid, etc. In the next phase the photon packages are initialised from a random position in your predefined geometry and launched in random directions. Once it enters the dusty medium, the photon can either interact (absorb or scatter) with a dust grain or travel through the system untouched. The position and the type of interaction are determined at random, according to the predetermined probabilities. Due to clever optimisation techniques like eternal forced scattering, continuous absorption and scattering, this process can be sped up significantly. The photon package lifetime ends when it is either absorbed by a dust grain or when it is detected by an instrument.

The next phase of the code is the dust emission phase, where the emitting sources are now the dust grains instead of the stellar system. From the stellar emission phase, the total amount of absorbed luminosity in each dust grid cell and at every wavelength is stored. From this information, the intensity of the interstellar radiation field (ISRF) is calculated and, using the appropriate dust emissivity parameters,

the dust emission at every position is determined. For every wavelength, a number of new photon packages are launched with position and luminosities corresponding to the determined emissivity. Notice that the simulation is not strictly separated in clear emission and absorption regimes, so self-absorption of photon packages by dust grains is possible. When all photon packages have been absorbed by the either the detector or a dust grain, the procedure starts again from an updated ISRF and the resulting dust emissivity. The dust emission phase stops when a convergence is reached for the absorption rate, the dust emissivity and the mean intensity. The last step then consists of reading out and calibrating the instruments.

An inevitable result of the Monte Carlo method is that always a certain level of Poisson noise is present in the final results. While, again, some optimisation techniques can be used to reduce these effects, the resulting frames will always contain a certain level of randomness. This will have to be taken into account when choosing a optimisation technique, as will be discusses in the next section.

```
<?xml version='1.0' encoding='UTF-8'?>
<skirt-simulation-hierarchy type="MonteCarloSimulation" format="6.1"
producer="Python Toolkit for SKIRT (SkiFile class)"
time="2014-10-29T14:09:55">
  <OligoMonteCarloSimulation packages="5e5">
    <random type="Random">
      <Random seed="4357"/>
    </random>
    <units type="Units">
      <ExtragalacticUnits/>
    </units>
    <instrumentSystem type="InstrumentSystem">
 <InstrumentSystem>
       <instruments type="Instrument">
         <MultiFrameInstrument instrumentName="lol"
         distance="19.6 Mpc" inclination="[inclination:90 deg]"
          azimuth="-90 deg"
          positionAngle="0 deg" writeTotal="false"
          writeStellarComps="true">
           <frames type="InstrumentFrame">
             <InstrumentFrame pixelsX="868" extentX="16083 pc"
              pixelsY="208" extentY="3954 pc"/>
             <InstrumentFrame pixelsX="868" extentX="16083 pc"
              pixelsY="208" extentY="3954 pc"/>
             <InstrumentFrame pixelsX="868" extentX="16083 pc"
              pixelsY="208" extentY="3954 pc"/>
             <InstrumentFrame pixelsX="868" extentX="16083 pc"
              pixelsY="208" extentY="3954 pc"/>
             <InstrumentFrame pixelsX="868" extentX="16083 pc"
              pixelsY="208" extentY="3954 pc"/>
           </frames>
         </MultiFrameInstrument>
       </instruments>
     </InstrumentSystem>
    </instrumentSystem>
    <wavelengthGrid type="OligoWavelengthGrid">
      <OligoWavelengthGrid wavelengths="0.354 micron, 0.475 micron,
       0.622 micron, 0.763 micron, 0.905 micron"/>
    </wavelengthGrid>
    <stellarSystem type="StellarSystem">
      <StellarSystem>
        <components type="StellarComp">
          <OligoStellarComp
          luminosities="1e15, 1e15, 1e15, 1e15, 1e15">
            <geometry type="Geometry">
              <OffsetGeometry offsetX="[xoffset: 0 pc]"
              offsetY="0 pc" offsetZ="[zoffset: 0 pc]">
                <geometry type="Geometry">
                  <ExpDiskGeometry
                  radialScale="[stellar_length: 4400 pc]"
                  axialScale="[stellar_height: 500 pc]"
                  radialTrunc="0 pc"
                  axialTrunc="0 pc"/>
                </geometry>
              </OffsetGeometry>
            </geometry>
          </OligoStellarComp>
          <OligoStellarComp
          luminosities="1e15, 1e15, 1e15, 1e15, 1e15">
```

Figure 2.10: Example ski file as constructed from a SKIRT Q&A session. Free parameters, as fitted by FitSKIRT, are bracketed in green (see Section 2.4.2).

```
            <geometry type="Geometry">
              <OffsetGeometry offsetX="[xoffset: 0 pc]"
              offsetY="0 pc" offsetZ="[zoffset: 0 pc]">
                <geometry type="Geometry">
                  <SpheroidalGeometry flattening="[flattening: 0.5]">
                    <geometry type="SpheGeometry">
                      <SersicGeometry index="[sersic: 2.5]"
                       radius="[bulge_radius: 2500 pc]"/>
                    </geometry>
                  </SpheroidalGeometry>
                </geometry>
              </OffsetGeometry>
            </geometry>
          </OligoStellarComp>
        </components>
      </StellarSystem>
    </stellarSystem>
    <dustSystem type="OligoDustSystem">
      <OligoDustSystem sampleCount="25" writeConvergence="false"
       writeDensity="false" writeQuality="false"
       writeCellProperties="false" writeCellsCrossed="false">
        <dustDistribution type="DustDistribution">
          <CompDustDistribution>
            <components type="DustComp">
              <DustComp>
                <geometry type="Geometry">
                  <OffsetGeometry offsetX="[xoffset: 0 pc]"
                  offsetY="0 pc" offsetZ="[zoffset: 0 pc]">
                    <geometry type="Geometry">
                      <ExpDiskGeometry
                      radialScale="[dust_length: 6600 pc]"
                      axialScale="[dust_height: 250 pc]"
                      radialTrunc="0 pc"
                      axialTrunc="0 pc"/>
                    </geometry>
                  </OffsetGeometry>
                </geometry>
                <mix type="DustMix">
                  <InterstellarDustMix writeMix="false"
                   writeMeanMix="false"/>
                </mix>
                <normalization type="DustCompNormalization">
                  <DustMassDustCompNormalization
                  dustMass="[dust_mass: 4e7 Msun]"/>
                </normalization>
              </DustComp>
            </components>
          </CompDustDistribution>
        </dustDistribution>
              <dustGridStructure type="DustGridStructure">
              <PowCubDustGridStructure writeGrid="false"
               extentX="2e4 pc"
               ratioX="50" pointsX="250" extentY="2e4 pc"
               ratioY="50" pointsY="250" extentZ="0.5e4 pc"
               ratioZ="50" pointsZ="200"/>
            </dustGridStructure>
      </OligoDustSystem>
    </dustSystem>
  </OligoMonteCarloSimulation>
</skirt-simulation-hierarchy>
```

Figure 2.10: (continued)

2.2.2 General overview of FitSKIRT

Our goal is to develop a fitting program that optimises the parameters of a 3D dusty galaxy model in such a way that its apparent image on the sky fits an observed image. In Figure 2.11 we can see how this problem can be translated to an optimisation problem. In this thesis, simulated frame, model image, best fitting frame, etc. will all be used for the top image, which is a result of the SKIRT radiative transfer code. The bottom frame is the observed or reference image. Both of these frames have a pixel dimension of $N_x \times N_y = N_{pix}$. The best fitting model is therefore the model which has the same values, or the closest possible values, in all of these pixels. This comes down to an optimisation problem, where the objective function to be minimised is the χ^2 value,

$$\chi^2(\boldsymbol{p}) = \sum_{j=1}^{N_{\text{pix}}} \left[\frac{I_{\text{mod},j}(\boldsymbol{p}) - I_{\text{obs},j}}{\sigma_j(\boldsymbol{p})} \right]^2 \tag{2.9}$$

In this expression, N_{pix} is the total number of pixels in the image, $I_{\text{mod},j}$ and $I_{\text{obs},j}$ represent the flux in the j'th pixel in the simulated and observed image respectively, σ_j is the uncertainty, and $\boldsymbol{p}$ represents the dependency on the parameters of the 3D model galaxy. Note that, contrary to most χ^2 problems, the uncertainty σ_j in our case depends explicitly on the model: it can be written as

$$\sigma_j(\boldsymbol{p}) = \sqrt{\sigma^2_{\text{obs},j} + \sigma^2_{\text{mod},j}(\boldsymbol{p})} \tag{2.10}$$

The factor $\sigma_{\text{mod},j}(\boldsymbol{p})$ represents the uncertainty on the flux in the j'th pixel of the simulated image corresponding to the Monte Carlo simulation with model parameters $\boldsymbol{p}$. It can be calculated during the Monte Carlo radiative transfer simulation according to the recipes from Gordon et al. (2001). However, in most cases it is very close to a Poisson distribution, which allows for significantly faster calculation. In this case, the noise is simply the square root of the signal. The factor $\sigma_{\text{obs},j}$ represents the uncertainty on the flux in the j'th pixel of the observed image, usually dominated by a combination of photon noise and read noise. It can be calculated using the so-called CCD equation (Newberry, 1991).

$$\frac{S}{N} = \frac{n_*}{\sqrt{n_* + \left(n_s + n_d + n_R^2\right)}} \tag{2.11}$$

Here, n_* stands for the intensity from the source, n_s is the sky noise contribution, n_d the contribution of the CCD's dark current and n_R is the bias or read-out noise. If we assume the exposure time is sufficient, such that the source is the dominating factor, this can be simplified to $S/N = 1/\sqrt{n_*}$ or again $\sigma_{\text{obs},j} = \sqrt{n_*}$.

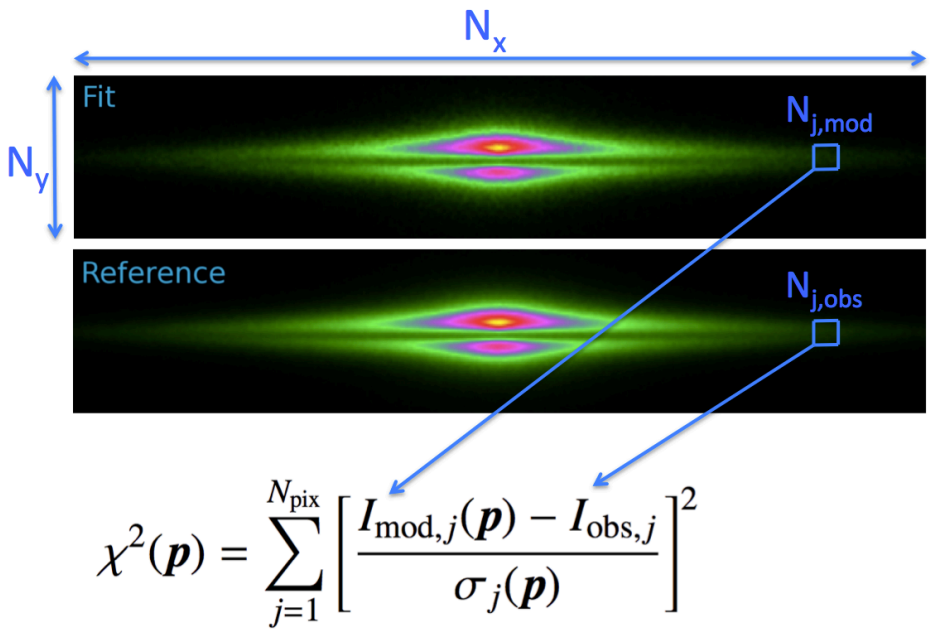

Figure 2.11: The top picture (fit or model) is the simulated frame which is a result of a SKIRT radiative transfer simulation. The bottom frame is the observed or reference image. Both frames have a pixel dimension of $N_x \times N_y = N_{pix}$. The χ^2 value is calculated by considering a pixel j at the same position in both the model and the observation. We then calculate the χ^2 value for this pixel as shown in Eq 2.9 and sum over all pixels.

The full problem we now face is to minimise the χ^2 measure (2.9) by choosing the best value of $\boldsymbol{p}$ in the model parameter space. As the link between the model image and the model parameters is non-trivial (it involves a complete radiative transfer simulation), this comes down to a multidimensional, non-linear, non-differentiable optimisation problem. On top of this, not only do the reference images contain noise, even our models have the Poisson noise, inherently part of the Monte Carlo approach to solve the RTEs. This is quite challenging as in many optimisation problems in astrophysics, for example a blackbody fit, the error on the model is zero as this is an analytically defined function.

It is for these problems that genetic algorithms have been known to be a valuable optimisation tool. Not only do they handle this complex parameter space, they have the advantage that many computations can be handled parallel instead of iteratively progressing from point to point. This helps to parallel the optimisation, as will be discussed in detail in Section 2.3.5. Additionally, the genetic algorithms handle the noise in both the reference frames and the models. This is also partly alleviated by convolving the simulated frames, as discussed in Section 2.3.2.

Our approach to this problem resulted in the FitSKIRT program, a code that com-

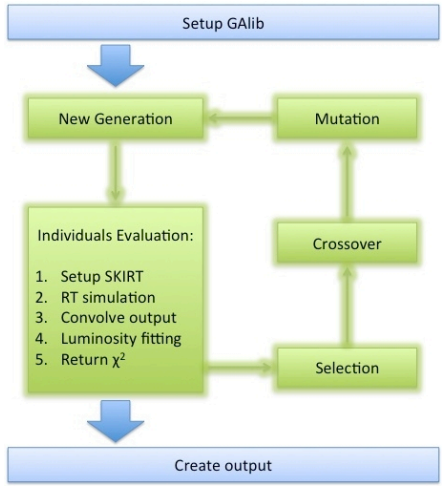

Figure 2.12: The main flowchart of the FitSKIRT procedure. Details on the different steps are given in the text.

bines the radiative transfer code SKIRT and the genetic algorithm library GAlib. FitSKIRT, like SKIRT, is completely written in C++, but is embedded in the Qt framework (Summerfield, 2010). This allows for more flexibility in both the implementation and the usability of the program. Figure 2.12 shows a flowchart of the FitSKIRT program. Each individual in this genetic algorithm contains the entire parameter set to perform a SKIRT radiative transfer simulation. By determining the individual that gives the lowest χ^2 value, we get a parameter set that results in the simulated frame with the best correspondence to the reference frame.

The first step in the process consists of setting up the ingredients for the genetic algorithm. This consists in the first place of defining the reference image and defining the parameterised model describing the distribution and properties of stars and dust in the model galaxy. Apart from setting up this model, we also select the range of the parameters in the model, and define all genetic algorithm parameters like crossover rate, selection and reproduction scheme, mutation rate, etc. How this is handled, together with a more detailed overview of the code structure is discussed in detail in Section 2.4.2.

In the second phase, the genetic algorithm loop (green flow) is started. The initial population is created by randomly drawing the parameter values $\boldsymbol{p}$ from the predefined ranges. The genetic algorithm hence starts out by being uniformly spread across the entire parameter space. The next step is to evaluate which individuals provide a good fit and which do not. This is done starting a monochromatic SKIRT simulation using the parameters $\boldsymbol{p}$ defined by the genes of the individual. Once the simulation is finished, we compare the resulting frame and the reference image

and give the corresponding individual an objective score. Between the creation of the image and returning the actual χ^2 value, the simulated frame is convolved with the point spread function (PSF) of the observed image. The third step is concluded by returning the final $\chi^2(\boldsymbol{p})$ for this individual. After the entire population has been evaluated the best models are selected and offspring is created by crossover. Depending on the mutation rate, some of the genes of these new individuals will undergo a random mutation. After this step we have obtained our new generation which is about to be evaluated next. This loop continues until a predefined number of generations is reached.

Finally, when the genetic algorithm loop ends, the convolved, best fitting frame is created again and the residual frame is determined. These residual frames are useful to investigate which areas of the references frames are well fitted and which are not. They can provide additional insight on the validity and consistency of the models themselves.

2.3 Particular aspects of FitSKIRT

2.3.1 Oligochromatic fitting

The method described above can essentially be applied to any image. However, not all the wavelengths contain the exact same information. As blue bands show clear signs of extinction by dust and which conceals information about the intrinsic stellar distribution, the opposite is true for longer wavelengths where a more accurate map of the stellar distribution is shown. However this comes at the cost of a detailed information on the dust properties. Consequently an ideal fitting routine should incorporate this information by simultaneously making use of the two wavelength regimes.

Therefore, a considerable amount of effort was spent to allow the possibility for this oligochromatic fitting in FitSKIRT. To do this, the objective function (2.9) needs to be slightly updated. Instead of summing over all pixels, we now need to sum over all pixels in the data cube, were each of the slices is the galaxy at a different wavelength. While this essentially does not seem to be that different from the monochromatic case, the implications of this updated objective function are less trivial. One has to be extremely cautious to avoid giving a certain frame or wavelength more weight in the fitting procedure than the other. Different noise values, pixel scales or simply a different number of pixels in the frame could cause a strong bias in the global χ^2 value. For example, if one of the observed frames has more pixels to fit or higher counts compared to the other frames, it could easily dominate the resulting χ^2 value. As a result, the oligochromatic fit would essentially become a computationally expensive monochromatic fit. To avoid this situation, the creation of the set

of reference images should be done as uniformly as possible. This is discussed in detail in Section 2.4.1.

The geometrical parameters of the model are set fixed for all bands. Only the luminosity for every stellar component is changed at every wavelength. This significantly increases the dimensionality of the problem at hand. For a typical case where we have five reference images and have a model with two stellar components, we have to constrain ten more free parameters. Luckily, however, the radiative transfer problem is linear with respect to the total luminosity of the system (which always is one of the parameters in the model). This allows us to treat the total luminosity separately from the other parameters, and determine its best value outside the genetic algorithm minimisation routine. This step effectively decreases the dimensionality of the parameter space the genetic algorithm has to investigate.

In principle, the genetic algorithm searches for the best fitting model in the entire N-dimensional parameter space, where N is the number of free parameters in the model. By fitting the luminosity separately the dimensionality of the parameter space the genetic algorithm has to investigate decreases from N to $N - (N_{*,comp} \times N_\lambda)$, where $N_{*,comp}$ is the number of stellar components used in the model and N_λ is the number of reference frames being fitted. In practice, this is implemented in the following way. Assume our 3D model is defined by the N parameters $\boldsymbol{p} = (p_1, \ldots, p_{N-(N_{*,comp}\times N_\lambda)}, L_{1,1}, \ldots, L_{i,j}, \ldots, L_{N_{*,comp},N_\lambda})$, where $L_{i,j}$ is the luminosity of the ith stellar component at the jth wavelength. In every step in the genetic algorithm, the code selects a set of $N - (N_{*,comp} \times N_\lambda)$ parameters $(p_1, \ldots, p_{N-(N_{*,comp}\times N_\lambda)})$ and starts a SKIRT radiative transfer simulation to create a model image, based on these $N - (N_{*,comp} \times N_\lambda)$ parameters with a dummy value for all $L_{i,j}$ luminosities, and this model image is convolved with the observed image PSF. Before the χ^2 value corresponding to this set of parameters is calculated, the code determines the best fitting total luminosity of the model that minimises the χ^2 value (2.9) for the particular values of these $N - (N_{*,comp} \times N_\lambda)$ parameters. How this is done in practice, for a varying number of stellar components, is discussed in Section 2.3.3.

The oligochromatic fitting has, in our case, two main advantages. In order to get acceptable constraints on the dust parameters, blue bands (for example B, V, R, u, g, etc.) should be included in the reference images. However, as will be discussed in Section 3.2, fitting to these bands alone makes it hard to distinguish the difference between a smaller, dense dust disk and a larger, less dense dust disk. Including redder bands (for example I, J, i, z, etc.), which are less hampered by dust attenuation, allows to discern these two scenarios. These bands also allow better constraints on parameters, like the Sérsic index, which are determined in the very center of the galaxy. Apart from the ability to handle some of the degeneracies monochromatic

modelling has to cope with, oligochromatic fitting allows for more stable convergence towards the optimal solution, especially for low S/N observations (Vika et al., 2013).

2.3.2 Convolution

An important step before correctly comparing the simulated frames with the observations is to incorporate the point spread function (PSF) of the observed images. For optical images taken with ground-based telescope, the PSF is usually dominated by the turbulence in the Earth's atmosphere. Due to this seeing a point-source will be smeared out over a region with an approximately normal distribution characterised by its full width at half-maximum (FWHM).

The images created by the radiative transfer code SKIRT are not immediately convolved to the same FWHM. Therefore, before comparing them to the observed images we convolve the frame by a Gaussian having the FWHM of the reference frame it will be compared to. In the left panel of Figure 2.13 we see the output image of the radiative transfer code with (an unrealistically) small number of photon packages. On the right we see the effect of the convolution on the resulting frame using a Gaussian kernel of 15 by 15 pixels with a FWHM of 5 pixels. Most point sources are clearly smoothed out as a discrete normal distribution. In most cases, however, for two or more neighbouring points (like the two most left points in the frame) these distributions might overlap to one broader region, therefore clearly smoothing the images.

While convolving slightly slows down the fitting procedures, especially for larger frames and large convolution kernels, it helps diminishing the contribution by noise in the frames. Consequently the resulting χ^2 value is slightly less prone to the number of photon packages used in the fitting procedure. As discussed before, this parameter plays an important role in determining the speed of the fitting process and convolving allows for the use of a smaller number of photon packages, again increasing the speed of the code.

2.3.3 Luminosity Fitting

One stellar component

Among the free parameters fitted by FitSKIRT, most have to be defined in advance of the radiative transfer simulation and can not be dealt with afterwards. The only exception to this is the luminosity of each stellar component. As the luminosity and the total intensity in the resulting output frame scale linearly it is possible to run the simulation with a dummy value for the luminosity. Afterwards we can set by

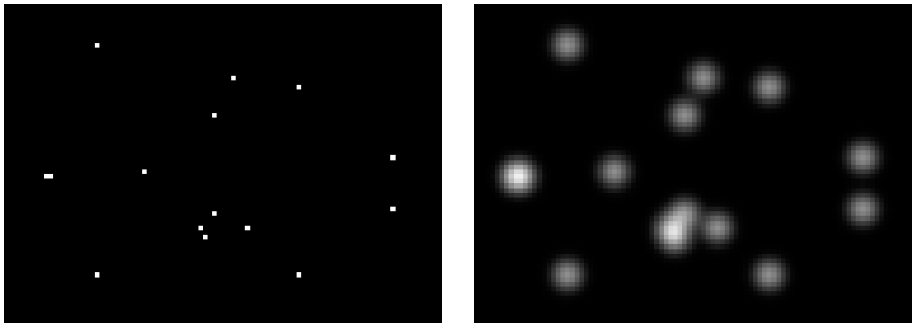

Figure 2.13: Left panel: Raw output frame from the radiative transfer code with photon packages only influencing a single pixel. Right panel: Convolved output image using a Gaussian kernel of 15 by 15 pixels with a FWHM of 5 pixels.

which value the simulated frame has to be multiplied to give the best fitting results. Finding the correct multiplication factor then comes down to performing a one-dimensional optimisation. The factor that results in the lowest χ^2 value for the given frame is therefore the best fitting luminosity for that given set of parameters. Since there is only one correct luminosity and there is no addition of noise in between the creation of the image and determining the correct multiplication factor, the χ^2 changes quite smoothly and without any local minima for varying luminosities. It is because of this feature that a golden section search is an ideal candidate for the determination of the correct multiplication factor.

The golden section search tries to bracket the interval in which the minimum is located and continues to do this iteratively until the interval is small enough, i.e. until the lower and upper bound are roughly the same. It does this by efficiently placing new evaluations and removing the part of the interval which clearly does not contain the best fitting value. In figure 2.14 the golden section search method is applied to an example function. To bracket the interval we first start by evaluating the points at the edge of the given interval; in this case, P_1 and P_2 are the lower and upper boundary, respectively.

When the function is evaluated at positions P_1 and P_2, it is clear that $f(P_2) > f(P_1)$. We now want to determine the next point that needs function evaluation so we can constrain the interval where the optimum is located as much as possible. Consider point P_3 to be a certain ratio w away from P_1 and P_2:

$$P_3 = P_1 + w(P_2 - P_1) \tag{2.12}$$

We will later determine the best option for this ratio w. The function values we get are $f(P_3) < f(P_1) < f(P_2)$. One might think that the next step is to drop P_2.

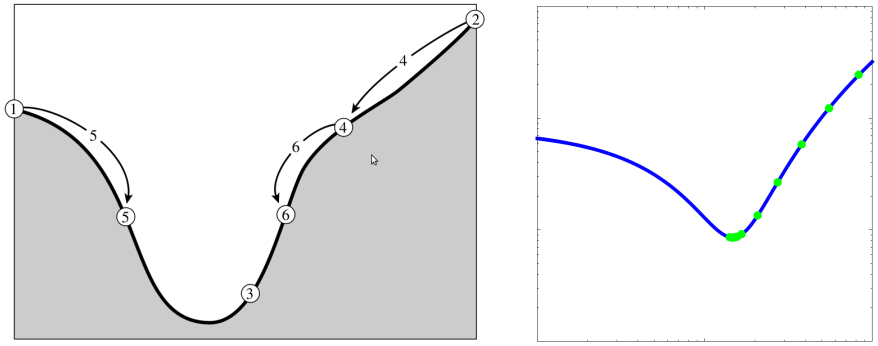

Figure 2.14: Left panel: One-dimensional golden section search method (Numerical recipes in C). Right panel: The one-dimensional parameter space of the χ^2 in function of the luminosity (blue) and the points evaluated by the golden section search method (green).

However, this would be too drastic as one can easily imagine a function with only one minimum in between P_2 and P_3 but which still goes through these three points. Therefore, to determine whether we have to drop point P_1 or P_2 we have to evaluate the function at another point in between P_2 and P_3. As a result, the optimal ratio for P_3 is not half-way in between P_1 and P_2 as one could naively think.

Since we again want to have one optimal ratio to determine the next point, we suppose that point P_4 is the same ratio away from P_3 as P_3 was from P_1 or :

$$P_4 = P_3 + w(P_2 - P_3) \tag{2.13}$$

Since $P_2 - P_3 = (P_2 - P_1) - (P_3 - P_1)$ we get using equation (2.12) and (2.13):

$$P_4 = P_3 + w(1 - w)(P_2 - P_1) \tag{2.14}$$

Because we do not want to make any assumptions whether P_1 or P_2 should be left out, P_4 should be chosen in such a way that $P_4 - P_1 = P_2 - P_3$ or $(P_3 - P_1) + (P_4 - P_3) = (P_2 - P_1) - (P_3 - P_1)$ so the two segments are equal. Using equations (2.12), (2.13), (2.14) we get:

$$w(P_2 - P_1) - w(w - 1)(P_2 - P_1) = (1 - w)(P_2 - P_1) \tag{2.15}$$

$$w^2 - 3w + 1 = 0 \tag{2.16}$$

The solutions are 0.38197 and 0.61803 which explains the name, golden section search. These represent the ratio of the new point compared to both ends so that if we apply it to equations (2.12) and (2.13) the correct value is $w = 0.38197$.
The optimisation method consists of evaluating the new point compared to the al-

ready known interval and then determining which boundary should be dropped. In this example we can see that $f(P_3) < f(P_4)$ so the interval changes to points (P_1, P_3, P_4) but since $f(P_1) > f(P_4)$ the new point, P_5 is now evaluated between P_1 and P_3. The iteration stops when the difference between the boundaries is below a certain value or after a certain number of iterations. This optimisation technique is extremely fast since it is able to rapidly exclude a large part of the observed interval. Since it is easy to implement, it can be easily written in any programming language without need of an additional library.

The optimisation now consists of starting the evaluation at the edges of the given luminosity interval and always choosing the new multiplication value so the new luminosity is at 0.38197 relative to the current interval. In the right panel of figure 2.14 we can see the optimisation process for a model image to a real reference image. The luminosity in this case vary between the unrealistic values of 10^{10} and 10^{50} $L_\odot$ and this method is able to determine the exact value to an extreme precision in only 40 evaluations. Although faster algorithms exist for this sort of one-dimensional optimisation exist, it should be clear that this is not at all the most time-consuming part of the program. Using this technique on frames with a typical value for real FitSKIRT simulations, 5 megapixels, FitSKIRT is able to determine the optimal luminosity in less than a second. The gold section search has the advantages that it is extremely fast, accurate and easy to implement. Its main drawback is that it can not handle any local minima because even only one *wrong* function evaluation has dramatic consequences. However, in our problem this is not the case so we can safely use this method.

Two stellar components

While a single stellar component might be easy to fit observations, this method does seldom provide an adequate description for real observed galaxies. As will be discussed in Section 4.3.1, the stellar distribution in most spiral galaxies need to be described by at least two components: a flat disc and an additional central, spheroidal bulge. While one could argue that this would only require one additional free parameter, i.e. the ratio between the stellar components, in practice these distributions correspond to distinct stellar populations. In fact, the stellar disk of spiral galaxies generally consists of considerably younger stars compared to the redder bulge (van der Kruit and Freeman, 2011).

In Figure 2.15 we see the different steps of how FitSKIRT handles multiple stellar components. In this case we consider two stellar components, one disk and one bulge, affected by the same dust distribution. We start by running a separate simulation for the disc and for the bulge component, each with a dummy input luminosity. Each of the frames is then convolved with the same kernel before determining

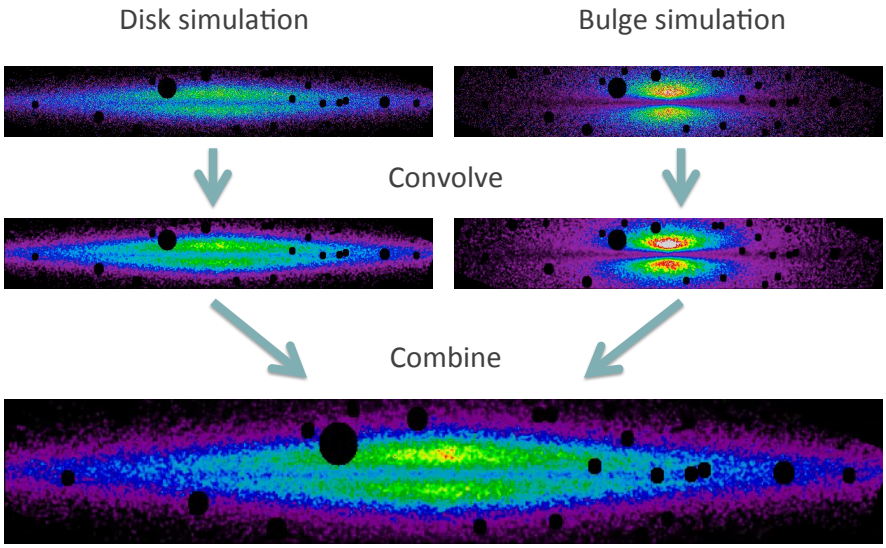

Figure 2.15: The different steps of the FitSKIRT code when handling two stellar components. In the first step each stellar component is written to a separate frame. Both frames are convolved and are then combine to the best fitting combination. This best fitting combination is determined by performing a 2-dimensional parameter search using downhill simplex optimisation.

which combination of the frames gives the best representation of the reference image. In this case, however, the parameter space consists of two dimensions since both the luminosity of the bulge and disk component have to be determined.

While the golden section search is very efficient in a one-dimensional parameter space, there is no straightforward analogue for higher dimensions. The downhill simplex method, also known as Nelder-Mead method or amoeba method (Nelder and Mead, 1965), is another commonly used non-linear optimisation technique. The method iteratively refines the search space defined by an $(N+1)$-dimensional simplex by replacing one of its defining points, typically the one with the worst objective function evaluation, with its reflection through the centroid of the remaining N points defining the simplex.

In relatively simple optimisation problems, the downhill simplex method is known to have a relatively poor convergence, i.e. it is not efficient in the number of objective function evaluations necessary to find the extremum. On the positive side, the method only needs the evaluation of the objective function itself and does not require additional information on the parameter space or the calculation of gradi-

ents.

As, in our case, we do not have any direct measure on the gradients without evaluating more points in the parameter space, downhill simplex optimisation seems an appropriate method to find the best matching combination of two stellar components.

In Figure 2.16 we see the progress of such a simplex optimisation starting from the upper left panel to the lower right one. The density map show high χ^2 values in blue and low values in red. In the upper left panel we see the extreme case where the simplex is initialised in the outer corner. Gradually the simplex first enlarges and moves towards the minimum. Once the minimum falls inside the boundaries, the simplex will start to contract to narrow down to the best fitting values.

As mentioned before, as both components correspond to different stellar populations, modelling the luminosities outside the main fitting procedure considerably reduces the free parameter space for the genetic algorithm. As each frame in our data set would require two additional free parameters, a realistic case could easily add up more than ten additional parameters if the luminosities were not handled separately.

An additional advantage of this approach is that no assumptions have to be made about the underlying stellar populations as they are entirely fitted. As will be discussed in Chapter 5, these luminosities can then be used to determine the best fitting stellar spectral energy distributions for the separate components.

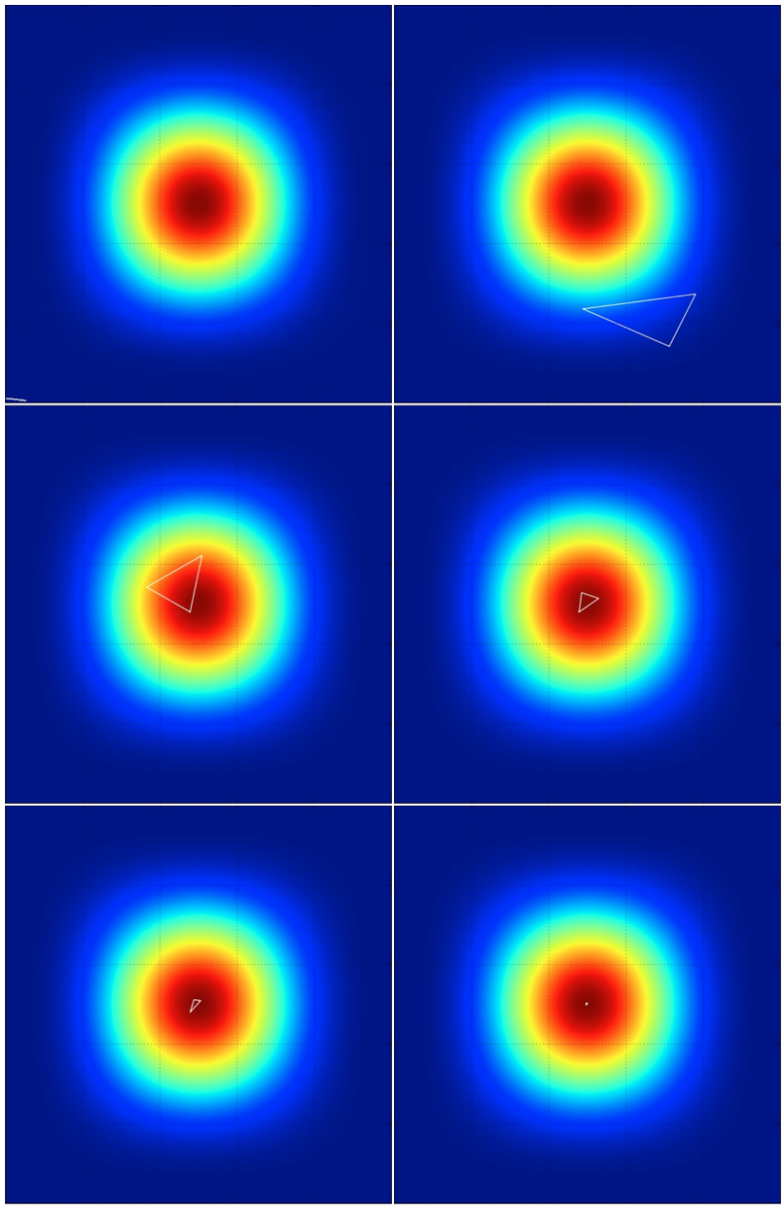

Figure 2.16: The upper left panel show the start of an extreme case where the simplex defining the luminosity values of both components stars out in the lower right corner of the parameter space. Blue represents bad fitting luminosities while red indicates the best fitting values. The upper right panel shows the same simplex a few steps further where we see the simplex became larger and starts moving towards the optimum in the center. In the end, the lower right panel, the simplex has contracted to a small region around the best fitting value.

Three or more stellar components

In most cases, two components suffice to get a decent first-order approximation of edge-on spiral galaxies. However, recent studies have shown that there might be more stellar populations having a different distribution. For example Schechtman-Rook and Bershady (2013b, 2014a) describe that NGC 891, among other galaxies, contains at least four distinctly different distributions. A thick, thin and ultra-thin stellar disk and a traditional bar/bulge component, each requiring its own stellar population. While FitSKIRT has, at this point, not been used to model galaxies with more than two components, the functionality to do so has been implemented for future usage. The difficulty that arises in this case is that, from three components on, one could conceivably have strong degeneracies, between different components. Even in the case of two stellar components, it is possible that some degeneracies appear, but at least one part of the parameter space will always lead down to the global minimum. As soon as we deal with three or more components, it is far more likely to encounter multiple local minima. In this test case we use three stellar components: a thick and thin stellar disk with a Sérsic central bulge. While the simplex method described in previous section works in higher dimensional parameter spaces as well, the method has difficulties in finding the global optimum. A logical choice is to again use the genetic algorithms library already present in our code to solve this problem. While we argue that, for lower dimensional cases, this might not be the best option, the ease of the application and the scalability of the algorithm made it our preferred method. Indeed, genetic algorithms have the advantage that they would not only solve the problem for three stellar components, but in principle for an arbitrarily large number of stellar components.

We have opted to scale the optimisation problem by using the number of stellar components multiplied by 20 as the number of individuals and half of that as evaluated generations. So for three stellar components, we use 30 generations of 60 individuals. Using this method we have a fitting scheme that scales with the problem itself. The 3D problem runs significantly slower than the 2D case using the simplex method, but our method was able to constrain the exact luminosities for a test case using SKIRT mock images. While the method has been tested and seems to work, the degeneracies in observed galaxies might be harder to disentangle and we recommend to use the code with caution until more extensive testing has been done.

Position fitting

An aspect of the code, that is briefly discussed here separately, is the determination of the center of the galaxy. While these two parameters, being the x and y coordi-

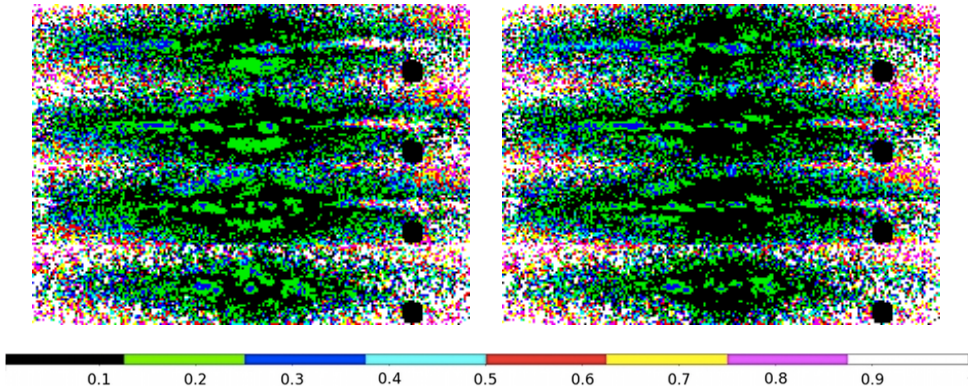

Figure 2.17: Left panel: The residuals of a fit not using position fitting. Right panel: The residuals of a fit using position fitting.

nate of the center, are essentially not fitted differently from the other geometrical parameters, they play a surprisingly important role, in the sense that their values strongly affect the other fitted model parameters. One could conceivably come up with a routine, much like the luminosity fitting, to fit these outside the genetic algorithm loop. However, in our approach, we have decided to model the offset as a physical offset of the distribution itself. In practice, this is done by shifting the center over a certain distance expressed in parsec. The main difference with this approach and a method that would fit the position outside the genetic algorithms, is that in our case, the distribution can shift over a distance smaller than the pixel scale of the reference image. As a results, this *sub-pixel fitting* allows for much better constraints. In practice, however, this will only make a difference for very low resolution frames. In Figure 2.17, we can see the difference of a fit to IC 2098, one including the a variable center (Right panel) and one having a fixed center, determined by eye (Left panel). These residual frames will be used frequently in this thesis to determine visually which regions are accurately fitted and which are not. The residual frame is calculated as

$$\text{Residual} = \frac{|\text{Reference} - \text{Simulated}|}{|\text{Reference}|} \tag{2.17}$$

The colour scale shows the pixels with a percentile difference in steps of 12.5%. In this case it is clear that the right model gives a better description of the data. The best fitted parameters are also more accurately determined with smaller errors on most of the parameters. It is therefore recommended to allow position fitting for smaller galaxies. The sample studied in Chapter 4, were all fitted using a variable center.

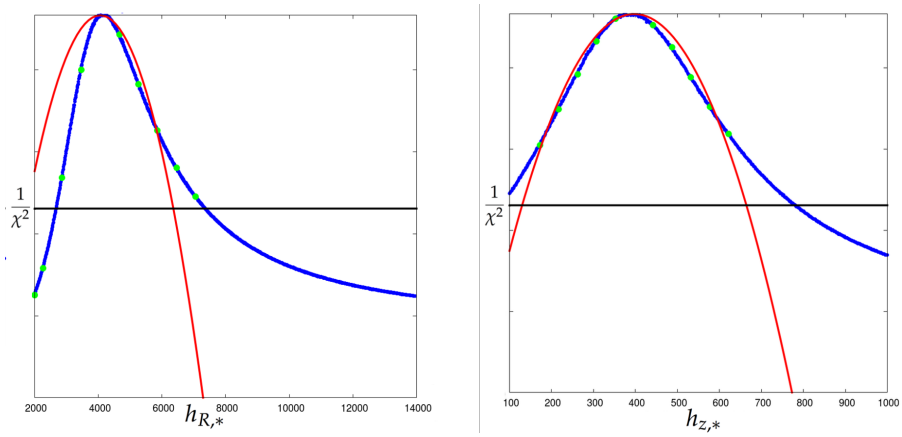

Figure 2.18: Left panel:The blue curve shows the shape of the 1D cut through the parameter space along the stellar scale length. The green dots are the additional function evaluations used to determine the parabola in red. The black solid line represents the inverse χ^2 value which would correspond to $\chi^2 = 2$. Right panel: The same as the left panel but for the stellar height.

2.3.4 Error analysis

Apart from finding the parameters that correspond to the model that is the best fit to the observed image, we also want a measure of the uncertainties on these parameters. A disadvantage of most stochastic optimisation methods, or more specific genetic algorithms, is that such a measure is not readily available. Traditionally this is done by determining what varying parameter values would still result in an *acceptable* χ^2 value. However, due to our non-standardised χ^2 definition, we have no absolute claims on what is an appropriate value. This can be done by fixing all parameters but one, and determining at what value this free parameter drops below the acceptable value. In Figure 2.18 we see a 1D normalised, inverse χ^2 value cut along the stellar length and stellar height of a best fitting model. Here, one would expect that this "acceptable" value is at 0.5, being the place where χ^2 value would be 2. As the χ^2 function should be closer to parabolic than Gaussian near the optimum, determining the FWHM of the parabola through this optimum would provide a reasonable measure of the uncertainty. The green dots represent a gridded way to determine this parabola with an acceptable number of additional function evaluations. It is clear from these images that here, this value would extremely overestimate the error on these parameters. Even more so, for some harder to determine parameters like the dust mass, this method often results in non-physical values.

A similar method is to use Bayes Theorem on a well sampled χ^2 function in order to get uncertainties on the derived parameters (Johnston et al., 2011; Menu et al., 2014).

However, the problem with this approach in our case is that, because of the vast dimensionality of our parameter space, our χ^2 function is not sufficiently sampled. Sampling it accordingly, either directly from the genetic algorithm evaluations or by using newly sampled points on a grid is simply not feasible computationally. Also with this approach, defining the $\Delta\ \chi^2$ which determines the acceptable value is not possible.

A way of partially solving this problem is by using a statistical resampling technique like bootstrapping or jackknifing (Press et al., 1992; Nesseris and Shafieloo, 2010; Nesseris and Garcia-Bellido, 2012). This basically comes down to iteratively replacing a predefined number of the simulated points by the actual data points and comparing the resulting objective function value. Still, even these estimations of the standards errors should not be used heedlessly to construct confidence intervals since they remain subject to the structure of the data. Bootstrapping also requires the distribution of the errors to be equal in the data set and the regression model (Sahinler and Topuz, 2007; Press et al., 1992). Since this is not entirely the case for this problem, as equation (2.9) shows, an alternative approach was used to determine the uncertainty on every parameter.

Since genetic algorithms are essentially random and the parameter space is so vast and complex, the fitting procedure can be repeated multiple times without resulting in the exact same solution. On top of that, the difficulty of differentiating between some individuals because of some closely correlated parameters will be reflected in the final solutions. The entire fitting procedure that is used here consists of running five independent FitSKIRT simulations, all with the same optimisation parameters. The standard deviation on these five solutions is set as an uncertainty on the "best" solution (meaning the lowest objective function value). While computationally expensive, this method still allows for better solutions to be found. The spread in the parameters give some insight in how well the fitting procedure is able to constrain some parameters and which parameters correlate. If the solutions are not at all coherent, this can also indicate something went wrong during the optimisation process (e.g. not enough individuals or generations).

One could argue that this is not an "error" determination in the strict sense as the case where we would obtain the same best fitting model every time, the error would unrealistically be zero. However, notice that, due to the randomness in our models, fitting to a resampled data set is already intrinsically built into our method. Indeed, because we start from a new initial generation, we shoot random photons, and the weights depend on the model parameters (see Equation 2.9), our approach is essentially equivalent to using a different subset of our reference images.

2.3.5 Parallelisation

While genetic algorithms are known to be computationally more demanding than some other optimisation methods, they have the advantage that many calculations can be handled parallel. Especially in our case, where every function evaluation requires a radiative transfer simulation, this is extremely useful. Essentially every individual can be calculated separately. For a typical FitSKIRT simulation, were we have around 200 individuals, this means we can handle up to 200 separate simulations. As this is the most time consuming part of our code and, in most cases, little memory is required for every simulation, this is particularly well suited to run on a high performance computer with multiple nodes. In fact, this problem scales almost linearly up to the available number of individuals therefore making the code almost 200 times faster than the iterative implementation.

In FitSKIRT we have chosen to implement a master-slave architecture, using openMPI, to distribute the separate radiative transfer simulations to different nodes and/or processors. While only the ranking and the determination of the new parameter values has to be done on a single node, this process becomes the master process which distributes the different radiative transfer simulations to the slave processes. As essentially only the input parameters need to be known, the overhead by communication between different nodes is very limited.

FitSKIRT has primarily been run on the Vlaamse SuperComputer (VSC), and a brief section explaining how to setup a MPIrun of FitSKIRT on this machine was added to the FitSKIRT users guide available at `http://www.skirt.ugent.be/`.

Essentially the code can even be used with more cores as a second parallelisation is present in the code. As the most time consuming part within one radiative transfer simulation is launching photon packages and that this can be done relatively independently in the optical regime, the code can parallelise this over multiple processors. However, in this case, this can only be done on shared-memory computers. As the setup of the code is not parallelised in this way, it is recommended to use the MPI parallelisation of the individuals rather than parallelising the launching of the photon packages.

2.4 A concise FitSKIRT user manual

2.4.1 Data preparation

This sections starts with the assumption that the user knows how to reduce (bias, dark, flat, stacked, calibration,...) optical data and resample them to have the same pixel scale and matching astrometry. This should not be considered a cookbook for

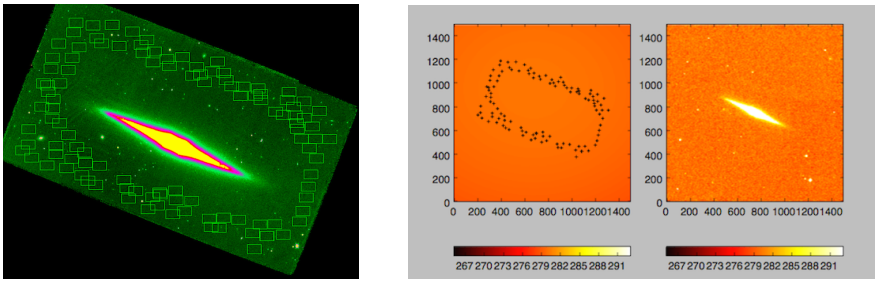

Figure 2.19: Left panel: Determining the sky contribution in optical images. The boxes are placed around the galaxy while avoiding other obvious sources as foreground stars or other galaxies. The values within these boxes is than averaged and these values are used to determine the best fitting plane (or polynomial surface) through these points. Right panel: The best fitting plane through the placed boxes and the result of the sky subtracted image.

optical data reduction but instead will only discuss the steps which are necessary to apply FitSKIRT to the data. The code comes with a set of python scripts to prepare the data and a detailed step-by-step tutorial is available at `http://www.skirt.ugent.be/pts/_fit_s_k_i_r_t_guide.html`

The frames should have the same Field-Of-View (FOV) (for some this will be partially filled with zero's) and dimension. The latter can be accomplished by using the IDL routine hastrom.pro or using the open-source software Montage. An example of how to accomplish this has been added to files used in the tutorial. Astrometry can be added to most images automagically using `http://nova.astrometry.net/upload`, either online or by installing the software. Strictly speaking the frames should not have the same dimensions, as the MultiFrameInstrument discussed in Section 2.2.1 was introduced for this particular reason. However, using different frame sizes will slightly affect the way the χ^2 function biases the frames so it is advisable to use the same dimensions and physical sizes if, at all, possible.

The first thing to consider when preparing data for FitSKIRT is to subtract the sky background in an appropriate way. Remember that in Equation 2.11, we have assumed that the noise contribution is negligible compared to the observed flux from the source. If the sky background is not subtracted, FitSKIRT has no way of distinguishing intensity belonging to the galaxy and background. The result will be incorrectly fitted data and untrustworthy models. Notice that the sky-background is not always a straight plane but sometimes higher order corrections are necessary to flatten the background. In Figure 2.19 we can see how this is done in the scripts provided with the code. First some boxes are placed around the galaxy while avoiding other obvious sources as foreground stars or other galaxies. The values within these boxes is averaged and are used to determine the best fitting plane (or polynomial surface) through these points. This surface is than subtracted from the image, which

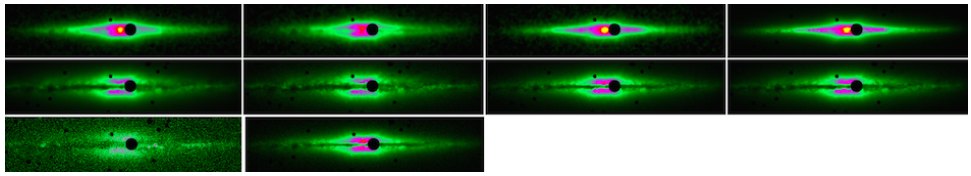

Figure 2.20: Example of a clean sample of different observations of NGC 4013, ready for FitSKIRT use.

should result in a flattened sky noise centred around 0. Additionally, together with this step, one should determine the FWHM of the PSF for each observations and store it. This can be done by determining the best fitting Gaussians through a set of unsaturated stars. The FWHM should be be added to the appropriate frames in the *fski* file as can be seen in Figure 2.22.

The next step is to rotate the frame so the galaxy is aligned with the horizontal axis. This, again, is not an absolute necessity as the position angle can be set as a free parameter in FitSKIRT. However, in order to reduce the parameter space it is recommended to do so, especially because this is easily done manually. In case of doubt, it is still possible to allow a small range of position angles in the simulation.

After rotating, it is useful to crop the frame to an appropriate size and make sure the center of the galaxy matches the center of the frame. Determining the appropriate size can be done "by eye" or by looking at the contour of the value which is at least 2 times above the deviation in the background. The galaxy center can usually be found by looking at the pixel with the highest value. When only optical data is available, this can become harder as the true center might be hidden behind a dust lane. Especially in these cases it is recommended to allow FitSKIRT to adjust the center of the image (see Section 2.3.3). However, users are strongly advised to provide an accurate guess so the boundaries on the central position are not exceedingly big. If the frames are large, it might be worth rebinning the frames to a smaller size as this increases the speed of fitting procedure. The next step consists of masking all the foreground stars and replacing the values by 0.0. Pixels with this value are not taken into account by FitSKIRT and the mask is copied to the model images.

As an important final step, it is highly recommended to normalise the total intensity of each of the frames. Setting the total flux to 1, makes sure that FitSKIRT gives a more or less equal weight to all frames in the data set. In case the frames were flux-calibrated in the beginning, it might be important to save this factor in order to translate the luminosities determined by FitSKIRT to calibrated values.

Figure 2.20 shows an example of how the final sample should look like.

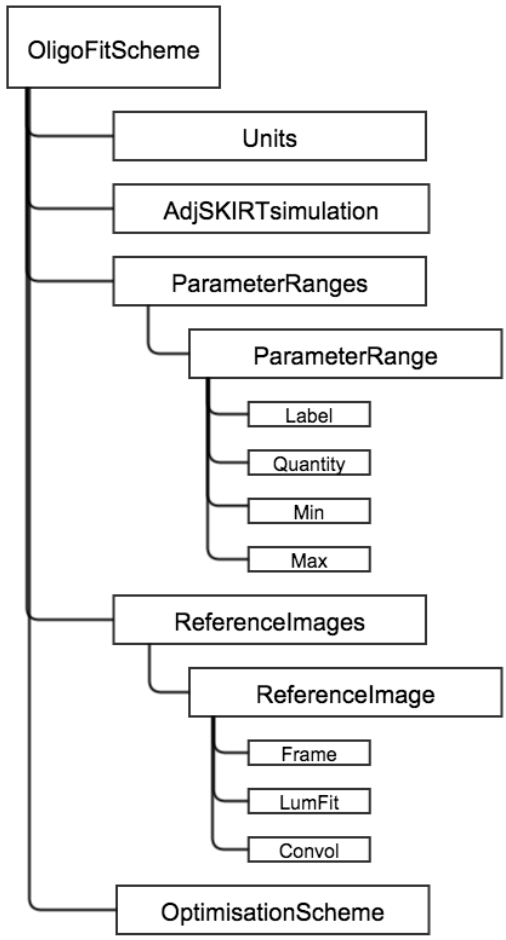

Figure 2.21: A schematic representation of the basic elements which need to be configured for a particular FitSKIRT simulation.

2.4.2 Structure and setup

In Figure 2.21, a schematic representation of the main items of a FitSKIRT simulation is shown. For now, the code only allows oligochromatic fitting. Panchromatic radiative transfer simulations, with the necessary dust emission, have the disadvantage that the wavelengths can no longer be treated independently. This has far-reaching implications that would require a completely different approach from the one which FitSKIRT is based on now. Not only would the luminosity fitting now have to be predetermined, also stellar SEDs and wavelength biases would have to be considered. This arduous tasks therefore falls out the scope of this thesis.

The first thing to consider is obviously the used units in the FitSKIRT simulation. In most cases, in fact to-date in all used FitSKIRT cases, this will be the same as the

corresponding SKIRT simulation. The second item is an AdjustableSKIRTSimulation item. In practice this is the path to a *ski* file which is used as a template for every radiative transfer simulation FitSKIRT will perform.

Next, FitSKIRT requires a list of ParameterRange objects each having a label (see Section 2.4.2), a quantity type describing what type of parameter it is (dimensionless, angle, length, ...) and a minimum and maximum value. This is essentially the list of all $p_{N-(N_{*,comp}\times N_{\lambda})}$ parameters, discussed in Section 2.3.1, and their upper and lower boundaries. Notice that these parameters do not include the luminosity and therefore all of them are the same at every wavelength in the simulation.

The ReferenceImages object is a list containing all the separate reference frames FitSKIRT will be constraining. This includes a path where to read in the frame, the luminosity boundaries for every stellar component for that image and the matching convolution parameters (the FWHM and the convolution kernel size).

The final component is the global optimisation method and the corresponding parameters. In the current version of FitSKIRT this is always genetic algorithms, but the code has been written in such a way that other methods can be incorporated in the future. In fact, other methods have been tested as well as will be discussed in Section 3.1.5.

When running the code for the first time, like is the case for SKIRT, the user will be entering a Q&A session which loops over all the necessary ingredients for the code. At the end of the session, the input provided by the user is stored as a *fski* file, in the same XML format as the *ski* file. Figure 2.22 shows an example of such a file, which corresponds to the *ski* file shown in Figure 2.10. This lists all the possible features and properties of the code. One of the properties are the labels of the `ParameteRanges`. In this case we have 11 parameters being: `stellar_height`, `stellar_length`, `dust_height`, `dust_length`, `dust_mass`, `sersic`, `bulge_radius`, `flattening`, `inclination`, `xoffset` and `zoffset`. These represent the parameters FitSKIRT will alter in the template *ski* file that was provided. It will alter this template for every SKIRT radiative transfer simulation it performs and fills in a value falling within the `minimumValue` and `maximumValue` range. When looking at the template *ski* file in Figure 2.10 we can see that these parameters (shown in green) and the corresponding label are put inside square brackets. The value inside these brackets after the colon, is only used as a default value when SKIRT and not FitSKIRT runs the ski file. It is not used at all by FitSKIRT.

While, at first, this might seem an overly complex way to setup a program like FitSKIRT, this approach offers a very clear advantage. By letting the users create his/her own SKIRT template and letting him/her decide which parameters are free and which are fixed, the list of possible applications of FitSKIRT increases enormously. In theory, every possible value for every geometry, dust grid, instrument,

dust property that can be set in SKIRT could be fitted by FitSKIRT. In practice, we only fit those parameters that can be constrained by optical images, but it should be clear that this method allows for a wide range of possible applications. In this thesis most of them will be edge-on spiral galaxies but this is by no means the only possible application of FitSKIRT. In Chapter 6 we will discuss some other applications shortly as well.

2.4.3 Results and analysis

Once the first Q&A session is finished and the *fksi* file is created, the program can be started by giving the file as an argument. After the simulation is finished, a number of output files are created. Because FitSKIRT can create a huge amount of output, it only keeps the best fitting frames and deletes any additional files. However, the allsimulations.dat file keeps all relevant information about all the performed radiative transfer models. The first digit of the line is the generation number. The following numbers are the parameter values for that model in the same order as they are given in the *fski* file. Next is the total χ^2 value, the luminosity at the first wavelength of the first (and consecutive) component(s), the luminosity at the second wavelength (and consecutive) component(s), etc. Finally, the χ^2 value of every reference frame is listed.

The BESTsimulations.dat file contains only the simulations which, at that point, were the best fitting models. The model on the first line is therefore the first radiative transfer model done, because by definition it was the best model at that point. The last line gives you the final solution. As this is not the clearest way to get an overview of your run, make sure to look at the fitskirt_results.py script that comes with the PTS toolkit (see `http://www.skirt.ugent.be/pts/_fit_s_k_i_r_t_guide.html`). The PTS routine fitskirt_results is a routine which automatically scans subdirectories for fitting results from a certain *fski* file. In a first step it reads all the free parameters and creates a "*_result.dat" file for every fit. The second phase consists out of finding the best solution and determining the uncertainty on each parameter. The combined result and uncertainty are written to "*_RESULT.dat".

The best fitting models are given as tutorial_Best_X_Y.fits where X corresponds to the best fitting solution in BESTsimulations.dat and Y is the wavelength index. These frames are adjusted to the best fitting luminosity, convolved with the appropriate beam and have the same masked regions as the reference frames (see Section 2.4.1). Additionally a corresponding residual frame is created, Residual_X_Y.fits, defined as Equation 2.17.

```
<?xml version="1.0" encoding="UTF-8"?>
<skirt-simulation-hierarchy type="FitScheme" format="6.1"
producer="FitSKIRT v7 (git 112-afe2193 built
on Oct 28 2014 at 16:42:11)" time="2014-10-29T14:44:30">
    <OligoFitScheme fixedSeed="false">
        <units type="Units">
            <ExtragalacticUnits fluxOutputStyle="Neutral"/>
        </units>
        <simulation type="AdjustableSkirtSimulation">
            <AdjustableSkirtSimulation skiName="exp.ski"/>
        </simulation>
        <parameterRanges type="ParameterRanges">
            <ParameterRanges>
                <ranges type="ParameterRange">
                    <ParameterRange label="stellar_height" quantityType="length"
                     minimumValue="10 pc" maximumValue="500 pc"/>
                    <ParameterRange label="stellar_length" quantityType="length"
                     minimumValue="2000 pc" maximumValue="8000 pc"/>
                    <ParameterRange label="dust_height" quantityType="length"
                     minimumValue="20 pc" maximumValue="500 pc"/>
                    <ParameterRange label="dust_length" quantityType="length"
                     minimumValue="1000 pc" maximumValue="12000 pc"/>
                    <ParameterRange label="dust_mass" quantityType="mass"
                     minimumValue="0.1e7 Msun" maximumValue="10e7 Msun"/>
                    <ParameterRange label="sersic" quantityType="dimless"
                     minimumValue="0.51" maximumValue="7.5"/>
                    <ParameterRange label="bulge_radius" quantityType="length"
                     minimumValue="250 pc" maximumValue="5000 pc"/>
                    <ParameterRange label="flattening" quantityType="dimless"
                     minimumValue="0.01" maximumValue="1"/>
                    <ParameterRange label="inclination" quantityType="posangle"
                     minimumValue="85 deg" maximumValue="90 deg"/>
                    <ParameterRange label="xoffset" quantityType="length"
                     minimumValue="-500 pc" maximumValue="500 pc"/>
                    <ParameterRange label="zoffset" quantityType="length"
                     minimumValue="-500 pc" maximumValue="500 pc"/>
                </ranges>
            </ParameterRanges>
        </parameterRanges>
```

Figure 2.22: Example fski file as constructed from a FitSKIRT Q&A session and corresponding to template ski file constructed in Figure 2.10.

```
        <referenceImages type="ReferenceImages">
            <ReferenceImages>
                <images type="ReferenceImage">
                    <ReferenceImage path="./reference/u.fits"
                    minLuminosities="1e5, 1e5" maxLuminosities="1e8, 1e8">
                        <convolution type="Convolution">
                            <Convolution fwhm="2" dimension="5"/>
                        </convolution>
                    </ReferenceImage>
                    <ReferenceImage path="./reference/g.fits"
                    minLuminosities="1e5, 1e5" maxLuminosities="1e8, 1e8">
                        <convolution type="Convolution">
                            <Convolution fwhm="2" dimension="5"/>
                        </convolution>
                    </ReferenceImage>
                    <ReferenceImage path="./reference/r.fits"
                    minLuminosities="1e5, 1e5" maxLuminosities="1e8, 1e8">
                        <convolution type="Convolution">
                            <Convolution fwhm="2" dimension="5"/>
                        </convolution>
                    </ReferenceImage>
                    <ReferenceImage path="./reference/i.fits"
                    minLuminosities="1e5, 1e5" maxLuminosities="1e8, 1e8">
                        <convolution type="Convolution">
                            <Convolution fwhm="2" dimension="5"/>
                        </convolution>
                    </ReferenceImage>
                    <ReferenceImage path="./reference/z.fits"
                    minLuminosities="1e5, 1e5" maxLuminosities="1e8, 1e8">
                        <convolution type="Convolution">
                            <Convolution fwhm="2" dimension="5"/>
                        </convolution>
                    </ReferenceImage>
                </images>
            </ReferenceImages>
        </referenceImages>
        <optim type="Optimization">
            <Optimization popsize="200" generations="100"
            pmut="0.1" pcross="0.65"/>
        </optim>
    </OligoFitScheme>
</skirt-simulation-hierarchy>
```

Figure 2.22: (continued)

Test cases

3

In this chapter we describe some of the cases that were used to test the accuracy and robustness of the FitSKIRT code. Some basic tests are run before applying the code to mock images created by the radiative transfer code SKIRT in Section 3.1. In the last Section of this chapter we apply the code to a real galaxy, NGC 4013, and compare the results from FitSKIRT with the results found by other radiative transfer codes.

3.1 Test case 1: monochromatic fitting to a mock image

In this section, we apply the FitSKIRT code on a simulated test image, in order to check the accuracy and effectiveness of this method in deriving the actual input parameters.

3.1.1 The model

The test model consists of a simple but realistic model for a dusty edge-on spiral galaxy, similar to the models that have been used to actually model observed edge-on spiral galaxies (e.g. Kylafis and Bahcall, 1987; Xilouris et al., 1997, 1999; Bianchi, 2007, 2008; Baes et al., 2010; Popescu et al., 2011; MacLachlan et al., 2011; Holwerda et al., 2012b). The system consists of a stellar disc, a stellar bulge and a dust disc.

The stellar disc is characterised by a double-exponential disc, described by the luminosity density

$$j(R,z) = \frac{L_{\mathrm{d}}}{4\pi\, h_{R,*}^2\, h_{z,*}} \exp\left(-\frac{R}{h_{R,*}}\right) \exp\left(-\frac{|z|}{h_{z,*}}\right) \tag{3.1}$$

with L_{d} the disc luminosity, $h_{R,*}$ the radial scale length and $h_{z,*}$ the vertical scale height. For the stellar bulge, we assume the following 3D distribution,

$$j(R,z) = \frac{L_{\mathrm{b}}}{q\, R_{\mathrm{e}}^3}\, \mathcal{S}_n\left(\frac{m}{R_{\mathrm{e}}}\right) \tag{3.2}$$

where

$$m = \sqrt{R^2 + \frac{z^2}{q^2}} \tag{3.3}$$

is the spheroidal radius and $\mathcal{S}_n(s)$ is the Sérsic function, defined as the normalised 3D luminosity density corresponding to a Sérsic surface brightness profile, i.e.

$$\mathcal{S}_n(s) = -\frac{1}{\pi} \int_s^\infty \frac{\mathrm{d}I}{\mathrm{d}t}(t) \, \frac{\mathrm{d}t}{\sqrt{t^2 - s^2}} \tag{3.4}$$

$$I(t) = \frac{b^{2n}}{\pi \, \Gamma(2n+1)} \exp\left(-b \, t^{1/n}\right) \tag{3.5}$$

This function can only be expressed in analytical form using special functions (Mazure and Capelato, 2002; Baes and Gentile, 2011; Baes and van Hese, 2011). Our bulge model has four free parameters: the bulge luminosity L_b, the effective radius R_e, the Sérsic index n and the intrinsic flattening q.

The dust in the model is also distributed as a double-exponential disc, similar to the stellar disc,

$$\rho_\mathrm{d}(R,z) = \frac{M_\mathrm{d}}{4\pi \, h_{R,\mathrm{d}}^2 \, h_{z,\mathrm{d}}} \exp\left(-\frac{R}{h_{R,\mathrm{d}}}\right) \exp\left(-\frac{|z|}{h_{z,\mathrm{d}}}\right) \tag{3.6}$$

with M_d the total dust mass, and $h_{R,\mathrm{d}}$ and $h_{z,\mathrm{d}}$ the radial scale-length and vertical scale-height of the dust respectively. The central face-on optical depth, often used as an alternative to express the dust content, is easily calculated

$$\tau_\mathrm{f} \equiv \int_{-\infty}^{\infty} \kappa \, \rho(0,z) \, \mathrm{d}z = \frac{\kappa \, M_\mathrm{d}}{2\pi \, h_{R,\mathrm{d}}^2} \tag{3.7}$$

where κ is the extinction coefficient of the dust.

parameter	unit	reference	1 parameter	3 parameters	11 parameters
$M_{\rm d}$	$10^7\ M_\odot$	4	4.00 ± 0.02	3.98 ± 0.08	3.75 ± 0.5
$\tau_{\rm f}$	–	0.80	0.80 ± 0.01	0.86 ± 0.08	0.98 ± 0.14
$h_{R,{\rm d}}$	kpc	6.6	–	6.50 ± 0.40	5.83 ± 0.75
$h_{z,{\rm d}}$	pc	250	–	241 ± 16	245 ± 30
$L_{\rm tot}$	$10^9\ L_\odot$	1	–	–	0.97 ± 0.09
$h_{R,*}$	kpc	4.4	–	–	4.36 ± 0.26
$h_{R,*}$	pc	500	–	–	519 ± 51
B/D	–	0.33	–	–	0.34 ± 0.08
$R_{\rm e}$	kpc	2	–	–	1.75 ± 0.24
n	–	2.5	–	–	2.5 ± 0.5
q	–	0.5	–	–	0.50 ± 0.04
i	deg	89	–	–	88.9 ± 0.1

Table 3.1: Input values and fitted values of the parameters of the model used in the test simulations in Section 3.1. The values used to create the reference image (see Figure 3.3) are given in the third column. The fourth, fifth and sixth column list the fitted values for these parameters, together with their 1σ error bars, for the fits with one, three and eleven free parameters respectively.

In total, this 3D model has 10 free parameters, to which the inclination i of the galaxy with respect to the line of sight should be added as an 11th parameter (as we assume that the position angle and the galaxy center are known for this test case). To construct our reference model, we selected realistic values for all parameters, based on average properties of the stellar discs, bulges and dust discs in spiral galaxies (Xilouris et al., 1999; Kregel et al., 2002; Hunt et al., 2004; Bianchi, 2007; Cortese et al., 2012). The set of parameters is listed in the third column of Table 3.1. We constructed a V-band image on which we will test the FitSKIRT code by running the SKIRT code in monochromatic mode on this model, fully taking into account absorption and multiple anisotropic scattering. The optical properties of the dust were taken from Draine and Li (2007). The resulting input image is shown in the top panel of Figure 3.3. It is 500×100 pixels in size, has a pixel scale of 100 pc/pixel and the reference frame was created using 10^7 photon packages. To make the case a bit more realistic we have assumed a Gaussian PSF with a FWHM of 2 pixels. Also, although ou model consists of two separate stellar components, at this point in the code, the ratio between them was fitted by the genetic algorithms and not by the simplex method. The overall luminosity was, however, fitted by the one-dimensional golden section search described before. While this is slightly different, as this problem is a 10+1 problem instead of a 9+2 problem, this difference is negligible for a monochromatic case.

We now apply the FitSKIRT code with the same parameter model to this artificial test image and investigate whether we can recover the initial parameters of the model. We proceed in different steps, first keeping a number of parameters in the model fixed to their input value and gradually increasing the number of free parameters.

3.1.2 One free parameter

To do some first basic testing with FitSKIRT, no luminosity fitting is used on any of the images. Apart from the dust mass M_d all parameters are fixed and set to the same of the simulated image. We let FitSKIRT search for the best fitting model with the dust mass ranging between 5×10^6 and 1.25×10^8 $M_\odot$. Note that this interval is not symmetric with respect to the model input value of 4×10^7 $M_\odot$, which makes it slightly more difficult to determine the real value.

Figure 3.1 shows the evolution of a population of 100 individuals through 20 generations with a mutation probability of 10% and a crossover rate of 70%. In fact, when using genomes with only one free parameter, the crossover rate becomes quite meaningless. This is because the crossover between two different genomes will result in an offspring that is essentially exactly the same as the best of the parent genomes. This duplication will, however, still result in a faster convergence since

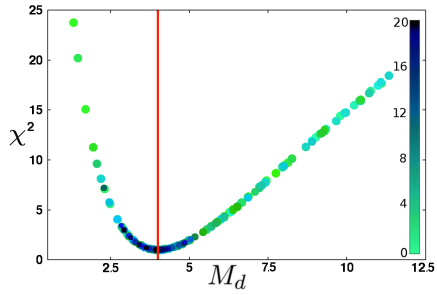

Figure 3.1: Evolution of the determination of the dust mass in the FitSKIRT test simulation with one free parameter. The plot shows the distribution of the χ^2 value for each of the 100 individuals for 20 generations. The colors represent the different generations and the input value is indicated by a red line.

the mutation around those genomes will generally be in a better area than around a random position. FitSKIRT recovers a dust mass of $(4.00 \pm 0.02) \times 10^7\ M_\odot$, exactly equal to the dust mass of the input model. This Figure 3.1 shows that the parameter space is indeed asymmetrical around the true value (indicated by the red line) and that the entire population is gradually shifting towards the optimal value.

3.1.3 Three free parameters

As a second step we consider the case where we fit three free parameters, more specifically the three parameters defining the dust distribution: the dust mass M_d, the radial scale length $h_{R,\mathrm{d}}$ and vertical scale height $h_{z,\mathrm{d}}$. The dust parameters are hard to determine individually since they have to be determined directly from the dust lane. The stellar parameters, on the other hand, are more easily determined and constrained in a larger region outside the dust lane. The problem is close to being degenerate when we look at the dust scale length and dust mass in exact edge-on, since changing them will roughly affect the same pixels.

We consider a wide possible range for the free parameters: the dust scale length is searched between 3 and 9 kpc, the scale height between 50 and 600 pc and for the dust mass we considered a range between 5×10^6 and $1.25 \times 10^8\ M_\odot$. In Figure 3.2 we can see the evolution of a population consisting of 100 individuals through 20 generations in the $h_{R,\mathrm{d}}$ versus $h_{z,\mathrm{d}}$ and the $h_{R,\mathrm{d}}$ versus M_d projections of the 3D parameter space. For now we only consider a crossover of 70% and disable the mutation so we can take a closer look at the global optimisation process. As we can see, the entire population slowly converges until, in the end, it is located entirely around the actual value. This is indeed what we would expect from a global optimisation process. The final best fit values are summarised in the fifth column of Table 3.1. With only three free parameters at the moment, FitSKIRT is still able to converge

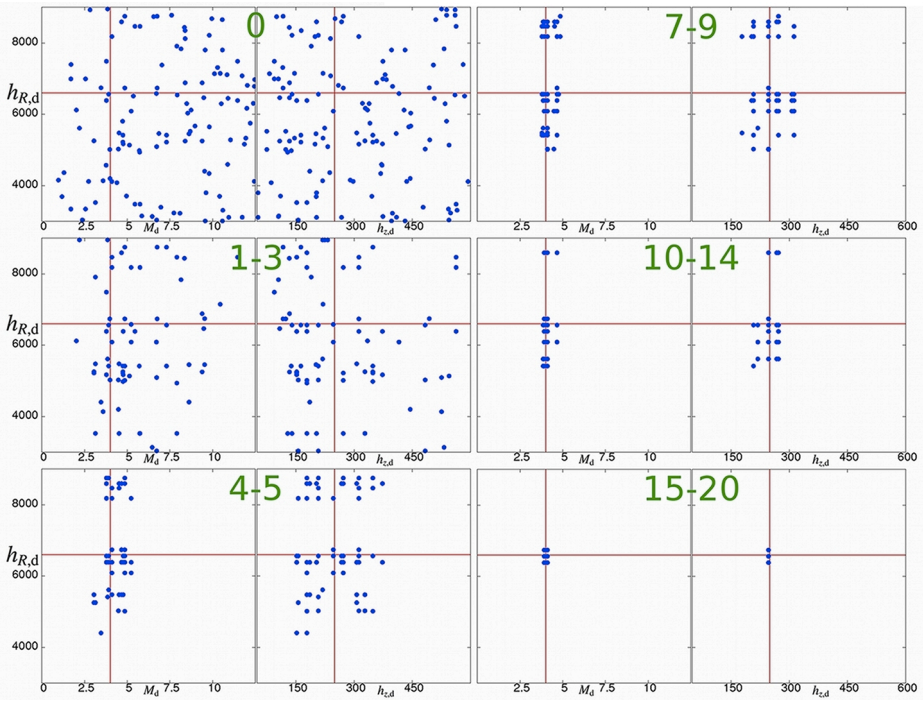

Figure 3.2: Evolution of the dust parameters for a population of 100 individuals for the test model with three free parameters. The different panels show the position of each individual in the $h_{R,d}$ versus $h_{z,d}$ and the $h_{R,d}$ versus M_d projections of the 3D parameter space, for different generations (indicated by the green numbers on the top of each panel). The input values of the parameters are indicated by red lines.

towards the exact values within the uncertainties. Notice that from all parameters, the dust scale length $h_{R,d}$ is the hardest to constrain for edge-on galaxies. The values can be constrained even more if we use the mutation operator because the search space is then investigated in a multi-dimensional normal distribution around these individuals. Since in the end most individuals reside in the same area, this area will be sampled quite well.

3.1.4 Eleven free parameters

As a final test, FitSKIRT was used to fit all 11 parameters of the model described in section 4.3.1. This corresponds to a full 10+1 dimensional optimisation problem (10 parameters fitted by the genetic algorithm and the total luminosity determined independently by a golden section search). In order to accommodate the significant increase of the parameter space, we also changed the parameters of the genetic algorithm fit: we consider 100 generations of 250 individuals each and set the mutation rate to 5% and the crossover rate to 60%. We also have to keep in mind that

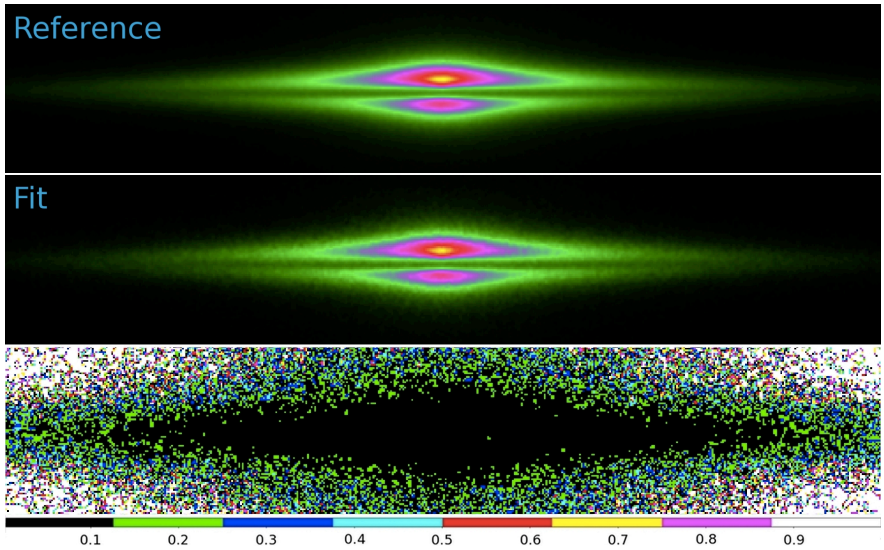

Figure 3.3: Results of the FitSKIRT radiative transfer fit to the artificial edge-on spiral galaxy with 11 free parameters. The reference input V-band image is shown on the top panel, the FitSKIRT solution is shown in the middle panel, and the bottom panel represents the residual frame.

larger populations are less sensitive to noise (Goldberg et al., 1991).

The result of this fitting exercise is given in the sixth column of Table 3.1. These results are also shown graphically in Figure 3.3. The central panel shows the simulated image of our best fitting model, to be compared with the reference image shown on the top panel. The bottom panel gives the residual image. This figure clearly shows that the reference image is reproduced quite accurately by FitSKIRT and the residual frame shows a maximum of 10% discrepancy in most of the pixels, which is quite impressive considering the complexity of the problem and vastness of the parameter space. Apart from a good global fit, also the individual parameters are recovered very well: we can recover all fitted parameters within the 1σ uncertainty interval (only the bulge effective radius is just outside this one standard deviation range). The uncertainty estimates are also useful to get more insight in which parameters are easily constrained and which are not. From Table 3.1 it is clear that the dust scale length and dust mass are the hardest to constrain. This is not surprising, given that they are degenerate in the sense that, in edge-on spiral galaxies, we are basically most sensitive to the edge-on optical depth, i.e. the dust column within the plane of the galaxy. Both a dust distribution with a large dust mass but a small scale length and a distribution with a small dust mass and a large scale length can conspire to give similar edge-on optical depths.

parameter	unit	reference	GA	DS
$M_{\rm d}$	$10^7\ M_\odot$	4	3.75 ± 0.5	4.57 ± 1.61
$\tau_{\rm f}$	–	0.80	0.98 ± 0.14	1.26 ± 0.37
$h_{R,{\rm d}}$	kpc	6.6	5.83 ± 0.75	7.90 ± 1.44
$h_{z,{\rm d}}$	pc	250	245 ± 30	284 ± 61
$L_{\rm tot}$	$10^9\ L_\odot$	1	0.97 ± 0.09	0.98 ± 0.13
$h_{R,*}$	kpc	4.4	4.36 ± 0.26	4.0 ± 0.5
$h_{z,*}$	pc	500	519 ± 51	505 ± 84
B/D	–	0.33	0.34 ± 0.08	0.23 ± 0.19
$R_{\rm e}$	kpc	2	1.75 ± 0.24	2.16 ± 0.45
n	–	2.5	2.5 ± 0.5	3.52 ± 0.65
q	–	0.5	0.50 ± 0.04	0.51 ± 0.17
i	deg	89	88.9 ± 0.1	89.2 ± 0.3

Table 3.2: Input values and fitted values of the parameters of the model used in the test simulations in Section 3.1. The values used to create the reference image (see Figure 3.3) are given in the third column. The fourth and fifth column list the fitted values for these parameters, together with their 1σ error bars, for the fits with eleven free parameters for the genetic algorithms and downhill simplex method respectively.

3.1.5 Tests using alternative optimisation methods

As discussed in previous chapter, the choice of genetic algorithms as our preferred optimisation routine was driven by the nature of our problem: the minimisation of a complex, numerical and noisy objective function in a large, multi-dimensional parameters space, characterised by several local minima. As we have demonstrated, the genetic algorithm approach turned out to be a powerful tool in this respect, and enabled us to reach our goals. In particular, concerning the problem of noisy objective functions, genetic algorithms are very effective: since they work on a population rather than iteratively on one point, then the random noise in the objective function is a much less determining factor in the final solution (Metcalfe et al., 2000; Larsen and Humphreys, 2003). On the other hand, the method is not entirely free of drawbacks: compared to some other optimisation routines, genetic algorithms have a relatively slow convergence rate on simple problems, and the error analysis is not easily treated in a natural way.

To further explore other possibilities and not limit ourselves to this one approach only, we have performed further tests adopting two other optimisation schemes that have been used in radiative transfer fitting problems, namely the Levenberg-Marquardt and the downhill-simplex methods. Both methods were applied to the test case we have considered in Section 3.1.4, and their performance is compared with genetic algorithms. In the following we briefly describe these two routines and present the results of the comparison.

The Levenberg-Marquardt algorithm or damped least-squares method (Levenberg, 1944; Marquardt, 1963) is an iterative optimisation method, that uses the gradient of the objective function and a damping factor based on the local curvature to find the next step in the iteration towards the final solution. The Levenberg-Marquardt method is one of the most widely used methods for nonlinear optimisation problems. It has been applied in inverse radiative transfer modelling by Xilouris et al. (1999) and Bianchi (2007). The choice of this algorithm was possible because the radiative transfer approach used by both was an (approximate) analytical model (Bianchi (2007) only used the Levenberg-Marquardt method for fits with ray-tracing radiative transfer simulations where scattering was taken not into account). In that case, the gradient in the multi-dimensional parameter space only requires a modest computational effort and is free of random noise.

As we are dealing with a Monte Carlo radiative transfer code with a full inclusion of multiple anisotropic scattering, adapting this method is not trivial. In particular, the presence of Monte Carlo noise on the objective function evaluation makes the (numerical) calculation of the gradient difficult. In an attempt to overcome this problem we combine two solutions:

- We increase the number of photon packages in every Monte Carlo simula-

tion. This reduces the noise to a minimum but leads to computationally more demanding simulations;

- We calculate the gradient based on several objective function evaluations in every parameter space dimension. This helps to mitigate both the high impact that the noise has on the gradient in regions close to the starting point, and also the unrealistic values that the gradient can yield when calculated on points located further away from the current position.

In our implementation, we found that the number objective function evaluations needed to make one single Levenberg-Marquardt step is around 70 for our optimisation problem containing 11 free parameters (Section 3.1.4). Keeping in mind that we have to use a larger number of photon packages, one single Levenberg-Marquardt step is comparable to approximately 400 evaluations performed in the genetic algorithms approach, in terms of computational effort.

Alternatively, we can also use the downhill simplex method as described in 2.3.3. as this method does not require any additional evaluations to determine the gradient. Importantly, the method also works better with noisy objective functions compared to Levenberg-Marquardt. Hence, coupling a downhill simplex routing to a Monte Carlo radiative transfer code requires no additional adjustments as instead needed in the case of Levenberg-Marquardt. The downhill simplex method was used by Bianchi (2007) for the general case, i.e. for fits in which scattering was included (and hence Monte Carlo noise was present).

When applying the Levenberg-Marquardt and downhill simplex algorithms to the problem discussed in Section 3.1.4, both methods are initialized in the same, randomly determined position and new evaluations are performed until there is no significant improvement in the values of the objective function. The left panel of Figure 3.4 shows the function evaluations (points) and the averaged path (lines) of the Levenberg-Marquardt (green) and downhill simpex (blue) methods for the dust mass and scale length of the dust disk, two parameters that are hard to constrain separately. The first evaluation –or starting point– is marked with a black open circle, while the "real" values are indicated by the red lines. The history of the function evaluations is colour coded (from black at the beginning to gradually green or blue, for the last evaluation).

This figure visually demonstrates a fundamental complication of both the Levenberg-Marquardt and downhill simplex methods: they both fail to reach the area of the parameter space located close to the true values. Even for parameters that should be more easily determined, like the scale length and height of the stellar disk (see the right panel in Figure 3.4), the methods do not succeed at reaching the region around the true values. This, however, should not come as a surprise since both methods are known to be local rather than global optimisation methods. This lim-

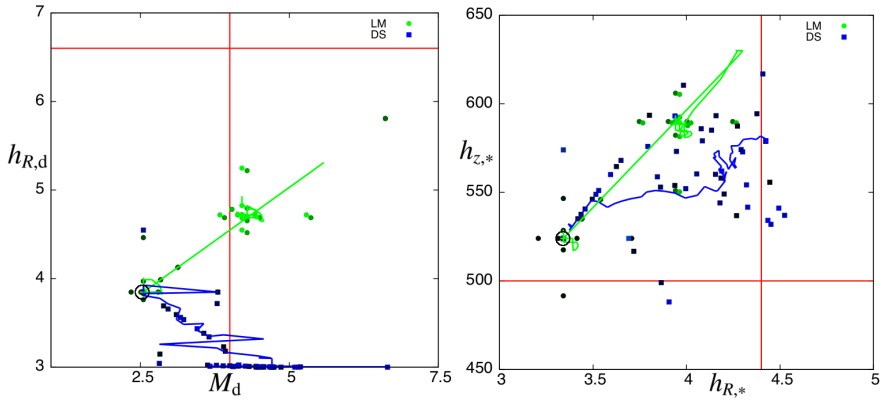

Figure 3.4: The function evaluations for both the Levenberg-Marquardt and downhill simplex method ranging from black (initial) to blue (DS) or green (LM) and the average path. The red lines indicate the values used to create the reference frame (Figure 3.3). Left: the variation of the dust mass and the scale length of the dust disk. Right: the variation of the scale length and scale height of the stellar disk.

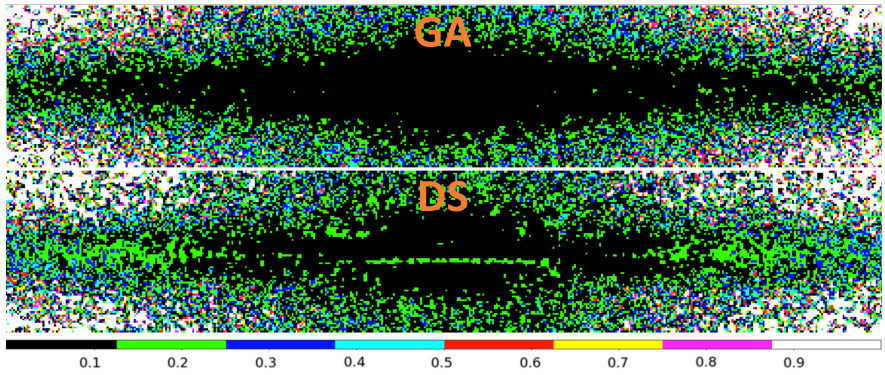

Figure 3.5: The residual frame of the reference image and the best fitting model as determined by the GA (top) and the repeatedly restarted Downhill Simplex method (Bottom). The parameter values are listed in Table 3.2. The green line in the bottom image is the result of slight inaccuracies in the reproduction of the dust lane.

itation can be partially overcome by repeatedly restarting the algorithm in a new random initial position. For the Levenberg-Marquardt method, this is simply unfeasible as it would result in a computationally exhausting task, as the number of photon packages used in every Monte Carlo simulation has to be increased substantially to mitigate the effects of Monte Carlo noise. It is therefore not considered to be a viable method for this problem.

To compare the downhill simplex method to genetic algorithms for our specific problem, we have followed the afore mentioned idea, repeatedly restarting the downhill simplex optimisation at random positions within the same boundaries, until the same number of function evaluations was reached. Table 3.2 lists the val-

ues of the best fit model, together with the error determined by the standard deviation of the five best models. In Figure 3.5 we show the residuals of the best fit models determined by the downhill simplex and genetic algorithms approaches. Comparing both the residuals and the best-fit parameter values, it is clear the downhill simplex method is not capable of reproducing the nominal values with the same degree of accuracy reached by the genetic algorithm approach. Also, the spread in the parameters of the final solutions is considerably larger compared to the values obtained using genetic algorithms. Again, this is the result of the "local" nature of the downhill simplex method. Genetic algorithms generally perform much better at both determining the global minimum and at handling the noise, turning out to be the most efficient and robust choice to solve this problem.

3.2 Test case 2: V-band fitting of NGC 4013

In this final section we apply FitSKIRT to recover the intrinsic distribution of stars and dust in the edge-on spiral galaxy NGC 4013. Located at a distance of about 18.6 Mpc (Willick et al., 1997; Russell, 2002; Tully et al., 2009) and with a D_{25} diameter of 5.2 arcmin, this galaxy is one of the most prominent edge-on spiral galaxies. It is very close to exactly edge-on and its dust lane can be traced to the edges of the galaxy. Conspicuous properties of this galaxy are its box- or peanut-shaped bulge (Kormendy and Illingworth, 1982; Jarvis, 1986; García-Burillo et al., 1999) and the warp in the gas and stellar distribution (Bottema et al., 1987; Florido et al., 1991; Bottema, 1995, 1996; Saha et al., 2009). The main reason why we selected this particular galaxy is that it has been modelled before twice using independent radiative transfer fitting methods, namely by Xilouris et al. (1999) and Bianchi (2007). This allows a direct comparison of the FitSKIRT algorithm with other fitting procedures in a realistic context.

We use a V-band image of NGC 4013, taken with the Telescopio Nazionale Galileo (TNG). Full details on the observations and data reduction can be found in Bianchi (2007). The image can be found in the top left panel of Figure 3.6. We apply the FitSKIRT program to reproduce this V-band image, in a field of approximatively $5.5' \times 1'$. The same model is used as the test simulations discussed in Section 3.1, i.e. a double-exponential disc and a flattened Sérsic bulge for the stellar distribution and a double-exponential disc for the dust distribution. We do not fix any parameters, i.e. we are again facing a 10+1 dimensional optimisation problem. The genetic algorithm parameters are the same as for the test problem, i.e. 100 generations of 250 individuals each, a mutation rate of 5% and a crossover rate of 60%.

The results of our FitSKIRT fit are given in the third column of Table 3.3. We find a V-band face-on optical depth of almost unity, corresponding to a dust mass of

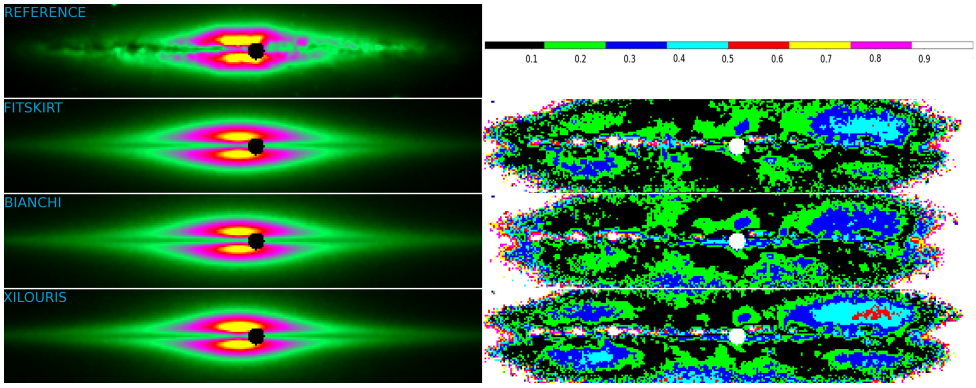

Figure 3.6: Radiative transfer model fits to a V-band image of NGC 4013. The top right panel shows the observed image, the subsequent rows show the best fitting SKIRT image, and the models by Bianchi (2007) and Xilouris et al. (1999). The panels on the right-hand side show the residual images corresponding to these models.

parameter	unit	FitSKIRT	B07	X99
τ_{f}	–	0.97 ± 0.36	1.46	0.67 ± 0.01
τ_{e}	–	15.1 ± 3.1	21.0	12.6
M_{d}	$10^6\ M_\odot$	9.9 ± 1.9	7.3	7.3
$h_{R,\mathrm{d}}$	kpc	3.00 ± 0.46	2.08	3.09 ± 0.13
$h_{z,\mathrm{d}}$	pc	192 ± 16	145	164 ± 13
$h_{R,*}$	kpc	2.12 ± 0.11	2.89	2.45 ± 0.13
$h_{z,*}$	pc	287 ± 104	376	278 ± 13
B/D	–	1.18 ± 0.32	2.13	1.47
R_{e}	kpc	2.30 ± 0.46	1.91	1.79 ± 0.05
n	–	3.2 ± 0.7	4	4
q	–	0.35 ± 0.03	0.37	0.44 ± 0.01
i	deg	90.0 ± 0.1	89.9	89.7 ± 0.1

Table 3.3: Parameters of the intrinsic distribution of stars and dust in NGC 4013 as obtained by FitSKIRT, by Bianchi (2007) and by Xilouris et al. (1999). For the latter two models, the values are scaled to our assumed distance of 18.6 Mpc and dust masses are calculated using the same values for the dust extinction coefficient κ as used in FitSKIRT.

$9.9 \times 10^6\ M_\odot$. In Figure 3.6 we plot the best fit to the observed V-band image of NGC 4013 and its residuals. These two panels show that our FitSKIRT model provides a very satisfactory fit to the observed image: the residuals between the image

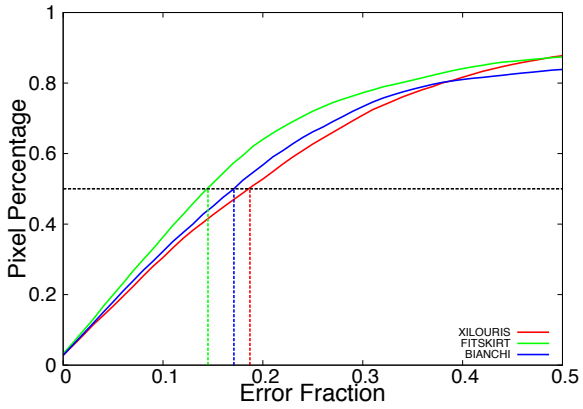

Figure 3.7: The cumulative distribution of the number of pixels with a residual smaller than a given percentage for the three model fits to the V-band image of NGC 4013. The green, red and blue solid lines correspond to the FitSKIRT model, the Xilouris et al. (1999) model and the Bianchi (2007) model respectively. The dashed horizontal line corresponds to half of the total number of pixels.

and fit are virtually everywhere smaller than 20%. The main exceptions where the fit is less accurate are the central-left region of the disc which contains discernible clumpy structures (which are obviously not properly described by our simple analytical model) and the top-right region, which is due to the warping of the disc in NGC 4013. The quality of our FitSKIRT fit is quantified in Figure 3.7, where we plot the cumulative distribution of the residual values of the innermost 15,000 pixels in the fit, i.e. the number of pixels with a residual smaller than a certain percentage. We see that half of the pixels have a residual less than 15%, and almost 90% of the pixels have a residual less than 50%.

In the last two columns of Table 3.3 we list the parameters found by Xilouris et al. (1999) and Bianchi (2007), scaled to our assumed distance of 18.6 Mpc and considering the same value for the dust extinction coefficient κ, necessary to convert optical depths to dust masses as in equation (3.7). In Figure 3.6 we also compare the images and their residuals for the models by Xilouris et al. (1999) and Bianchi (2007) with the FitSKIRT model. We reconstructed these models by taking the parameters from Table 3.3 and build a V-band model image of the galaxy with SKIRT. The same quantitative analysis on the residual frames as for the FitSKIRT solution is also plotted in Figure 3.7.

Looking at the model fits and their residuals, it is immediately clear that the three models are very similar. The largest deviations from the observed image are found at the same locations for the three models and hence seem to be due to the impossi-

bility of our smooth analytical model to represent the true distribution of stars and dust in the galaxie rather than due to the fitting techniques. Figure 3.7 seems to suggest that the FitSKIRT solution provides a slightly better overall fit to the image, but this judgement might be biased by the fact that we reproduced the other models with our SKIRT code (their model might be slightly different). Looking at the model parameters in Table 3.3, it is clear that the most prominent differences between the three models are the different values of the face-on optical depth and the dust scale length. This finding is not surprising given that we already found in Section 3.1.3 and 3.1.4 that these parameters are the hardest to constrain. This also corresponds to what Bianchi (2007) states as the reason for the high optical depth: the large optical depth is compensated by the smaller scale length of the dust disk.

An important aspect to take into account when comparing the results from the three models is the slight variations in the model setup and the strong differences in the radiative transfer calculations and the fitting techniques. Xilouris et al. (1999) used an approximate analytical method to solve the radiative transfer, based on the so-called method of scattered intensities pioneered by Henyey (1937) and subsequently perfectionized and applied by Kylafis and Bahcall (1987), Xilouris et al. (1997, 1998, 1999), Baes and Dejonghe (2001a), Popescu et al. (2000, 2011) and Möllenhoff et al. (2006). To do the fitting, they used a Levenberg-Marquardt algorithm. They used an approximation of a de Vaucouleurs model to fit the bulge and excluded the central 200 pc from the fit. The modelling of NGC 4013 by Bianchi (2007) on the other hand was based on the Monte Carlo code TRADING (Bianchi et al., 1996, 2000; Bianchi, 2008). For the actual fitting, he used a combination of the Levenberg-Marquardt algorithm (applied to models without scattering) and the amoeba downhill simplex algorithm. He also used an approximation of a de Vaucouleurs model to fit the bulge. Given these differences from the FitSKIRT approach, the agreement between the parameters of the three models is very satisfactory.

3.3 Test case 3: Oligochromatic Fitting

As a third test case, we extend the monochromatic test case of Section 3.1 The model is similar with the main exception that we now generate images at the g, r, i and z bands using the SKIRT code. To set the values of the luminosities of the two components, we assume that the bulge consists of an old stellar population with an age of 12 Gyr, while the disc is characterised by a young stellar component of 1 Gyr. They are normalised such that the intrinsic bulge-to-disc ratio is 0.33 and the disc luminosity is $10^9\ L_\odot$ in the V band, corresponding to values of 0.27, 0.37, 0.42 and 0.50 for the bulge-to-disc ratios and 1.33, 1.23, 0.97 and $0.80 \times 10^9\ L_\odot$ for the disc luminosity in the g, r, i and z band, respectively. The left column of the left-hand

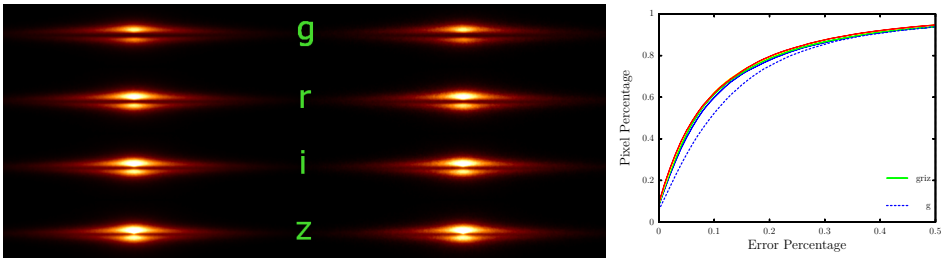

Figure 3.8: *Left-hand* panel: Reference frame on the left, best fitting model of an oligochromatic *griz*-fitting on the right. *Right-hand* panel: The cumulative pixel percentage distribution within a certain error percentage deviation of the reference frame. The oligochromatic model is shown as solid lines, each one representing a different band, while the g-band monochromatic model is shown as a dashed line. The other monochromatic fits are similar to the g-band fit.

Parameter	unit	reference	griz $\pm$ RMS	g $\pm$ RMS
$h_{R,*}$	kpc	4.4	4.36 ± 0.11	4.46 ± 0.17
$h_{z,*}$	kpc	0.5	0.51 ± 0.02	0.50 ± 0.02
$L_g^{\rm tot}$	$10^9\ L_\odot$	1.33	1.30 ± 0.12	1.31 ± 0.12
$R_{\rm eff}$	kpc	2	2.2 ± 0.7	2.1 ± 0.8
n	—	2.5	2.3 ± 0.7	2.1 ± 1.2
q	—	0.5	0.51 ± 0.03	0.48 ± 0.04
B/T_g	—	0.21	0.19 ± 0.04	0.22 ± 0.05
$h_{R,\rm d}$	kpc	6.6	6.5 ± 0.6	6.4 ± 1.1
$h_{z,\rm d}$	kpc	0.25	0.25 ± 0.01	0.24 ± 0.03
$M_{\rm d}$	$10^7\ M_\odot$	4	4.2 ± 0.4	3.9 ± 0.6
i	deg	89	89.1 ± 0.1	89.0 ± 0.3

Table 3.4: Reference values, Best values and RMS values for the mock galaxy determined FitSKIRT results. The RMS is calculated in the same way as done in De Geyter et al. (2013)

panel in Figure 3.8 shows the resulting g, r, i and z band images at an inclination of 88 degrees. Both the increasing bulge-to-disc ratio and the decreasing level of extinction with increasing wavelength are clearly visible.

The right column of the left-hand panel in Figure 3.8 shows the result of an oligochromatic FitSKIRT fit to this set of four images. The only clear difference between the corresponding left and central column images is a lower signal-to-noise in the model images. This is the result of the significantly lower number of photon packages used within the FitSKIRT fitting routine. Indeed, as each FitSKIRT fit typically

runs several tens of thousands of individual SKIRT radiative transfer calculations, it is clear that one has to find a balance between run time and noise suppression (De Geyter et al., 2013). The most important conclusion of this test calculation is that all of the free parameters in the model are recovered within the uncertainties. The input parameters and values recovered by both the g-band monochromatic fit and the g-, r-, i- and z-band oligochromatic fit are listed in Table 3.4.

In order to investigate the strength of the new fitting routine, we also compared the result of our oligochromatic FitSKIRT fit to the results of individual monochromatic FitSKIRT fit. The right panel in Figure 3.8 shows the distribution of cumulative pixel percentage in the residual frames for both the oligochromatic g, r, i and z images and the monochromatic g-band image (the other monochromatic fits have residuals which are comparable to the g-band fit). To avoid the low signal-to-noise pixels and focus on the relevant ones we only include the 25,000 most central pixels of the 501×101 pixels frames. We note that both fitting methods produce models where about 80% of the pixels have a deviation within 25% of the reference image. It is also clear that the oligochromatic fit does not bias any band over the other which is a nice validation of our precautions. It has to be noted, however, that, in this case, all the images have the same signal-to-noise, which is usually not the case of realistic data sets.

The oligochromatic models have smaller error bars on most of the fitted model parameters than the individual monochromatic models. This is particularly true for the parameters of the dust disc, where the oligochromatic fitting clearly has an added value. Even for the g-band image, where the effects of extinction are most prominent, the dust parameters are determined less accurately in the monochromatic case compared to the oligochromatic fit. This can be explained when we keep in mind the problems that the monochromatic fitting procedures have to deal with: monochromatic fits to edge-on spiral galaxies experience some degeneracy when trying to determine the dust disc. A dense, small dust disc or a less opaque but radially more extended dust disc can both give very similar images when looking at one wavelength. When combining information from blue and red bands, however, we can partially lift this degeneracy as in this case a denser dust disc would affect the red bands more heavily. Consequently, a fitting procedure incorporating this information would be able to differentiate these two cases and yield better constraints on the dust disc parameters.

3.4 Conclusions

In this chapter we have applied the FitSKIRT to three separate test cases. The code was tested on an artificial reference image of a dusty edge-on spiral galaxy model created by the SKIRT radiative transfer code. This reference image was fed to the FitSKIRT code in a series of tests with an increasing number of free parameters. The reliability of the code was evaluated by investigating the residual frames as well as the recovery of the input model parameters. From both the one and three parameter fits we concluded that the optimisation process is stable enough and does not converge too fast towards local extrema . FitSKIRT recovered the input parameters very well, even for the full problem in which all 11 parameters of the input model were left unconstrained. We have compared the results of genetic algorithms with two more commonly used optimisation methods, Levenberg-Marquardt and downhill simplex optimisation. The Levenberg-Marquardt method seems to be an inefficient method to solve this problem as it needs additional function evaluations to estimate the gradient. Defining a reliable gradient in this large, noise parameter space proved to be to computationally too demanding to be feasible. The downhill simplex could be used but in our case it quickly diverted towards a local minimum even for a simple test case. We conclude that the noise handling properties together with the ability to uniformly investigate and optimise a complex parameter space, make genetic algorithms an ideal candidate to use in combination with a Monte Carlo radiative transfer code. We could overcome the main shortcoming of the genetic algorithm approach, the lack of appropriate error bars on the model parameters, by deriving the spread of the individual parameters when applying the optimisation process several times with different initial conditions.

Next, the FitSKIRT method was applied to determine the physical parameters of the stellar and dust distribution in the edge-on spiral galaxy NGC 4013 from a single V-band image. Looking at the cumulative distribution of the number of pixels in the residual map, we found that FitSKIRT was able to fit half of the pixels with a residual of less than 15% and almost 90% of the pixels with a residual of less than 50%. Given that the image of NGC 4013 clearly shows a number of regions that cannot be reproduced by a smooth model (due to obvious clumping in the dust lane and a warp in the stellar and gas distribution), these statistics are very encouraging. The values of the fitted parameters and the quality of the fit were compared to similar but completely independent radiative transfer fits done by Xilouris et al. (1999) and Bianchi (2007). There are some deviations between the results, and we argue that these can be explained by the degeneracy between the dust scale length and face-on optical depth, and the differences in the model setup, radiative transfer technique and optimisation strategy. In general, the agreement between the parameters of the three models is very satisfactory.

The final section revisit the first test case where but now we fit to a set of artificial reference image of a dusty edge-on spiral galaxy model created by the SKIRT radiative transfer code. The geometrical parameters are kept the same, only some additional luminosity values need to be introduced. We find that the oligochromatic method yields smaller error bars on most of the fitted model parameters than the individual monochromatic models. In particular, the dust disk parameters are retrieved with higher accuracy. Using a set of observations allows for better discrepancy between smaller, dense dust disks and larger, more opaque disks. In almost all cases it is therefore advisable to use the oligochromatic method to constrain the models. In the next chapter we will use this method to determine the best fitting models for a set of 12 edge-on spiral galaxies.

Sample of edge-on spiral galaxies

4

In this chapter we study a set of edge-on spiral galaxies by using detailed radiative transfer models in order to determine their stellar and dust morphology and, subsequently, their face-on optical depth. The selection of our sample, the largest sample so far upon which detailed radiative transfer modelling has been applied, is discussed in Sect. 4.2. The results of our fits and an individual discussion of each galaxy in our sample is presented in Sect. 4.4. We make some remarks about the quality of the models in general, compare and validate our results against results available from other studies, and discuss the results of both the stellar and dust properties of our sample in Sect. 4.5. Our conclusions are presented in Sec. 4.6.

4.1 Radiative transfer modelling of edge-on spiral galaxies

As the creation of radiative transfer models of spiral galaxies can be an arduous task, most of these studies focus on a very limited number of targets or even a single galaxy (e.g. Kylafis and Bahcall, 1987; Popescu et al., 2000, 2011; Bianchi et al., 2000; Matthews and Wood, 2001; Misiriotis et al., 2001; Baes et al., 2010; MacLachlan et al., 2011; De Looze et al., 2012b,a; Schechtman-Rook et al., 2012). Most of these studies have targeted spiral galaxies with an inclination close to 90 degrees, as these offer some unique advantages. In particular, because of the edge-on projection, the separate components of the galaxy, i.e. the stellar disc, dust disc and central bulge, are clearly distinguishable. Unfortunately, the varying observational input used for the modelling, and the different assumptions, geometries and physical ingredients in the radiative transfer models themselves make it almost impossible to compare these studies and draw general implications on the amount and distribution of dust in spiral galaxies. What is needed is a radiative transfer study of a sizeable sample of galaxies, all modelled in a homogeneous way based on similar data.

There have been only two such efforts in the literature: Xilouris et al. (1997, 1998, 1999, hereafter X99) and Bianchi (2007, hereafter B07) both modelled a set of seven edge-on spiral galaxies with prominent dust lanes. The main conclusions of these works are that the dust disc tends to be larger radially than the stellar disc while being thinner in the vertical direction. However, there is still some uncertainty on the

ratio of the dust and stellar scale length as different methods to determine the size of the dust disc results in values from being from only 10% larger (Muñoz-Mateos et al., 2009a) up to 100% or even more (Holwerda et al., 2005; Tempel et al., 2010; MacLachlan et al., 2011). In the cases where the FIR/submm observations were able to resolve the dust disc, similar values for the dust scale height and length were found as the ones determined from fitting radiative transfer models to optical/NIR observations (Verstappen et al., 2013; Hughes et al., 2014a).

One of the most important quantities concerning the dust distribution in spiral galaxies is the face-on optical depth τ_V^f. A large number of papers looked into this parameter, resulting in often contradicting conclusions (Valentijn, 1990, 1994; Burstein et al., 1991; Bosma et al., 1992; Byun, 1993; Bottinelli et al., 1995; Buat and Burgarella, 1998; Masters et al., 2003). The importance of this value is not to be underestimated: galaxies with $\tau_V^f < 1$ would be almost completely transparent when seen face-on, whereas higher values for τ_V^f would indicate that a significant fraction of the stars in spiral galaxies could be invisible. The latter case has far-reaching consequences for the use of spiral galaxies in a cosmological context, as it would, for example, invalidate most determinations of mass-to-light ratios.

Another important aspect to consider is the ratio between the stellar and dust scale height. According to Dalcanton et al. (2004) there should be a clear transition at the critical rotation speed of 120 $\mathrm{km\,s^{-1}}$ where the more massive galaxies have a well-defined, thin dust disc, while the less massive galaxies have a more diffuse and bloated dust disc. A similar feature was also observed by MacLachlan et al. (2011) whose radiative transfer models contain a dust disc which has a scale height similar to or larger than the stellar disc and therefore does not have an obvious dust lane, contrary to the relatively much thinner dust discs in galaxies with a higher surface brightness. They suggest that the origin might be a combination of the two possible explanations: either their galaxies have a larger stability against vertical collapse, as expected using the results described in Dalcanton et al. (2004), or the extraordinary thin nature of the stellar discs in their sample.

4.2 Sample selection

Our starting point is the Calar Alto Legacy Integral Field Area Survey (CALIFA) sample (Sánchez et al., 2012). This is a statistically well-defined sample of 600 nearby galaxies, selected from the Sloan Digital Sky Survey (SDSS) DR7 photometric catalog (Abazajian et al., 2009) by using two additional conditions: the redshift range is limited to $0.005 < z < 0.03$ and only galaxies with an isophotal *r*-band diameter between 45 and 80 arcsec are considered. The CALIFA survey is one of the largest integral field spectroscopic surveys: by completion of the survey, all galaxies

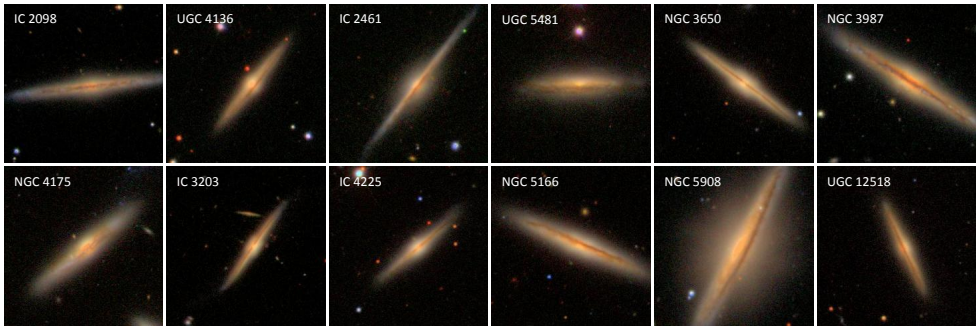

Figure 4.1: SDSS thumbnail images for the 12 galaxies in our sample with a FoV of 90″ by 90″.

will have been observed using the PMAS/PPAK integral field spectrograph (Roth et al., 2005; Kelz et al., 2006) in the wavelength range between 3700 and 7000 Å. This will allow the construction of detailed two-dimensional maps of the stellar kinematics, the ages and metallicities of the stellar populations, and the distribution, excitation mechanisms, chemical abundances and kinematics of the ionised gas. The first CALIFA public data release took place in November 2012 (Husemann et al., 2013) and several scientific results based on these data have been published (e.g., Kehrig et al., 2012; Sánchez et al., 2013, 2014; Marino et al., 2013; González Delgado et al., 2014). The size of the sample and the wealth of information that is (or will be) available for all galaxies in a homogeneous way make it an ideal starting sample from which we select ours.

From the CALIFA sample, edge-on spiral galaxies with a clear dust lane morphology are selected by visual inspection of the SDSS images of the galaxies. Interacting or visibly strongly asymmetrical galaxies are rejected from the sample. In order to do a reliable radiative transfer fitting, it is crucial that the galaxies have sufficient resolution. In particular, if we want to derive information on the distribution of the dust, the dust lane must be properly resolved in the vertical direction. Based on previous experience with the fitting code, FitSKIRT (De Geyter et al., 2013), we exclude galaxies with a major axis smaller than 1 arcmin or a minor axis smaller than 8 arcsec. The final sample, listed in Table 4.1, consists of 12 edge-on spiral galaxies with distances ranging from 42 to 119 Mpc. Figure 4.1 shows SDSS thumbnail images of the sample galaxies.

Apart from their statistical properties, an added value of these galaxies over other SDSS galaxies is the fact that their integral field spectroscopy might be used in follow-up studies. The Hα/Hβ line ratio could be used to have an independent measure of the attenuation in our sample (Tuffs et al., 2004; Boselli et al., 2013). Additionally, the CALIFA data might be used to determine the gas-phase metallicity gradients across star-forming disks (Sánchez et al., 2013). Combining maps of the

metallicity distribution with our ancillary data to simultaneously trace the gas, stellar and dust content, enables us to study the relationships between the key phases of the baryons in the ISM. The relationship between stellar mass, oxygen abundance and gas content found in large scale, integrated observations (Hughes et al., 2013; Bothwell et al., 2013) could therefore be tested on local scales. The predicted relationship between the gas-to-dust ratio and the gas-phase metallicity may also be used to constrain theoretical models of chemical evolution (Draine et al., 2007). Furthermore, we can directly test for the accretion of cold gas by searching for pristine, unenriched gas in the exterior of the disks (Bresolin et al., 2009). We therefore have many opportunities for follow-up studies.

For all sample galaxies, homogeneous u, g, r, i and z-band images are available from the SDSS, so, in principle, we could use these five bands for our multi-wavelength radiative transfer fits. However, we do not include the u-band images, as the image quality is insufficient for most galaxies. Additional near-infrared J, H and K_s imaging is available for all galaxies from the Two Micron All Sky Survey (2MASS, Skrutskie et al., 2006), but also here the signal-to-noise ratio was inadequate for most galaxies in the sample. An alternative could be deep NIR imaging from the UKIRT Infrared Deep Sky Survey (UKIDSS, Lawrence et al., 2007), but this is available only for a few galaxies in the sample. As we want to keep the data set homogeneous, we do not include these data.

This complete and uniform sample of g, r, i and z-band data is an ideal set to investigate the dust properties in extinction in a systematic way: the g band is clearly attenuated by the dust while the z band observations contain more accurate information about the stellar properties.

4.3 Radiative transfer modelling

4.3.1 The model

The model we use here is an extension of the model described in Section 4.3.1. We use the same geometrical parameters at all wavelengths. Only the luminosities of the bulge and disc are determined individually at each wavelength. While there is evidence that e.g. disc scale lengths are wavelength-dependent (Peletier et al., 1994; Corradi et al., 1996; Xilouris et al., 1999), we choose this approach to limit the number of free parameters in our models. A geometrical parameter that is expected to change as a function of wavelength is the bulge-to-disc ratio: typically, it increases steadily from blue wavelengths, where young stars in the disc dominate, into the near-infrared, where old stellar populations in the bulge contribute the most. The fact that the individual luminosities of disc and bulge at each band

Galaxy	RA (J2000)	Dec (J2000)	Distance (Mpc)	Major axis (arcmin)	Minor axis (arcmin)	Type	r-band (mag)
IC 2098	04:50:44	−05:25:07	47.8	2.3	0.3	Sc	13.8
UGC 4136	07:59:54	+47:24:47	90.8	1.7	0.4	Sa	13.5
IC 2461	09:19:58	+37:11:29	54.2	2.4	0.4	Sbc	13.3
UGC 5481	10:09:51	+30:19:15	90.2	1.5	0.5	Sa	13.1
NGC 3650	11:22:35	+20:42:14	59.7	1.7	0.3	SAb	13.4
NGC 3987	11:49:30	−01:05:11	61.4	2.2	0.4	Sb	13.8
NGC 4175	12:12:31	+29:10:06	42.2	1.8	0.4	Sbc	13.2
IC 3203	12:21:46	+25:53:05	119.2	1.5	0.2	Sb	14.2
IC 4225	13:20:01	+31:58:53	73.9	1.3	0.3	S0/a	13.9
NGC 5166	13:28:15	+32:01:57	62.6	2.3	0.4	Sb	12.9
NGC 5908	15:16:43	+55:24:33	53.4	3.2	1.2	SAb	12.0
UGC 12518	23:20:13	+07:55:55	51.6	1.3	0.2	Sb	14.0

Table 4.1: The final sample of 12 edge-on galaxies selected out of the CALIFA sample.

are free parameters in our model, allows us to simulate this wavelength dependent behaviour.

The geometry of the dust disc is also characterised by a scale length $h_{R,\mathrm{d}}$ and scale height $h_{z,\mathrm{d}}$. Apart from the geometrical distribution of the dust, the optical properties (absorption efficiency, scattering efficiency and scattering phase function) and the total amount of dust need to be set. We use the standard BARE-GR-S model of Zubko et al. (2004), which consists of a combination of PAH, graphitic and silicate dust grains. The relative distributions of each component have been weighted to best match the extinction, abundances, and emission associated with the Milky Way dust properties ($R_V = 3.1$). By using a physical dust model, we have fixed the wavelength dependence of the optical properties of the dust, and the only free parameter left to determine is the total amount of dust. This can be characterised in different ways, e.g. as the total dust mass M_d or the face-on or edge-on optical depth at any wavelength (for a given geometry and fixed dust model, these parameters are equivalent).

Although stellar discs are often truncated at 3 to 4 scale lengths (Pohlen et al., 2000, 2007; de Grijs et al., 2001; Kregel et al., 2002), we have not included an explicit truncation profile for either the dust or stellar disc. For the dust disc, we use a grid to partition the dust distribution that is four times the upper boundary of the dust scale length. This results in an implicit truncation of the dust distribution, but as only a very small fraction of the dust mass falls outside this radius, our discs are essentially not truncated. Note that X99 and B07 use a truncation of the dust disc at 3 – 4 scale lengths, which could potentially complicate a direct comparison.

The last three parameters to be determined are the inclination i of the system and the x and y coordinate of the centre of the galaxy on the plane of the sky. In total, our model has 19 free parameters (5 stellar geometry parameters, 8 luminosities, 2 dust geometry parameters, the total dust mass and 3 projection parameters). Our problem comes down to finding the combination of these 19 parameters that results in a set of simulated g, r, i and z-band images that reproduce the observed images best.

4.3.2 FitSKIRT fits

We have applied FitSKIRT to the set of 12 edge-on spiral galaxies selected from the CALIFA survey. The computations are done using the high performance cluster of the Flemish Supercomputer Center (Vlaams Supercomputer Centrum, VSC), located at the Ghent University premises. As described in Sect. 4.2, we use the SDSS g, r, i and z-band images for each galaxy, which are presented in the left-hand panels of Figure 4.2. The central column contains the fitted images in the corresponding bands, and the right-hand column gives the residual images. The values of free parameters in the model for the 12 galaxies, with their error bars, can be found in Table 4.2.

Parameter	unit	IC 2098	UGC 4136	IC 2461	UGC 5481	NGC 3650	NGC 3987
$h_{R,*}$	kpc	4.71 ± 0.06	6.41 ± 0.20	3.42 ± 0.09	4.24 ± 0.10	3.66 ± 0.08	7.36 ± 0.28
$h_{z,*}$	kpc	0.43 ± 0.06	0.66 ± 0.04	0.15 ± 0.01	0.59 ± 0.06	0.62 ± 0.02	1.08 ± 0.05
R_{eff}	kpc	2.88 ± 0.54	1.19 ± 0.07	2.83 ± 0.26	5.99 ± 0.59	0.91 ± 0.09	1.79 ± 0.12
n	—	3.0 ± 0.7	2.0 ± 0.2	4.0 ± 0.1	6.1 ± 0.4	2.9 ± 0.7	1.2 ± 0.2
q	—	0.35 ± 0.03	0.85 ± 0.01	0.66 ± 0.04	0.39 ± 0.01	0.83 ± 0.03	0.48 ± 0.01
$h_{R,\mathrm{d}}$	kpc	2.6 ± 0.18	29.33 ± 0.46	5.65 ± 1.47	10.33 ± 1.51	4.58 ± 1.26	4.62 ± 0.39
$h_{z,\mathrm{d}}$	kpc	0.20 ± 0.02	0.33 ± 0.04	0.12 ± 0.03	0.51 ± 0.09	0.15 ± 0.01	0.40 ± 0.02
M_{d}	$10^7\ M_\odot$	1.3 ± 0.1	22.0 ± 1.6	2.3 ± 0.8	15.2 ± 3.0	1.4 ± 0.3	6.1 ± 0.5
$\tau_{\mathrm{V}}^{\mathrm{f}}$	—	1.65 ± 0.17	0.24 ± 0.10	0.62 ± 0.11	1.22 ± 0.32	0.57 ± 0.17	1.98 ± 0.17
$\tau_{\mathrm{V}}^{\mathrm{e}}$	—	21.9 ± 1.2	17.5 ± 1.5	29.8 ± 4.9	25.0 ± 8.7	17.4 ± 2.1	23.7 ± 1.2
i	deg	88.9 ± 0.1	85.5 ± 0.1	87.1 ± 0.2	82.3 ± 0.6	89.0 ± 0.2	89.9 ± 0.1
L_g^{tot}	$10^9\ L_\odot$	0.75 ± 0.12	4.12 ± 0.22	2.59 ± 0.48	8.71 ± 1.43	1.77 ± 0.26	1.74 ± 0.23
L_r^{tot}	$10^9\ L_\odot$	1.20 ± 0.15	6.69 ± 0.42	3.74 ± 0.51	12.93 ± 1.49	2.83 ± 0.39	3.12 ± 0.36
L_i^{tot}	$10^9\ L_\odot$	1.97 ± 0.23	8.92 ± 0.54	4.74 ± 0.45	16.65 ± 1.76	3.84 ± 0.52	4.47 ± 0.46
L_z^{tot}	$10^9\ L_\odot$	2.85 ± 0.05	11.79 ± 0.31	6.43 ± 0.32	21.6 ± 0.57	4.99 ± 0.06	6.3 ± 0.11
B/T_g	—	0.33 ± 0.06	0.45 ± 0.03	0.47 ± 0.1	0.61 ± 0.12	0.30 ± 0.05	0.41 ± 0.06
B/T_r	—	0.42 ± 0.06	0.48 ± 0.04	0.53 ± 0.09	0.64 ± 0.09	0.32 ± 0.04	0.45 ± 0.06
B/T_i	—	0.46 ± 0.02	0.47 ± 0.01	0.56 ± 0.02	0.64 ± 0.02	0.32 ± 0.01	0.47 ± 0.01
B/T_z	—	0.48 ± 0.02	0.48 ± 0.01	0.55 ± 0.03	0.59 ± 0.01	0.33 ± 0.01	0.48 ± 0.01

Table 4.2: Results of the oligochromatic FitSKIRT radiative transfer fits to the 12 edge-on spiral galaxies in our sample. For each galaxy we list all physical free parameters with their 1σ error bar as determined by FitSKIRT. For the meaning of the different parameters and determination of the error bars, see Sect. 4.3.1 and/or Sect. 3.1 from De Geyter et al. (2013).

Parameter	unit	NGC 4175	IC 3203	IC 4225	NGC 5166	NGC 5908	UGC 12518
$h_{R,*}$	kpc	2.78 ± 0.12	5.56 ± 0.09	3.38 ± 0.05	3.92 ± 0.17	4.71 ± 0.28	2.92 ± 0.20
$h_{z,*}$	kpc	0.33 ± 0.04	0.83 ± 0.02	0.84 ± 0.04	0.66 ± 0.04	0.44 ± 0.02	0.29 ± 0.05
R_{eff}	kpc	0.92 ± 0.05	1.83 ± 0.06	1.25 ± 0.04	3.17 ± 0.59	7.54 ± 0.42	4.81 ± 1.16
n	—	0.9 ± 0.1	1.2 ± 0.1	1.1 ± 0.1	5.8 ± 0.9	5.4 ± 0.8	5.2 ± 1.2
q	—	0.75 ± 0.04	0.73 ± 0.03	0.69 ± 0.03	0.26 ± 0.04	0.63 ± 0.02	0.50 ± 0.04
$h_{R,\mathrm{d}}$	kpc	3.33 ± 0.46	11.98 ± 2.81	10.01 ± 2.74	5.81 ± 1.12	5.74 ± 1.87	8.51 ± 1.95
$h_{z,\mathrm{d}}$	kpc	0.25 ± 0.07	0.22 ± 0.02	0.24 ± 0.02	0.34 ± 0.06	0.12 ± 0.04	0.14 ± 0.02
M_{d}	$10^7\ M_\odot$	1.5 ± 0.4	3.4 ± 0.7	2.1 ± 0.5	4.8 ± 0.9	10.8 ± 1.0	3.2 ± 1.6
$\tau_{\mathrm{V}}^{\mathrm{f}}$	—	1.17 ± 0.19	0.20 ± 0.08	0.18 ± 0.17	1.23 ± 0.37	2.84 ± 0.99	0.90 ± 0.25
$\tau_{\mathrm{V}}^{\mathrm{e}}$	—	15.5 ± 2.2	11.0 ± 1.6	7.4 ± 0.8	21.2 ± 4.7	132 ± 56	19.6 ± 2.9
i	deg	83.2 ± 0.4	87.6 ± 0.4	89.3 ± 0.1	87.6 ± 0.5	83.4 ± 0.4	87.3 ± 0.1
L_g^{tot}	$10^9\ L_\odot$	1.24 ± 0.19	3.03 ± 0.24	1.63 ± 0.24	4.57 ± 0.91	5.69 ± 0.35	0.95 ± 0.14
L_r^{tot}	$10^9\ L_\odot$	1.86 ± 0.23	5.07 ± 0.37	2.48 ± 0.26	7.18 ± 1.14	10.91 ± 0.61	1.67 ± 0.15
L_i^{tot}	$10^9\ L_\odot$	2.58 ± 0.3	6.87 ± 0.47	3.27 ± 0.28	9.58 ± 1.16	16.08 ± 0.91	2.44 ± 0.23
L_z^{tot}	$10^9\ L_\odot$	3.34 ± 0.17	9.26 ± 0.1	4.16 ± 0.1	11.39 ± 0.51	22.09 ± 0.5	3.17 ± 0.1
B/T_g	—	0.26 ± 0.05	0.34 ± 0.03	0.39 ± 0.06	0.45 ± 0.1	0.55 ± 0.04	0.52 ± 0.09
B/T_r	—	0.32 ± 0.05	0.37 ± 0.03	0.4 ± 0.05	0.49 ± 0.09	0.57 ± 0.04	0.53 ± 0.06
B/T_i	—	0.34 ± 0.02	0.38 ± 0.01	0.4 ± 0.01	0.49 ± 0.02	0.58 ± 0.01	0.54 ± 0.03
B/T_z	—	0.39 ± 0.02	0.4 ± 0.01	0.43 ± 0.01	0.45 ± 0.02	0.55 ± 0.01	0.52 ± 0.02

Table 4.2: (continued)

In this section we give more detailed description of the FitSKIRT fits to the individual galaxies before giving a more general overview of the entire sample in Section 4.5.

4.4.1 IC 2098

This galaxy is a late-type Scd, at a distance of about 47.8 Mpc (the mean of the Tully-Fisher based distances determined by Theureau et al. 2007 and Parnovsky and Parnowski 2010). Both the stellar and dust disc of this galaxy have a fairly irregular morphology, which is not unexpected for a late-type galaxy. A warp is not present (Sánchez-Saavedra et al., 2003). In spite of the flocculent morphology, our smooth model fit is quite satisfactory, with the relative difference between observation and model below 25% over the entire extent of the galaxy. Looking at the parameters in Table 4.2, we note that the dust disc seems to be smaller than the stellar disc in the radial direction. The radial extent of the dust disc might be underestimated by the fitting mechanism since the brighter regions have considerably more weight in our χ^2 objective function. It has to be noticed this is not the same as the degeneracy between a dense dust disc or larger, less dense disc discussed in Sect. 3.3 as in this case all bands would be affected. Consequently the face-on optical depth of this galaxy might be overestimated as the central attenuation is fitted using a higher density disc instead of a more radially extended, optically thinner disc.

4.4.2 UGC 4136

At a distance of 90.8 Mpc (Falco et al., 1999), this bulge-dominated Sa-type galaxy (Nair and Abraham, 2010) is one of the most distant galaxies in our sample. The best fitting model provides a satisfactory fit to the images in all four bands, although there is a clear signature of the dust lanes visible in the residual maps, especially in the *r* and *i* bands. The radial scale length of the dust disc on the other hand is extremely large, especially compared to the moderate stellar scale length. Actually, the dust scale length was found to tend towards the maximum value allowed in the fitting procedure, even when this value was increased. The most likely explanation is that this galaxy has an intrinsic dust distribution which is not properly described by our analytic model. The dust distribution may have a ring structure rather than an exponential disc, which is not uncommon for early-type disc galaxies (e.g., Kennicutt et al., 2011; Ciesla et al., 2012; De Looze et al., 2012b). When we try to fit a galaxy with a central dust cavity using an exponential disc model, it is natural that the disc scale length will tend towards extremely large values (i.e. flat

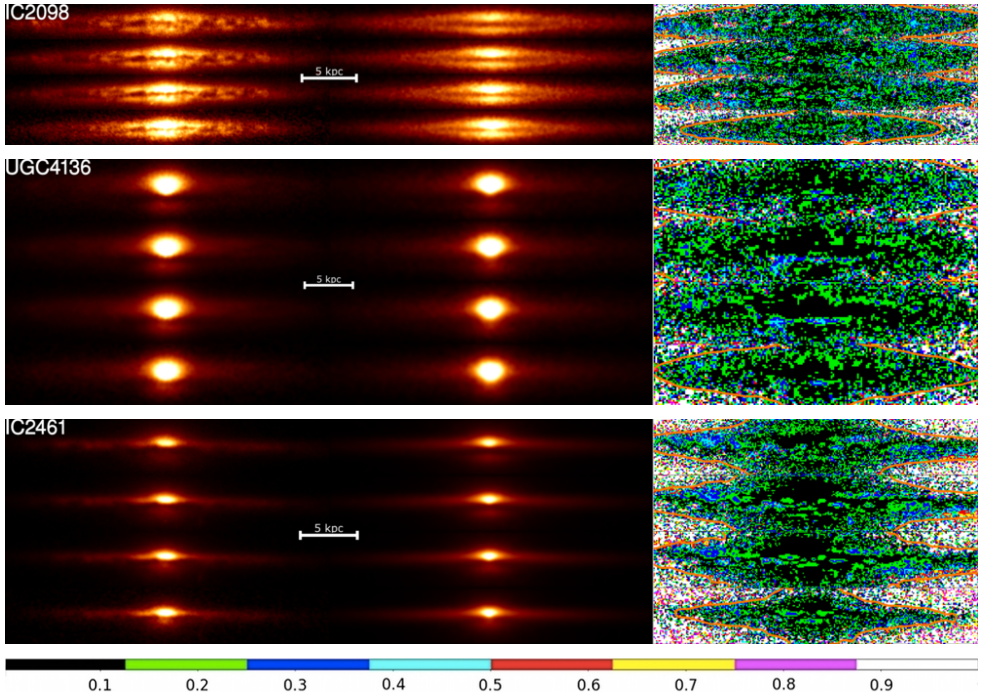

Figure 4.2: Results of the oligochromatic FitSKIRT radiative transfer fits to the 12 edge-on spiral galaxies in our sample. In each panel, the left-hand column represents the observed images in the g, r, i and z bands (from top to bottom), and the middle column contains the corresponding fits in the same bands. The right-hand column contains the residual images, that indicate the relative deviation between the fit and the image. A colour bar with the scaling of the latter is indicated at the bottom. The orange contour in the residuals frames represents the signal-to-noise 3 level of the reference image.

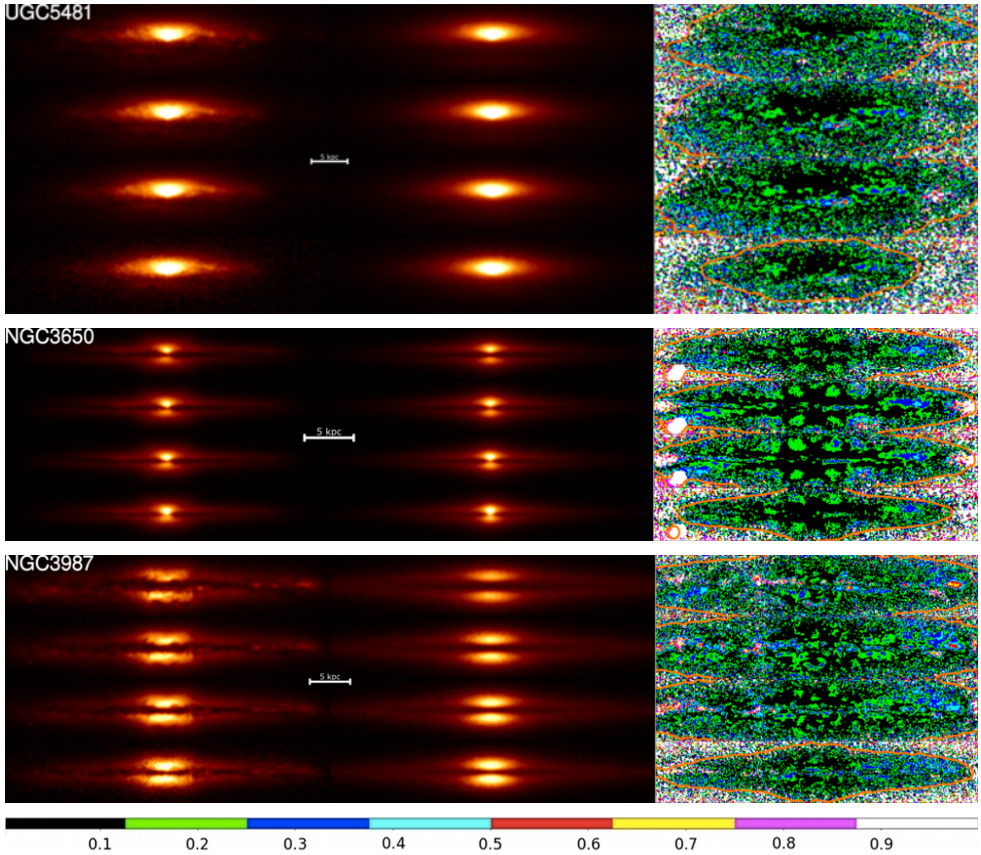

Figure 4.2: (continued)

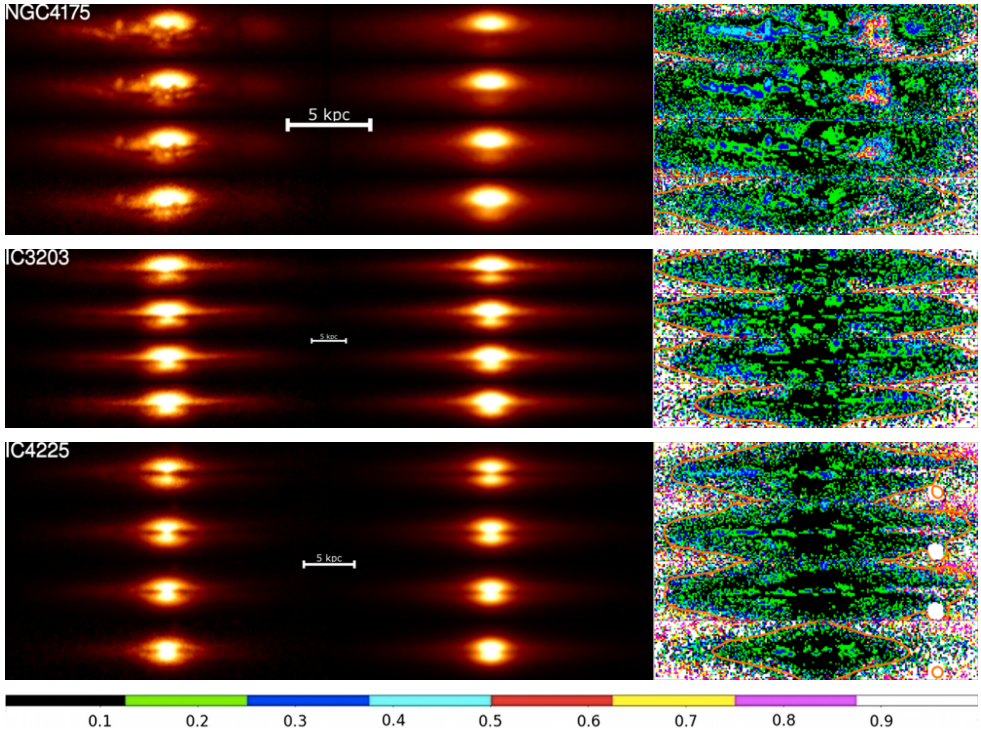

Figure 4.2: (continued)

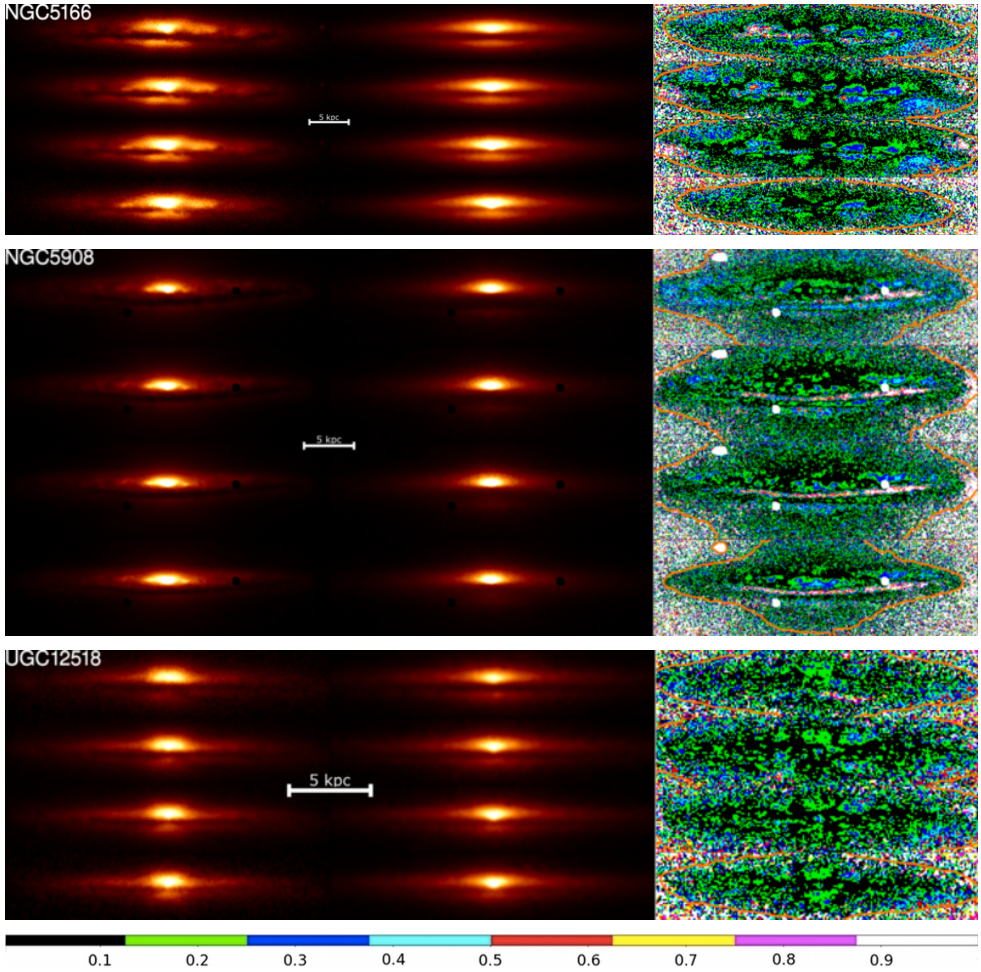

Figure 4.2: (continued)

distributions), as this is the only way to avoid a strong central concentration. As the dust distribution can not be described accurately with the use of an exponential disc, this results found for this galaxy are not included in the discussion of a sample as a whole.

4.4.3 IC 2461

This galaxy, with a classification varying from S0 (van den Bergh et al., 2003) to Sbc (Hakobyan et al., 2008), has received quite some attention in the literature due to the fact that it was the host galaxy of the type II supernova SN 2002bx (Matheson et al., 2002). Fairly recently, it was detected from soft to ultra-hard X-rays (Noguchi et al., 2009; Cusumano et al., 2010; Koss et al., 2011), revealing a deeply buried Seyfert 2 nucleus (Parisi et al., 2012). In the optical SDSS images, it is a regular galaxy without evidence for perturbations. We assumed a distance of 54.2 Mpc (the average of Tully-Fisher based distances (Theureau et al., 2007; Springob et al., 2009; Parnovsky and Parnowski, 2010)). The FitSKIRT model reproduces the images quite accurately. Not only do the residuals show very little deviation or irregularities, also the error bars on each of the derived parameters are modest.

4.4.4 UGC 5481

This rather anonymous galaxy at a distance of 90.2 Mpc (Theureau et al., 2007) is one of the smallest galaxies in the sample in angular size. With an axis ratio of over 25% it is the galaxy furthest from edge-on (the fitted value of the inclination is 82.3 ± 0.6 deg). As a result, the dust lane is not as sharp and prominent as for most other galaxies in the sample. In spite of this rather large deviation from edge-on, the fits are surprisingly satisfactory. The error bars on the fitted parameters are not larger than average, and the residual maps are quite smooth and without strong irregularities.

4.4.5 NGC 3650

This nice Sb type galaxy at a distance of 59.7 Mpc (Falco et al., 1999) is very close to exactly edge-on and characterised by a very clear and strong dust lane. According to Sanchez-Saavedra et al. (1990), it has a barely perceptible warp. The bulge is strongly peanut-shaped (Lütticke et al., 2000a), which shows as a X-shape pattern in the residual maps (our standard model of a flattened Sérsic bulge cannot reproduce peanut-shaped bulges). Apart from this feature, the FitSKIRT fits reproduce the SDSS images particularly well and the parameters of the model are well constrained.

4.4.6 NGC 3987

This almost exactly edge-on Sb galaxy ($i = 89.9 \pm 0.2$ deg) shows a very prominent, albeit somewhat irregularly shaped dust lane. It was one of the first edge-on galaxies in which the surface brightness distribution was studied in detail (Davis, 1975). It is one of the best known galaxies in our sample, mainly thanks to hosting the type Ia supernova SN 2001V (Vinkó et al., 2003). Redshift-independent distances in the literature vary from 41 Mpc (Amanullah et al., 2010) to 70 Mpc (Theureau et al., 2007); we use an average value 61.4 Mpc. NGC 3987 is a bright radio source and strong emitter at infrared and submillimeter wavelengths (Yun et al., 2001; Vlahakis et al., 2005). The FitSKIRT fit to the SDSS images is not perfect, with many artefacts visible in the residual maps. Looking at the best fitting parameters, we note that the stellar disc seems to be more radially extended than the dust disc, as we previously obtained for IC 2098. In this case, however, the dust disc is probably underestimated due to a warp in the dust lane. Indeed, the residual frames clearly show the region where the fit and model differ significantly: the dust lane deviates from the major axis in opposite directions on either side of the galaxy. Interestingly, Vlahakis et al. (2005) have observed that the 850 μm submillimeter emission in NGC 3987 is slightly offset from the galaxy's plane. As our analytic model does not include such feature it will break off at radius where the dust disc deviates away from the plane of the galaxy. The resulting face-on optical depth is therefore probably overestimated.

4.4.7 NGC 4175

Together with the two lenticular galaxies NGC 4169 and NGC 4174, this Sbc type galaxy forms the Hickson (1982) compact group HCG 61. At a distance of about 42.2 Mpc (Theureau et al., 2007), NGC 4175 is the most nearby galaxy in our sample. It has an active galactic nucleus (Martínez et al., 2010) with a strong emission at MIR, FIR and radio wavelengths (e.g., Surace et al., 2004; Johnson et al., 2007; Gallagher et al., 2008), and a significantly disturbed morphology in the inner regions. The SDSS images show a clear asymmetry between the two sides of the disc in all four bands. FitSKIRT is unable to fit these asymmetries using our smooth 2D model, so these features stand out in the residual maps as well. Nevertheless the fit is acceptable when looking at the residuals and most parameters are quite well constrained.

4.4.8 IC 3203

At a distance of 119.2 Mpc (Willick et al., 1997; Theureau et al., 2007), IC 3203 is the most distant galaxy from the sample, and among the smallest on the sky. It has

been classified both as S0 (van den Bergh et al., 2003) and Sb (Hakobyan et al., 2008), and was home of a rare type IIb supernova, SN 2003ac (Filippenko and Chornock, 2003). As it is resolved quite poorly, the uncertainty on the dust parameters is larger compared to other galaxies. The residual maps indicate that the bulge is moderately peanut-shaped. The face-on optical depth derived from the FitSKIRT fit ($\tau_V^{\mathrm{f}} = 0.20 \pm 0.08$) is quite low and might be underestimated because of the poorly resolved and smoothened dust lane.

4.4.9 IC 4225

IC 4225 is a rather anonymous Sa galaxy in the Coma supercluster region at a distance of about 73.9 Mpc (Ramella et al., 1995). It is oriented almost perfectly edge-on ($i = 89.3 \pm 0.1$ deg), but unfortunately has the smallest angular extent of all galaxies in our sample. The SDSS images and the residual images clearly show an asymmetry between the left an right side of the galaxy, which might be due to spiral structure. In general, however, the FitSKIRT fits are satisfactory with residual errors below 25% for most of the pixels in the images.

4.4.10 NGC 5166

NGC 5166 is a rather ordinary Sb type galaxy at a Tully-Fisher based distance of 62.6 Mpc (Theureau et al., 2007). It has a prominent but somewhat asymmetric dust lane. Its bulge is known to be strongly peanut-shaped (Lütticke et al., 2000a), which shows up in the residual frames (in this case mostly in the *r*-band) as the typical butterfly or X-shape pattern. Apart from these features, the overall radiative transfer fit is remarkably good.

4.4.11 NGC 5908

This Sb galaxy forms a weakly interacting pair with NGC 5905 at a distance of 53.4 Mpc (Theureau et al., 2007). Its surface brightness distribution has been studied extensively in the past two decades (e.g. Peletier and Balcells, 1997; Laurikainen and Salo, 2000; Schwarzkopf and Dettmar, 2000). Similarly to UGC 5481 and NGC 4175, it has a fairly large deviation from an edge-on inclination ($i \sim 83$ deg). In apparent size, it is the largest galaxy in our sample, but the poorest radiative transfer fit: the fitted edge-on optical depth value is unrealistically high at $\tau_V^{\mathrm{e}} \sim 132$, and strong structures remain visible in the residual images. Although the bright regions are recovered reasonably, the dust lane is fitted very poorly with relative errors exceeding 100%. Both the observations and the residuals show that the dust is distributed in a smooth ring rather than the standard double-exponential disc we use for our fits. In fact, with its relatively smooth dust ring, bright bulge and extended halo,

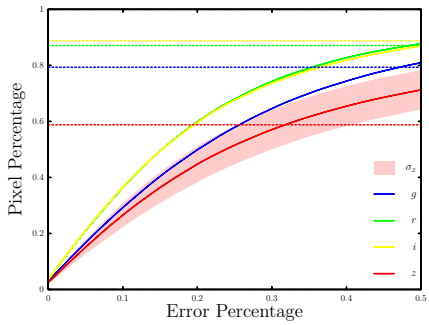

Figure 4.3: Cumulative pixel distribution of all the residual frames for all 12 galaxies. The standard deviation within the sample is given for the z-band. The dashed lines represent the fraction of the pixels in the observed images with a signal-to-noise of three or higher.

the galaxy reminds strongly of the Sombrero galaxy (Gadotti and Sánchez-Janssen, 2012; De Looze et al., 2012b), a fact already noted by de Vaucouleurs et al. (1964). Because the geometry clearly deviates from an exponential disc, this galaxy was discarded when determining the average quantities of our sample.

4.4.12 UGC 12518

The last galaxy in our sample is again a rather unexceptional Sb galaxy, located at 51.6 Mpc (Springob et al., 2009). Together with IC 3203, it has the smallest apparent vertical size of the entire sample. Consequently, the dust lane is only a few pixels thick making it hard to get accurate constraints on the dust distribution parameters. Moreover, the SDSS images and the residual images show that the bulge is clearly box-shaped. The result is that the fit is moderately good, although the dust parameters are recovered with relatively large error bars.

4.5 Discussion

4.5.1 Quality of the FitSKIRT radiative transfer fits

Looking at the results, we conclude that in general most galaxies are modelled accurately, especially when keeping in mind that the FitSKIRT models only consist of three basic components and they are determined by an automated procedure over a large parameters space without strong initial boundary conditions. Only two of our galaxies, NGC 5980 and UGC 4136, could not be accurately described by the model we presume. The dust geometry in these two systems is probably better described by a ring-like geometry rather than an exponential disc. The values found by FitSKIRT do not have any significant meaning for these two galaxies and using them

could bias our results. Although it is likely that other galaxies in our sample also have a geometry that deviates from our model, we do not find strong indications of systematic deviations. Most of the variations seen in the residual maps are the result of small perturbations in the galaxy rather than a larger-scale and systematic deviation.

To quantify the accuracy of the fits, Figure 4.3 shows the cumulative pixel distribution of the residuals of the entire sample, averaged for each band separately. The solid lines on this figure show which fraction of the pixels are reproduced by the models with a relative error smaller than the value on the horizontal axis, the shaded region indicates the dispersion on this curve for the z-band (it is representative for the other bands as well). The dashed lines represent the fraction of the pixels in the observed images with a signal-to-noise of three or higher.

The r and i-band images show the least deviation between the model and the corresponding SDSS reference images. In other words, FitSKIRT provides the best fits to the r and i band images. The g-band images are fitted slightly worse – the reason is probably that the dust extinction is strongest in this band and that asymmetries and small-scale irregularities are most prominent. Finally, the z-band observations, where only about 60% of the pixels have a signal-to-noise above three, are fitted least accurately. The most likely reason is the relatively poor signal-to-noise ratio. In Section 3.3 it was shown that in our test case, where the signal-to-noise was equal in all bands, there was no significant biasing of one band over the other. In general, we find that, in any band, more than half of the pixels have a deviation of 25% or better, and this improves to 15% in the r and i bands.

The last column in Table 4.3 lists the average 1σ error bar on each of the fitted values for the free parameters in the model. Notice that these errors do not take into account possible systematic errors. The inclination is the best constrained parameter: in all cases it is determined with an accuracy of less than half a degree. The parameters linked to the stellar geometry are better constrained than the dust parameters, which is consistent with the results found in De Geyter et al. (2013). The stellar disc parameters are determined with a relative accuracy of less than 10% while the bulge parameters are derived with an uncertainty of approximately 15%. The error bars for the scale height of the dust disc and the edge-on optical depth, two parameters that have a direct effect on the appearance of the dust lane in edge-on spiral galaxies, are also of the order of 15%. For the dust mass and the face-on optical depth, parameters that do not have as direct an impact on the morphology, the error bar is between 20 and 30%. Both the disc and bulge luminosity are recovered more precisely when we go to redder bands. This is not so peculiar as the attenuation in the blue bands makes it harder to recover the intrinsic luminosity. Overall the deviations on the luminosity are of order of 15% or less. The third column in Table 4.3

Parameter	unit	mean $\pm$ RMS	1σ (%)
$h_{R,*}$	kpc	4.23 ± 1.23	3
$h_{z,*}$	kpc	0.51 ± 0.27	7
$R_{\rm eff}$	kpc	2.31 ± 1.59	11
n	—	2.61 ± 1.80	14
q	—	0.56 ± 0.20	6
$h_{R,\rm d}$	kpc	6.03 ± 2.92	19
$h_{z,\rm d}$	kpc	0.23 ± 0.10	13
$M_{\rm d}$	$10^7\ M_\odot$	3.02 ± 2.21	23
$\tau_{\rm V}^{\rm f}$	—	0.76 ± 0.60	28
$\tau_{\rm V}^{\rm e}$	—	18.0 ± 7.1	15
i	deg	86.7 ± 2.5	0.4
$L_g^{\rm tot}$	$10^9\ L_\odot$	2.70 ± 2.40	15
$L_r^{\rm tot}$	$10^9\ L_\odot$	4.12 ± 3.54	12
$L_i^{\rm tot}$	$10^9\ L_\odot$	5.64 ± 4.50	10
$L_z^{\rm tot}$	$10^9\ L_\odot$	7.35 ± 5.72	3
B/T_g	—	0.41 ± 0.11	17
B/T_r	—	0.45 ± 0.11	14
B/T_i	—	0.46 ± 0.11	4
B/T_z	—	0.46 ± 0.08	3

Table 4.3: Mean values, RMS values, and average 1σ error bars for the different model parameters for the galaxies in our sample. For the parameters of the dust, UGC 4163 and NGC 5908 are not included, as these galaxies are poorly described by our standard double exponential disc model.

contains the mean values and the RMS of the physical free parameters derived from the radiative transfer fits.

The general conclusion drawn from our radiative transfer fits is that most galaxies can be modelled appropriately with an exponential disc for the stars and the dust and a Sérsic profile describing the central bulge. In most cases the parameters of the different components can be constrained with a satisfactory level of accuracy.

4.5.2 The stellar disc and bulge

As none of the galaxies in our sample have been modelled using radiative transfer simulations before, we cannot directly compare the values we obtain for individual galaxies. As a useful sanity check, however, we can check whether the average values of the derived parameters are in agreement with general values for the global galaxy population. This applies in particular to the parameters of the stellar geometry, which can be derived from large samples of galaxies without the need of full radiative transfer calculations.

Concerning the properties of the stellar disc, an interesting sample to compare our results to is the set of 34 edge-on spiral galaxies by Kregel et al. (2002). They fit a combination of a double-exponential disc and a Sérsic bulge to I-band images, carefully masking the dust lane region. Averaging the values of their Table 1, we find a mean scale length of 4.73 ± 2.57 kpc and scale height of 0.57 ± 0.25 kpc. These values are in agreement with our results of 4.23 ± 1.23 kpc and 0.51 ± 0.27 kpc, respectively. The mean intrinsic flattening of the stellar disc, i.e. the ratio $h_{R,*}/h_{z,*}$, in the Kregel et al. (2002) sample is 8.21 ± 2.36, again in excellent agreement with our value of 8.26 ± 3.44.

For the properties of the bulge, we can compare our average values to the Gadotti (2009) sample, which contains nearly 1000 face-on galaxies selected from the SDSS for which detailed morphological decomposition was applied. When we eliminate the elliptical galaxies from the sample and look at the r-band values, we find for the Sérsic index a mean value 2.37 ± 1.35, consistent with our value of 2.61 ± 1.80.

Interesting is the effective radius of the bulge: the typical value obtained by Gadotti (2009) is 0.84 ± 0.36 kpc, which is significantly smaller than (but still compatible within the error bars with) the value of 2.31 ± 1.59 kpc we obtain. One reason for this distinction could be that we do not take into account a bar in our radiative transfer fits, whereas Gadotti (2009) do fit a combination of a disc, bulge and bar to their images. The addition of a bar in the fitting has a significant effect on the resulting properties of the bulge. A second important aspect is the effect of dust attenuation on the derived properties: the presence of dust can severely affect the apparent pa-

rameters in bulge-disc decomposition, even at low inclinations (e.g. Graham and Worley, 2008; Gadotti et al., 2010; Pastrav et al., 2013a,b). In particular, Gadotti et al. (2010) demonstrate using detailed radiative transfer modelling that if the effects of dust are not taken into account then bulge effective radii are systematically underestimated. Another possible cause for this difference is that one of the selection criterions for our sample was presence of a dust lane. Galaxies with a large bulge are more likely to show a prominent dust lane than galaxies with a small bulge, so this selection criterion could be in part responsible for the rather large bulges in our sample.

Similarly interesting is the value of the bulge-to-disc ratio or the bulge-to-total ratio. Since Gadotti (2009) uses a disc, a bar and a bulge in his fits, we can not directly compare the bulge-to-total values between both samples. Consequently we have to add their bulge and bar component when calculating the bulge-to-total ratio which would be found by a two-component fit. This results in 0.32 ± 0.22, 0.33 ± 0.20 and 0.33 ± 0.20 for the *g*-, *r*- and *i*-band respectively. The bulges of the galaxies in our sample seem about 25% more luminous compared to the sample of Gadotti (2009). A similar flattening of the bulge-to-total ratio is found when going to longer wavelengths.

We can conclude that in general the parameters found for the stellar disc and bulge are in good agreement with other studies and there no large systematic deviations in our sample or fitting procedure.

4.5.3 The star-dust geometry

Table 4.3 also lists the average scale length and scale height of the dust disc and their spread within our sample. The dust scale height is in good agreement with the values 0.23 ± 0.08 kpc and 0.25 ± 0.11 kpc found using radiative transfer fits on V-band images by X99 and B07 respectively.

We find a relatively good agreement of the relative sizes of the dust and stellar discs. For the ratios of the dust to stellar scale height we find 0.50 ± 0.22, which is consistent with the conclusion found by X99, 0.58 ± 0.13, and B07, 0.52 ± 0.49. For the dust scale length to stellar scale length ratio we find 1.73 ± 0.83. This is slightly larger in average and in spread but still in agreement with X99, 1.36 ± 0.17 and B07, 1.53 ± 0.55. We can hence confirm the results from these studies, that the dust in spiral galaxies is typically distributed in a disc only half as thick but radially more than 50% larger the stellar disc.

To investigate a similar feature in our sample, we calculate the stellar masses using the intrinsic luminosities and $g - z$ colour difference according to the recipe described in Zibetti et al. (2009). The left panel of Figure 4.4 shows the dust to stellar

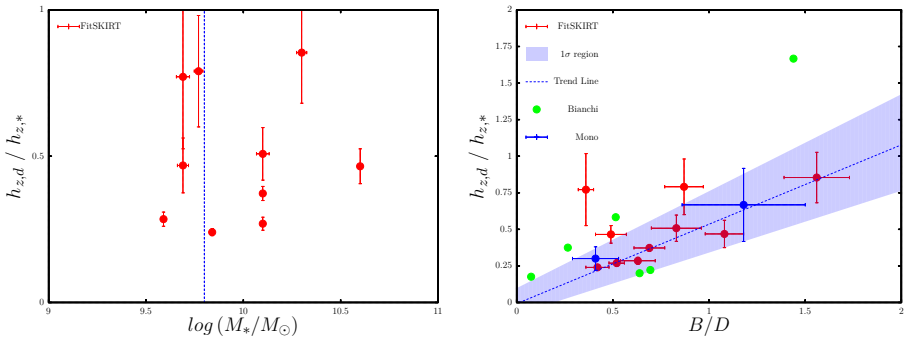

Figure 4.4: Left: The ratio of the dust to stellar scale heights in function of the stellar mass. The blue line marks the stellar mass at the which the rotation speed exceeds 120 km s^{-1} marking the transition from dynamically stable discs to perturbed discs prone to vertical "collapse" as discussed in Dalcanton et al. (2004). Right: the relation between ratio of the dust scale height and the stellar scale height and the bulge-to-disc ratio for the entire sample. The blue line shows the best fitting linear fit while the blue region is the one-sigma deviation calculated out of the uncertainties on the best fitting values. The blue dots are previous monochromatic FitSKIRT results for NGC 4565 (De Geyter et al., 2013) and NGC 4013 (De Looze et al., 2012a). The green dots are the values found by Bianchi (2007).

scale heights as a function of stellar mass. The vertical line shows the stellar mass of a bulgeless galaxy corresponding to the rotation speed of 120 km s^{-1} using the baryonic Tully-Fisher relation (Bell and de Jong, 2001; Dalcanton et al., 2004). Although most of our galaxies have a higher stellar mass and are therefore expected to rotate faster, four of the ten galaxies fall below the transition line. It should be noted that using the stellar mass instead of the actual rotation speed is only an approximation and that our sample contains galaxies with moderate to large bulges while the sample of Dalcanton et al. (2004) consists of bulgeless galaxies.

To check whether the presence of a bulge has an effect on the relative size of the dust disc, we investigate the dust to stellar scale height in function of the g-band bulge-to-disc ratio. These ten galaxies with corresponding uncertainties are shown in the right panel of Figure 4.4. To extend our sample and as a sanity check we have added two galaxies modelled previously with FitSKIRT in blue dots (De Geyter et al., 2013; De Looze et al., 2012a), and V-band values of the galaxies modelled by B07 in green dots. However, as there was no error determination for the parameters determined by B07, they are not taken into account in the determination of the best fitting trend line. The galaxies modelled by X99 do not come with a clear bulge-to-disc ratio and are therefore not included.

Looking at the right panel of Figure 4.4, it appears there is a correlation between the ratio of the dust to stellar scale height and the bulge-to-disc luminosity ratios, i.e. galaxies with more prominent bulges tend to have dust scale heights increasingly similar to the stellar scale heights. Again, we have to consider a bias due to our

sample selection criteria. As discussed before, galaxies with larger bulges often have more noticeable dust lanes. Therefore it is not surprising to find vertically more extended dust discs in galaxies with a more prominent bulge compared to thinner, bulgeless galaxies. This, however, does not explain why there is a lack of thin dust discs for galaxies with larger bulges. Consequently, this potential bias in the selection process alone can not explain the trend found for this sample.

Another small bias might be the fact that only one exponential disc is used to describe the stellar population. It is known that galaxies can have distinct separation of stellar populations where the young stars are in a thin yet heavily obscured disc while the older stellar population is distributed in a thicker disc (see also Pierini et al., 2004; Popescu et al., 2011; Schechtman-Rook et al., 2012). As the thin, bulgeless galaxies typically possess a younger, yet obscured stellar population, the resulting stellar scale height might be overestimated. Therefore the result is a smaller dust to stellar scale height ratio.

Whether or not these biases in the sample can completely explain the correlation is unclear. One possible physical explanation for the lack of thin dust discs for bulge-dominated galaxies may lie in variations of the dominant dust heating mechanisms. Dust has been found to be predominantly heated by either diffuse emission from the total stellar population (e.g. Bendo et al., 2010, 2012; Boquien et al., 2011; Groves et al., 2012) or by star-forming regions (Galametz et al., 2010; Hughes et al., 2014a). In a typical star-forming disk, dust and other ISM material are heated locally by star-forming regions. In galaxies with prominent bulges, the dust heating from star-forming regions may be supplemented with an additional source of dust heating originating from the diffuse emission of the older stellar population in the bulge. One may hypothesise that a greater contribution to the dust heating by the total stellar population in galaxies with increasing bulge-to-disc ratio, may lead to an increase in net heating of the ISM and, subsequently, a thickening of the dust disc. However, whilst the tendency of bulge-dominated galaxies to experience a thickening of the dust disc due to increased dust heating from the stellar population in the bulge may plausibly explain the lack of thin dust discs found at high bulge-to-disc ratios, we strongly warn that this physical mechanism is highly uncertain, speculative, and only included for completeness in our discussion. Further studies, in which we extend our sample size, wavelength range and the capability of the models to describe multiple stellar populations, are necessary in order to provide further insight into a possible physical explanation for this relation.

4.5.4 Optical depth

The galaxies analysed by X99, have a V-band face-on optical depth of 0.49 ± 0.19 and none of them with a value higher than one, which would indicate these galaxies

would be completely transparent if they are to be seen face-on. B07 used a Monte Carlo radiative transfer code to model a different sample of galaxies (two galaxies are in common with the X99 sample). He found a slightly larger spread in V-band optical depths, ranging up to $\tau_V^f = 1.46$ for NGC 4013. The average value for the sample studied by B07 is 0.58 ± 0.45.

In our sample of 10 galaxies, we find a larger spread in face-on V-band optical depth, ranging from a mere 0.18 for IC 4225 to 1.98 for NGC 3987. The average value and RMS for our sample is 0.76 ± 0.60, formally consistent with the mean value found by X99 and B07. The larger spread however seems to suggest that spiral galaxies, although on average optically thin, a non-negligible part is not entirely transparent. This slightly larger value for the optical depth can at least partly be ascribed to the different selection criteria. X99 and B07 considered very nearby galaxies, whereas our galaxies are significantly more distant (the average distances to the galaxies in the samples are 21, 30, and 64 Mpc for X99, B07 and our sample respectively). The combination of the larger distance with the requirement that the galaxies need to show a prominent dust lane, might bias our sample toward galaxies with more dust than average, and hence with an average optical depth larger than the more nearby samples of X99 and B07. Whether or not this can fully explain the difference is hard to tell.

One might suspect that differences in the optimisation and the radiative transfer treatment itself could be a possible origin for this difference. However, it does not seem likely that FitSKIRT systematically overestimates the optical depth: for NGC 4013, the one galaxy that has been modelled using the three codes, the optical depth found by FitSKIRT lies in between the values obtained by the two other teams (De Geyter et al., 2013).

4.5.5 Dust mass and the dust energy balance

Since the launch of the *Herschel* Space Observatory, dust masses for thousands of nearby galaxies have been determined by fitting simple modified blackbody or more complicated SED models to the observed far-infrared and submm fluxes. Our radiative transfer models provide us with a completely independent and alternative technique to estimate the dust mass in galaxies. The average dust mass for our galaxy sample is $\langle \log M_d / M_\odot \rangle = 7.48 \pm 0.32$. When we compare this value to the typical values found for normal late-type galaxies based on *Herschel*FIR/submm SEDs, we find fairly compatible results. For example, Davies et al. (2012) find $\langle \log M_d / M_\odot \rangle = 7.06 \pm 0.45$ in a 500 μm selected sample of 78 optically bright galaxies from the HeViCS survey (Davies et al., 2010), Galametz et al. (2012b) found $\langle \log M_d / M_\odot \rangle = 7.34 \pm 0.30$ for a sample of 11 nearby galaxies from the KINGFISH sample (Kennicutt et al., 2011), and Smith et al. (2012a) obtained $\langle \log M_d / M_\odot \rangle =$

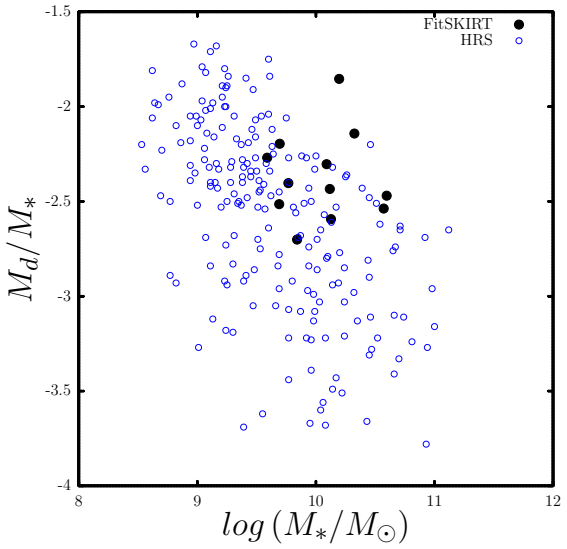

Figure 4.5: The dust to stellar mass ratio (specific dust mass) in function of the stellar mass. The black dots represent the 12 galaxies in our sample while the open circle are the values found for the Herschel Reference Survey galaxies (Cortese et al., 2012). Notice that our CALIFA sample seems to be more dust rich compared the HRS sample.

8.01 for a sample of more than thousand $z < 0.35$ galaxies selected from the H-ATLAS survey (Eales et al., 2010).

In Figure 4.5 we plot the dust-to-stellar mass ratio as a function of the stellar mass for our sample galaxies. We also show on this plot the late-type galaxies from the Herschel Reference Survey (HRS), a complete volume-limited survey of 323 normal galaxies in the nearby universe (Boselli et al., 2010). The dust masses for the HRS galaxies are obtained by an empirical recipe based on the SPIRE flux densities, calibrated against modified blackbody SED models and the Draine and Li (2007) dust model (Cortese et al., 2012). For both samples, stellar masses are determined from the i-band luminosities using the $g - i$ colour-dependent stellar mass-to-light ratio relation from Zibetti et al. (2009), assuming a Chabrier (2003) initial mass function. The dust-to-stellar mass ratios for our galaxies fall in the range as the HRS galaxies, but tend to populate the upper regions of this plot. In other words, for a given stellar mass, our sample galaxies tend to be rather dustier compared to the general HRS population.

This is quite surprising in the light of the so-called dust energy balance inconsistency that seems to be applicable for spiral galaxies. For a small number of edge-on spiral galaxies for which detailed radiative transfer fits have been made, the predicted FIR emission from the models generally underestimates the observed FIR

fluxes by a factor of about three (Popescu et al., 2000, 2011; Misiriotis et al., 2001; Alton et al., 2004; Dasyra et al., 2005; Baes et al., 2010; De Looze et al., 2012a,b). One would therefore expect that dust masses based on SED fits to the observed FIR/-submm, such as those for the HRS galaxies in Figure 4.5, would tend to be several times higher than the dust masses based on radiative transfer modelling of optical images, such as the ones we derived for our sample.

A possible explanation could, again, be the different selection criteria of the two samples. All HRS galaxies are located at a distance between 15 and 25 Mpc, and the late-type galaxy subsample was selected based on a *K*-band flux limit (as a proxy for the stellar mass). Our sample, on the other hand, is more distant and was chosen to show prominent dust lanes, and as such it might be biased to more dust-rich galaxies than the general HRS population. The only way to really test whether this can explain the different location of the samples in Figure 4.5 is by calculating the FIR/submm emission that is to be expected from the radiative transfer models for the galaxies in our sample, and comparing it to the observed FIR/submm flux densities (at least for those galaxies for which such data are available). This is beyond the scope of the present work and will be the subject of a subsequent work.

4.6 Conclusions

We have selected 12 edge-on, spiral galaxies from the CALIFA survey in order to constrain both their stellar and dust distribution. This was done by computing accurate radiative transfer models to the SDSS *g*-, *r*-, *i*- and *z*-band images simultaneously. As the galaxies are part of the CALIFA survey they already comply to the following criteria: the redshift ranges between $0.005 < z < 0.03$ and the isophotal *r*-band diameter ranges from 45 to 80 arcsec. The galaxies with an obvious dust lane are then selected while avoiding the strongly asymmetrical or interacting ones. As final selection criterium we exclude galaxies with a major axis smaller than 1 arcmin or a minor axis smaller than 8 arcsec as to ensure the dust lane has a high enough resolution to be modelled accurately.

The results of the fits to the 12 galaxies in our sample can be found in Table 4.2 while the sample averages, spread and accuracy can be found in Table 4.3.

For only two galaxies (UGC 4163 and NGC 5908) in our sample, we found that the model, consisting of a exponential disc to describe the stellar and dust distribution and a Sérsic profile to model the central bulge, was not able to accurately reproduce the observations. In all other cases we are able to model the galaxies and constrain the parameters to an acceptable accuracy. In all of the residual frames more than half of the pixels show deviations of at most 25 %. Stellar disc and bulge parameters

are determined within 10 and 15% respectively while the dust parameters are less certain, with error bars rising up to 20 or 30% for the face-on optical depth.

We find that the average disc scale length and intrinsic disc flattening is in good agreement with the results described by Kregel et al. (2002) and Gadotti (2009). Our sample, on the other hand, does seem to have larger bulges with an average effective radius of 2.31 ± 1.59 kpc. Possible explanations for this difference are the fact that we do not include a bar in our model and a possible selection effect due to the necessity to have a clear dust lane while Gadotti (2009) does not take into account the effect of dust attenuation on the determined bulge parameters. Consequently a slightly higher bulge-to-total ratio is found although we find a similar trend in the ratios as a function of wavelength.

For the dust scale length and height we find a good agreement with X99 and B07. Also the relative sizes of the dust disc compared to the stellar disc are in good agreement where we find that the dust disc is about 70% more extended, which is slightly larger than found by X99 and B07, but twice as thin as the stellar disc. From Dalcanton et al. (2004) we should expect to see a transition for galaxies with a rotation speed of 120 $\mathrm{km\,s^{-1}}$ where the slower rotating ones should have a dust disc scale height similar to the one of the stellar disc. Using the baryonic Tully-Fisher relation to get estimates on the rotation speed based on the stellar mass of the galaxies we do not seem to find a similar trend in our sample. A possible explanation might again be that our sample has a clear tendency for larger bulges compared to the bulgeless galaxies investigated by Dalcanton et al. (2004) and MacLachlan et al. (2011).

An important aspect of the dust distribution in spiral galaxies is the face-on optical depth. A value of higher than 1 means a significant part of the light would be blocked even when the galaxy is seen face-on. In our sample we find a large spread ranging from 0.18 to 1.98 with an average V-band value of 0.76 and spread within the sample of 0.60. As a result, a fraction of the galaxies should not be transparent even when seen completely face-on. This is a slightly larger value in optical depth and in spread than what was previously found by X99 and B07. This could be the result of our galaxies requiring a visible dust lane while the galaxies are at larger distance compared to the sample investigated by X99 and B07. Therefore the galaxies in our sample are relatively more dust rich than galaxies selected on a dust lane at smaller distances.

The same difference in distance of this sample and the HRS sample investigated in Cortese et al. (2012) could explain why our galaxies reside on the higher side of the relation between the dust-to-stellar mass and the stellar mass. This is an unexpected result, as deriving the dust mass from extinction usually results in values which underestimate the actual dust mass determined from FIR observations by a factor of 3 (Popescu et al., 2000, 2011; Misiriotis et al., 2001; Alton et al., 2004).

Dust energy balance study

5

In order to explain this discrepancy, we require a sufficiently large set of galaxies that have the needed multi-wavelength data available and are modelled in a homogeneous way, such that physical effects can be disentangled from effects connected to the modelling. Since fitting radiative transfer models to images is a very computationally expensive job, most dust energy balance studies have concentrated on a single or at most a very modest set of galaxies. Moreover, the parameter space of the different galaxy models is often degenerate, in the sense that strongly different galaxy models can result in similar attenuation maps (Bianchi, 2007; De Geyter et al., 2013). Fortunately, these dust energy balance studies can now be taken to the next level, thanks to two recent developments.

In this chapter, we will make use of these two recent developments to investigate the energy balance in two edge-on spiral galaxies, IC 4225 and NGC 5166. In Section 5.1 we describe the rationale behind the selection of these two galaxies, and present the available data. The construction and results of our radiative transfer modeling is presented in Section 5.2. In Section 5.3 we discuss these results and the possible implications on the dust energy balance problem and present our conclusions.

The first improvement concerns the determination of the dust mass based on optical data. Recently, different attempts have been undertaken in the radiative transfer community to make the fitting of radiative transfer models to data more automated and objective (e.g., Steinacker et al., 2005; Robitaille et al., 2007; Bianchi, 2007; Schechtman-Rook et al., 2012). One of the challenges here is that, in order to fit Monte Carlo radiative transfer models to data, one has to take into account that the model images themselves are not noise-free, which implies that normal gradient-search optimisation methods are problematic. De Geyter et al. (2013) showed that optimisation by means of genetic algorithms is an ideal solution for this problem. Moreover, the degeneracy in the parameter space can be minimised by means of oligochromatic radiative transfer modelling, i.e., by simultaneously fitting radiative transfer models to images in several optical wavebands (De Geyter et al., 2014, hereafter DG14).

The second development is the launch of the *Herschel Space Observatory* (Pilbratt

et al., 2010), which has been a major boost for the study of the interstellar dust medium in nearby galaxies. Thanks to *Herschel*, we can finally construct complete dust SEDs, easily trace even the cold dust grains and get a more realistic and tighter constraint on the total dust mass.

The target galaxies were observed as part of the H-ATLAS survey (Eales et al., 2010). This was the largest extragalactic survey undertaken by *Herschel*, with a total of 600 hours dedicated observing time. In total, about 600 deg^2 of extragalactic sky was mapped simultaneously with the PACS (Poglitsch et al., 2010) and SPIRE (Griffin et al., 2010) instruments in 5 bands centred at 100, 160, 250, 350 and 500 μm. The scientific goals of the H-ATLAS programme are diverse, ranging from the search for debris disks and the characterisation of the Galactic cirrus (Thompson et al., 2010; Bracco et al., 2011), statistical studies of the local and the high-redshift galaxy population (Dunne et al., 2011; Lapi et al., 2011; Smith et al., 2012a), to the investigation of extreme objects like blazars and gravitational lenses (Negrello et al., 2010; Cox et al., 2011; Fu et al., 2012; López-Caniego et al., 2013).

5.1 The targets

5.1.1 Target selection

The starting point for our target selection was the sample of 12 edge-on spiral galaxies considered by DG14. This sample was selected from the CALIFA survey (Sánchez et al., 2012), based on the criteria of an edge-on orientation with a dust-lane morphology, a major axis diameter larger than 1 arcmin and a minor axis diameter larger than 8 arcsec. Each of these galaxies were modelled in exactly the same way: a stars+dust radiative transfer model was fitted to the SDSS *g*, *r*, *i* and *z* images, using the oligochromatic FitSKIRT code.

In this chapter, we want to extend this analysis to a panchromatic study, and compare the dust "observed" in the optical SDSS images to the dust seen in emission in the FIR/submm. We hence select from the sample of DG14 those galaxies that have *Herschel* data to cover the FIR/submm SED.

Of the 12 galaxies, three galaxies have been observed by *Herschel*: IC 2461, IC 4225, and NGC 5166. We decided to leave out IC 4261 from this study – it turned out to be an extreme system with a deeply buried Seyfert 2 nucleus (Parisi et al., 2012), that is emitting high-energy emission even in the ultra-hard X-ray bands (Koss et al., 2011; Baumgartner et al., 2013). Additionally, we lack the required UV observations from GALEX, which provides an important constraint on the younger stellar population.

Both of the remaining galaxies are located in the North Galactic Plane (NGP) field of the H-ATLAS survey. IC 4225 is situated in the Coma supercluster region at a distance of about 73.9 Mpc (Slezak et al., 1988; Ramella et al., 1995). It is classified as an S0/a galaxy (de Vaucouleurs et al., 1991) and is about 1.3 by 0.3 arcmin. NGC 5166 is an Sb type galaxy at a Tully-Fisher based distance of 62.6 Mpc (de Vaucouleurs et al., 1991; Theureau et al., 2007). It has a prominent but somewhat asymmetric dust lane and has a larger angular extent of 2.3 by 0.4 arcmin.

5.1.2 Data

For the panchromatic radiative transfer modelling that we will perform, we need imaging data over a wavelength range as broad as possible. Both galaxies have been observed by the Sloan Digital Sky Survey (SDSS, Abazajian et al., 2009) and therefore have u, g, r, i and z band observations. Additionally they were observed by the Galaxy Evolution Explorer (GALEX, Martin et al., 2005), the Two Micron All Sky Survey (2MASS, Skrutskie et al., 2006) and the Wide-field Infrared Survey Explorer (WISE, Wright et al., 2010). Unfortunately, neither of the galaxies had a clear detection in the GALEX FUV band at 0.152 μm, so only the NUV flux density of the GALEX survey could be used. For each of these observations, we followed standard data reduction procedures using IDL routines. After masking foreground stars, integrated flux densities were determined by means of aperture photometry using DS9 Funtools (Mandel et al., 2001) instead of using the catalog values to ensure that there is no contamination from nearby sources.

PACS and SPIRE images and flux densities were extracted from the H-ATLAS catalogue. Details on the PACS and SPIRE data reduction, map-making, source extraction and catalogue generation for H-ATLAS can be found in Ibar et al. (2010), Pascale et al. (2011), Rigby et al. (2011) and Valiante et al. (in prep.). For NGC 5166 additional data were used from the IRAS Faint Source Catalog (Moshir et al., 1992) at 25, 60 and 100 μm. The galaxy was also detected at 350 and 550 μm by *Planck* where we have used the flux density determined using the aperture photometry (APREFLUX) listed in the Planck Catalogue of Compact Sources v1.0 (Planck Collaboration, 2014).

All the flux densities and their corresponding errors for IC 4225 and NGC 5166 are listed Table 5.1.

5.2 Panchromatic radiative transfer modelling

5.2.1 Modelling approach

DG14 determined the dust distribution in 12 edge-on spiral galaxies, including

Survey	wavelength [μm]	IC 4225 [mJy]	NGC 5166 [mJy]
GALEX	0.226	0.40 ± 0.12	0.87 ± 0.17
SDSS	0.354	1.3 ± 0.1	2.4 ± 0.1
SDSS	0.475	5.73 ± 0.1	11.9 ± 0.2
SDSS	0.622	12.3 ± 0.2	26.1 ± 0.3
SDSS	0.763	19.0 ± 0.3	40.5 ± 0.4
SDSS	0.905	26.6 ± 0.3	55.0 ± 0.4
2MASS	1.25	40.3 ± 0.5	80.0 ± 0.7
2MASS	1.64	53.0 ± 0.5	127.6 ± 1.0
2MASS	2.17	47.0 ± 0.5	119.6 ± 0.9
WISE	3.4	23.0 ± 0.2	51.1 ± 0.3
WISE	4.6	13.6 ± 0.2	33.0 ± 0.3
WISE	12	15.5 ± 0.2	85.8 ± 0.4
WISE	22	11.5 ± 0.8	170 ± 3.0
IRAS	25	—	155 ± 38
IRAS	60	—	845 ± 59
IRAS	100	—	2880 ± 259
PACS	100	640 ± 72	3132 ± 252
PACS	160	709 ± 85	3506 ± 262
SPIRE	250	490 ± 35	2315 ± 167
SPIRE	350	190 ± 15	961 ± 74
Planck	350	—	1062 ± 272
SPIRE	500	54 ± 7	327 ± 33
Planck	550	—	356 ± 219

Table 5.1: Observed flux densities and corresponding errors for IC 4225 and NGC 5166.

IC 4225 and NGC 5166, based on optical images. More specifically, they used the oligochromatic FitSKIRT code to construct a radiative transfer model with 19 free parameters that can simultaneously reproduce the SDSS g, r, i and z band data for these galaxies. For more details on the fitting procedure we refer to Section 3 of DG14. The goal of the modelling in the present chapter is to extend these oligochromatic models to fully panchromatic models that can reproduce not only the images at optical wavelengths, but also explain the thermal emission by dust, as observed in the MIR/FIR/submm in a self-consistent way.

The modelling is done using SKIRT (Baes et al., 2003, 2011; Camps and Baes, 2015), a Monte Carlo radiative transfer code designed to solve the 3D dust radiative transfer problem. It is mainly applied to simulate dusty galaxies (e.g., Gadotti et al., 2010; Gomez et al., 2010; De Looze et al., 2012b, 2014), but has also been used to model active galactic nuclei (Stalevski et al., 2012) and dusty discs around evolved stars (Vidal and Baes, 2007; Deschamps et al., 2014).

Our modelling goes in two phases: our first set of models (case A, Section 5.2.2) are constrained by the optical images only. In a second set of models (case B, Section 5.2.3), we add a component to account for additional UV radiation.

5.2.2 Case A models

The FitSKIRT results from DG14 form the ansatz for the models. The stellar distribution consists of an double-exponential disk to describe the stellar disk and a flattened Sérsic profile to describe the bulge. The dust distribution is represented by a double-exponential disk with scale length $h_{R,\mathrm{d}}$ and scale height $h_{z,\mathrm{d}}$. This is a commonly used distribution in dust radiative transfer simulations (Xilouris et al., 1999; Misiriotis et al., 2001; Tuffs et al., 2004; Bianchi, 2007; Popescu et al., 2011). Recently, it has been shown, using high resolution PACS and SPIRE maps, that such a distribution forms a suitable description of the FIR morphology in both radial and vertical direction (Verstappen et al., 2013; Hughes et al., 2014b). The standard BARE-GR-S model of Zubko et al. (2004) was used to set the absorption efficiency, the scattering efficiency and scattering phase function of the dust. The total dust mass M_{d} completes the characterisation of the dust content in the model.

One remarkable result from this fitting is that IC 4225 has an exceptionally large dust disk (see Table 3 in DG14 for the parameter values and uncertainties). Especially when compared in relative size to the stellar disk, it is almost three times more extended. It is even more surprising keeping in mind that this galaxy was classified as a S0/a galaxy, for which it has been shown that the dust emission should be compact (Bendo et al., 2007; Muñoz-Mateos et al., 2009b; Smith et al., 2012d). Most likely however, due to the smaller angular size, the morphology of IC 4225 was misclassified.

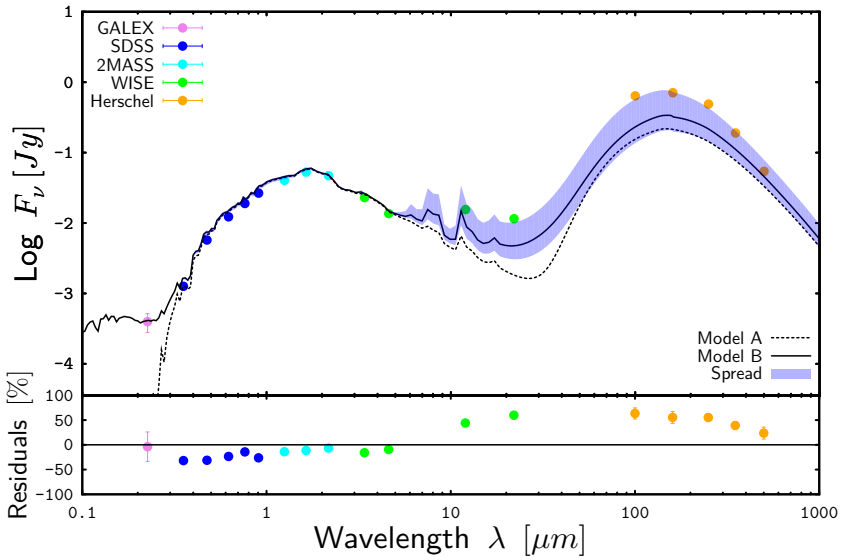

Figure 5.1: The SED of IC 4225 (top) and NGC 5166 (bottom). The coloured dots with error bars correspond to the flux densities listed in Table 5.1. The dotted lines are the simple models based only on the optical data (case A), the solid lines are the models in which an additional young stellar component in taken into account (case B). The blue transparent band represent the spread in the FIR emission of the models within one error bar of the best fitting models. The parameters and corresponding uncertainties ca be found in Table 4.2. The bottom panels below the SEDs show the residuals between the observed SED and the case B model.

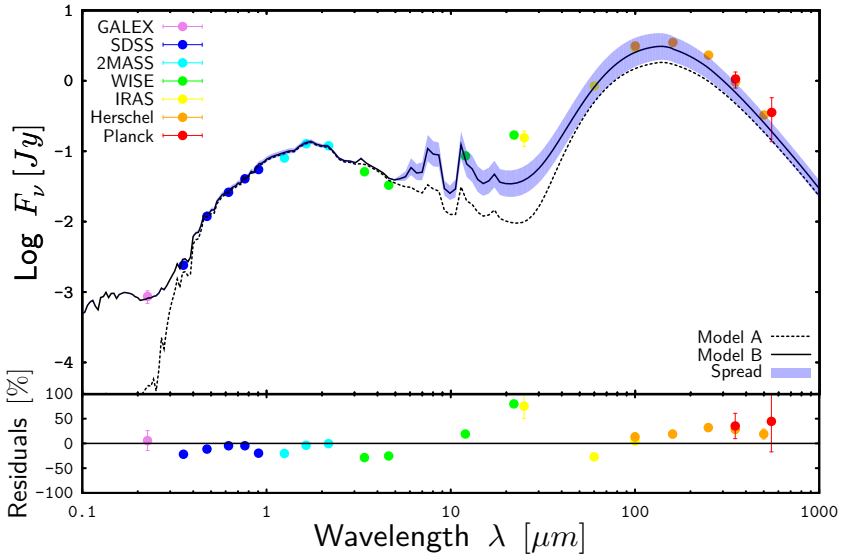

Figure 5.1: (continued)

The large dust disk, combined with a total dust mass close to the average of the modelled sample, results in a face-on V-band optical depth of a mere 0.18. Because of the relatively small angular extent of the galaxy (it is the galaxy with the smallest angular extent of the sample considered by DG14), the uncertainties on the dust parameters are quite large compared to the average values for the sample. In spite of the large uncertainties, the model reproduces the optical images to an acceptable level with only a small irregularity in the outer regions, possibly due to the projection of a spiral structure (see Figure 4.2 of Section 4.4).

On the contrary, the model for NGC 5166 is a very stereotypical model. The dust disk is about 50% more extended and about half as thick as the stellar disk, which corresponds to the classical image of edge-on spiral galaxies (Xilouris et al., 1999; Bianchi, 2007). The dust parameters were constrained with a higher accuracy compared to IC 4225. The model has a bulge that is quite large, relative to the disk. As was found by Lütticke et al. (2000b) and can be clearly seen from the residuals in Figure 3*j* in DG14, the bulge has a strong peanut shape, a feature that is quite common when looking at edge-on spiral galaxies (Lütticke et al., 2000a). As was the case for IC 4225, a small asymmetry can be seen, possibly due to a spiral structure. In general, the fit is very satisfactory with most pixels only showing a maximum deviation of 25%.

The first step in our analysis consists of adjusting these oligochromatic FitSKIRT models in order to calculate the view of the galaxy in the entire UV to submm domain, rather than only in a few selected optical bands. This implies that the both the properties for the stars and dust need to be set over this entire wavelength domain.

For both stellar components, we assume an intrinsic Bruzual and Charlot (2003) single stellar population SED, which is based on Chabrier (2003) initial mass function and assuming a solar metallicity. The ages of the best fitting SSPs were determined from the dereddened luminosities reported in DG14 using an adapted version of the SED fitting tool from Hatziminaoglou et al. (2008, 2009). For IC 4225, we found ages of 7 Gyr for the stellar disk and 12 Gyr for the bulge component. The best fitting stellar populations for NGC 5166 are slightly younger at 4 Gyr for the stellar disk and 11 Gyr for the bulge component. The entire SED was normalised to match the *i*-band luminosity.

Concerning the dust, the standard BARE-GR-S dust model was used to set the optical properties in the entire UV–submm wavelength domain. Note that the SKIRT code considers individual silicate, graphite and PAH grain populations for the calculation of the dust emission spectrum, and that it fully takes into account the transient heating of PAHs and very small grains, using techniques described in Guhathakurta and Draine (1989) and Draine and Li (2001).

In Figure 5.1 we compare the SED obtained for the case A model (dotted lines) with the observed flux densities for both galaxies. It is clear that in both cases the models cannot explain the observed SEDs. The radiative transfer models reproduce the optical SED very well, which is not surprising given that the the geometrical parameters of the model and the characteristics of the intrinsic SEDs were determined to reproduce the optical images. They can also successfully explain the NIR data points. On the contrary, the model SEDs underestimate the observed flux densities both in the UV and in the thermal MIR/FIR/submm regions.

5.2.3 Case B models

It is clear that the simple case A models considered above before need to be extended with an additional component that can account for the observed UV radiation. We will account for this by adding a third stellar component associated with young, unobscured star forming regions. Unfortunately, in both cases, the GALEX NUV images are too noisy to be used to constrain the geometry of the younger component without any prior assumptions. Young stellar populations in spiral galaxies are usually located in a thin disk with scale heights similar or smaller than the dust disk (Schechtman-Rook and Bershady, 2013a, 2014b). In our models, the scale height of this young stellar disk is taken to be half that of the dust disk[1]. The values we use are 120 and 170 pc for IC 4225 and NGC 5166 respectively, similar to what was found as the scale height of the young stellar disk in the Milky Way (Bahcall and Soneira, 1980).

For the intrinsic SED of this young component, we used a Starburst99 SED template which represents a stellar population with a constant, continuous star formation rate and an evolution up to 100 Myr (Leitherer et al., 1999). In this case, the initial mass function is a Salpeter (1955) IMF with masses between 1 $M_\odot$ and 100 $M_\odot$ and again assuming a solar metallicity. The luminosity of this component is constrained by the GALEX NUV flux density. As the contribution of this SED is negligible in the optical bands, adding this component does not affect the models in the SDSS and 2MASS bands. As it does, however, affect the energy balance of the dust, a new set of radiative transfer simulations has to be run in order to constrain the NUV flux and determine the resulting images over the entire wavelength range.

The solid line in the left panel of Figure 5.1 compares the model SED of this new case B model with the observed flux densities for IC 4225. Compared to the simple model without young stellar component, this model is a clear improvement. The optical/NIR SED is still reproduced as accurately as in the simple model, but the

[1] For both galaxies we ran additional simulations with different values for the scale height of the young stellar population, ranging between one third of the dust scale height to the same value. This effect, however, was hardly noticeable, as was also found by De Looze et al. (2014).

model now also reproduces the UV portion of the SED. As a result of the additional energy input of the young stellar populations, much of which is absorbed by the dust, the infrared part of the SED is also boosted. However, it is clear that a FIR excess still remains: the model FIR/submm flux densities still underestimate the observed data points by a factor of a few.

Interestingly, we obtain a different picture for NGC 5166. There was also a clear FIR/submm inconsistency between the data and the simple case A model. Contrary to IC 4225, however, this inconsistency disappears almost completely when we include a young stellar component: not only does the model now reproduce the UV part of the SED, but it almost provides sufficiently additional dust emission to account for the observed FIR/submm emission. The only data points that are still strongly underestimated by the model are the WISE 22 μm and IRAS 25 μm, which are usually linked to obscured star formation (Calzetti et al., 2007, 2010; Lee et al., 2013).

To investigate the effect of the uncertainty on the dust distribution of IC 4225, we have modelled the spread in the FIR emission when starting from a model with slightly altering parameter values. Table 3 in DG14 mentions both the best fitting values and the uncertainties for every free parameter. The highest FIR emission can be expected to be the model with the smallest dust disk and highest dust mass while the lowest FIR emission is found in the opposite case. Figure 5.1 shows the spread on the Case B model where the luminosity of the young stellar component was adjusted to reproduce the original value. By using this approach we investigate the FIR emission of models that still appropriately model the optical bands and make no additional assumptions using MIR/FIR data.

It is clear that for IC 4225, the spread on the FIR emission is larger, resulting from the higher uncertainty on the dust distribution. The observed data points are only barely compatible with the densest dust disk model. However, in this case even the 22 μm flux is recovered. For NGC 5166, the spread in the FIR is considerably smaller and not much variation on the shape of the SED can be expected.

In Figures 5.2 and 5.3 we compare a set of images corresponding to the case B models to the actual observed images of the two galaxies in different wavebands across the entire wavelength range calculated in the simulations. The simulated images have been convolved with the appropriate point spread function: for GALEX, SDSS, 2MASS and WISE we used a simple Gaussian with the correct FMHM, for the PACS and SPIRE data we used the kernels provided by Aniano et al. (2011).

From the GALEX NUV image it is clear that for IC 4225, the unobscured young stellar component is considerably more concentrated in the center, than what is assumed in our model. Additionally, the MIR and FIR images seem to suggest that, especially the warm dust, is also concentrated closer to the centre of the galaxy. It is

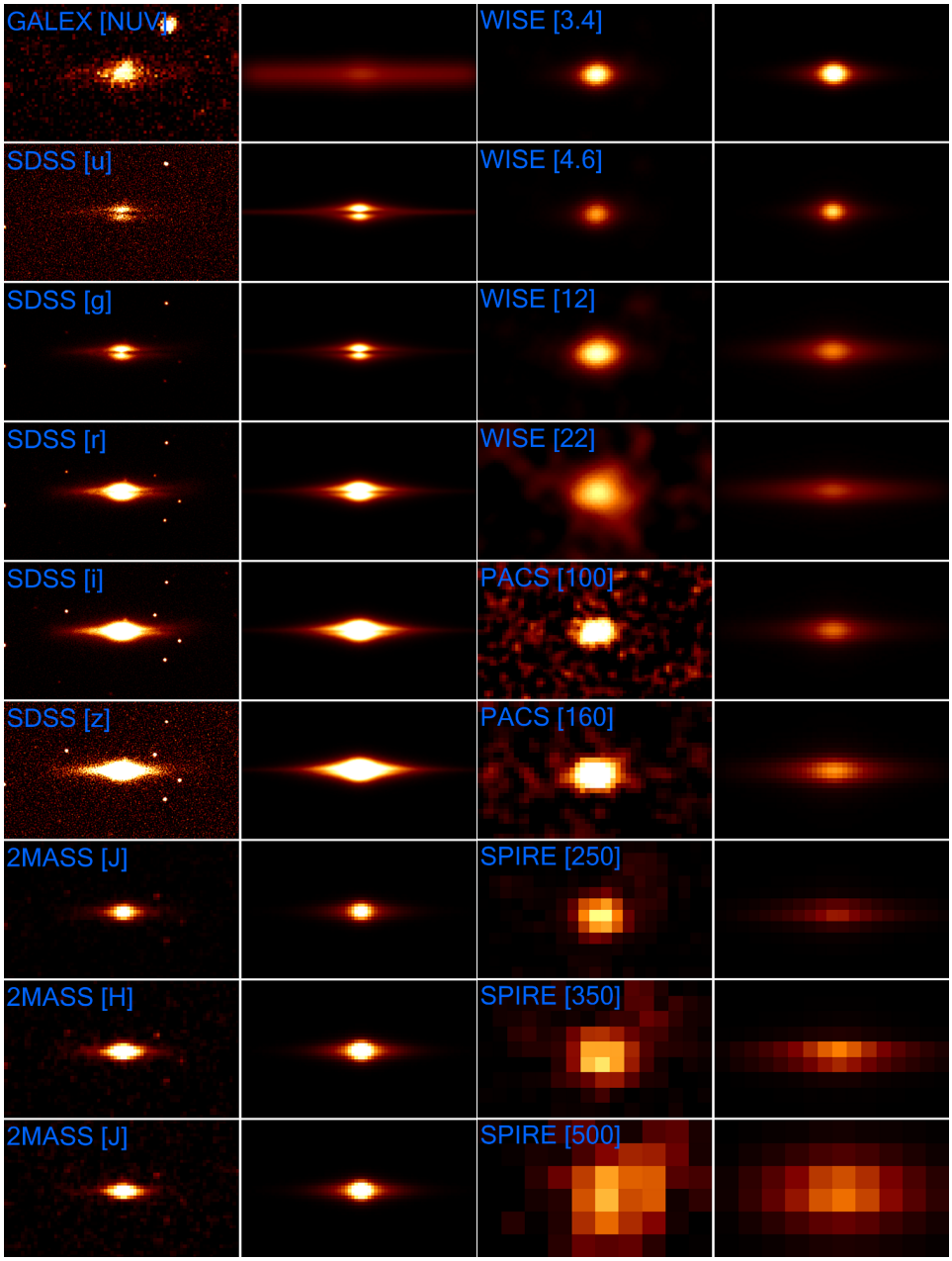

Figure 5.2: [
Comparison between the observations (left) and model images (right) for IC 4225. All images correspond to the case B model.

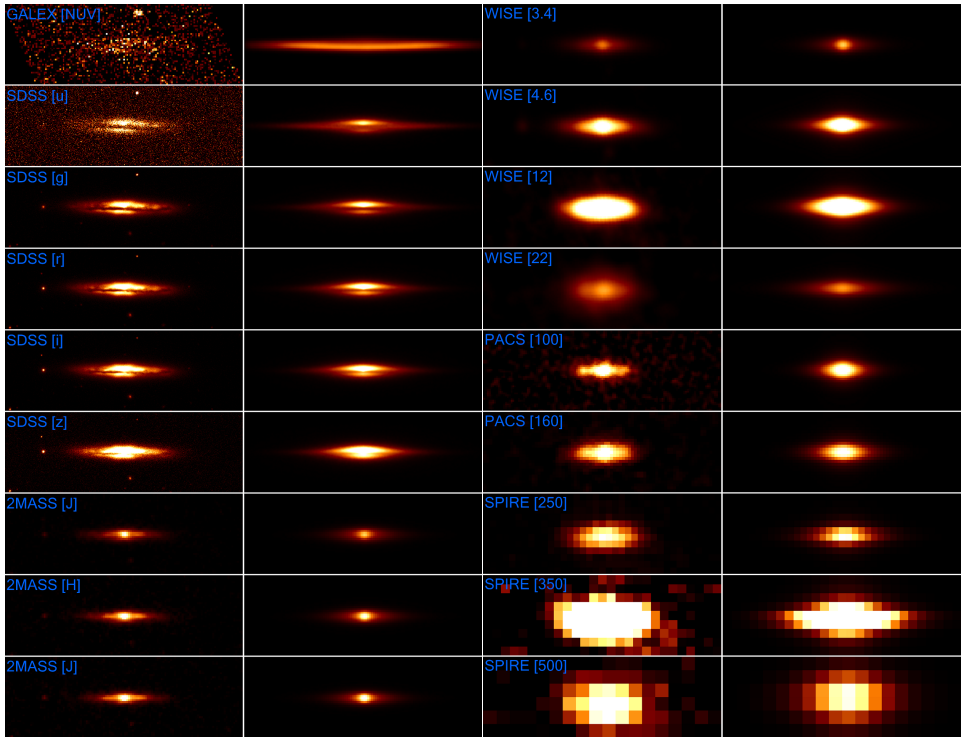

Figure 5.3: Same as Figure 5.2, but now for NGC 5166.

clear that the dust disk as obtained in DG14, is clearly not a realistic model for this galaxy. While it successfully reproduces the optical images, the disk is too extended to reproduce the UV and MIR/FIR observations. Interestingly, our radiative transfer model was capable of recovering the 500 μm flux density. However, it seems that the model does not really predict the correct morphology: the model image at 500 μm is spatially extended, while the observed SPIRE 500 μm image seems much more centrally concentrated.

For NGC 5166 the comparison between model and observations is much more satisfactory. In general, the geometry of the model images seems to match the observations reasonably well. While hard to tell from the low signal-to-noise image, the NUV images seem to be in better agreement than was the case for IC 4225. Apart from the boxy/peanut shaped bulge and some small bright, additional features, probably projected spiral arms, the near-infrared images also match quite well. These off-centre features also seem to be slightly noticeable at 100 μm but, in general, the agreement is fulfilling the expectations.

5.3 Discussion and conclusions

The ambition of this work was to use the state-of-the-art, both observationally and in radiative transfer, modelling to investigate the so-called dust energy balance problem for edge-on spiral galaxies. For both galaxies, IC 4225 and NGC 5166, the observed SED shows a clear FIR excess compared to a standard model that is based only on optical images, and hence only contains evolved stellar populations. This is similar as what is found by various teams (e.g., Popescu et al., 2000; Misiriotis et al., 2001; Alton et al., 2004; Dasyra et al., 2005; Bianchi, 2008; Baes et al., 2010; Popescu et al., 2011; Holwerda et al., 2012b).

However, things change when a young stellar population is included in the modelling: while a substantial FIR excess still remains for IC 4225, the FIR fluxes are recovered almost exactly for our model of NGC 5166. For the latter galaxy, the case B model does not only reproduce the observed SED, the predicted images over the entire UV–submm wavelength range also provide a good match to the observed images.

Why these two galaxies show such a different behaviour is an interesting question. It is possible that this is a consequence of the modelling. For both galaxies, we used exactly the same approach, adopted the same assumptions and used the same data as input. Moreover, the FitSKIRT fitting of radiative transfer models to the optical images in both cases resulted in fits of similar (and satisfactory) quality. One aspect that is different, though, is the different angular size of the galaxies.

IC 4225 is the smallest galaxy, in angular size, of the sample studied in DG14. As a result, some of the parameters in the model were not constrained as well as for most of the other galaxies. In particular, the derived intrinsic properties of the dust disk in IC 4225 are rather exceptional: the dust disk scale length retrieved is approximately 10 kpc, which is especially large when compared to the more moderate stellar disk with a scale length of 3.4 kpc. However, when using the uncertainties on the derived parameters from optical modelling, the model with the highest FIR output is just within range of the observed values.

NGC 5166, on the other hand, is one of the largest galaxies in the sample, and the recovered star–dust geometry is more in line with the average results of other studies of edge-on spiral galaxies (Xilouris et al., 1999; Bianchi, 2007). While this difference in apparent size and hence resolution might be partly responsible for the different results, it remains strange that NGC 5166 shows hardly any FIR/submm excess. Indeed, this is the galaxy with the most "regular" star–dust geometry, and one would expect that this galaxy would show a FIR/submm excess as most other "regular" edge-on spiral galaxies. The main difference between our analysis, compared to previous work on other edge-on galaxies, is a more self-consistent radiative transfer modelling in the optical, since we fit our models to multiple bands simultaneously. Whether or not this is an important aspect remains to be investigated.

While we have modelled both galaxies in the same way, it is not impossible that these two systems are intrinsically different. One of the possible FIR sources not included in our modelling is the emission coming from obscured star forming regions. A part of the younger stellar population is deeply embedded in dense dust clouds and therefore does not contribute significantly to the observed UV. Indeed, as shown in De Looze et al. (2012a), obscured star forming regions can add significantly to the observed FIR emission. A different ratio of obscured versus unobscured star formation in IC 4225 and NGC 5160 might also partly contribute to the observed differences. While it is possible to reproduce the entire SED for both galaxies, for example by adding HII-region template from the Groves et al. (2008) library, the degeneracy in the parameters is too large to gain valuable insights.

The main conclusion of our investigation is that, instead of gaining more insight in the driving mechanism for the dust energy balance problem, we seem to find that the problem might be more complex than anticipated or hoped for. If we want to get a more detailed insight in the mechanisms involved in the dust energy balance, it is necessary to perform this panchromatic radiative transfer modelling on a larger scale. Up to now, such modelling has almost exclusively been applied to individual galaxies, with different models, assumptions and codes making the comparison or search for correlations essentially impossible. A uniform modelling effort on a larger sample of edge-on galaxies would be highly desirable.

One necessary tool for such an effort is the availability of radiative transfer fitting codes that can efficiently search large parameter spaces and work semi-automatically; the work by DG14 demonstrates that this is nowadays possible. Another crucial ingredient is obviously the availability of suitable targets. Excellent catalogs of edge-on spiral galaxies are available nowadays (Kautsch et al., 2006; Bizyaev et al., 2014), and the fact that relatively large areas of the extragalactic sky have been observed with *Herschel* in the frame of projects such as H-ATLAS opens possibilities.

The combined HEROES (Verstappen et al., 2013) and NHEMESES (Holwerda et al., 2012a) samples contain 19 nearby edge-on spiral galaxies that have been observed with PACS and SPIRE. These galaxies are the ideal candidates for a follow-up study as they have a spatial resolution that is an order of magnitude better than the two galaxies studied here. We are currently collecting the necessary optical data to start the modelling of this sample.

Apart from systematically modelling larger sets of edge-on spiral galaxies, there are other options that need further exploration. One interesting option is looking at face-on spiral galaxies (De Looze et al., 2014). In this case, smaller scale structures remain present in the observations instead of getting smoothed out over the line of sight. The disadvantage of this approach is that there is no direct analogue for the dust lanes in edge-on spiral galaxies, by which the dust mass can be estimated. Additionally, because of the lack of information on the vertical distribution, assumptions have to be made which are based on results from the study of edge-on spiral galaxies.

Another necessary follow up study is the influence of the assumed dust model on our models. While it is clear that changing the dust opacities and grain composition might not change the difference between both galaxies extremely, the overall influence of the made assumptions on the global SED was not investigated.

Finally, a different path that needs further inspection is modelling of mock observations using radiative transfer simulated galaxies. The use of artificial data, in which the intrinsic properties are known and compared to those obtained after the radiative transfer modelling, can yield interesting clues on biases or systematic effects in the modelling. The pioneering work by Misiriotis et al. (2000) and Misiriotis and Bianchi (2002), who investigated the effects spiral arms and a clumpy ISM respectively, was still based on relatively uncomplicated toy models.

A more advanced option is using the results of 3D hydrodynamical simulations, which have managed to produce more realistic spiral galaxies in the past few years (e.g., Guedes et al., 2011; Renaud et al., 2013; Marinacci et al., 2014; Schaye et al., 2015). Our initial results based on applying FitSKIRT to two of these models seems to suggest that the complex and inhomogeneous dusty medium in spiral galaxies could "hide" significant amounts of dust (Saftly et al., 2015). One aspect, very rel-

evant for the present study, that could also investigated using such models is the role of resolution in radiative transfer modelling. Given the various strengths and weaknesses of each these approaches, pursuing all three options might be the best approach to gain a conclusive answer on the driving mechanisms causing the dust energy balance.

Other applications 6

While FitSKIRT has been mainly applied to fitting models to edge-on spiral galaxies, some other cases were investigated too. In the first section we briefly discuss some other applications of the FitSKIRT code. For some cases we discuss the possible implications on the dust energy balance discussed in previous chapter. The final section is reserved to describe a few possible, future additions to this work.

6.1 FitSKIRT applications

6.1.1 The edge-on spiral galaxy NGC 5908

Two of the galaxies modelled in Chapter 4 could not be accurately described by our model. This model consisted of a double exponential disk for the dust and stellar disk. The bulge was modelled by a 3D distribution which, in projection, results a Sérsic profile. As can be seen in Figure 4.2, the residuals for NGC 5908 clearly show a ring like feature. This is not uncommon in spiral galaxies, as for example in the Andromeda Galaxy (Smith et al., 2012c; Viaene et al., 2014) and the Sombrero Galaxy (Gadotti and Sánchez-Janssen, 2012; De Looze et al., 2012b). In order to provide a more accurate description of the optical images, FitSKIRT was used with a new model with the dust distributed a ring described by

$$\rho\,(R,z) \;=\; A\; exp\left[-\frac{(R-R_0)^2}{2w^2}\right] exp\left[-\frac{|z|}{h_z}\right] \tag{6.1}$$

This ring geometry contains four free parameters that define the dust distribution in our model. The R_0 is the ring radius while w describes the radial dispersion. h_z, similar to the value used for the exponential disk, is the vertical scale height. The final parameter, A, is the normalisation parameter related to the total dust mass. This model only adds one additional free parameter compared to the model used in Chapter 4. However, it was found that using only this geometry to describe the dust distribution, the best fitting ring was smeared out over a large distance. Consequently, the residuals again showed a clear ring-like feature. As this model

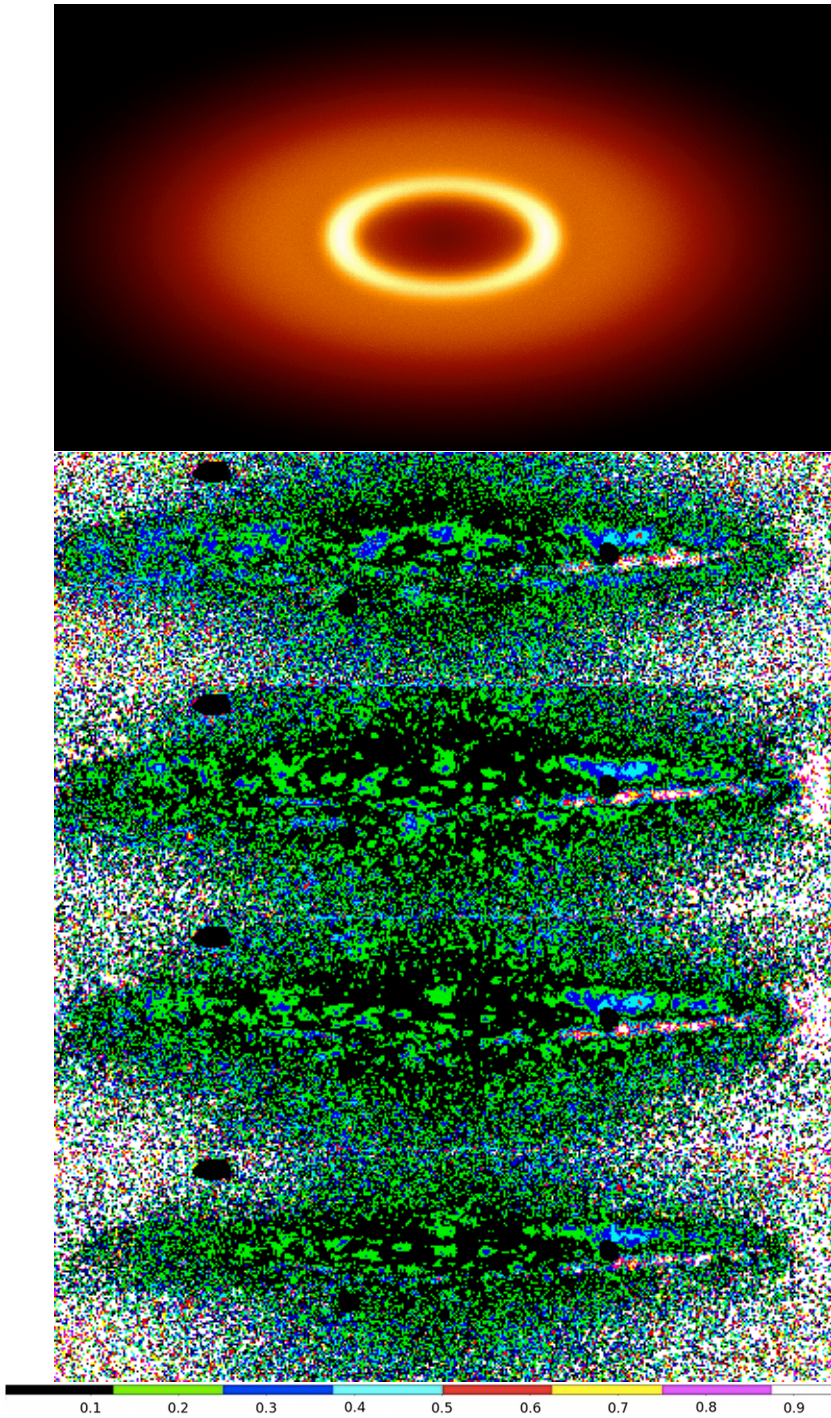

Figure 6.1: Top panel: The superposition of two ring geometries seen at an inclination of 60 degrees. One rings is acting as an extended disk with a central cavity and one ring describes a local over-density. Bottom panel: The residuals between observations and the model using two rings to describe the dust geometry in NGC 5908.

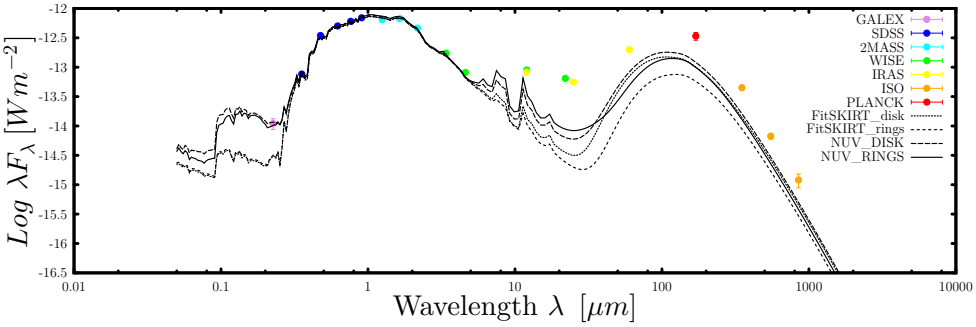

Figure 6.2: The observed fluxes and SED obtained for the models using a disk and two rings with and without a younger stellar component. The FitSKIRT lines are the models that do no include a younger stellar component. The NUV models are the same models but with an additional component to account for the the younger stellar population in the galaxies. The last ones are constrained by the GALEX NUV flux.

included a second dust ring, an additional four free parameters are added to fee parameters. We find that a model using two rings, one ring operating as an extended disk with a central cavity and another, narrower, ring describing the over-density, significantly increases the quality of the fits. An example of how the superposition of two rings looks like is shown in the top panel of Figure 6.1.

Comparing between Figure 4.2 and the bottom panel of Figure 6.1, it is clear that the model with two rings provides a more adequate description. Although a ring-like shape feature is still present in the residuals, in this case it is not present over the entire extent of the galaxy and, most likely, the result of an intrinsic asymmetry. It should be noted that one ring is so extended, the combination of an exponential disk and a small ring to describe the over-density might also be a valuable option. Therefore, as this models has more free parameters than the original model, it should come as no surprise that the fit is better. Nonetheless, this central cavity in our new model might be more realistic and seems to provide a better fit of the inner regions as well. Modelling this with an exponential disk, which reaches a maximum optical depth in the center, is simply not feasible. Of course, this investigation is only possible in galaxies that are inclined slightly less than edge-on. It could be that more galaxies in our sample are actually better described by our second model than the model used in Chapter 4 but are too edge-on to be noticeable. In particular, the models with a small radial scale length for the dust disk could in reality be over-dense rings.

Additionally, these *wrong* fits might be a possible explanation for the observed dust energy balance problem discussed in Chapter 5. We use the same approach as used before and compare the resulting SED from a panchromatic radiative transfer simulation for both models. The first model is the best fit we found in Chapter 4 and

we make the same assumptions for the remaining parameter as used in Chapter 5. We immediately take into account the younger stellar component, constrained by the NUV flux. In case of the two ring model, we assume the younger stars to be present in both rings with a luminosity divided proportionally to the dust mass in each component. The FitSKIRT lines are the models which do no include a younger stellar component. The NUV models are the same models but with an additional component to account for the the younger stellar population in the galaxies. The last ones are constrained by the GALEX NUV flux. As can be seen from Fig. 6.2, the model with a double-exponential disk and the two-rings model result in very similar SEDs and both fail to reproduce the observed far-infrared fluxes. Therefore, misclassification of dust rings as dust disk seems to have no significant effect on the predicted far-infrared emission and can not even partially explain the far-infrared deficit found in many dust energy balance studies. However, this is just a solitary case and applying a similar approach might provide more insight into this matter. Studying a larger sample might also reveal wether the galaxies with a relatively smaller dust disk compared to the stellar disk are, in fact, galaxies with a ring structure.

6.1.2 Large edge-on spiral galaxies from the HEROES sample

Perhaps the most straightforward follow-up study for the work presented in this thesis is the application of FitSKIRT to the HEROES galaxies (Verstappen et al., 2013). HEROES, an acronym for HERschel Observations of Edge-on Spirals, is a sample of seven massive, nearby edge-on spiral galaxies. Due to their proximity, the optical observations have a significantly higher resolution than the sample studied in Chapter 4. In addition, all of them have been observed separately with both PACS and SPIRE, allowing for a more in-depth study of both the warm and cold dust content. Their FIR morphologies have been studied in Verstappen et al. (2013) and were compared to morphologies estimated from optical bands in other studies. In Figure 6.3 we can see the V-band image, PACS and SPIRE observations of NGC 4013, all on the same physical scale. It should be clear that, when comparing with Figure 5.2 and Figure 5.3, the FIR image contain more information than was the case in the two galaxies studied in Chapter 5.

However, the optical models compared to were a combination of results from different radiative transfer codes, optimisation methods, etc. As was shown in Chapter 3, the inverse radiative transfer fitting results may vary among different modelling methods. As a possible improvement, FitSKIRT models could be used to provide a more unbiased, systematic way of defining the best fitting model to optical bands. Additionally, as FitSKIRT fits to a set of images, a more detailed set of models can

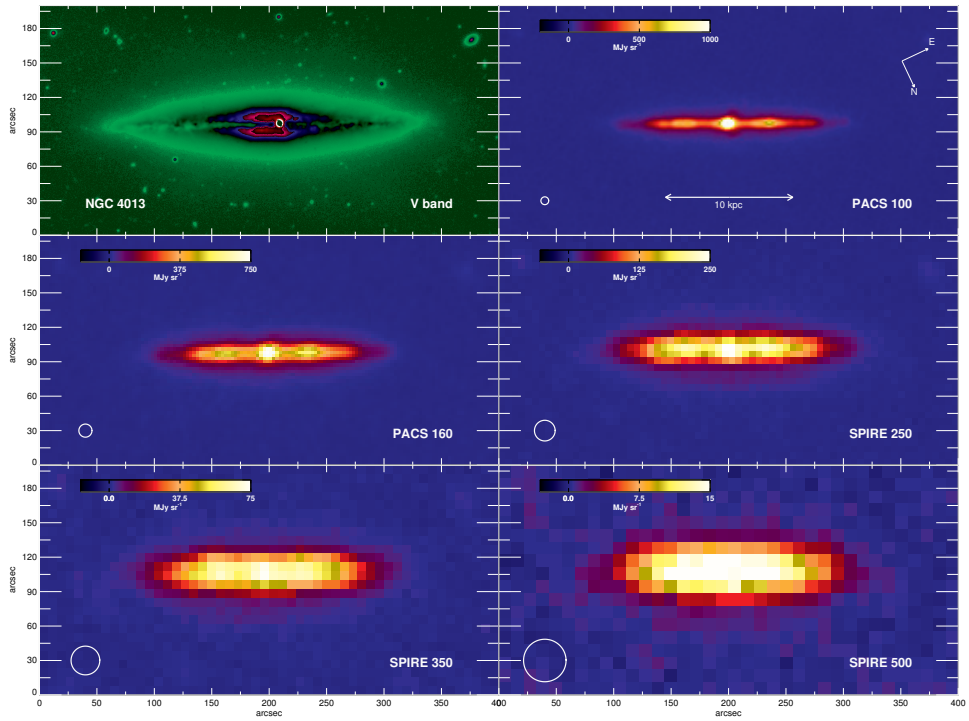

Figure 6.3: V-band image,PACS and SPIRE bands of NGC 4013, one of the galaxies from the HEROES sample (Verstappen et al., 2013).

be constructed. As a possible ansatz for this study, we provide a fit to the seven galaxies in the exact same way as the sample in Chapter 4 was modelled. Figure 6.4 shows the results of the observations (left), the best fitting models (middle) and the residual frames (right) for all HEROES galaxies. All galaxies were fitted by constraining the u, g, r, i and z band, apart from IC 2531 and NGC 5529, were B, V, R band and g, r, i and z band were used respectively. It is clear that, in first order, most galaxies are fitted reasonably well. In particular the fit for UGC 4277, is remarkably accurate considering the large resolution of the image and the simplicity of our model. On the other hand, four galaxies, NGC 4013, IC 2531, UGC 2048 and NGC 5529, have a clear peanut/boxy shaped bulge. This is not present in our models and results in the typical butterfly-shaped residuals. This is considerably more than what was observed in the sample of 12 edge-on spiral galaxies investigated in Chapter 4. The most likely possibility is that the increased resolution in this sample makes the peanut shape more clear. In Section 6.2.1, we continue the discussion on peanut shaped bulges.

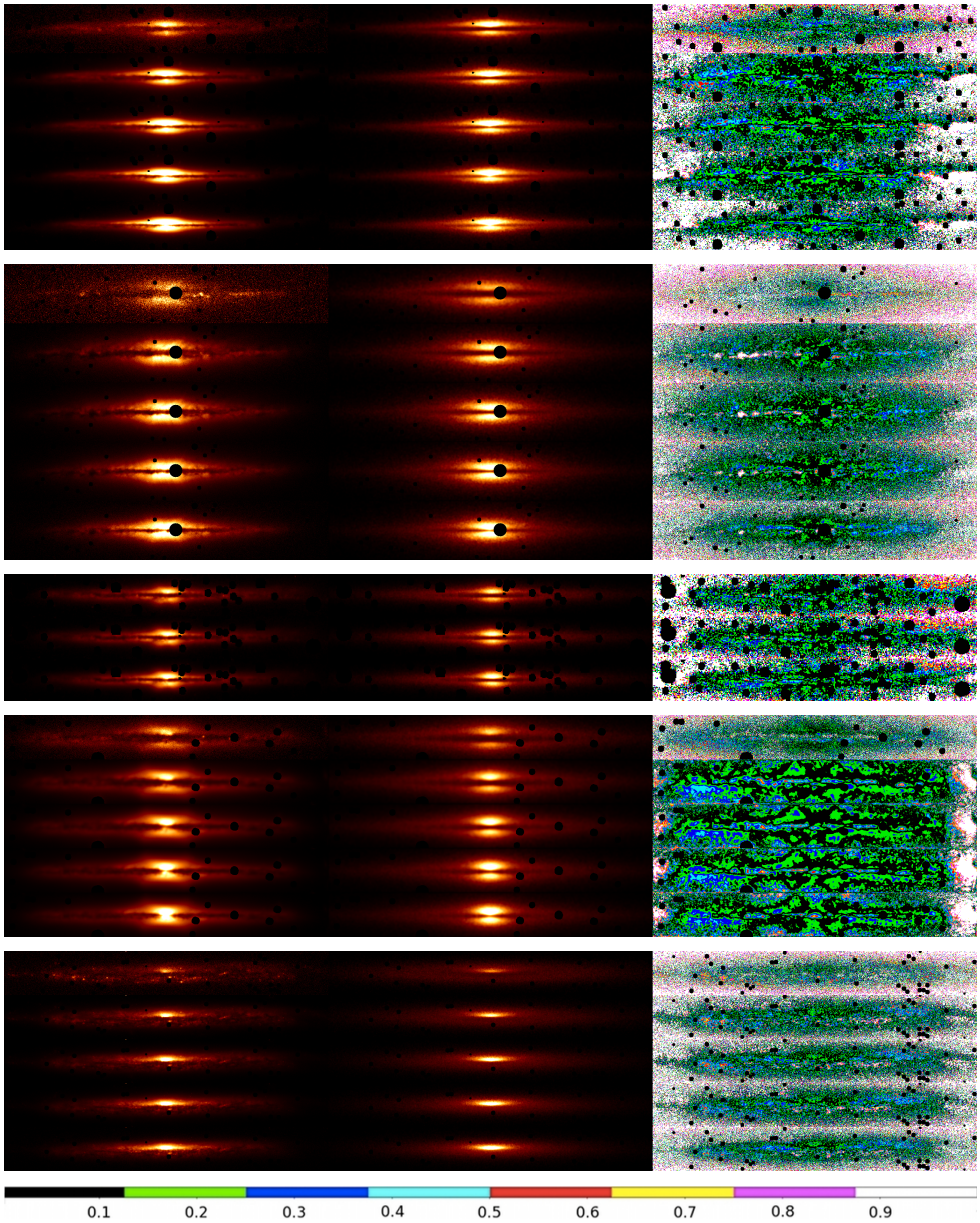

Figure 6.4: Results of the oligochromatic FitSKIRT radiative transfer fits to the HEROES galaxies. Top to bottom UGC 4277, NGC 4013, IC 2531,UGC 2048, NGC 5907, NGC 4217 and NGC 5529 respectively. IC 2531 was fitted to B, V and R band images while the other two were fitted to SDSS data u, g, r, i and z band respectively from top to bottom. Only NGC 5529 was not fitted to u-band image as this was too noisy to be used in our fitting method.

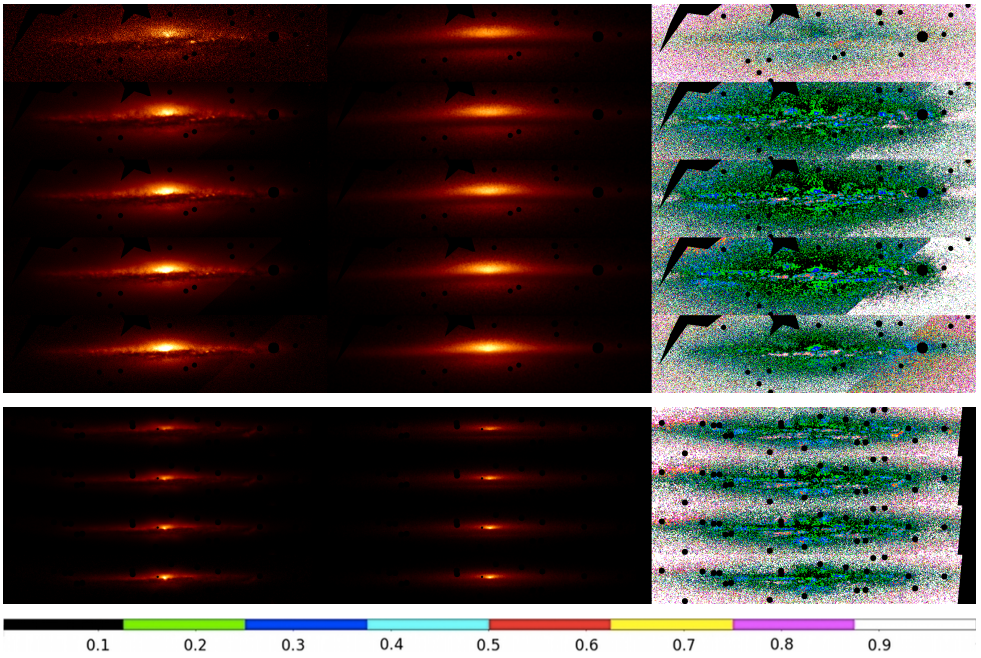

Figure 6.4: (continued)

The best fitting values and uncertainties of our fits are presented in Table 6.1. A striking result is that for five out of the seven galaxies, we find a dust disk that is smaller than the stellar disk. Again, this is considerably more than we found in the previously studied sample. A possible explanation for this is again the increased resolution. In fact, due to the χ^2 function favouring higher value pixels, any increase of observed luminosity along the dust lane forces the fitting mechanism to truncate the dust disk at that position. As the dust disk itself is not clumpy and, by definition, low intensity, we always get a lower scale length due to irregularities. This should not be confused with the degeneracy between a dense, small or a large, more opaque dust disk discussed in Section 3.2. Here we have a degeneracy due to the intrinsic irregularity of the galaxy present at every wavelength, while the latter was a wavelength specific problem which could primarily be solved by including more observations in the fitting routine.

In order to test that it is indeed the smaller scale structures that cause the radial scale length of dust disk to be truncated too soon, these galaxies could be modelled at different resolution. In fact, if the small scale structures are responsible, rebinning the frames to a lower resolution would yield larger scale lengths for the dust disk as the main irregularities get smoothed out.

Parameter	unit	UGC 4277	NGC 4013	IC 2531	UGC 2048	NGC 5907	NGC 4217	NGC 5529
$h_{R,*}$	kpc	10.34 ± 0.25	3.66 ± 0.48	10.37 ± 0.32	9.68 ± 0.19	3.56 ± 1.05	3.41 ± 0.53	8.20 ± 0.22
$h_{z,*}$	kpc	0.96 ± 0.06	0.80 ± 0.31	1.06 ± 0.05	1.75 ± 0.02	0.33 ± 0.65	0.22 ± 0.14	0.40 ± 0.02
$R_{\rm eff}$	kpc	6.42 ± 1.22	1.46 ± 1.07	2.69 ± 0.08	2.13 ± 0.12	1.73 ± 0.77	5.64 ± 1.45	6.65 ± 0.25
n	—	5.8 ± 0.7	3.4 ± 0.4	0.8 ± 0.1	1.4 ± 0.1	2.6 ± 0.8	1.9 ± 0.7	2.67 ± 0.25
q	—	0.33 ± 0.02	0.32 ± 0.01	0.60 ± 0.02	0.50 ± 0.01	0.15 ± 0.03	0.33 ± 0.01	0.32 ± 0.02
$h_{R,\rm d}$	kpc	8.57 ± 1.47	1.78 ± 0.61	3.71 ± 0.48	4.92 ± 0.23	2.64 ± 2.17	7.68 ± 2.63	11.47 ± 0.44
$h_{z,\rm d}$	kpc	0.32 ± 0.04	0.17 ± 0.03	0.14 ± 0.02	0.38 ± 0.01	0.07 ± 0.20	0.34 ± 0.05	0.18 ± 0.03
$M_{\rm d}$	$10^7\ M_\odot$	7.4 ± 0.5	9.6 ± 1.9	3.3 ± 2.6	5.5 ± 2.4	9.0 ± 8.7	5.7 ± 1.7	10.0 ± 0.7
i	deg	88.6 ± 0.2	89.6 ± 0.1	87.9 ± 0.2	88.5 ± 0.1	85.3 ± 0.63	87.4 ± 0.5	85.4 ± 0.1

Table 6.1: Results of the oligochromatic FitSKIRT radiative transfer fits to the HEROES. For each galaxy we list all physical free parameters with their 1σ error bar as determined by FitSKIRT. For the meaning of the different parameters and determination of the error bars, see Sect. 4.3.1 and/or Sect. 3.1 from De Geyter et al. (2013).

In addition to this test, more complicated models could be used to model these galaxies. Given their superb angular resolution, more information is present to constrain more advanced models including bars, spirals, peanut bulges, clumps, etc. This, however, falls beyond the work and goals of this thesis. The models provided here could be used as a starting point for more accurate fits. Additionally, this sample could be used to extend the sample of two galaxies studied in Chapter 5. Not only would the new models provide more detailed description of the optical fits, the FIR observations contain more structure and could be compared to the simulated frames predicted by a panchromatic radiative transfer.

6.1.3 The dusty early-type galaxy NGC 4370

In Chapter 2 we have described how the FitSKIRT code was constructed in such a way that a variety of models could be constrained, given that the reference images contain adequate information. However, the method was mainly tested and applied on edge-on spiral galaxies as it was originally constructed for this specific case. Here we investigate NGC 4370, a galaxy with a clear dust lane, which is slightly peculiar given that is an early-type galaxies.

Little is known about the dust content of the early-type galaxies. In particular, it is not clear whether they possess a diffuse dust component beside the dust concentrated in optically visible dust lanes and patches. The existence of such an additional diffuse dust component was postulated to compensate for the relatively small dust masses estimated from UV/optical images compared to the dust mass determined from FIR emission.

In Viaene et al. (2015) several methods to estimate the dust from optical images are applied in NGC 4370. Among them is the use of FitSKIRT to determine the best fitting models for a disk and ring geometry to a set of optical observations. Figure 6.5 shows the observations (left), the best fitting model, in this case a ring geometry (middle) and the residuals (right). The stellar distribution is first determined by using a multi-gaussian expansion on the images, while masked the dust lane. This allows for a fast and very accurate results and effectively decreases the size of the free parameter space. FitSKIRT is then used to determine the best fitting dust model in combination with this fixed stellar component. The best fitting dust mass found by FitSKIRT is considerably higher than what is found using and more traditional, empirical methods, and more in line with the mass estimates based on FIR flux densities. As possible explanations for this are the overly simplistic star-dust geometries and the neglect of scattering effects in the latter case. This study strongly shows the need of an actual inverse radiative transfer code. Viaene et al. (2015) conclude that there is no need for a diffuse dust component to explain the observed FIR/submm fluxes in NGC 4370.

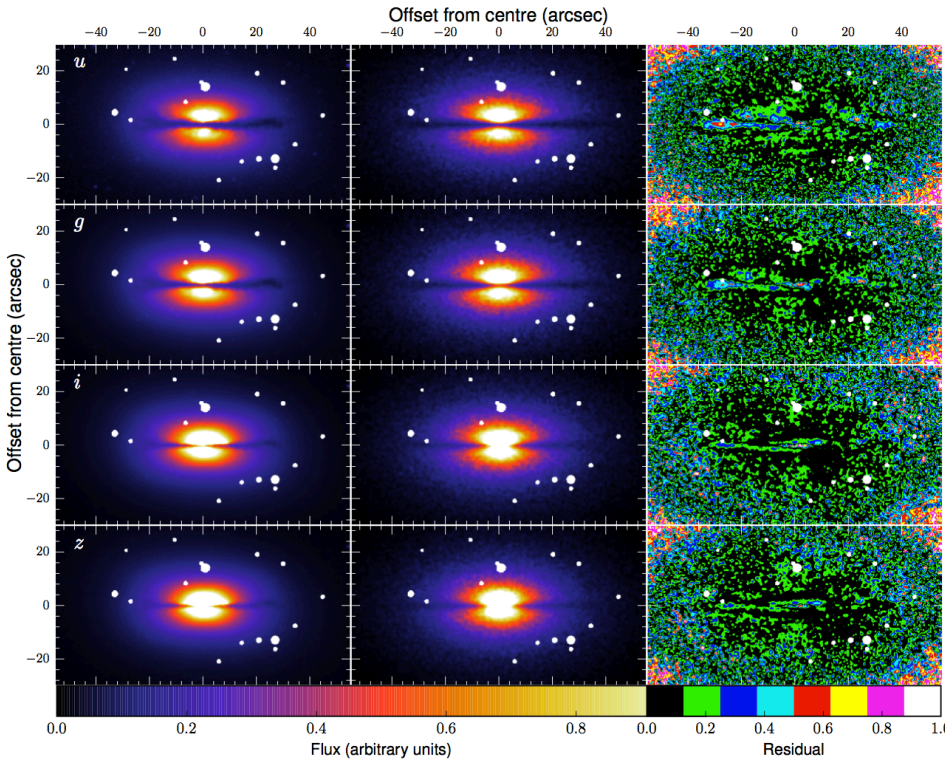

Figure 6.5: FitSKIRT model results for the ring dust geometry. Left column are the observations, with masked out foreground stars. Middle column are the corresponding model images. The residuals are shown in the right column.

6.1.4 Mock galaxies from hydrodynamical simulations

As a completely different but interesting application, FitSKIRT was also applied to model the output of hydrodynamical simulations. As briefly discusses in Section 5.3, modelling these galaxies has the advantage that intrinsic information is known and, contrary to our other artificial galaxies, they have more realistic small and large scale structures. Saftly et al. (2015) studies two galaxies, shown in Figure 2.8.

One galaxy (ERIS) is modelled using a smoothened particles hydrodynamics code (ERIS) (Guedes et al., 2011) and is one of the most advanced and realistic simulations of the formation of a Milky Way class galaxy. Eris was set up as a zoom-in cosmological simulation, powered by the N-body/SPH GASOLINE code. The simulation includes gravity, hydrodynamical forces, Compton cooling, atomic cooling, metallicity-dependent radiative cooling at low temperatures, the ionising effect of a uniform UV background, star formation and supernova feedback. The simulation box used in our case has 7.8 million star particles and 0.25 million gas particles, with a total stellar mass of $3.5 \times 10^{10}\ M_\odot$ and a total gas mass of $4.3 \times 10^{9}\ M_\odot$ (about $5 \times 10^{3}\ M_\odot$ per star particle and $2 \times 10^{4}\ M_\odot$ per gas particle). The smoothing length of the gas particles ranges between 56 and 2455 pc.

The other galaxy (RT13) is a self-consistent hydrodynamical simulation of a Milky Way-like galaxy performed with the Adaptive Mesh Refinement (AMR) code RAMSES (Renaud et al., 2013). The focus of this simulation was to get the structure of the interstellar medium at the highest resolution possible and less on the cosmological aspects of the formation of this isolated grand-design galaxy. The simulation resolves the structure of the interstellar medium at sub-parsec resolution of 0.05 pc, and includes stellar feedback through photo-ionisation, radiative pressure and supernovae.

First the radiative transfer code SKIRT was used on these simulations to create a set of u, g, r, i and z band images while the galaxy is inclined at 90 degrees. In a second phase, we modelled these mock images with FitSKIRT in exactly the same way as we have done for real galaxies throughout this thesis. The best fitting FitSKIRT model for these galaxies are shown in Figure 6.6. Although FitSKIRT is able to provide adequate reproductions of the images, the recovered dust mass is about an order of three lower than the actual total dust mass in these galaxies. This is about the same as found in IC 4225 studied in Chapter 5 and also found in other edge-on spiral galaxies. FitSKIRT was also tested to fit two artificial, quasi-analytical models, one including a spiral and one including a clumpy dust component. In these cases, FitSKIRT was able to reproduce both the images as well as the input parameters. Consequently, it seems that these quasi-analytical models are still far away from the complexity of the star-dust geometry in real galaxies. Therefore it

seems that the asymmetries and small scale structure of real and hydrodynamical simulated galaxies are a lot more efficient at "hiding" dust than the rather contrived geometries in analytical models.

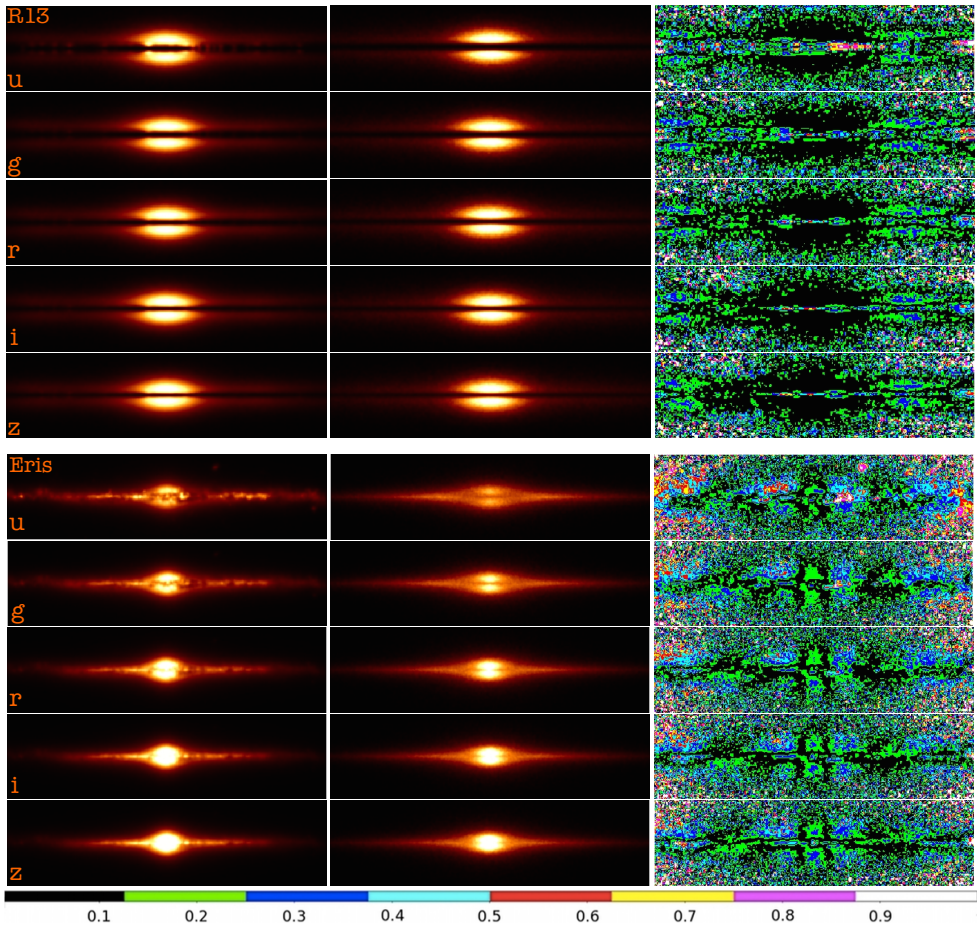

Figure 6.6: Results of the FitSKIRT radiative transfer fits for the R13 galaxy, looking at the head of the bar (upper half), and for the Eris galaxy (lower half). The left column shows the reference images produced by SKIRT in each of the u, g, r, i, and z bands. The middle column shows the corresponding fit obtained with FitSKIRT. The right column contains residual images showing the relative deviation between the fit and the reference image. The colour bar at the bottom presents the scale of the deviation in the residual images.

As for some galaxies, for example NGC 5166 investigated in Chapter 5, the dust mass recovered by FitSKIRT is in the same order, it seems that the quiescence of galaxies plays an important role. It might be that for complex, more perturbed galaxies, the edge-on projection smooths out too much relevant information in order to get a global picture of the dust content from extinction effects only.

6.1.5 Irregular edge-on galaxies

In Peters et al. (2013), the HI observations of a sample of eight edge-on spiral galaxies are presented. The goal of this project is to study the shape of the dark matter halo surrounding these galaxies by comparing the observed and the theoretical HI and stellar kinematics. Apart from IC 2531, which is also present in the HEROES sample, most galaxies have no clear dust lane and/or are have a more irregular shape. FitSKIRT was applied to these galaxies with a similar model as used in Chapter 4. In most cases an adequate fit was found, in some cases by fitting the left and right side of the galaxies separately to deal with asymmetries. Especially the fit for UGC 7321, by far the most regular one of the sample, is particularly good. In Figure 6.7, the best fitting FitSKIRT model for UGC 7321 to the I, J, R and wise1 (3.4 μm) bands is shown. Each band consists of three panels: the observations (top), the best-fit models (middle) and the residual maps (bottom). It has to be noted that, since this galaxy has no visible dust lane and the bands used are not very prone to dust extension, only the stellar parameters for fit should be trusted. The results and best fitting parameters of the entire sample can be found in Peters (2014).

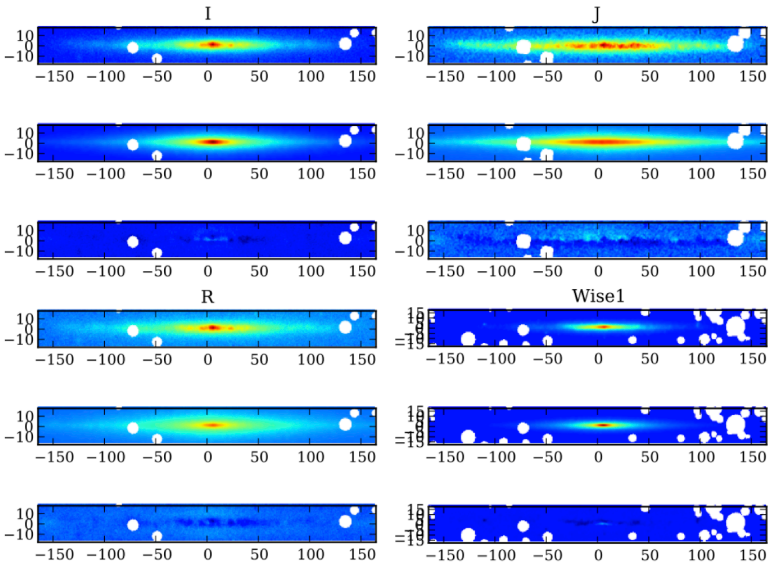

Figure 6.7: Stellar decompositions for UGC 7321. Each band consists of three panels: the observations (top), the best-fit models (middle) and the residual maps (bottom). The colour scaling is equal between the three panels. The scale of the images is in arcsec. Taken from `http://dissertations.ub.rug.nl/faculties/science/2014/s.p.c.peters/`.

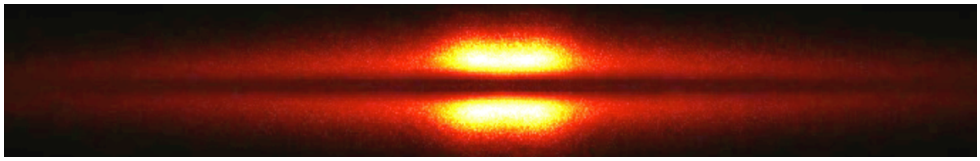

Figure 6.8: Model for a peanut shaped bulge using two identical Sérsic bulges to provide the peanut shape and one Sérsic to describe the central bulge.

6.2 Future improvements

6.2.1 Peanut/Boxy bulges

A possible improvement to our fits, especially in the light of the observed relation between the relative scale height of the dust and stars and the bulge-to-disk ratio described in Section 4.5.3, would be to include a more accurate model of peanut/boxy bulges. For face-on galaxies the combination of a Sérsic profiles and an exponential disk is able to accurately describe the separate components, bar/bulge/disk. A basic model was constructed, shown in Figure 6.8, with two identical Sérsic bulge, as described in Section 4.3.1, to provide the peanut shape and one Sérsic to describe the central bulge. However, as visually this might seem like an accurate representation, fitting to galaxies with a peanut shape bulge, like IC 2531, did not provide an adequate fit. In fact, while the shape of the bulge might be similar the intensity profile in the vertical direction is, in reality, quite different. In order to come up with a more advanced model, a future work might be to come up with a (semi-)analytical model from stacking all stellar orbits as found by hydrodynamical simulations (Athanassoula, 2008). Once such a model is found, it might be worthwhile to revisit the HEROES and/or sample investigated in Chapter 4 to get a more accurate view on the relation between the relative disks heights and the bulge-to-disk ratio. This, however, falls beyond the work and goals of this thesis.

6.2.2 Spiral arms and clumpiness

In Saftly et al. (2015), FitSKIRT was used to model two sets of mock images with the same parameters as the test case modelled in Chapter 3. However, here one set included a spiral arm geometry and one set included a clumpy dust component. In both cases it was found the FitSKIRT was able to recover the original parameters, regardless of the added complexity. While it was shown that using this geometry did not solve the underestimated dust mass, the model did describe the galaxies quite accurately. FitSKIRT could therefore be used to study a sample of galaxies and study the impact of the spiral arms structure. While it was shown in Misiriotis et al. (2000) that the regular exponential distribution is a good first-order approximation,

some galaxies might be modelled considerably better by adding spiral arms.

In Figure 6.9, we show the residuals of the best fitting models found using FitSKIRT by fitting to an R-band image of NGC 891. One fit shows the results of a fit using only an exponential disk (top) while the other shows the model with added spiral arms (bottom). While the center might be more accurately described by the simple model, the overall quality (and χ^2 value) is slightly improved with a spiral arm geometry. However, this is only the first step of a possible study as the R-band is not heavily influenced by the spiral arm geometry (in this case it was chosen for its high angular resolution). Indeed, when looking at Figure 1.3, the bluer bands show the asymmetry more clearly. The left part is bluer, since the star forming regions are slightly more visible, while the right side is more attenuated. Using FitSKIRT to fit to a range of images of NGC 891 might constrain the model even better and provide a clearly more appropriate fit than using a regular exponential disk.

In addition, if including the GALEX FUV and NUV, in the sample, the model could be used to study the existence of diffuse extraplanar dust. Indeed, starlight scattering of dust grains would results in extended emission in these bands (Seon et al., 2014). As scattering is so important in this case, an inverse 3D radiative transfer method would be crucial in constraining this diffuse component from a set of observations.

FitSKIRT could also be used to constrain a clumpy model. In this cade, however, one has to think of a way to compensate for the randomness of the clumps as well. In fact, the large variation in clump sizes creates an extra difficulty in the comparison between reference image and model. Schechtman-Rook et al. (2012) have investigated NGC 891 using a spiral arm geometry and a fractal dust distribution. In this case shape let analysis and genetic algorithms were used to determine the 30 best statistically fitting models. A similar technique could be implemented in FitSKIRT so that a larger sample of galaxies can be studied. In this way the effect of quiescence on the dust energy balance could also be studied more quantitatively and in an unbiased, systematic way.

6.2.3 Different optimisation techniques

As already mentioned in Chapter 3, a future improvement would be to include a different optimisation technique. These methods should at least have the following three properties: a global optimisers that can handle degeneracies, it should contain noise handling capabilities and preferably computationally feasible (albeit by parallelisation). The most obvious is to look within the same class of population based, (meta)heuristic optimisation methods like ant colony (Colorni et al., 1991) of particle swarm optimisation (Kennedy, 2010). As they are less commonly

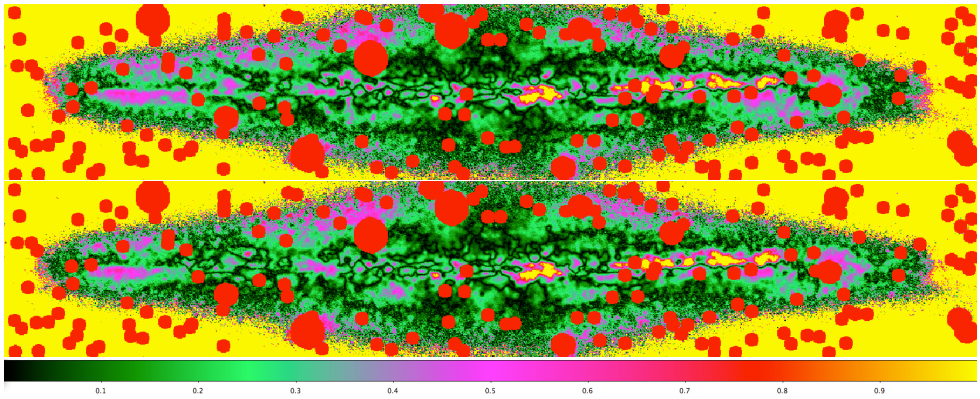

Figure 6.9: Residuals of the best fitting model found using FitSKIRT by fitting to an R-band image of NGC 891. The top image shows the best fitting model for a regular exponential disk. The bottom image shows the best fitting exponential disk with an added spiral arm geometry.

used they have the disadvantage that their mechanisms are even more poorly understood than genetic algorithms. However, for some specific cases they can yield significantly better results. As they are population based, they possess the same advantages concerning parallelisation and noise handling. However, as is the case for genetic algorithms, they lack a clear way to determine the uncertainty on the derived fit.

A possible promising approach is to use a Bayesian nested sampling method (Skilling, 2004; Corsaro and De Ridder, 2014). They are the population based equivalent of the commonly used Monte Carlo Markov Chain (Andrieu et al., 2003) and generally result in more stable convergence towards the global optimum. This method also has the advantage that the error is more naturally determined from the fit without the loss of the advantages of genetic algorithms. However, in most cases, the method is computationally more demanding to get to the same level of best fit as genetic algorithms. However, as in our case determining the error also leads to additional function evaluations, this options is surely worth looking into.

The methods described above, could potentially improve the speed of the code by a few factors (very optimistic) but not but a few orders of magnitude. This is because the function evaluation still requires a full radiative transfer simulation. A more drastic improvement could therefore be to somehow skip this step. This could for example be achieved by learning an Artificial Neural Network by the means of a huge database of radiative transfer models (slightly similar to what was done for GRASIL (Silva et al., 2012)). Although the creation of such database would require a huge computational effort as well, once it is there it could speed up the fitting precedes by several orders of magnitude, consequently improving the sample size

that could be modelled. However, this approach is not so straightforward as it seems. As the library is predefined, the frames will naturally have a different pixel scale then the reference image. Rescaling these images becomes even harder as also the distances to the observed target and the simulated target might differ. While it is clear that this approach requires some effort, the reward for that investment might be worth the trouble. Even if the results are less accurate, it could provide FitSKIRT with an appropriate guess and limited parameter space it has to investigate.

6.2.4 Panchromatic modelling

Probably the most drastic improvement to the code would be the extension of the investigated wavelength range. In the present version, all wavelengths are considered to be independent;this limits the applicability to wavelengths up to NIR. In fact, as soon as dust emission becomes an important part of the simulation, this assumption is no longer valid. While it might seem straightforward to include dust emission in the radiative transfer code and compare the images with observations at these wavelengths, the fundaments of the code would have to be adjusted significantly. For example, the luminosity fitting can no longer be handled separately as the linearity between luminosity and observed intensity in the final frames is no longer guaranteed. While it is easy to just assume a stellar population and use the luminosity as one additional parameter in the genetic algorithms optimisation, the results on the χ^2 definition are far greater. Because we can no longer fit the luminosity of the separate components and wavelengths, all images would have to be calibrated to the exact output units of the radiative transfer code in order to get the correct luminosity. As a result, the reference frames can not be normalised and the guarantee of uniform fitting is lost. Additionally, as FIR observations are usually orders of magnitude less resolved than the optical counterparts, rebinning all frames to the same resolution in order to get a more uniform fitting would results in significant information loss. On top of this, dealing with an entire panchromatic simulation for all χ^2 function evaluations is also at least an order of magnitude more demanding computationally. This could potentially be solved by combining it with the intelligent library approach as described in previous section so that the full radiative transfer simulation is estimated rather than completely modelled.

While none of these problems might be impossible to deal with, it is clear that it is far from a small adjustment but rather a significantly new approach. On the other hand, the reward could potentially be worth the trouble. Not only would we be able to fit the entire SED of galaxies with an complete radiative transfer model, we would also constrain the observed images.Using such a tool would be a great step forward to what is currently available. Simultaneously constraining both the geometry and the fluxes from FUV to FIR using complex radiative transfer models

would be the ideal to study and gain more insight the dust content and its heating mechanisms of spiral galaxies.

Conclusion 7

The main goal of this thesis was to create a method to efficiently solve the inverse 3D dust radiative transfer problem. In particular, we have focused on modelling edge-on spiral galaxies and investigated what the results tell us about their star-dust geometry. Our efforts resulted in the FitSKIRT code, a code that optimises the output of the radiative transfer code SKIRT to a single or multiple observations simultaneously.

In Chapter 2 we start by explaining the optimisation method, genetic algorithms, we have chosen. Next we present the setup and structure of the 3D Monte Carlo radiative transfer code SKIRT. Section 2.3 explains the FitSKIRT code itself in depth. We explain the χ^2-function which needs to be minimised and how genetic algorithms can be used for this goal. The code is constructed in such a way that it can in principle be applied to a large variety of objects as it is not restricted to a specific geometry or other radiative transfer related options. We have explicitly spent some effort to implement the code such that the users is free to constrain any variety of models and free parameters as he/she sees fit.

In Chapter 3, the FitSKIRT code was applied to three specific test cases. First, FitSKIRT was used to model an artificial reference image of a dusty edge-on spiral galaxy model created by the SKIRT. The reliability of the code was evaluated by investigating the residual frames as well as the recovery of the input model parameters. FitSKIRT recovered the input parameters very well, even for the full problem in which all 11 parameters of the input model were left unconstrained. We have compared the results of genetic algorithms with two more commonly used optimisation methods, Levenberg-Marquardt and downhill simplex optimisation. We conclude that the noise handling properties together with the ability to uniformly investigate and optimise a complex parameter space, make genetic algorithms an ideal candidate to use in combination with a Monte Carlo radiative transfer code. Consequently, the FitSKIRT method was applied to determine the physical parameters of the stellar and dust distribution in the edge-on spiral galaxy NGC 4013 from a single V-band image. The values of the fitted parameters and the quality of the fit were compared to similar but completely independent radiative transfer fits done by Xilouris et al. (1999) and Bianchi (2007). The small deviations between these results can be explained by the degeneracy between the dust scale length and face-on

optical depth, and the differences in the model setup, radiative transfer technique and optimisation strategy. The third test case applies FitSKIRT to a set of artificial reference images of an edge-on spiral galaxy model, again created by the SKIRT. We conclude that the oligochromatic method yields smaller error bars on most of the fitted model parameters than the individual monochromatic models. In particular, using a set of observations allows for better distinction between smaller, dense dust disks and larger, more opaque disks.

Chapter 4 describes the application of FitSKIRT to a sample of 12 edge-on spiral galaxies, through a simultaneous fitting of the SDSS *g*-, *r*-, *i*- and *z*-band images. These were selected from the CALIFA survey in order to constrain both their stellar and dust distribution. The results of the fits to the 12 galaxies in our sample can be found in Table 4.2 while the sample averages, spread and accuracy can be found in Table 4.3. For two galaxies (UGC 4163 and NGC 5908), we find that the model, consisting of a exponential disc to describe the stellar and dust distribution and a Sérsic profile to model the central bulge, was not able to accurately reproduce the observations. In all other cases we are able to model the galaxies and constrain the parameters to an acceptable accuracy. We find that the average disk scale length and intrinsic disk flattening is in good agreement with the results described by Kregel et al. (2002) and Gadotti (2009). The slightly bigger bulges in our sample can possible be explained by the fact that we do not include a bar in our model and a possible selection effect due to the necessity to have a clear dust lane while Gadotti (2009) does not take into account the effect of dust attenuation when determining the bulge parameters. The dust disks we find are in good agreement with X99 and B07. The relative size of the dust disc is twice as thin as the stellar disc and about 70% more extended radially, which is slightly larger than found by X99 and B07. However, we did not find a transition for galaxies with a rotation speed of 120 $\mathrm{km\,s^{-1}}$ where the slower rotating ones should have a dust disc scale height similar to the one of the stellar disc as suggested by Dalcanton et al. (2004). In our sample we find a large spread in the optical depth ranging from 0.18 to 1.98 with an average V-band value of 0.76 and rms spread within the sample of 0.60. As a result, a fraction of the galaxies should not be transparent even when seen completely face-on. However, due to the selection criteria our sample contains more dust rich galaxy than previous studies. The same reason would also be the explanation why we find that the galaxies in our sample reside on the higher side of the relation between the dust-to-stellar mass ratio and the stellar mass compared to the HRS sample studied in Cortese et al. (2012).

In Chapter 5, we use the results from previous chapter to investigate the so-called dust energy balance problem for edge-on spiral galaxies. We investigate two galaxies, IC 4225 and NGC 5166, which were observed as part of the H-ATLAS survey (Eales et al., 2010). We combine the new, advanced radiative transfer models with a

range of data, including PACS and SPIRE data to get constraints on both the warm and cold dust component. For both galaxies, the observed SED shows a clear FIR excess compared to a standard model that is based only optical images, and hence only contains evolved stellar populations. This is similar as what is found by various teams (e.g., Popescu et al., 2000; Misiriotis et al., 2001; Alton et al., 2004; Dasyra et al., 2005; Bianchi, 2008; Baes et al., 2010; Popescu et al., 2011; Holwerda et al., 2012b). However, things change when a young stellar population is included in the modelling: while a substantial FIR excess still remains for IC 4225, the FIR fluxes are recovered almost exactly for our model of NGC 5166. While we have modelled both galaxies in the same way, it is not impossible that these two systems are intrinsically different. One of the possible FIR sources not included in our modelling is the emission from obscured star forming regions. A fraction of the younger stellar population is deeply embedded in dense dust clouds and therefore does not contribute significantly to the observed UV. The main conclusion of our investigation is that, instead of gaining more insight in the driving mechanism for the dust energy balance problem, we seem to find that the problem might be more complex than anticipated or hoped for. If we want to get a more detailed insight in the mechanisms involved in the dust energy balance, it is necessary to perform this panchromatic radiative transfer modelling on a larger scale. One necessary tool for such an effort is the availability of radiative transfer fitting codes that can efficiently search large parameter spaces and work semi-automatically; the results published in this thesis demonstrate that this is nowadays possible.

In Chapter 6 we discuss some other past and future applications of the FitSKIRT code. One of the galaxies that could not be accurately modelled in Chapter 4, NGC 5908, is modelled again using two rings to model the dust distribution. While this provides an accurate more accurately fitted model in the optical bands, the effect on the total SED is negligible. Perhaps one of the most interesting future applications of the code is a set of 7 nearby, massive edge-on galaxies, called HEROES (Verstappen et al., 2012). We have provided fits using the same approach as used in Chapter 4 as a starting point. However, as these galaxies are an order of magnitude more extended, more complex models could be used to model the optical bands. As we have obtained higher resolution PACS ands SPIRE data for these galaxies, a more extended and rigorous analysis than was done in Chapter 5 will be possible. We also briefly describe the resuls of a set of 8 irregular edge-on galaxies that were modelled using FitSKIRT. In this set only a few galaxies had any clear extinction features. The results were used to determine the mass-to-light ratio in order to study the shape of the dark matter halo (Peters, 2014). FitSKIRT was also used to model the dust lane of NGC 4370. Contrary to the other galaxies fitted before, this is an early-type with a clear dust lane. Viaene et al. (2015) use a few different techniques to determine the dust mass from optical images and compare it to the

mass determined from FIR observations. It was shown that, apart from FitSKIRT, all techniques underestimated the dust mass showing the importance of an inverse radiative transfer code. As a completely different application, FitSKIRT was used to model a set of mock images created from hydrodynamical simulations. It was shown that, although FitSKIRT was able to provide acceptable fits to the optical images, the recovered dust mass was about three times lower than the actual value. The explanations for this discrepancy is that the small scale structure of the stardust geometry, which get smoothed out in the edge-on projection, does not actively contribute to the global observed extinction. Therefore, the use of too basic models on realistic galaxies might be an explanation for the observed dust energy balance. The last section described four possible, future improvements to the code. One is the inclusion of a new geometry to more accurately model the central bulge. In particular, the boxy/peanut shaped bulges, which were present in the galaxies modelled in this thesis, are interesting route to be studied. A second method would be to use a spiral and/or clumpy structure to model the galaxies. This would be useful to model the observed asymmetry in some galaxies. We also briefly discuss how the code could benefit from different optimisation techniques. A new technique might not only be more stable and faster, it might also more naturally incorporate the uncertainty on the derived parameters. Probably the most drastic improvement would come from the extension of the fitted wavelength range. FitSKIRT could, in principle, be adjusted to fit a wide range of observations ranging from FUV to FIR, therefore combining SED modelling with geometrical fits to the images. This, hypothetical, tool would provide incredibly useful in the more complete and rigorous study of the dust heating mechanisms in spiral galaxies.

Samenvatting

8

Het voornaamste doel van deze thesis was het ontwikkelen van een methode die op een efficiënte manier de geïnverteerde 3D radiatieve stralingsoverdrachtsvergelijkingen oplost. Specifiek hebben we ons gericht op het modelleren van spiraalstelsels die van op hun zijkant worden bekeken en onderzochten we wat we konden leren over de ster-stof geometrie. Galaxieën die op hun kant worden gezien, zoals te zien is in Figuur 8.1, hebben namelijk het voordeel dat zowel de verticale als radiale structuur zeer goed zichtbaar is. Onze inspanningen resulteerden in het FitSKIRT programma, een programma dat de output van de radiatieve stralingsoverdracht code SKIRT optimaliseerde aan de hand van één of meerdere observaties tegelijkertijd.

In Hoofdstuk 2 starten we met het uitleggen van de gekozen optimalisatie techniek, genetische algoritmen. Vervolgens tonen we het opzetten en de structuur van de 3D radiatieve overdrachtscode SKIRT. Sectie 2.3 legt op gedetailleerde manier uit hoe het FitSKIRT programma werkt. We leggen uit wat de χ^2-functie, te zien in Figuur 8.2, is die moet worden geminimaliseerd en hoe genetische algoritmen dit verwezenlijken. Het programma is op zo een manier geconstrueerd zodat het, in principe, kan worden toegepast op een hele reeks van objecten. Het is op geen enkele manier gebonden aan een specifieke geometrie of andere stralingsoverdracht gerelateerde parameters. Dit is expliciet zo gemaakt zodat de gebruiker zelf kan kiezen welke parameters hij wil modelleren met het programma.

In Hoofdstuk 3, wordt het FitSKIRT programma toegepast op drie specifieke testen. In de eerste test wordt FitSKIRT gebruikt om een artificiëel gemaakt referentie beeld van een spiraal stelsel op zijn kant te modelleren. De betrouwbaarheid van de code wordt geëvalueerd door het onderzoeken van de residu beelden en het terug vinden van de originele input waarden. FitSKIRT kan de originele waarden goed recupereren, zelfs voor het model waar we alle 11 parameters vrij laten. We hebben de resultaten van de genetische algoritmen methode vergeleken met de Levengberg-Marquardt methode en neerwaartse simplex methode. We besluiten dat genetische algoritmen door de ruisbehandelende eigenschappen en de eigenschap om op uniforme wijze de complexe parameterruimte te onderzoeken, de ideale kandidaat is om te combineren met een Monte Carlo radiatieve stralingsoverdracht code. Het

Figure 8.1: NGC 891, een nabijgelegen spiraalstelsel dat van op zijn zijkant bekeken wordt. (`http://www.feraphotography.com/AM14/pics/`)

FitSKIRT programma werd nadien gebruikt om de fysische parameters van de ster en stof distributie van NGC 4013, weergegeven in Figuur **??** te onderzoeken aan de hand van een V-band beeld. De waarden van de gevonden parameters en de kwaliteit van het gevonden model werden vergeleken met resultaten van andere radiatieve stralingsoverdracht codes door Xilouris et al. (1999) and Bianchi (2007). De kleine afwijkingen van deze resultaten kunnen worden verklaard door de ontaarding, tussen de stofschijf schaal-lengte en optische diepte, en verschillen in het model, radiatieve stralingsoverdracht technieken en optimalisatie methode. In de derde test keren we terug naar de artificiëel gemaakte referentiebeelden uit de eerste test. In dit geval worden echter verschillende beelden op verschillende golflengtes tegelijkertijd gemodelleerd. We besluiten dat deze oligochromatische methode resulteert in kleinere onzekerheden op de gevonden waarden dan de monochromatische methode. Meer specifiek, kan dankzij het gebruik van een set van beelden beter onderscheid worden gemaakt tussen een kleine, dichte stofschijf en een grote schijf met lagere dichtheid.

Hoofdstuk 4 behandeld de toepassing van FitSKIRT op een set van 12 spiraalstelsels, gezien van op hun kant, door het gelijktijdig modelleren van de SDSS g-, r-, i- and z-band beelden, zie Figuur 8.3. Deze werden geselecteerd uit het CALIFA onderzoek met de bedoeling om hun ster en stof distributie te bepalen. De resultaten van de 12 galaxieën kunnen gevonden worden in Tabel 4.2 en de gemiddelde waarden, variantie en nauwkeurigheid in Tabel 4.3. Voor twee galaxieën, UGC 4163 en NGC 5908, vinden we dat het model, bestaande uit een exponentiële schijf voor de ster- en stofschijf en een Sérsic profiel om de centrale bult te beschrijven, de beelden niet accuraat beschrijft. In alle andere gevallen was FitSKIRT in staat om de galaxieën voldoende te reconstrueren en de parameters nauwkeurig te bepalen. We vinden dat de gemiddelde stellaire schaallengte en de intrinsieke schijf afplatting in goede overeenkomst is met de resultaten gepubliceerd in Kregel et al. (2002) en Gadotti (2009). De iets grotere centrale bulten in onze set kunnen worden verklaard door het feit dat we niet expliciet een balk in ons model opnemen en door een mogelijk selectie-effect door de noodzakelijkheid van een stofband. Bovendien

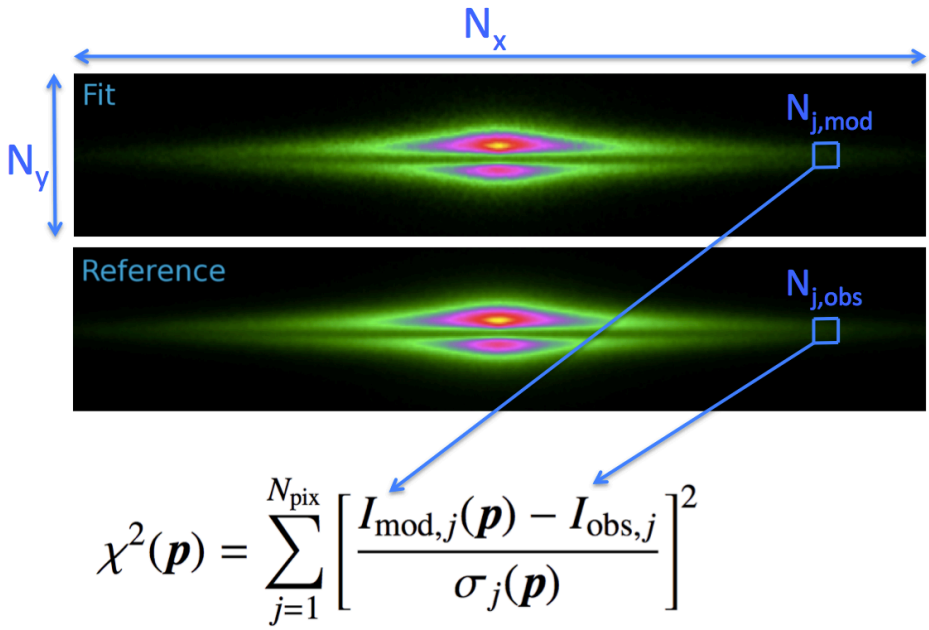

Figure 8.2: Het bovenste beeld toont het model, afkomstig uit FitSKIRT. Het onderste beeld toont het referentiebeeld. De χ^2 waarde wordt bepaald door dezelfde pixel in het referentiebeeld en het model te vergelijken.

neemt Gadotti (2009) de verduisteringseffecten van het interstellaire stof ook niet expliciet in rekening.

De afmetingen van de stofschijven zijn in goede overeenkomst met die gevonden door X99 en B07. De stofschijven zijn half zo dun en ongeveer 70% langer dan de bijhorende stellaire schijven, iets groter dan gevonden door X99 en B07. We vinden echter geen transitie bij een rotatiesnelheid van 120 km s^{-1}, zoals voorgesteld door Dalcanton et al. (2004) en waar de traag roterende spiraalstelsels een gelijkaardige schaalhoogte zouden moeten hebben voor stof en stellaire schijf. In onze set vinden we een grotere verspreiding in de optische diepte, gaande van 0.18 tot 1.98 met een gemiddelde waarde van 0.76 in de V-band met een rms waarde van 0.60 in de set. Bijgevolg is een deel van de spiraalstelsels dus niet volledig transparent, zelfs wanneer frontaal bekeken. Als gevolg van onze selectieprocedure kan het wel zijn dat onze set bestaat uit zeer stofrijke stelsels. Waarschijnlijk is het ook om deze reden dat onze set aan de bovenzijde ligt van de relatie tussen de stofster massaverhouding en de ster massa, in vergelijking met de set bestudeerd door Cortese et al. (2012).

In Hoofdstuk 5, gebruiken we de resultaten uit het vorige hoofdstuk om de stofenergie balans probleem in spiraal stelsels op hun kant te onderzoeken. We bestuderen daarom twee stelsels, IC 4225 and NGC 5166, die werden geobserveerd als

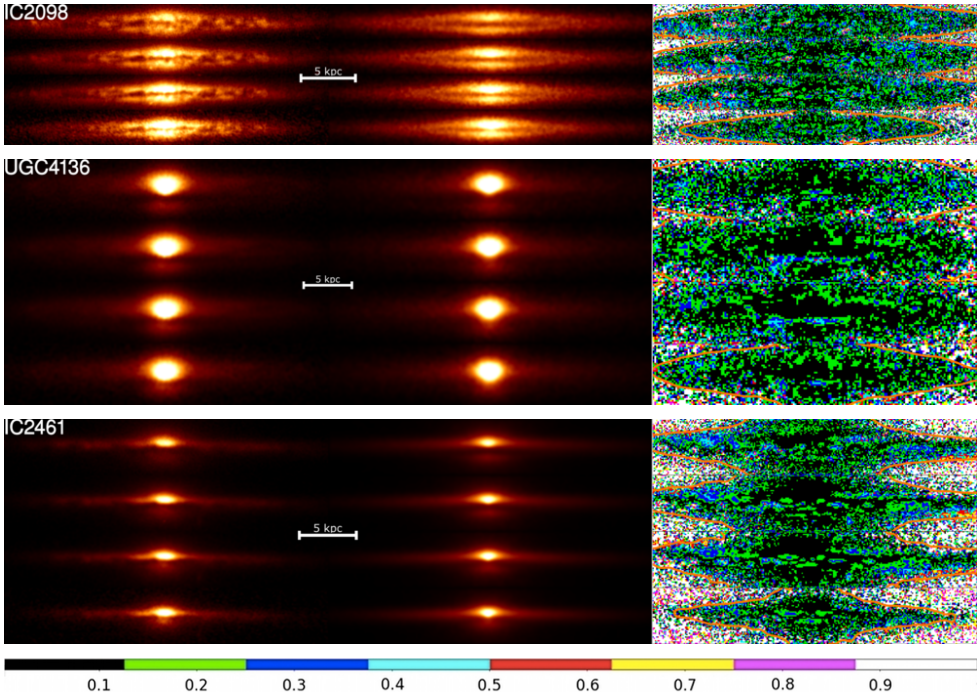

Figure 8.3: Resultaten van een FitSKIRT voor een deel van de onderzochte set. Links zien we de geobserveerde beelden in de SDSS g, r, i en z banden (van boven naar beneden). In het midden zien we het best passende model gevonden door FitSKIRT. Rechts zien we de residuele beelden tussen observatie en model.

deel van het H-ATLAS onderzoek (Eales et al., 2010). We combineren nieuwe, geavanceerde radiatieve stralingsoverdracht modellen met een reeks van data, inclusief PACS en SPIRE, om zowel het warme als koude stof te traceren. In beide gevallen toont de geobserveerde spectrale energiedistributie (SED) een duidelijke overschot aan ver-infrarood emissie in vergelijking met het standaard model, dat bepaald werd aan de hand van optische beelden. Dit is gelijkaardig aan wat al in vele andere onderzoeken werd gevonden (e.g., Popescu et al., 2000; Misiriotis et al., 2001; Alton et al., 2004; Dasyra et al., 2005; Bianchi, 2008; Baes et al., 2010; Popescu et al., 2011; Holwerda et al., 2012b). Dingen veranderen echter wanneer we een jongere stellaire populatie in rekening brengen in onze modellen: het geobserveerde overschot in het ver-infrarood blijft aanwezig voor IC 4225 maar bijna alle waarden worden exact terug gevonden voor NGC 5166, zie Figuur 8.4. Hoewel beide stelsels op exact dezelfde manier werden gemodelleerd is het niet onmogelijk dat er intrinsieke verschillen deze uitkomst veroorzaken. Een mogelijke bron van ver-infrarood emissie die niet in ons model is opgenomen is de emissie komende van sterk verduisterde stervormingsgebieden. Een deel van de jonge sterren is namelijk diep verstopt in zeer dichte stofwolken en hebben daarom amper een bijdrage in het

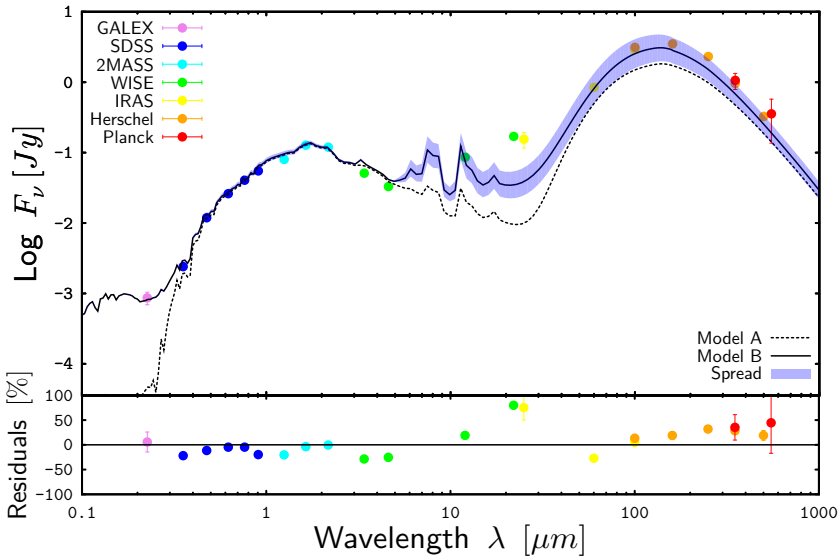

Figure 8.4: De SED voor NGC 5166 (bottom). De gekleurde punten met foutbalken zijn de geobserveerde waarde. De stippellijn en volle lijn zijn respectievelijk het simpele model zonder en met contributie van de jonge sterren.

ultraviolet. De voornaamste conclusie van dit onderzoek is dat, in de plaatse van een duidelijker beeld te krijgen van de stofenergie balans, we een probleem vinden dat complexer is dan gehoopt. Als we een dieper inzicht in de drijvende krachten achter deze ongelijkheid willen krijgen moet een grotere set van stelsels onderzocht worden. Een noodzakelijk instrument in dit onderzoek is de mogelijkheid om op efficiënte wijze en op semi-automatische manier een grote parameterruimte kan onderzoeken. De resultaten in deze thesis tonen aan dat dit vandaag de dag mogelijk is.

In Hoofdstuk 6 bespreken we enkele oude en toekomstige toepassingen van het FitSKIRT programma. Een stelsel dat niet goed kon worden gemodelleerd in Hoofdstuk 4, NGC 5908, werd opnieuw behandeld met een model bestaande uit twee stofringen. Hoewel dit resulteerde in een betere reconstructie van de optische beelden is het effect op de SED verwaarloosbaar. Een van de meest interessante, toekomstige toepassingen van het FitSKIRT programma is het modelleren van zeven nabijgelegen spiraalstelsels, HEROES (Verstappen et al., 2012). In dit hoofdstuk tonen we de resultaten van FitSKIRT, met dezelfde aannames als gemaakt in Hoofdstuk 4, en die kunnen dienen als de start voor verder onderzoek. Aangezien deze beelden echter een veel grotere resolutie hebben, kunnen in de toekomst meer complexe geometrieën aan deze beelden gefit worden. Door het gebruik van de diepere PACS en SPIRE beelden, kan er een betere studie worden uitgevoerd als degene voorgesteld

in Hoofdstuk 5. We bespreken ook kort de resultaten van de modellering van acht onregelmatige stelsels. In deze set hebben slechts enkele een duidelijke verduistering door stof. De resultaten werden gebruikt om de massa-lichtkracht verhouding te bepalen om vervolgens de vorm van de donkere materiehalo rond stelsels te bepalen (Peters, 2014). FitSKIRT werd ook toegepast op NGC 4370. In tegenstelling tot de stelsels die voordien gemodelleerd werden is dit een elliptisch stelsel met een duidelijke stofband. In Viaene et al. (2015), worden enkele verschillende technieken gebruikt om de stofmassa te bepalen vanuit optische beelden en worden dan vergeleken met de massa bepaald uit ver-infrarood waarden. Het werd aangetoond dat, behalve voor FitSKIRT, elke techniek de stofmassa onderschat; wat het belang van een inverse radiatieve stralingsoverdracht code aantoont. Als volledig andere toepassing werd FitSKIRT ook gebruikt om een set van hydrodynamische gesimuleerde beelden te gaan reconstrueren. Hoewel FitSKIRT op accurate wijze de beelden kan modelleren, blijkt de gevonden stofmassa ongeveer drie keer lager dan de werkelijke waarde. De reden voor dit verschil is dat de kleinere structuren in de ster-stof geometrie, die worden uitgesmeerd als galaxieën op hun kant worden bekeken, niet bijdragen tot de globale verduistering door stof. Bijgevolg zijn de modellen die gebruikt worden om stelsels te modelleren te simpel om de werkelijke massa te achterhalen. De laatste sectie beschrijft vier mogelijke, toekomstige verbeteringen aan de code. De eerste is het invoeren van een nieuw model om de centrale bult van stelsels beter te modelleren. Vooral het beschrijven van de pindanootvormige bulten is een interessante optie als studie. Een andere mogelijkheid is het invoeren van spiraal en/of onregelmatige structuur in de schijven. Dit zou kunnen gebruikt worden om sommige geobserveerde asymmetrische stelsels nauwkeurig te gaan modelleren. We bespreken ook kort wat de voordelen kunnen zijn van een andere optimalisatie techniek dan genetische algoritmen. Een andere techniek kan mogelijk niet alleen sneller en stabieler zijn, maar ook de onzekerheden op de gevonden waarden beter inschatten. De potentiëel grootste wijziging kan komen van het invoeren van een techniek die niet alleen optische beelden modelleert maar meteen alle beelden van het ver-ultraviolet tot het ver-infrarood reconstrueert. FitSKIRT zou dan niet dan alleen de SED fitten maar meteen ook de geometrie van stelsels over deze gehele breedte bepalen. Dit, hypothetische instrument, zou een ongelofelijk krachtig middel zijn om een meer volledig beeld te krijgen van het interstellaire stof in spiraalstelsels.

Bibliography

Abazajian, K. N., Adelman-McCarthy, J. K., Agüeros, M. A., et al. (2009). The Seventh Data Release of the Sloan Digital Sky Survey. *ApJS*, 182:543–558.

Alton, P. B., Xilouris, E. M., Misiriotis, A., Dasyra, K. M., and Dumke, M. (2004). The emissivity of dust grains in spiral galaxies. *A&A*, 425:109–120.

Amanullah, R., Lidman, C., Rubin, D., et al. (2010). Spectra and Hubble Space Telescope Light Curves of Six Type Ia Supernovae at 0.511 ¡ z ¡ 1.12 and the Union2 Compilation. *ApJ*, 716:712–738.

Andrieu, C., De Freitas, N., Doucet, A., and Jordan, M. I. (2003). An introduction to mcmc for machine learning. *Machine learning*, 50(1-2):5–43.

Aniano, G., Draine, B. T., Gordon, K. D., and Sandstrom, K. (2011). Common-Resolution Convolution Kernels for Space- and Ground-Based Telescopes. *PASP*, 123:1218–1236.

Athanassoula, E. (2008). Boxy/peanut and discy bulges : formation, evolution and properties. *ArXiv e-prints*.

Baes, M. (2008). Smart detectors for Monte Carlo radiative transfer. *MNRAS*, 391:617–623.

Baes, M., Davies, J. I., Dejonghe, H., et al. (2003). Radiative transfer in disc galaxies - III. The observed kinematics of dusty disc galaxies. *MNRAS*, 343:1081–1094.

Baes, M. and Dejonghe, H. (2001a). Radiative transfer in disc galaxies - I. A comparison of four methods to solve the transfer equation in plane-parallel geometry. *MNRAS*, 326:722–732.

Baes, M. and Dejonghe, H. (2001b). Radiative transfer in disc galaxies - II. The influence of scattering and geometry on the attenuation curve. *MNRAS*, 326:733–744.

Baes, M. and Dejonghe, H. (2002). Kinematics of elliptical galaxies with a diffuse dust component - III. A Monte Carlo approach to include the effects of scattering. *MNRAS*, 335:441–458.

Baes, M., Fritz, J., Gadotti, D. A., et al. (2010). Herschel-ATLAS: The dust energy balance in the edge-on spiral galaxy UGC 4754. *A&A*, 518:L39.

Baes, M. and Gentile, G. (2011). Analytical expressions for the deprojected Sérsic model. *A&A*, 525:A136.

Baes, M., Stamatellos, D., Davies, J. I., et al. (2005). Radiative equilibrium in Monte Carlo radiative transfer using frequency distribution adjustment. *New A*, 10:523–533.

Baes, M. and van Hese, E. (2011). Analytical expressions for the deprojected Sérsic model. II. General expressions in terms of the Fox H function. *A&A*, 534:A69.

Baes, M., Verstappen, J., De Looze, I., et al. (2011). Efficient Three-dimensional NLTE Dust Radiative Transfer with SKIRT. *ApJS*, 196:22.

Bahcall, J. N. and Soneira, R. M. (1980). The universe at faint magnitudes. I - Models for the galaxy and the predicted star counts. *ApJS*, 44:73–110.

Baier, A., Kerschbaum, F., and Lebzelter, T. (2010). Fitting of dust spectra with genetic algorithms. I. Perspectives and limitations. *A&A*, 516:A45.

Baumgartner, W. H., Tueller, J., Markwardt, C. B., et al. (2013). The 70 Month Swift-BAT All-sky Hard X-Ray Survey. *ApJS*, 207:19.

Bell, E. F. and de Jong, R. S. (2001). Stellar Mass-to-Light Ratios and the Tully-Fisher Relation. *ApJ*, 550:212–229.

Bendo, G. J., Boselli, A., Dariush, A., et al. (2012). Investigations of dust heating in M81, M83 and NGC 2403 with the Herschel Space Observatory. *MNRAS*, 419:1833–1859.

Bendo, G. J., Calzetti, D., Engelbracht, C. W., et al. (2007). Variations in 24-μm morphologies among galaxies in the Spitzer Infrared Nearby Galaxies Survey: new insights into the Hubble sequence. *MNRAS*, 380:1313–1334.

Bendo, G. J., Wilson, C. D., Pohlen, M., et al. (2010). The Herschel Space Observatory view of dust in M81. *A&A*, 518:L65.

Bianchi, S. (2007). The dust distribution in edge-on galaxies. Radiative transfer fits of V and K'-band images. *A&A*, 471:765–773.

Bianchi, S. (2008). Dust extinction and emission in a clumpy galactic disk. An application of the radiative transfer code TRADING. *A&A*, 490:461–475.

Bianchi, S., Davies, J. I., and Alton, P. B. (2000). Monte Carlo predictions of far-infrared emission from spiral galaxies. *A&A*, 359:65–81.

Bianchi, S., Ferrara, A., and Giovanardi, C. (1996). Monte Carlo Simulations of Dusty Spiral Galaxies: Extinction and Polarization Properties. *ApJ*, 465:127.

Bianchi, S., Gonçalves, J., Albrecht, M., et al. (2003). Dust emissivity in the submm/mm. SCUBA and SIMBA observations of Barnard 68. *A&A*, 399:L43–L46.

Bizyaev, D. V., Kautsch, S. J., Mosenkov, A. V., et al. (2014). The Catalog of Edge-on Disk Galaxies from SDSS. I. The Catalog and the Structural Parameters of Stellar Disks. *ApJ*, 787:24.

Bjorkman, J. E. and Wood, K. (2001). Radiative Equilibrium and Temperature Correction in Monte Carlo Radiation Transfer. *ApJ*, 554:615–623.

Boquien, M., Calzetti, D., Combes, F., et al. (2011). Dust Heating Sources in Galaxies: The Case of M33 (HERM33ES). *AJ*, 142:111.

Boselli, A., Eales, S., Cortese, L., et al. (2010). The Herschel Reference Survey. *PASP*, 122:261–287.

Boselli, A., Hughes, T. M., Cortese, L., Gavazzi, G., and Buat, V. (2013). Integrated spectroscopy of the Herschel Reference Survey. The spectral line properties of a volume-limited, K-band-selected sample of nearby galaxies. *A&A*, 550:A114.

Bosma, A., Byun, Y., Freeman, K. C., and Athanassoula, E. (1992). The opacity of spiral disks. *ApJ*, 400:L21–L24.

Bothwell, M. S., Maiolino, R., Kennicutt, R., et al. (2013). A fundamental relation between the metallicity, gas content and stellar mass of local galaxies. *MNRAS*, 433:1425–1435.

Bottema, R. (1995). The prodigious warp of NGC 4013. II. Detailed observations of the neutral hydrogen gas. *A&A*, 295:605.

Bottema, R. (1996). The prodigious warp of NGC 4013. III. Analysis of the structure and kinematics. *A&A*, 306:345.

Bottema, R., Shostak, G. S., and van der Kruit, P. C. (1987). The prodigious warp of NGC4013. *Nature*, 328:401–403.

Bottinelli, L., Gouguenheim, L., Paturel, G., and Teerikorpi, P. (1995). Optical thickness of spiral galaxies. *Astrophysical Letters and Communications*, 31:143.

Bracco, A., Cooray, A., Veneziani, M., et al. (2011). Herschel-ATLAS: statistical properties of Galactic cirrus in the GAMA-9 Hour Science Demonstration Phase Field. *MNRAS*, 412:1151–1161.

Bresolin, F., Ryan-Weber, E., Kennicutt, R. C., and Goddard, Q. (2009). The Flat Oxygen Abundance Gradient in the Extended Disk of M83. *ApJ*, 695:580–595.

Bruzual, G. and Charlot, S. (2003). Stellar population synthesis at the resolution of 2003. *MNRAS*, 344:1000–1028.

Bruzual A., G., Magris, G., and Calvet, N. (1988). A model for the effects of dust on the spectra of disk galaxies. I - General treatment. *ApJ*, 333:673–688.

Buat, V. and Burgarella, D. (1998). The observation of the nearby universe in UV and in FIR: an evidence for a moderate extinction in present day star forming galaxies. *A&A*, 334:772–782.

Burgarella, D., Buat, V., and Iglesias-Páramo, J. (2005). Star formation and dust attenuation properties in galaxies from a statistical ultraviolet-to-far-infrared analysis. *MNRAS*, 360:1413–1425.

Burstein, D., Haynes, M. P., and Faber, M. (1991). Dependence of galaxy properties on viewing angle. *Nature*, 353:515–521.

Byun, Y.-I. (1993). Tests for dust opacity of spiral galaxies. *PASP*, 105:993–995.

Byun, Y. I., Freeman, K. C., and Kylafis, N. D. (1994). Diagnostics of dust content in spiral galaxies: Numerical simulations of radiative transfer. *ApJ*, 432:114–127.

Calzetti, D., Kennicutt, R. C., Engelbracht, C. W., et al. (2007). The Calibration of Mid-Infrared Star Formation Rate Indicators. *ApJ*, 666:870–895.

Calzetti, D., Wu, S.-Y., Hong, S., et al. (2010). The Calibration of Monochromatic Far-Infrared Star Formation Rate Indicators. *ApJ*, 714:1256–1279.

Camps, P. and Baes, M. (2015). SKIRT: An advanced dust radiative transfer code with a user-friendly architecture. *Astronomy and Computing*, 9:20–33.

Camps, P., Baes, M., and Saftly, W. (2013). Using 3D Voronoi grids in radiative transfer simulations. *A&A*, 560:A35.

Cantó, J., Curiel, S., and Martínez-Gómez, E. (2009). A simple algorithm for optimization and model fitting: AGA (asexual genetic algorithm). *A&A*, 501:1259–1268.

Chabrier, G. (2003). Galactic Stellar and Substellar Initial Mass Function. *PASP*, 115:763–795.

Chandrasekhar, S. (1960). *Radiative transfer*. Dover.

Charbonneau, P. (1995). Genetic Algorithms in Astronomy and Astrophysics. *ApJS*, 101:309.

Cherchneff, I. (2010). Dust Formation in Massive Stars and Their Explosive Ends. In Leitherer, C., Bennett, P. D., Morris, P. W., and Van Loon, J. T., editors, *Hot and Cool: Bridging Gaps in Massive Star Evolution*, volume 425 of *Astronomical Society of the Pacific Conference Series*, page 237.

Ciesla, L., Boquien, M., Boselli, A., et al. (2014). Dust Spectral Energy Distributions of Nearby Galaxies: an Insight from the Herschel Reference Survey. *A&A*, in press (arXiv.1402.3597).

Ciesla, L., Boselli, A., Smith, M. W. L., et al. (2012). Submillimetre photometry of 323 nearby galaxies from the Herschel Reference Survey. *A&A*, 543:A161.

Colorni, A., Dorigo, M., Maniezzo, V., et al. (1991). Distributed optimization by ant colonies. In *Proceedings of the first European conference on artificial life*, volume 142, pages 134–142. Paris, France.

Corradi, R. L. M., Beckman, J. E., del Rio, M. S., di Bartolomeo, A., and Simonneau, E. (1996). New radiative transfer models of disc galaxies and the scale-length test for dust diagnostics. In Block, D. L. and Greenberg, J. M., editors, *New Extragalactic Perspectives in the New South Africa*, volume 209 of *Astrophysics and Space Science Library*, page 523.

Corsaro, E. and De Ridder, J. (2014). DIAMONDS: A new Bayesian nested sampling tool. Application to peak bagging of solar-like oscillations. *A&A*, 571:A71.

Cortese, L., Ciesla, L., Boselli, A., et al. (2012). The dust scaling relations of the Herschel Reference Survey. *A&A*, 540:A52.

Cox, P., Krips, M., Neri, R., et al. (2011). Gas and Dust in a Submillimeter Galaxy at z = 4.24 from the Herschel Atlas. *ApJ*, 740:63.

Cusumano, G., La Parola, V., Segreto, A., et al. (2010). The Palermo Swift-BAT hard X-ray catalogue. II. Results after 39 months of sky survey. *A&A*, 510:A48.

da Cunha, E., Charlot, S., and Elbaz, D. (2008). A simple model to interpret the ultraviolet, optical and infrared emission from galaxies. *MNRAS*, 388:1595–1617.

Dalcanton, J. J., Yoachim, P., and Bernstein, R. A. (2004). The Formation of Dust Lanes: Implications for Galaxy Evolution. *ApJ*, 608:189–207.

Dale, D. A., Aniano, G., Engelbracht, C. W., et al. (2012). Herschel Far-infrared and Submillimeter Photometry for the KINGFISH Sample of nearby Galaxies. *ApJ*, 745:95.

Darwin, C. (1859). On the origin of species by means of natural selection, 1859. *Murray, London*.

Dasyra, K. M., Xilouris, E. M., Misiriotis, A., and Kylafis, N. D. (2005). Is the Galactic submillimeter dust emissivity underestimated? *A&A*, 437:447–456.

Davies, J. I., Baes, M., Bendo, G. J., et al. (2010). The Herschel Virgo Cluster Survey. I. Luminosity function. *A&A*, 518:L48.

Davies, J. I., Bianchi, S., Cortese, L., et al. (2012). The Herschel Virgo Cluster Survey - VIII. The Bright Galaxy Sample. *MNRAS*, 419:3505–3520.

Davis, M. (1975). Television surface photometry of the edge-on spiral galaxies NGC 3987 and NGC 5907. *AJ*, 80:188–193.

De Geyter, G., Baes, M., Camps, P., et al. (2014). The distribution of interstellar dust in CALIFA edge-on galaxies via oligochromatic radiative transfer fitting. *MNRAS*, 441:869–885.

De Geyter, G., Baes, M., Fritz, J., and Camps, P. (2013). FitSKIRT: genetic algorithms to automatically fit dusty galaxies with a Monte Carlo radiative transfer code. *A&A*, 550:A74.

de Grijs, R., Kregel, M., and Wesson, K. H. (2001). Radially truncated galactic discs. *MNRAS*, 324:1074–1086.

De Looze, I., Baes, M., Bendo, G. J., et al. (2012a). The dust energy balance in the edge-on spiral galaxy NGC 4565. *MNRAS*, 427:2797–2811.

De Looze, I., Baes, M., Fritz, J., and Verstappen, J. (2012b). Panchromatic radiative transfer modelling of stars and dust in the Sombrero galaxy. *MNRAS*, 419:895–903.

De Looze, I., Baes, M., Zibetti, S., et al. (2010). The Herschel Virgo Cluster Survey . VII. Dust in cluster dwarf elliptical galaxies. *A&A*, 518:L54.

De Looze, I., Fritz, J., Baes, M., et al. (2014). High-resolution, 3D radiative transfer modeling. I. The grand-design spiral galaxy M 51. *A&A*, 571:A69.

de Souza, R. E., Gadotti, D. A., and dos Anjos, S. (2004). BUDDA: A New Two-dimensional Bulge/Disk Decomposition Code for Detailed Structural Analysis of Galaxies. *ApJS*, 153:411–427.

de Vaucouleurs, G., de Vaucouleurs, A., Corwin, Jr., H. G., et al. (1991). *Third Reference Catalogue of Bright Galaxies. Volume I: Explanations and references. Volume II: Data for galaxies between 0^h and 12^h. Volume III: Data for galaxies between 12^h and 24^h.* Springer.

de Vaucouleurs, G. H., de Vaucouleurs, A., and Shapley, H. (1964). *Reference catalogue of bright galaxies*. University of Texas Press.

Deschamps, R., Braun, K., Jorissen, A., et al. (2014). Non-conservative evolution in Algols: where is the matter? *A&A*, submitted.

di Bartolomeo, A., Barbaro, G., and Perinotto, M. (1995). Internal extinction in spiral disc galaxies. *MNRAS*, 277:1279–1292.

Disney, M., Davies, J., and Phillipps, S. (1989). Are galaxy discs optically thick? *MNRAS*, 239:939–976.

Draine, B. T. (1988). The discrete-dipole approximation and its application to interstellar graphite grains. *ApJ*, 333:848–872.

Draine, B. T., Dale, D. A., Bendo, G., et al. (2007). Dust Masses, PAH Abundances, and Starlight Intensities in the SINGS Galaxy Sample. *ApJ*, 663:866–894.

Draine, B. T. and Li, A. (2001). Infrared Emission from Interstellar Dust. I. Stochastic Heating of Small Grains. *ApJ*, 551:807–824.

Draine, B. T. and Li, A. (2007). Infrared Emission from Interstellar Dust. IV. The Silicate-Graphite-PAH Model in the Post-Spitzer Era. *ApJ*, 657:810–837.

Dunne, L., Gomez, H. L., da Cunha, E., et al. (2011). Herschel-ATLAS: rapid evolution of dust in galaxies over the last 5 billion years. *MNRAS*, 417:1510–1533.

Dupac, X., Bernard, J.-P., Boudet, N., et al. (2003). Inverse temperature dependence of the dust submillimeter spectral index. *A&A*, 404:L11–L15.

Dwek, E. (1998). The Evolution of the Elemental Abundances in the Gas and Dust Phases of the Galaxy. *ApJ*, 501:643.

Dwek, E. and Cherchneff, I. (2011). The Origin of Dust in the Early Universe: Probing the Star Formation History of Galaxies by Their Dust Content. *ApJ*, 727:63.

Eales, S., Dunne, L., Clements, D., et al. (2010). The Herschel ATLAS. *PASP*, 122:499–515.

Falco, E. E., Kurtz, M. J., Geller, M. J., et al. (1999). The Updated Zwicky Catalog (UZC). *PASP*, 111:438–452.

Ferrarotti, A. S. and Gail, H.-P. (2006). Composition and quantities of dust produced by AGB-stars and returned to the interstellar medium. *A&A*, 447:553–576.

Filippenko, A. V. and Chornock, R. (2003). Supernovae. *IAU Circ.*, 8085:2.

Fletcher, S. T., Chaplin, W. J., and Elsworth, Y. (2003). Use of genetic algorithms to determine low-l rotational p-mode splittings at high frequencies. *MNRAS*, 346:825–832.

Florido, E., Prieto, M., Battaner, E., et al. (1991). Photometric observations of the warped disks of NGC 4013, NGC 4565 and NGC 6504. *A&A*, 242:301–312.

Forrest, S. (1993). Genetic Algorithms: Principles of Natural Selection Applied to Computation. *Science*, 261:872–878.

Foyle, K., Wilson, C. D., Mentuch, E., et al. (2012). The dust and gas properties of M83. *MNRAS*, 421:2917–2929.

Fu, H., Jullo, E., Cooray, A., et al. (2012). A Comprehensive View of a Strongly Lensed Planck-Associated Submillimeter Galaxy. *ApJ*, 753:134.

Gadotti, D. A. (2009). Structural properties of pseudo-bulges, classical bulges and elliptical galaxies: a Sloan Digital Sky Survey perspective. *MNRAS*, 393:1531–1552.

Gadotti, D. A., Baes, M., and Falony, S. (2010). Radiative transfer in disc galaxies - IV. The effects of dust attenuation on bulge and disc structural parameters. *MNRAS*, 403:2053–2062.

Gadotti, D. A. and Sánchez-Janssen, R. (2012). Surprises in image decomposition of edge-on galaxies: does Sombrero have a (classical) bulge? *MNRAS*, 423:877–888.

Galametz, M., Kennicutt, R. C., Albrecht, M., et al. (2012a). Mapping the cold dust temperatures and masses of nearby Kingfish galaxies with Herschel. *ArXiv e-prints*.

Galametz, M., Kennicutt, R. C., Albrecht, M., et al. (2012b). Mapping the cold dust temperatures and masses of nearby KINGFISH galaxies with Herschel. *MNRAS*, 425:763–787.

Galametz, M., Madden, S. C., Galliano, F., et al. (2010). Herschel photometric observations of the nearby low metallicity irregular galaxy NGC 6822. *A&A*, 518:L55.

Gallagher, S. C., Johnson, K. E., Hornschemeier, A. E., Charlton, J. C., and Hibbard, J. E. (2008). The Revealing Dust: Mid-Infrared Activity in Hickson Compact Group Galaxy Nuclei. *ApJ*, 673:730–741.

Galliano, F., Dwek, E., and Chanial, P. (2008). Stellar Evolutionary Effects on the Abundances of Polycyclic Aromatic Hydrocarbons and Supernova-Condensed Dust in Galaxies. *ApJ*, 672:214–243.

Galliano, F., Hony, S., Bernard, J.-P., et al. (2011). Non-standard grain properties, dark gas reservoir, and extended submillimeter excess, probed by Herschel in the Large Magellanic Cloud. *A&A*, 536:A88.

García-Burillo, S., Combes, F., and Neri, R. (1999). Interferometer (12) CO observations of the box-shaped bulge spiral NGC 4013. *A&A*, 343:740–750.

Goldberg, D. E. (1989). *Genetic Algorithms in Search, Optimization and Machine Learning*. Addison-Wesley Longman Publishing Co., Inc., Boston, MA, USA, 1st edition.

Goldberg, D. E., Deb, K., and Clark, J. H. (1991). Genetic algorithms, noise, and the sizing of populations. *Complex Systems*, 6:333–362.

Gomez, H. L., Baes, M., Cortese, L., et al. (2010). The dust morphology of the elliptical Galaxy M 86 with SPIRE. *A&A*, 518:L45.

González Delgado, R. M., Pérez, E., Cid Fernandes, R., et al. (2014). The star formation history of CALIFA galaxies: Radial structures. *A&A*, 562:A47.

Gordon, K. D., Misselt, K. A., Witt, A. N., and Clayton, G. C. (2001). The DIRTY Model. I. Monte Carlo Radiative Transfer through Dust. *ApJ*, 551:269–276.

Graham, A. W. and Worley, C. C. (2008). Inclination- and dust-corrected galaxy parameters: bulge-to-disc ratios and size-luminosity relations. *MNRAS*, 388:1708–1728.

Griffin, M. J., Abergel, A., Abreu, A., et al. (2010). The Herschel-SPIRE instrument and its in-flight performance. *A&A*, 518:L3.

Groves, B., Dopita, M. A., Sutherland, R. S., et al. (2008). Modeling the Pan-Spectral Energy Distribution of Starburst Galaxies. IV. The Controlling Parameters of the Starburst SED. *ApJS*, 176:438–456.

Groves, B., Krause, O., Sandstrom, K., et al. (2012). The heating of dust by old stellar populations in the bulge of M31. *MNRAS*, 426:892–902.

Guedes, J., Callegari, S., Madau, P., and Mayer, L. (2011). Forming Realistic Late-type Spirals in a ΛCDM Universe: The Eris Simulation. *ApJ*, 742:76.

Guhathakurta, P. and Draine, B. T. (1989). Temperature fluctuations in interstellar grains. I - Computational method and sublimation of small grains. *ApJ*, 345:230–244.

Hakobyan, A. A., Petrosian, A. R., McLean, B., et al. (2008). Early-type galaxies with core collapse supernovae. *A&A*, 488:523–531.

Hatziminaoglou, E., Fritz, J., Franceschini, A., et al. (2008). Properties of dusty tori in active galactic nuclei - I. The case of SWIRE/SDSS quasars. *MNRAS*, 386:1252–1264.

Hatziminaoglou, E., Fritz, J., and Jarrett, T. H. (2009). Properties of dusty tori in active galactic nuclei - II. Type 2 AGN. *MNRAS*, 399:1206–1222.

Henyey, L. G. (1937). The Illumination of Reflection Nebulae. *ApJ*, 85:107.

Hickson, P. (1982). Systematic properties of compact groups of galaxies. *ApJ*, 255:382–391.

Holland, W. S., Robson, E. I., Gear, W. K., et al. (1999). SCUBA: a common-user submillimetre camera operating on the James Clerk Maxwell Telescope. *MNRAS*, 303:659–672.

Hollenbach, D. and Salpeter, E. E. (1971). Surface Recombination of Hydrogen Molecules. *ApJ*, 163:155.

Holwerda, B. W., Bianchi, S., Baes, M., et al. (2012a). New HErschel Multi-wavelength Extragalactic Survey of Edge-on Spirals (NHEMESES). In Tuffs, R. J. and Popescu, C. C., editors, *IAU Symposium*, volume 284 of *IAU Symposium*, pages 128–131.

Holwerda, B. W., Bianchi, S., Böker, T., et al. (2012b). Herschel/SPIRE observations of the dusty disk of NGC 4244. *A&A*, 541:L5.

Holwerda, B. W., Gonzalez, R. A., Allen, R. J., and van der Kruit, P. C. (2005). The Opacity of Spiral Galaxy Disks. IV. Radial Extinction Profiles from Counts of Distant Galaxies Seen through Foreground Disks. *AJ*, 129:1396–1411.

Hughes, T. M., Baes, M., Fritz, J., et al. (2014a). A resolved analysis of cold dust and gas in the nearby edge-on spiral NGC 891. *A&A*, in press (arXiv:1402.5967).

Hughes, T. M., Baes, M., Fritz, J., et al. (2014b). A resolved analysis of cold dust and gas in the nearby edge-on spiral NGC 891. *A&A*, 565:A4.

Hughes, T. M., Cortese, L., Boselli, A., Gavazzi, G., and Davies, J. I. (2013). The role of cold gas and environment on the stellar mass-metallicity relation of nearby galaxies. *A&A*, 550:A115.

Hunt, L. K., Pierini, D., and Giovanardi, C. (2004). Near-infrared observations of galaxies in Pisces-Perseus. V. On the origin of bulges. *A&A*, 414:905–918.

Husemann, B., Jahnke, K., Sánchez, S. F., et al. (2013). CALIFA, the Calar Alto Legacy Integral Field Area survey. II. First public data release. *A&A*, 549:A87.

Ibar, E., Ivison, R. J., Cava, A., et al. (2010). H-ATLAS: PACS imaging for the Science Demonstration Phase. *MNRAS*, 409:38–47.

Indebetouw, R., Matsuura, M., Dwek, E., et al. (2014). Dust Production and Particle Acceleration in Supernova 1987A Revealed with ALMA. *ApJ*, 782:L2.

Inoue, A. K. (2005). Attenuation law of normal disc galaxies with clumpy distributions of stars and dust. *MNRAS*, 359:171–182.

Jarvis, B. J. (1986). A search for box- or peanut-shaped bulges. *AJ*, 91:65–69.

Johnson, K. E., Hibbard, J. E., Gallagher, S. C., et al. (2007). The Infrared Properties of Hickson Compact Groups. *AJ*, 134:1522–1543.

Johnston, K. G., Keto, E., Robitaille, T. P., and Wood, K. (2011). The standard model of low-mass star formation applied to massive stars: multiwavelength modelling of IRAS 20126+4104. *MNRAS*, 415:2953–2968.

Jonsson, P. (2006). SUNRISE: polychromatic dust radiative transfer in arbitrary geometries. *MNRAS*, 372:2–20.

Juvela, M. and Ysard, N. (2012a). The degeneracy between the dust colour temperature and the spectral index. The problem of multiple χ^2 minima. *A&A*, 541:A33.

Juvela, M. and Ysard, N. (2012b). The effect of temperature mixing on the observable (T, β)-relation of interstellar dust clouds. *A&A*, 539:A71.

Kautsch, S. J., Grebel, E. K., Barazza, F. D., and Gallagher, III, J. S. (2006). A catalog of edge-on disk galaxies. From galaxies with a bulge to superthin galaxies. *A&A*, 445:765–778.

Kehrig, C., Monreal-Ibero, A., Papaderos, P., et al. (2012). The ionized gas in the CALIFA early-type galaxies. I. Mapping two representative cases: NGC 6762 and NGC 5966. *A&A*, 540:A11.

Kelly, B. C., Shetty, R., Stutz, A. M., et al. (2012). Dust Spectral Energy Distributions in the Era of Herschel and Planck: A Hierarchical Bayesian-fitting Technique. *ApJ*, 752:55.

Kelz, A., Verheijen, M. A. W., Roth, M. M., et al. (2006). PMAS: The Potsdam Multi-Aperture Spectrophotometer. II. The Wide Integral Field Unit PPak. *PASP*, 118:129–145.

Kennedy, J. (2010). Particle swarm optimization. In *Encyclopedia of Machine Learning*, pages 760–766. Springer.

Kennicutt, R. C., Calzetti, D., Aniano, G., et al. (2011). KINGFISH – Key Insights on Nearby Galaxies: A Far-Infrared Survey with Herschel: Survey Description and Image Atlas. *PASP*, 123:1347–1369.

Kessler, M. F., Steinz, J. A., Anderegg, M. E., et al. (1996). The Infrared Space Observatory (ISO) mission. *A&A*, 315:L27–L31.

Kormendy, J. and Illingworth, G. (1982). Rotation of the bulge components of disk galaxies. *ApJ*, 256:460–480.

Koss, M., Mushotzky, R., Veilleux, S., et al. (2011). Host Galaxy Properties of the Swift Bat Ultra Hard X-Ray Selected Active Galactic Nucleus. *ApJ*, 739:57.

Kramer, C., Richer, J., Mookerjea, B., Alves, J., and Lada, C. (2003). Dust properties of the dark cloud IC 5146. Submillimeter and NIR imaging. *A&A*, 399:1073–1082.

Kregel, M., van der Kruit, P. C., and de Grijs, R. (2002). Flattening and truncation of stellar discs in edge-on spiral galaxies. *MNRAS*, 334:646–668.

Küppers, M., Bertini, I., Fornasier, S., et al. (2005). A large dust/ice ratio in the nucleus of comet 9P/Tempel 1. *Nature*, 437:987–990.

Kwok, S. (2007). *Physics and Chemistry of the Interstellar Medium*. University Science Books.

Kylafis, N. D. and Bahcall, J. N. (1987). Dust distribution in spiral galaxies. *ApJ*, 317:637–645.

Lapi, A., González-Nuevo, J., Fan, L., et al. (2011). Herschel-ATLAS Galaxy Counts and High-redshift Luminosity Functions: The Formation of Massive Early-type Galaxies. *ApJ*, 742:24.

Larsen, J. A. and Humphreys, R. M. (2003). Fitting a Galactic Model to an All-Sky Survey. *AJ*, 125:1958–1979.

Laurikainen, E. and Salo, H. (2000). BVRI imaging of M 51-type pairs. II. Bulge and disk parameters. *A&AS*, 141:103–111.

Lawrence, A., Warren, S. J., Almaini, O., et al. (2007). The UKIRT Infrared Deep Sky Survey (UKIDSS). *MNRAS*, 379:1599–1617.

Lee, J. C., Hwang, H. S., and Ko, J. (2013). The Calibration of Star Formation Rate Indicators for WISE 22 μm-Selected Galaxies in the Sloan Digital Sky Survey. *ApJ*, 774:62.

Leitherer, C., Schaerer, D., Goldader, J. D., et al. (1999). Starburst99: Synthesis Models for Galaxies with Active Star Formation. *ApJS*, 123:3–40.

Levenberg, K. (1944). A method for the solution of certain nonlinear problems in least squares. *Q. Appl. Math*, 2:164–168.

López-Caniego, M., González-Nuevo, J., Massardi, M., et al. (2013). Mining the Herschel-Astrophysical Terahertz Large Area Survey: submillimetre-selected blazars in equatorial fields. *MNRAS*, 430:1566–1577.

Lucy, L. B. (1999). Computing radiative equilibria with Monte Carlo techniques. *A&A*, 344:282–288.

Lütticke, R., Dettmar, R.-J., and Pohlen, M. (2000a). Box- and peanut-shaped bulges. I. Statistics. *A&AS*, 145:405–414.

Lütticke, R., Dettmar, R.-J., and Pohlen, M. (2000b). Box- and peanut-shaped bulges. II. NIR observations. *A&A*, 362:435–446.

MacLachlan, J. M., Matthews, L. D., Wood, K., and Gallagher, J. S. (2011). The Stability of Low Surface Brightness Disks Based on Multi-wavelength Modeling. *ApJ*, 741:6.

Mandel, E., Murray, S. S., and Roll, J. B. (2001). Funtools: An Experiment with Minimal Buy-in Software. In Harnden, Jr., F. R., Primini, F. A., and Payne, H. E., editors, *Astronomical Data Analysis Software and Systems X*, volume 238 of *Astronomical Society of the Pacific Conference Series*, page 225.

Marinacci, F., Pakmor, R., and Springel, V. (2014). The formation of disc galaxies in high-resolution moving-mesh cosmological simulations. *MNRAS*, 437:1750–1775.

Marino, R. A., Rosales-Ortega, F. F., Sánchez, S. F., et al. (2013). The O3N2 and N2 abundance indicators revisited: improved calibrations based on CALIFA and T_e-based literature data. *A&A*, 559:A114.

Marquardt, D. W. (1963). An Algorithm for Least-Squares Estimation of Nonlinear Parameters. *SIAM Journal on Applied Mathematics*, 11(2):431–441.

Martin, D. C., Fanson, J., Schiminovich, D., et al. (2005). The Galaxy Evolution Explorer: A Space Ultraviolet Survey Mission. *ApJ*, 619:L1–L6.

Martínez, M. A., Del Olmo, A., Coziol, R., and Perea, J. (2010). AGN Population in Hickson Compact Groups. I. Data and Nuclear Activity Classification. *AJ*, 139:1199–1211.

Masters, K. L., Giovanelli, R., and Haynes, M. P. (2003). Internal Extinction in Spiral Galaxies in the Near-Infrared. *AJ*, 126:158–174.

Matheson, T., Jha, S., Challis, P., Kirshner, R., and Calkins, M. (2002). Supernovae 2002bs, 2002bv, 2002bx. *IAU Circ.*, 7868:2.

Matthews, L. D. and Wood, K. (2001). Modeling the Interstellar Medium of Low Surface Brightness Galaxies: Constraining Internal Extinction, Disk Color Gradients, and Intrinsic Rotation Curve Shapes. *ApJ*, 548:150–171.

Mattila, K. (1970). Interpretation of the surface brightness of dark nebulae. *A&A*, 9:53–63.

Mazure, A. and Capelato, H. V. (2002). Exact solutions for the spatial de Vaucouleurs and Sérsic laws and related quantities. *A&A*, 383:384–389.

Meixner, M., Galliano, F., Hony, S., et al. (2010). HERschel Inventory of The Agents of Galaxy Evolution (HERITAGE): The Large Magellanic Cloud dust. *A&A*, 518:L71.

Menu, J., van Boekel, R., Henning, T., et al. (2014). On the structure of the transition disk around TW Hydrae. *A&A*, 564:A93.

Metcalfe, T. S., Nather, R. E., and Winget, D. E. (2000). Genetic-Algorithm-based Asteroseismological Analysis of the DBV White Dwarf GD 358. *ApJ*, 545:974–981.

Misiriotis, A. and Bianchi, S. (2002). The influence of clumping on surface brightness fits of edge-on spiral galaxies. *A&A*, 384:866–871.

Misiriotis, A., Kylafis, N. D., Papamastorakis, J., and Xilouris, E. M. (2000). Is the exponential distribution a good approximation of dusty galactic disks? *A&A*, 353:117–123.

Misiriotis, A., Popescu, C. C., Tuffs, R., and Kylafis, N. D. (2001). Modeling the spectral energy distribution of galaxies. II. Disk opacity and star formation in 5 edge-on spirals. *A&A*, 372:775–783.

Mitchell, M. (1998). *An Introduction to Genetic Algorithms (Complex Adaptive Systems)*. A Bradford Book, 3rd edition.

Möllenhoff, C., Popescu, C. C., and Tuffs, R. J. (2006). Modelling the spectral energy distribution of galaxies. IV. Correcting apparent disk scalelengths and central surface brightnesses for the effect of dust at optical and near-infrared wavelengths. *A&A*, 456:941–952.

Moshir, M., Kopman, G., and Conrow, T. A. O. (1992). *IRAS Faint Source Survey, Explanatory supplement version 2*. Pasadena: Infrared Processing and Analysis Center, California Institute of Technology.

Muñoz-Mateos, J. C., Gil de Paz, A., Boissier, S., et al. (2009a). Radial Distribution of Stars, Gas, and Dust in Sings Galaxies. II. Derived Dust Properties. *ApJ*, 701:1965–1991.

Muñoz-Mateos, J. C., Gil de Paz, A., Zamorano, J., et al. (2009b). Radial Distribution of Stars, Gas, and Dust in SINGS Galaxies. I. Surface Photometry and Morphology. *ApJ*, 703:1569–1596.

Nair, P. B. and Abraham, R. G. (2010). A Catalog of Detailed Visual Morphological Classifications for 14,034 Galaxies in the Sloan Digital Sky Survey. *ApJS*, 186:427–456.

Negrello, M., Hopwood, R., De Zotti, G., et al. (2010). The Detection of a Population of Submillimeter-Bright, Strongly Lensed Galaxies. *Science*, 330:800.

Nelder, J. A. and Mead, R. (1965). A simplex method for function minimization. *Computer Journal*, 7:308–313.

Nesseris, S. and Garcia-Bellido, J. (2012). A new perspective on Dark Energy modeling via Genetic Algorithms. *ArXiv e-prints*.

Nesseris, S. and Shafieloo, A. (2010). A model-independent null test on the cosmological constant. *MNRAS*, 408:1879–1885.

Neugebauer, G., Habing, H. J., van Duinen, R., et al. (1984). The Infrared Astronomical Satellite (IRAS) mission. *ApJ*, 278:L1–L6.

Newberry, M. (1991). Signal-to-noise considerations for sky-subtracted CCD data. *astronomical society of the pacific*, 103:122–130.

Noguchi, K., Terashima, Y., and Awaki, H. (2009). A New Sample of Buried Active Galactic Nuclei Selected from the Second XMM-Newton Serendipitous Source Catalogue. *ApJ*, 705:454–467.

Noll, S., Burgarella, D., Giovannoli, E., et al. (2009). Analysis of galaxy spectral energy distributions from far-UV to far-IR with CIGALE: studying a SINGS test sample. *A&A*, 507:1793–1813.

Parisi, P., Masetti, N., Jiménez-Bailón, E., et al. (2012). Accurate classification of 29 objects detected in the 39 month Palermo Swift/BAT hard X-ray catalogue. *A&A*, 545:A101.

Parnovsky, S. L. and Parnowski, A. S. (2010). Large-scale collective motion of RFGC galaxies. *Ap&SS*, 325:163–175.

Pascale, E., Auld, R., Dariush, A., et al. (2011). The first release of data from the Herschel ATLAS: the SPIRE images. *MNRAS*, 415:911–917.

Pastrav, B. A., Popescu, C. C., Tuffs, R. J., and Sansom, A. E. (2013a). The effects of dust on the derived photometric parameters of disks and bulges in spiral galaxies. *A&A*, 553:A80.

Pastrav, B. A., Popescu, C. C., Tuffs, R. J., and Sansom, A. E. (2013b). The effects of dust on the photometric parameters of decomposed disks and bulges. *A&A*, 557:A137.

Peletier, R. F. and Balcells, M. (1997). Near-infrared surface photometry of bulges and disks of spiral galaxies. The data. *New A*, 1:349–362.

Peletier, R. F., Valentijn, E. A., Moorwood, A. F. M., and Freudling, W. (1994). The distribution of dust in Sb's and Sc's - K-band infrared imaging of a diameter limited sample of 37 galaxies. *A&AS*, 108:621–641.

Peng, C. Y., Ho, L. C., Impey, C. D., and Rix, H.-W. (2002). Detailed Structural Decomposition of Galaxy Images. *AJ*, 124:266–293.

Peters, S. P. C. (2014). *A closer look at the anatomy of spiral galaxies*. PhD thesis, Rijksuniversiteit Groningen.

Peters, S. P. C., van der Kruit, P. C., Allen, R. J., and Freeman, K. C. (2013). The Shape of Dark Matter Halos in Edge-on Galaxies: I. Overview of HI observations. *ArXiv e-prints*.

Pierini, D., Gordon, K. D., Witt, A. N., and Madsen, G. J. (2004). Dust Attenuation in Late-Type Galaxies. I. Effects on Bulge and Disk Components. *ApJ*, 617:1022–1046.

Pilbratt, G. L., Riedinger, J. R., Passvogel, T., et al. (2010). Herschel Space Observatory. An ESA facility for far-infrared and submillimetre astronomy. *A&A*, 518:L1.

Pinte, C., Ménard, F., Duchêne, G., and Bastien, P. (2006). Monte Carlo radiative transfer in protoplanetary disks. *A&A*, 459:797–804.

Planck Collaboration (2014). Planck 2013 results. XXVIII. The Planck Catalogue of Compact Sources. *A&A*, 571:A28.

Poglitsch, A., Waelkens, C., Geis, N., et al. (2010). The Photodetector Array Camera and Spectrometer (PACS) on the Herschel Space Observatory. *A&A*, 518:L2.

Pohlen, M., Dettmar, R.-J., and Lütticke, R. (2000). Cut-off radii of galactic disks . A new statistical study on the truncation of galactic disks. *A&A*, 357:L1–L4.

Pohlen, M., Zaroubi, S., Peletier, R. F., and Dettmar, R.-J. (2007). On the three-dimensional structure of edge-on disc galaxies. *MNRAS*, 378:594–616.

Popescu, C. C., Misiriotis, A., Kylafis, N. D., Tuffs, R. J., and Fischera, J. (2000). Modelling the spectral energy distribution of galaxies. I. Radiation fields and grain heating in the edge-on spiral NGC 891. *A&A*, 362:138–150.

Popescu, C. C. and Tuffs, R. J. (2002). The percentage of stellar light re-radiated by dust in late-type Virgo Cluster galaxies. *MNRAS*, 335:L41–L44.

Popescu, C. C., Tuffs, R. J., Dopita, M. A., et al. (2011). Modelling the spectral energy distribution of galaxies. V. The dust and PAH emission SEDs of disk galaxies. *A&A*, 527:A109.

Press, W. H., Teukolsky, S. A., Vetterling, W. T., and Flannery, B. P. (1992). *Numerical recipes in FORTRAN. The art of scientific computing*. Cambridge: University Press, 2nd edition.

Rajpaul, V. (2012). Genetic algorithms in astronomy and astrophysics. In Basson, I. and Botha, A. E., editors, *Proceedings of SAIP2011, the 56th Annual Conference of the South African Institute of Physics*.

Ramella, M., Geller, M. J., Huchra, J. P., and Thorstensen, J. R. (1995). The redshift-space neighborhoods of 36 loose groups of galaxies. 1: The data. *AJ*, 109:1458–1475.

Renaud, F., Bournaud, F., Emsellem, E., et al. (2013). A sub-parsec resolution simulation of the Milky Way: global structure of the interstellar medium and properties of molecular clouds. *MNRAS*, 436:1836–1851.

Rigby, E. E., Maddox, S. J., Dunne, L., et al. (2011). Herschel-ATLAS: first data release of the Science Demonstration Phase source catalogues. *MNRAS*, 415:2336–2348.

Robitaille, T. P. (2011). HYPERION: an open-source parallelized three-dimensional dust continuum radiative transfer code. *A&A*, 536:A79.

Robitaille, T. P., Whitney, B. A., Indebetouw, R., and Wood, K. (2007). Interpreting Spectral Energy Distributions from Young Stellar Objects. II. Fitting Observed SEDs Using a Large Grid of Precomputed Models. *ApJS*, 169:328–352.

Roth, M. M., Kelz, A., Fechner, T., et al. (2005). PMAS: The Potsdam Multi-Aperture Spectrophotometer. I. Design, Manufacture, and Performance. *PASP*, 117:620–642.

Russell, D. G. (2002). The H I Line Width/Linear Diameter Relationship as an Independent Test of the Hubble Constant. *ApJ*, 565:681–695.

Rybicki, G. B. and Lightman, A. P. (1979). *Radiative processes in astrophysics*. Wiley.

Saftly, W., Baes, M., and Camps (2014). Hierarchical octree and k-d tree grids for 3D radiative transfer simulations. *A&A*, 561:A77.

Saftly, W., Baes, M., De Geyter, G., and Camps, P. (2015). Large/small-scale structures and the dust energy balance problem in spiral galaxies. *MNRAS*, in press.

Saftly, W., Camps, P., Baes, M., et al. (2013). Using hierarchical octrees in Monte Carlo radiative transfer simulations. *A&A*, 554:A10.

Saha, K., de Jong, R., and Holwerda, B. (2009). The onset of warps in Spitzer observations of edge-on spiral galaxies. *MNRAS*, 396:409–422.

Sahinler, S. and Topuz, D. (2007). Bootstrap and jackknife resampling algorithms for estimation of regression parameters. *Journal of Applied Quantitative Methods*, 408:188–199.

Salpeter, E. E. (1955). The Luminosity Function and Stellar Evolution. *ApJ*, 121:161.

Sánchez, S. F., Kennicutt, R. C., Gil de Paz, A., et al. (2012). CALIFA, the Calar Alto Legacy Integral Field Area survey. I. Survey presentation. *A&A*, 538:A8.

Sánchez, S. F., Rosales-Ortega, F. F., Iglesias-Paramo, J., et al. (2014). A characteristic oxygen abundance gradient in galaxy disks unveiled with CALIFA. *A&A*, in press (arXiv:1311.7052).

Sánchez, S. F., Rosales-Ortega, F. F., Jungwiert, B., et al. (2013). Mass-metallicity relation explored with CALIFA. I. Is there a dependence on the star-formation rate? *A&A*, 554:A58.

Sanchez-Saavedra, M. L., Battaner, E., and Florido, E. (1990). Frequency of Warped Spiral Galaxies at Visible Wavelengths. *MNRAS*, 246:458.

Sánchez-Saavedra, M. L., Battaner, E., Guijarro, A., López-Corredoira, M., and Castro-Rodríguez, N. (2003). A catalog of warps in spiral and lenticular galaxies in the Southern hemisphere. *A&A*, 399:457–467.

Schaye, J., Crain, R. A., Bower, R. G., et al. (2015). The EAGLE project: simulating the evolution and assembly of galaxies and their environments. *MNRAS*, 446:521–554.

Schechtman-Rook, A. and Bershady, M. A. (2013a). Near-infrared Detection of a Super-thin Disk in NGC 891. *ApJ*, 773:45.

Schechtman-Rook, A. and Bershady, M. A. (2013b). Near-Infrared Detection of Super-Thin Disks of Massive Spiral Galaxies. In *American Astronomical Society Meeting Abstracts*, volume 221 of *American Astronomical Society Meeting Abstracts*, page 146.22.

Schechtman-Rook, A. and Bershady, M. A. (2014a). Discovery of Super-Thin Disks in Nearby Edge-on Spiral Galaxies. In Seigar, M. S. and Treuthardt, P., editors, *Astronomical Society of the Pacific Conference Series*, volume 480 of *Astronomical Society of the Pacific Conference Series*, page 85.

Schechtman-Rook, A. and Bershady, M. A. (2014b). Near-infrared Structure of Fast and Slow-rotating Disk Galaxies. *ApJ*, 795:136.

Schechtman-Rook, A., Bershady, M. A., and Wood, K. (2012). The Three-dimensional Distribution of Dust in NGC 891. *ApJ*, 746:70.

Schwarzkopf, U. and Dettmar, R.-J. (2000). The influence of interactions and minor mergers on the structure of galactic disks I. Observations and disk models. *A&AS*, 144:85–121.

Semionov, D. and Vansevičius, V. (2005). Radiative Transfer Problem in Dusty Galaxies: Galactic Fog Engine. *Baltic Astronomy*, 14:543–553.

Seon, K.-i., Witt, A. N., Shinn, J.-h., and Kim, I.-j. (2014). Diffuse Extraplanar Dust in NGC 891. *ApJ*, 785:L18.

Shetty, R., Kauffmann, J., Schnee, S., and Goodman, A. A. (2009). The Effect of Noise on the Dust Temperature-Spectral Index Correlation. *ApJ*, 696:676–680.

Shirley, Y. L., Huard, T. L., Pontoppidan, K. M., et al. (2011). Observational Constraints on Submillimeter Dust Opacity. *ApJ*, 728:143.

Silva, L., Fontanot, F., and Granato, G. L. (2012). Fast radiative transfer of dust reprocessing in semi-analytic models with artificial neural networks. *MNRAS*, 423:746–755.

Siringo, G., Kreysa, E., Kovács, A., et al. (2009). The Large APEX BOlometer CAmera LABOCA. *A&A*, 497:945–962.

Skilling, J. (2004). Nested Sampling. In Fischer, R., Preuss, R., and Toussaint, U. V., editors, *American Institute of Physics Conference Series*, volume 735 of *American Institute of Physics Conference Series*, pages 395–405.

Skrutskie, M. F., Cutri, R. M., Stiening, R., et al. (2006). The Two Micron All Sky Survey (2MASS). *AJ*, 131:1163–1183.

Slezak, E., Mars, G., Bijaoui, A., Balkowski, C., and Fontanelli, P. (1988). Study of a field in the Coma supercluster. I - Automated galaxies count. *A&AS*, 74:83–106.

Smith, D. J. B., Dunne, L., da Cunha, E., et al. (2012a). Herschel-ATLAS: multi-wavelength SEDs and physical properties of 250 μm selected galaxies at z ¡ 0.5. *MNRAS*, 427:703–727.

Smith, D. J. B., Hardcastle, M. J., Jarvis, M. J., et al. (2013). Isothermal dust models of Herschel-ATLAS galaxies. *MNRAS*, 436:2435–2453.

Smith, M. W. L., Eales, S. A., Gomez, H. L., et al. (2012b). The Herschel Exploitation of Local Galaxy Andromeda (HELGA) II: Dust and Gas in Andromeda. *ArXiv e-prints*.

Smith, M. W. L., Eales, S. A., Gomez, H. L., et al. (2012c). The Herschel Exploitation of Local Galaxy Andromeda (HELGA). II. Dust and Gas in Andromeda. *ApJ*, 756:40.

Smith, M. W. L., Gomez, H. L., Eales, S. A., et al. (2012d). The Herschel Reference Survey: Dust in Early-type Galaxies and across the Hubble Sequence. *ApJ*, 748:123.

Springob, C. M., Masters, K. L., Haynes, M. P., Giovanelli, R., and Marinoni, C. (2009). Erratum: "SFI++ II: A New I-Band Tully-Fisher Catalog, Derivation of Peculiar Velocities and Data Set Properties" ¡A href="bib_query?2007ApJS..172..599S"¿ (2007, ApJS, 172, 599)¡/A¿. *ApJS*, 182:474–475.

Stalevski, M., Fritz, J., Baes, M., Nakos, T., and Popović, L. Č. (2011). AGN Dusty Tori as a Clumpy Two-Phase Medium: the 10 μ m Silicate Feature. *Baltic Astronomy*, 20:490–494.

Stalevski, M., Fritz, J., Baes, M., Nakos, T., and Popović, L. Č. (2012). 3D radiative transfer modelling of the dusty tori around active galactic nuclei as a clumpy two-phase medium. *MNRAS*, 420:2756–2772.

Steinacker, J., Bacmann, A., Henning, T., Klessen, R., and Stickel, M. (2005). 3D continuum radiative transfer in complex dust configurations. II. 3D structure of the dense molecular cloud core ρ Oph D. *A&A*, 434:167–180.

Steinacker, J., Baes, M., and Gordon, K. D. (2013). Three-Dimensional Dust Radiative Transfer*. *ARA&A*, 51:63–104.

Steinacker, J., Henning, T., Bacmann, A., and Semenov, D. (2003). 3D continuum radiative transfer in complex dust configurations around stellar objects and active galactic nuclei. I. Computational methods and capabilities. *A&A*, 401:405–418.

Summerfield, M. (2010). *Advanced Qt Programming: Creating Great Software with C++ and Qt 4*. Prentice Hall Open Source Software Development Series. Addison-Wesley.

Surace, J. A., Sanders, D. B., and Mazzarella, J. M. (2004). An IRAS High Resolution Image Restoration (HIRES) Atlas of All Interacting Galaxies in the IRAS Revised Bright Galaxy Sample. *AJ*, 127:3235–3272.

Tempel, E., Tamm, A., and Tenjes, P. (2010). Dust-corrected surface photometry of M 31 from Spitzer far-infrared observations. *A&A*, 509:A91.

Theis, C. and Kohle, S. (2001). Multi-method-modeling of interacting galaxies. I. A unique scenario for NGC 4449? *A&A*, 370:365–383.

Theureau, G., Hanski, M. O., Coudreau, N., Hallet, N., and Martin, J.-M. (2007). Kinematics of the Local Universe. XIII. 21-cm line measurements of 452 galaxies with the Nançay radiotelescope, JHK Tully-Fisher relation, and preliminary maps of the peculiar velocity field. *A&A*, 465:71–85.

Thompson, M. A., Smith, D. J. B., Stevens, J. A., et al. (2010). A search for debris disks in the Herschel-ATLAS. *A&A*, 518:L134.

Tielens, A. G. G. M. (2005). *The Physics and Chemistry of the Interstellar Medium*. Cambridge University Press.

Tuffs, R. J., Popescu, C. C., Völk, H. J., Kylafis, N. D., and Dopita, M. A. (2004). Modelling the spectral energy distribution of galaxies. III. Attenuation of stellar light in spiral galaxies. *A&A*, 419:821–835.

Tully, R. B., Rizzi, L., Shaya, E. J., et al. (2009). The Extragalactic Distance Database. *AJ*, 138:323–331.

Valentijn, E. A. (1990). Opaque spiral galaxies. *Nature*, 346:153–155.

Valentijn, E. A. (1994). The Opacities of Spiral Galaxies Using Volume Representative Samples. *MNRAS*, 266:614.

van den Bergh, S., Li, W., and Filippenko, A. V. (2003). Classifications of the Host Galaxies of Supernovae, Set II. *PASP*, 115:1280–1288.

van der Kruit, P. C. and Freeman, K. C. (2011). Galaxy Disks. *ARA&A*, 49:301–371.

Veneziani, M., Ade, P. A. R., Bock, J. J., et al. (2010). Properties of Galactic Cirrus Clouds Observed by BOOMERANG. *ApJ*, 713:959–969.

Verstappen, J., Baes, M., Fritz, J., et al. (2012). Herschel Observations of Edge-on Spirals (HEROES): I. Data presentation and dust mass determination. *MNRAS, submitted*.

Verstappen, J., Fritz, J., Baes, M., et al. (2013). HERschel Observations of Edge-on Spirals (HEROES). I. Far-infrared morphology and dust mass determination. *A&A*, 556:A54.

Viaene, S., De Geyter, G., Baes, M., and Fritz, J. (2015). The Herschel Virgo Cluster SurveyXIX. A diffuse dust component in the dusty lenticular NGC 4370? *A&A*, submitted.

Viaene, S., Fritz, J., Baes, M., et al. (2014). The Herschel Exploitation of Local Galaxy Andromeda (HELGA). IV. Dust scaling relations at sub-kpc resolution. *A&A*, 567:A71.

Vidal, E. and Baes, M. (2007). D Dust Radiative Transfer Simulations in the Inhomogeneous Circumstellar Medium. *Baltic Astronomy*, 16:101–103.

Vika, M., Bamford, S. P., Häußler, B., et al. (2013). MegaMorph - multiwavelength measurement of galaxy structure. Sérsic profile fits to galaxies near and far. *MNRAS*, 435:623–649.

Vinkó, J., Bíró, I. B., Csák, B., et al. (2003). The Type Ia Supernova 2001V in NGC 3987. *A&A*, 397:115–120.

Vlahakis, C., Dunne, L., and Eales, S. (2005). The SCUBA Local Universe Galaxy Survey - III. Dust along the Hubble sequence. *MNRAS*, 364:1253–1285.

Wall, M. (1996). Galib: A c++ library of genetic algorithm components. *PhD thesis, Mechanical Engineering Department, Massachusetts Institute of Technology*.

Watson, D. M., Leisenring, J. M., Furlan, E., et al. (2009). Crystalline Silicates and Dust Processing in the Protoplanetary Disks of the Taurus Young Cluster. *ApJS*, 180:84–101.

Werner, M. W., Roellig, T. L., Low, F. J., et al. (2004). The Spitzer Space Telescope Mission. *ApJS*, 154:1–9.

Willick, J. A., Courteau, S., Faber, S. M., et al. (1997). Homogeneous Velocity-Distance Data for Peculiar Velocity Analysis. III. The Mark III Catalog of Galaxy Peculiar Velocities. *ApJS*, 109:333.

Witt, A. N. (1977). Multiple scattering in reflection nebulae. I - A Monte Carlo approach. *ApJS*, 35:1–6.

Witt, A. N., Thronson, Jr., H. A., and Capuano, Jr., J. M. (1992). Dust and the transfer of stellar radiation within galaxies. *ApJ*, 393:611–630.

Wright, E. L., Eisenhardt, P. R. M., Mainzer, A. K., et al. (2010). The Wide-field Infrared Survey Explorer (WISE): Mission Description and Initial On-orbit Performance. *AJ*, 140:1868–1881.

Xilouris, E. M., Alton, P. B., Davies, J. I., et al. (1998). Optical and NIR modelling of NGC 891. *A&A*, 331:894–900.

Xilouris, E. M., Byun, Y. I., Kylafis, N. D., Paleologou, E. V., and Papamastorakis, J. (1999). Are spiral galaxies optically thin or thick? *A&A*, 344:868–878.

Xilouris, E. M., Kylafis, N. D., Papamastorakis, J., Paleologou, E. V., and Haerendel, G. (1997). The distribution of stars and dust in spiral galaxies: the edge-on spiral UGC 2048. *A&A*, 325:135–143.

Xilouris, E. M., Tabatabaei, F. S., Boquien, M., et al. (2012). Cool and warm dust emission from M 33 (HerM33es). *A&A*, 543:A74.

Yun, M. S., Reddy, N. A., and Condon, J. J. (2001). Radio Properties of Infrared-selected Galaxies in the IRAS 2 Jy Sample. *ApJ*, 554:803–822.

Yusef-Zadeh, F., Morris, M., and White, R. L. (1984). Bipolar reflection nebulae - Monte Carlo simulations. *ApJ*, 278:186–194.

Zibetti, S., Charlot, S., and Rix, H.-W. (2009). Resolved stellar mass maps of galaxies - I. Method and implications for global mass estimates. *MNRAS*, 400:1181–1198.

Zubko, V., Dwek, E., and Arendt, R. G. (2004). Interstellar Dust Models Consistent with Extinction, Emission, and Abundance Constraints. *ApJS*, 152:211–249.